



HAL
open science

Multi-Messenger astronomy, localisation of transient sources of gravitational waves and optical follow-up of gravitational wave candidates

Pierre-Alexandre Duverne

► To cite this version:

Pierre-Alexandre Duverne. Multi-Messenger astronomy, localisation of transient sources of gravitational waves and optical follow-up of gravitational wave candidates. High Energy Astrophysical Phenomena [astro-ph.HE]. Université Paris-Saclay, 2022. English. NNT : 2022UPASP117 . tel-03885486

HAL Id: tel-03885486

<https://theses.hal.science/tel-03885486>

Submitted on 5 Dec 2022

HAL is a multi-disciplinary open access archive for the deposit and dissemination of scientific research documents, whether they are published or not. The documents may come from teaching and research institutions in France or abroad, or from public or private research centers.

L'archive ouverte pluridisciplinaire **HAL**, est destinée au dépôt et à la diffusion de documents scientifiques de niveau recherche, publiés ou non, émanant des établissements d'enseignement et de recherche français ou étrangers, des laboratoires publics ou privés.

Multi-Messenger astronomy, localisation of transient sources of gravitational waves and optical follow-up of gravitational wave candidates.

*Astronomie Multi-Messagers: de la localisation des sources
transitoires d'ondes gravitationnelles au suivi optique*

Thèse de doctorat de l'université Paris-Saclay

École doctorale n° 576, Particules, Hadrons, Énergie, Noyau, Instrumentation, Imagerie,
Cosmos et Simulation (PHENIICS)

Spécialité de doctorat: Astroparticules et Cosmologie

Graduate School : Physique. Référent : Faculté des sciences d'Orsay

Thèse préparée dans l'unité de recherche: IJCLab (Université Paris-Saclay, CNRS), 91405, Orsay,
France, sous la direction de Patrice HELLO, Professeur des universités, le co-encadrement de
Sarah ANTIER, Astronome adjoint, Observatoire de la Côte d'Azur.

Thèse soutenue à Paris-Saclay, le 25 Octobre 2022, par

Pierre-Alexandre DUVERNE

Composition du jury

Membres du jury avec voix délibérative

Sophie HENROT-VERSILLÉ Directrice de recherche, Université Paris-Saclay	Présidente
Pierre ANTILOGUS Directeur de recherche, Sorbonne Université	Rapporteur & Examineur
Samaya NISSANKE Professeure des universités, Université d'Amsterdam	Rapporteuse & Examinatrice
Christopher BERRY Professeur Assistant, University of Glasgow	Examineur
Frédéric PIRON Directeur de recherche, Université de Montpellier	Examineur

CONTENTS

Synthèse	1
Introduction	9
1 Dawn and rise of the Multi-Messenger Astronomy	13
1.1 Gravitational waves	13
1.1.1 Theory	13
1.1.2 Sources	15
1.1.3 Gravitational Waves Detectors Overview	19
1.1.4 Ground-Based GW Detectors	21
1.1.5 Gravitational waves searches	26
1.2 Electromagnetic counterparts to GW	27
1.2.1 Gamma-ray Bursts	28
1.2.2 Kilonovae	28
1.2.3 Other counterparts	31
1.3 Combining GW and EM observations	31
1.3.1 GW-GRB joint observations	32
1.3.2 GW-Kilonova joint observations	33
1.3.3 Multi-messenger searches during O3	36
1.4 August 17 th , 2017	37
1.4.1 Gravitational wave signal: GW170817	37
1.4.2 Gamma-ray counterpart: GRB170817A	37
1.4.3 Optical counterpart: AT170817gfo	39
1.4.4 X-ray counterpart	40
1.4.5 Radio counterpart	40
1.4.6 Neutrino emission	40
1.5 Scientific outcomes of GW170817	40
1.5.1 Inferences on the merger	40
1.5.2 Fundamental physics	43
1.6 Was GW170817 a lucky event?	44
2 GW-Based Multi-Messenger Astronomy	45
2.1 Searching for GW in low latency	45
2.1.1 Unmodelled searches	45
2.1.2 CBC searches	45
2.2 PyCBC Live	46
2.2.1 Waveform	46
2.2.2 Matched-filtering	48

2.2.3	Template bank	49
2.2.4	Identifying Gravitational Wave candidates	52
2.2.5	Significance of a GW candidate event	53
2.3	Low latency spatial localisation	55
2.3.1	Localising a GW	55
2.3.2	Bayestar	57
2.4	Testing Bayestar 's self-consistency	61
2.4.1	Motivation	61
2.4.2	Simulated Astrophysical populations	61
2.4.3	Baseline Percentile-Percentile test	64
2.4.4	Finding bias origin	67
2.4.5	ξ parameter effect	70
2.4.6	Real Noise Influence on Localisation	70
2.4.7	Jittering Localization Parameters	72
2.4.8	Jittering Chirp Mass	74
2.5	End-to-end simulation with PyCBC Live	74
2.5.1	On-line search with the O3 bank	76
2.5.2	Template bank influence on localization	79
2.6	Conclusion on Bayestar Accuracy	79
3	Optical follow-up of gravitational waves	81
3.1	Kilonova observational difficulties	81
3.1.1	Intrinsic difficulties	81
3.1.2	Extrinsic difficulties	82
3.1.3	Addressing Observational Constraints	86
3.2	GRANDMA	86
3.2.1	Meet GRANDMA	86
3.2.2	Observational strategy	87
3.2.3	The O3 infrastructure	88
3.3	Muphoten	89
3.3.1	Motivation	89
3.3.2	Pipeline Overview	89
3.3.3	Error Budget	95
3.3.4	Additional Features	95
3.3.5	First test and application: AT2018cow	97
3.3.6	Conclusion on Muphoten	105
3.4	GRANDMA during O3	105
3.4.1	O3 overview	105
3.4.2	Follow-up of S200213t	105
3.4.3	Follow-up of SN2019wxt	109
3.5	Preparing O4 (I) : ZTF/Fink campaign	110
3.5.1	Motivation	110
3.5.2	The Kilonova-Catcher initiative	110

3.5.3	FINK and the alert selection	111
3.5.4	ReadyforO4 overview	113
3.5.5	Observation Summary	115
3.5.6	Offline source modeling	120
3.5.7	Conclusion and Lessons	120
Conclusion		121
Appendix		125
A Contribution to the GWTC-3 catalog		125
B Photometric Systems		129
C Preparing O4 (II) : Swift GRB campaign		135

SYNTHÈSE

L'astronomie multi-messagers (AMM) vise à combiner les informations apportées par différents objets physiques, les messagers. À l'heure actuelle, il y a quatre messagers astrophysiques pouvant être impliqués dans le suivi d'un événement astrophysique:

- Les neutrinos: ce sont des particules neutres, interagissant très faiblement avec la matière. Ils sont émis en grandes quantités lors d'événements cataclysmiques comme les supernovæ ou les coalescences de binaires d'étoiles à neutrons.
- Les rayons cosmiques de très hautes énergies: ce sont des particules chargées, généralement des protons, pouvant atteindre des énergies du domaine de l'exaélectronvolt. Si les sources de ces rayonnements sont encore mal connues, certaines sont très probablement d'origine extra-galactique.
- Les ondes gravitationnelles: ce sont des vibrations de l'espace-temps se propageant à la vitesse de la lumière. Elles sont émises lorsque des masses sont accélérées, mais les signaux sont si faibles qu'elles ne deviennent détectables que lorsque des objets compacts et massifs tels que des trous noirs ou des étoiles à neutrons fusionnent.
- Les photons: de loin les plus communément utilisées pour l'observation du ciel. Les photons sont observés à toutes les énergies, des plus basses avec les ondes radios au plus élevées avec les rayons X et gammas, en passant par le domaine optique pour des énergies modérées.

Le domaine de l'AMM est particulièrement vaste et cette thèse est circonscrite à l'étude du suivi par des instruments optiques de phénomènes transitoires d'ondes gravitationnelles. Dans un premier temps, le champ de l'AMM est présenté en partant de l'événement du 17 août 2017, lors duquel une onde gravitationnelle a été détectée en coïncidence avec des émissions électromagnétiques sur tout le spectre. Puis, dans le second chapitre, on présente la recherche en ligne des ondes gravitationnelles, leur localisation rapide par l'algorithme **Bayestar** ainsi qu'une étude sur la recherche de biais systématique pour ce dernier outil afin de maximiser les chances de détection de contreparties électromagnétiques. Finalement, le dernier chapitre présente le suivi optique des candidats d'ondes gravitationnelles. En particulier, le travail réalisé dans le réseau GRANDMA et le code destiné à la réduction des images des instruments et qui constitue le cœur de ce travail.

La naissance de l'astronomie multi-messagers

Le 17 août 2017, les deux détecteurs d'ondes gravitationnelles LIGO situés aux États-Unis observent un signal émis par la coalescence de deux étoiles à neutrons. En coïncidence

avec l'onde gravitationnelle, le satellite Fermi détecte un sursaut gamma 1.7s plus tard. Les deux signaux sont compatibles à la fois d'un point de vue spatial et temporel et cette observation conjointe a déclenché une campagne d'observation afin de trouver la contrepartie optique de l'événement. Elle est détectée 11 h plus tard par le télescope One-Meter, Two-Hemispheres dans la bande i . Cinq autres équipes indépendantes confirment la détection. Celle-ci est située dans une galaxie située à une distance de 40 Mpc. Les spectres acquis et la caractérisation photométrique de la source confirme qu'il s'agit de la première kilonova clairement identifiée. Les émissions *afterglow* X et radio sont détectées neuf et seize jours plus tard par le satellite Chandra et le radio-télescope VLA respectivement. Les observations gravitationnelles et électromagnétiques sont rassemblées dans la Figure 1.

Cet événement a eu des retombées considérables pour de nombreux domaines. Il a confirmé, entre autre, que les fusions d'étoiles à neutrons sont les progéniteurs de certains sursauts gamma courts. Mais il a aussi fourni une estimation de la constante de Hubble, ou des contraintes sur l'équation d'état de la matière nucléaire. Si les observations apportées par GW170817 ne permettent pas encore d'atteindre les contraintes fournis par d'autres observations, elles montrent l'intérêt qu'auraient de nouvelles détections multi-messagers. Ce constat aboutit à la naissance de l'astronomie multi-messagers basées sur les ondes gravitationnelles étudiées dans cette thèse.

Détecter et localiser des ondes gravitationnelles en ligne

Afin de permettre le suivi des détections d'ondes gravitationnelles par les détecteurs LIGO et le détecteur européen Virgo, il est nécessaire d'analyser les données qu'ils produisent en ligne. PyCBC Live est l'un des algorithmes utilisés pour trouver les signaux dans les données et produire des alertes diffusées aux autres communautés d'astronomes. Il est basé sur du *filtrage adapté* des données dans le domaine fréquentiel. Cette méthode permet de détecter des signaux d'ondes gravitationnelles dont la forme est connue dans des données bruitées. Le filtrage se fait en corrélant les données avec un modèle ayant la même forme que le signal recherché. Dans le cas des ondes gravitationnelles, le signal cherché n'est pas connu par avance. C'est pourquoi, avant de lancer une analyse, une banque de modèles de forme d'onde gravitationnelle est généré pour filtrer les données des détecteurs. La banque est produite en simulant des fusions d'objets compacts avec différentes masses et différents spins. Lors de la dernière acquisition de données de LIGO et Virgo, la banque utilisée par PyCBC Live contenait 400,000 modèles.

Une fois que le filtrage a permis d'identifier un signal dans les données, une estimation de la localisation de la source doit être faite afin de pouvoir poursuivre les observations dans le domaine électromagnétique. Comme les ondes gravitationnelles sont détectées avec un réseau de trois instruments fournissant le temps d'arrivée du signal, la localisation est basé sur de la triangulation. Une paire d'instruments ayant observé le signal permet de contraindre la région d'émission à un anneau sur le ciel. Si plus de deux détecteurs sont impliqués dans la détection, il y a un anneau par paire et la source se trouve

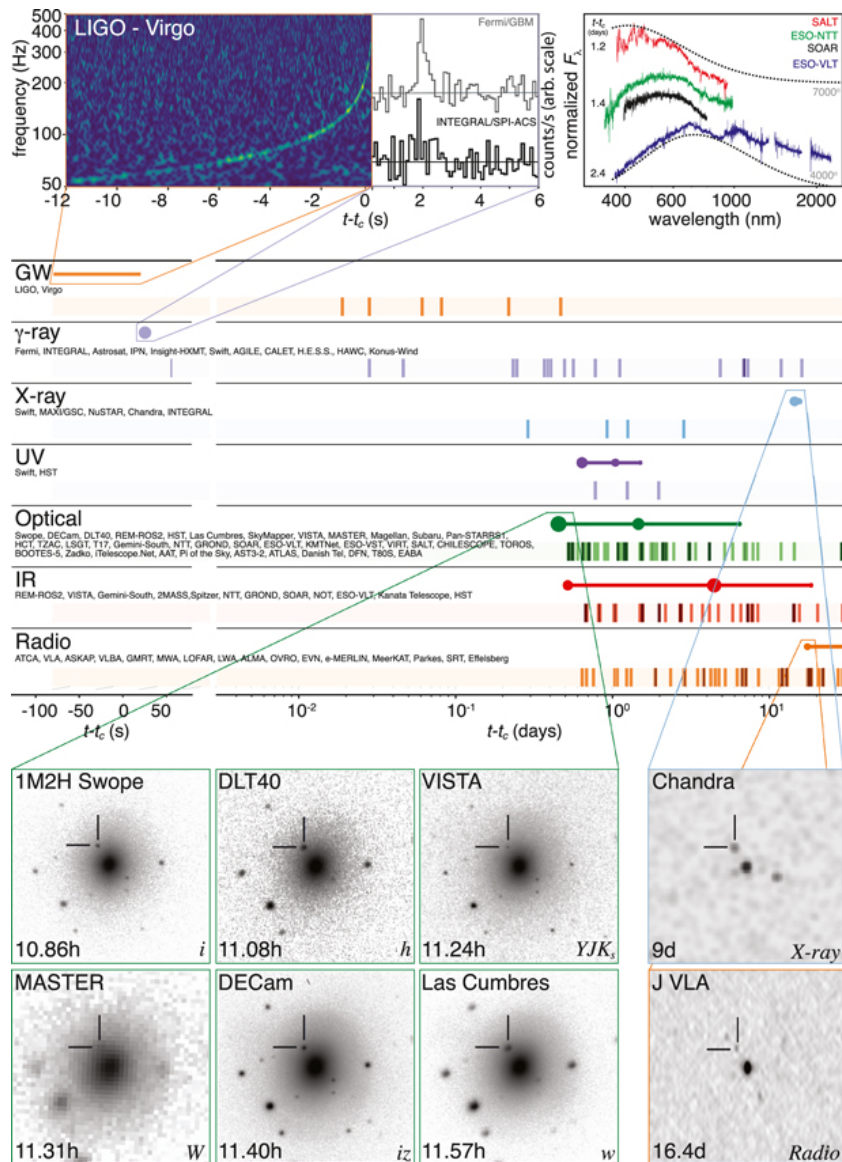


Figure 1: Aperçu des observations de 170817. Le graphe en haut à gauche montre le signal gravitationnel et sa forme caractéristique : le *chirp*. Au centre, sont présentées les courbes de lumière du sursaut gamma observé par les satellites Fermi et INTEGRAL. Les spectres de la kilonova pris par différents télescope au sol sont présentés en haut à droite. Le centre de la figure montre en détails les observations ayant permis de découvrir et de caractériser les différentes contreparties électromagnétiques de GW170817. La partie inférieure droite de la figure montre les six images des télescopes optiques ayant permise la découverte de la kilonova AT2017gfo. La partie à gauche montre les observations X (en haut) et radios (en bas) qui ont conduit à la découverte des afterglows. Cette figure est extraite de [159].

à l'intersection de tous les anneaux. Pour maximiser les chances de détections, cette localisation doit être faite rapidement. Ceci est fait grâce à l'algorithme **Bayestar**, qui permet d'avoir une localisation en quelques secondes à une minute en triangulant le signal via une approche Bayésienne.

Tester la précision de Bayestar

Les cartes de localisation fournies par **Bayestar** sont cruciales pour le suivi électromagnétique des alertes d'ondes gravitationnelles. C'est pourquoi, une partie de cette thèse est dédiée à la recherche de biais systématique dans l'algorithme **Bayestar**. Cette étude est faite en générant une population de signaux d'OG injectés dans du bruit Gaussien et stationnaire, puis **Bayestar** est utilisé pour localiser le signal. Ensuite, pour chaque carte produite, la plus petite région contenant la vraie position de l'injection est estimée ainsi que la probabilité cumulée contenue dans celle-ci. Cette probabilité est appelée *probabilité de recherche* (PR). Il est possible d'estimer si la localisation de **Bayestar** est biaisée étudiant la distribution cumulative de PR pour la population de signaux simulés via un test pourcentage-pourcentage. Si la distribution n'est pas biaisée, le graphe pourcentage-pourcentage (un exemple est donné par la Figure 2) est diagonal, dans le cas où elle se trouve au-dessus de la diagonale, **Bayestar** surestime les incertitudes de localisation, en dessous, il les sous-estime.

Pour un premier jeu de simulation, la distribution de PR, visible dans la Figure 2, montre une déviation significative dans la direction d'une surestimation des erreurs pour les fusions de trous noirs et celles d'étoiles à neutrons.

Afin de trouver l'origine de cette déviation, plusieurs hypothèses ont été testées:

- le nombre de détecteurs dans le réseau
- la position des instruments
- la force des signaux injectés.

Aucun de ces tests n'est concluant, la déviation est toujours visible dans les graphes pourcentage-pourcentage. Le dernier test a consisté à chercher un biais interne à **Bayestar**. Dans la publication originale, un test pourcentage-pourcentage est réalisé, et si le graphe présenté est diagonal, c'est grâce à l'utilisation d'un facteur $\xi = 0.83$, codé en dur. Ce dernier fonctionne en redimensionnant l'amplitude du signal avant que **Bayestar** ne triangule le signal, ce qui, *in fine*, dilate la carte de localisation. Pour vérifier que le biais observé précédemment est bien lié à ξ , le code a été recompilé et utilisant $\xi = 1.0$, ce qui annule son effet. Dans ce cas, la Figure 2.13 résultant de ces simulations ne montre plus de déviation, confirmant que le biais est bien causé par ξ .

À la recherche de l'origine de ξ

Bien que le facteur ξ soit toujours présent dans **Bayestar**, plusieurs questions sont encore en suspens à ce stade. En particulier, la raison pour laquelle il a dû être implémenté lors

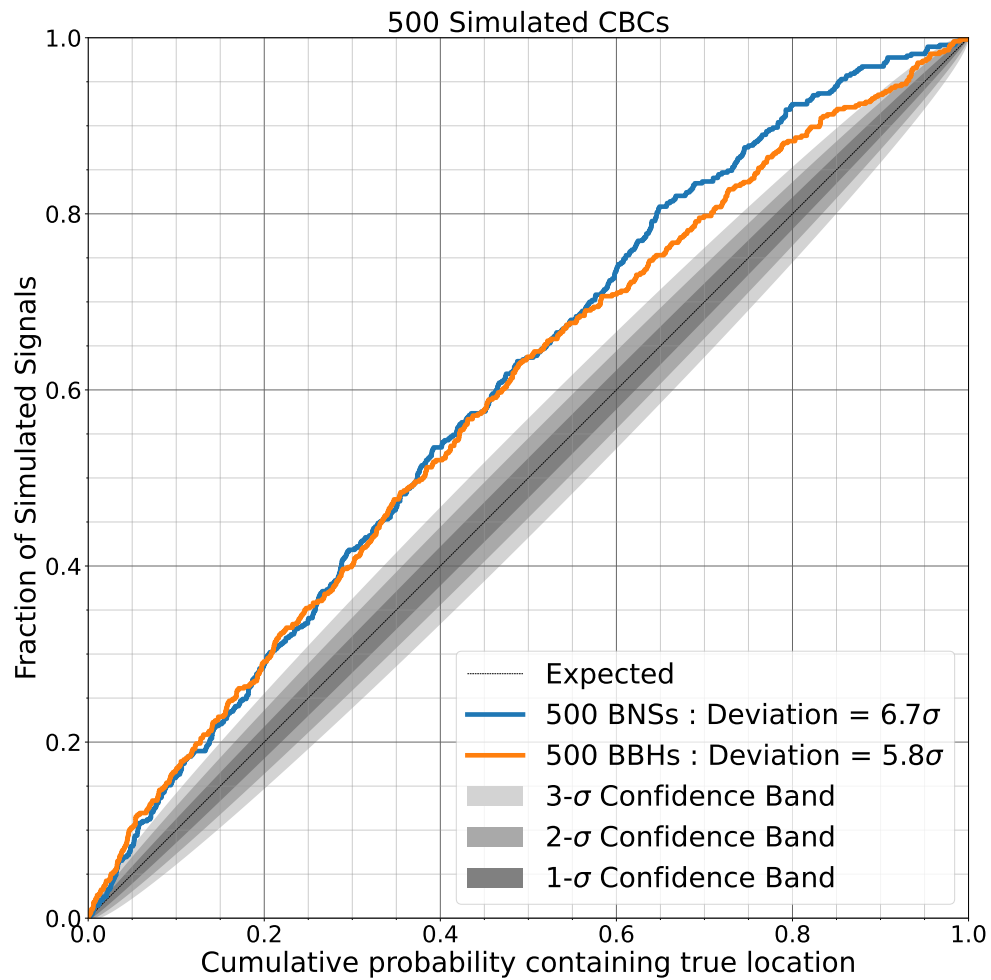


Figure 2: Graphe pourcentage-pourcentage pour une population de fusion de trous noirs (BBH) et une population de fusion d'étoile à neutrons (BNS). La courbe bleue correspond à la distribution de PR pour les cartes de 500 BNS et la courbe orange à celle de 500 BBH. Les régions grisées correspondent aux intervalles de confiance à 1, 2 et 3- σ pour la variabilité attendue pour les populations de signaux simulés.

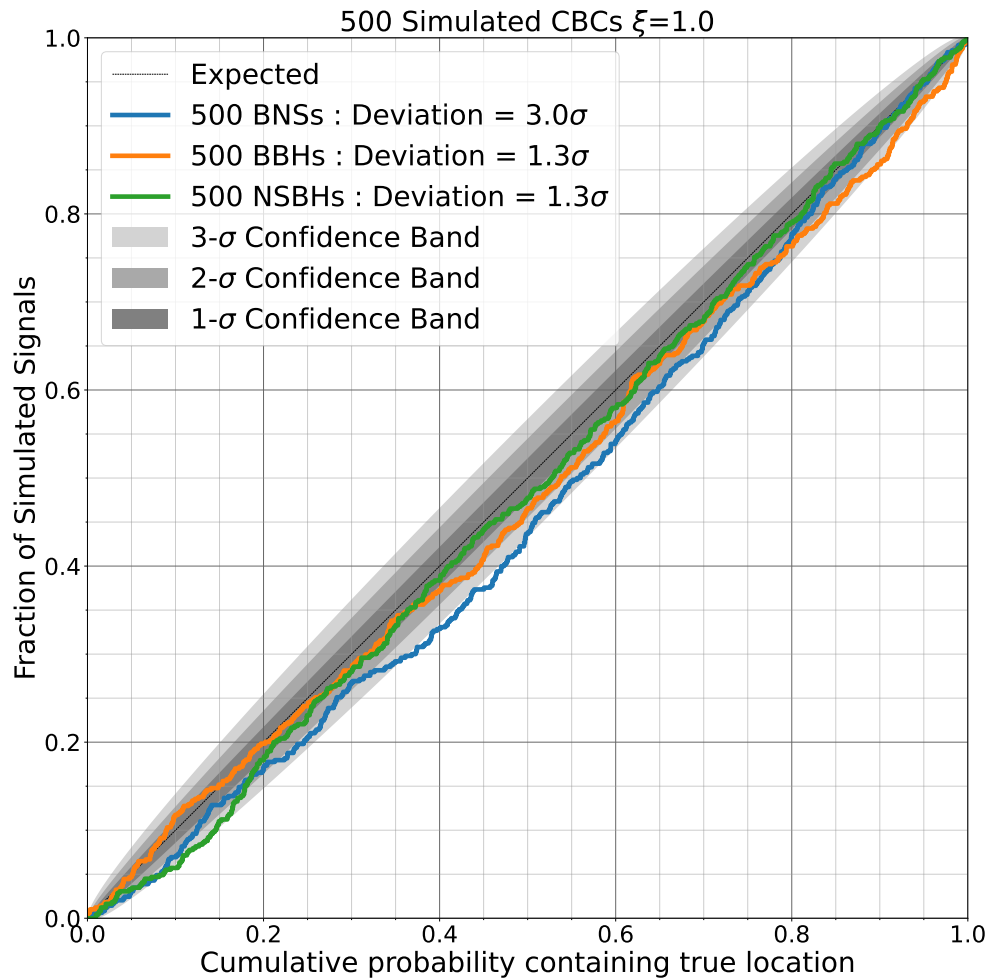


Figure 3: Graphe pourcentage-pourcentage pour différentes populations de coalescences en utilisant $\xi = 1.0$. Les BBH sont en orange, les BNS en bleu et les fusions étoile à neutrons avec un trou noir (NSBH) sont en vert. Les déviations sont dans les trois cas inférieures à $3\text{-}\sigma$, indiquant qu'il n'y a plus de biais décelable dans la localisation.

de la création du code n'est pas précisée. C'est pourquoi de nouveaux tests ont été menés pour, d'une part vérifier si ξ doit être maintenu dans le code, et d'autre part trouver la raison pour laquelle il a dû être utilisé en premier lieu.

La première hypothèse testée est l'influence des non-gaussianités et des instationnarités des données du détecteurs. En effet, pour les premiers tests, les injections ont été faites dans du bruit Gaussien. En utilisant les données produites lors des dernières observations de LIGO et Virgo pour faire les injections, le test pourcentage-pourcentage montre toujours une déviation lorsque $\xi = 0.83$. Ainsi, l'utilisation de bruit Gaussien pour les simulations n'a pas d'influence visible sur la localisation. C'est pourquoi, les tests suivants sont faits avec des données entièrement simulées, comme précédemment.

Par la suite, on utilise une instance de PyCBC Live pour vérifier l'influence d'une recherche en ligne sur la localisation. On crée alors des données contenant des injections de BNS que l'on analyse avec PyCBC Live. Les candidats retrouvés par l'algorithme de recherche sont ensuite localisés avec **Bayestar** afin de produire le graphe pourcentage-pourcentage. Au final, le graphe produit montre que cette fois, ξ est nécessaire pour retrouver un graphe diagonal. Ce résultat, visible dans le chapitre 2, permet d'affirmer que ξ doit être utilisé pour des candidats produits par une analyse en ligne. D'autre part, il permet aussi d'émettre une hypothèse sur l'origine de ξ . Ce dernier est nécessaire afin de compenser la différence entre les masses et spins des objets ayant produit l'OG et les valeurs de ces paramètres pour le modèle ayant produit le candidat.

Afin de tester la dernière hypothèse, on utilise une méthode proche des premiers tests, la différence étant que cette fois, avant de localiser les injections, les masses et spins du modèle utilisé par **Bayestar** ne sont plus exactement les mêmes que ceux de l'injection. Ceci permet de reproduire les effets de la recherche en ligne sans en utiliser une. Les résultats montrent que cette fois, il est à nouveau nécessaire d'utiliser ξ pour obtenir un graphe diagonal, ce qui confirme que l'hypothèse testée est correcte.

Finalement, le dernier test a consisté à tester l'influence de la disparité de la banque sur la localisation. Pour cela, on réanalyse les injections utilisées pour le test avec PyCBC Live, mais avec différentes banques contenant uniquement des BNS. Les trois banques utilisées couvrent plus ou moins finement le même espace de recherche. Les résultats obtenus montrent que la valeur de ξ permettant d'obtenir un graphe diagonal est la même pour chacune des banques. On conclut de cela qu'il n'y a pas ou peu d'influence de la finesse de la banque sur la localisation.

Cette étude a permis de montrer que la localisation à faible latence des candidats d'OG est dépendante d'un paramètre ξ pour obtenir des cartes de localisations correctement estimées. On a aussi montré que l'échantillonnage de la banque utilisée pour les recherches en ligne n'a pas ou peu d'influence sur la localisation.

Observer de nouvelles kilonovae

L'autre partie de cette thèse est centrée sur le suivi optique des alertes d'OG produite par les analyses en ligne de données de LIGO et Virgo. L'objectif de tels suivis est d'observer de nouvelles kilonovae, la contrepartie optique d'une OG émise par une fusion

d'étoile à neutrons. La seule kilonova clairement identifiée est celle observée à la suite de GW170817. Cependant, si ces transitoires peuvent apporter des contraintes observationnelles dans de nombreux domaines, elles sont particulièrement difficiles à observer. Ce sont des phénomènes peu brillants - la magnitude absolue au pic est de -16 mag, dont l'évolution est très rapide - une kilonova est visible de quelques heures à quelques semaines - et actuellement, le meilleur moyen de les observer actuellement est d'utiliser les OG. Or, ces dernières sont mal localisées - les cartes fournies par **Bayestar** font typiquement plusieurs centaines à plusieurs milliers de degrés carrés. C'est pour répondre à ses contraintes que le réseau de télescopes GRANDMA a été créé en 2018. Le réseau a été actif pendant la campagne O3 de LIGO-Virgo, sans trouver de kilonova, et est actuellement en train de préparer la campagne O4 qui devrait commencer au printemps 2023.

Muphoten

Si l'utilisation de GRANDMA permet d'espérer l'observation de nouvelles kilonovae, elle apporte de nouvelles contraintes pour l'analyse d'images produites par les instruments. En particulier, les télescopes étant très hétérogènes, si l'analyse n'est pas faite de manière homogène, l'interprétation des courbes de lumière devient difficile. C'est pourquoi le code Muphoten a été développé pendant cette thèse. Il a pour objectif de fournir une estimation photométrique homogène de phénomènes transitoires suivis par GRANDMA.

Muphoten est écrit en python, et utilise aussi des bibliothèques externes, en particulier pour la soustraction d'images de références. Pour chaque image analysée, le code détecte toutes les sources visibles dans le champ de vue, et calcule leur magnitude instrumentale. Cependant, cette quantité ne peut pas être utilisée telle quelle: elle dépend de l'instrument et des conditions d'observations. Pour pouvoir étalonner l'image, les positions des sources détectées dans l'image sont comparées aux magnitudes tabulées dans un catalogue de référence, usuellement Pan-STARRS. On peut ainsi établir pour chaque image la relation entre la magnitude instrumentale et la magnitude tabulée, ce qui permet d'extraire le point-zéros de l'image et d'obtenir la relation d'étalonnage. Par ailleurs, il est fréquent que les phénomènes transitoires (supernovae, kilonova, etc, ...) se produisent dans une galaxie hôte. Cependant, le flux de cette dernière doit être soustrait afin de ne pas contaminer la mesure finale. Pour ce faire, Muphoten utilise HOTPANTS, un algorithme permettant de soustraire une image de référence, sans le transitoire afin d'enlever le flux de la galaxie hôte. Finalement, en calculant la magnitude instrumentale du transitoire dans l'image soustraite, on peut appliquer la relation d'étalonnage afin d'extraire la magnitude finale.

En appliquant cette méthode à tous les instruments du réseau, on peut obtenir des courbes de lumière homogènes permettant de faire une analyse physique du phénomène suivi. Afin de vérifier la fiabilité de la méthode utilisée dans Muphoten, on utilise les images prise lors du suivi d'une supernova détectée en 2018 nommée SN2018cow. Ce choix est fait, car d'une part, c'est le premier événement suivi par la collaboration GRANDMA et que d'autre part, plusieurs collaborations indépendantes ont produit des courbes de

lumière de SN2018cow qui pourront donc servir de comparaison. Par ailleurs, les images du Liverpool sont publiques et celles du KPED ont été prêtées pour l’occasion, et sont déjà analysées dans la littérature. Elles pourront donc servir à évaluer la présence d’un biais systématique dans l’analyse. Les résultats finaux sont présentés dans la Figure 3.13, et montrent que non seulement Muphoten permet de reproduire les résultats déjà publiés pour les images du Liverpool Telescope et du KPED, mais que l’analyse d’images indépendantes produites par des télescopes de GRANDMA donne des résultats similaires. Il n’y a par ailleurs aucun biais détectable dans le code.

En plus de l’analyse photométrique principale, Muphoten contient des fonctions supplémentaires permettant d’une part de mettre un veto sur des images de mauvaise qualité. Il y a deux vetos implémentés dans le code. Le premier est basé sur le calcul de la fonction d’étalement du point (FEP): pour un télescope donné, dans une bande donnée, toutes les images ayant une FEP dont la largeur à mi-hauteur est en dehors de l’intervalle $Mediane \pm 3\sigma$ est rejetée. Pour le second veto, on utilise une étoile connue, dont la magnitude est tabulée dans le catalogue de référence utilisé pour l’étalonnage. On utilise la relation d’étalonnage pour estimer la magnitude de l’étoile de référence et si ce résultat est incompatible avec celui du catalogue, alors l’image est rejeté pour la courbe de lumière finale. D’autre part, il est aussi possible d’estimer la magnitude limite d’une image grâce à Muphoten en comparant le nombre de sources détectées dans l’image au nombre de sources connues dans le catalogue Pan-STARRS.

Préparation de la campagne O4 par le réseau GRANDMA

La prochaine campagne de détection d’OG par LIGO et Virgo commencera au printemps 2023, et afin de la préparer, GRANDMA effectue une série de campagnes observationnelles préparatoires. La première d’entre elle, nommée ReadyforO4, s’est déroulée de mai à septembre 2021. Elle a consisté à suivre des transitoires optiques trouvés par le télescope ZTF, et classée par l’algorithme Fink comme de bon candidat pour être des kilonovae. Au total, 12 alertes ont été suivies pendant la campagne par des télescopes de GRANDMA ainsi que des télescopes amateur participant à la branche de science participatives de GRANDMA: Kilonova-Catcher. Parmi ces alertes, une a été classée comme variable cataclysmique, 4 ont été classées comme des objets du système Solaire et 7 comme des Supernovae.

Pour l’analyse des images de la campagne, Muphoten a été utilisé ainsi qu’une autre analyse interne nommée STDpipe. Cette dernière est entièrement indépendante de Muphoten et a été développée avec le même objectif: fournir une photométrie homogène pour les télescopes hétérogènes de GRANDMA. Le fait que les deux analyses soient menées en parallèle et de manière indépendante, a permis de faire une recherche de biais systématiques. La Figure 3.23 montre qu’il n’y a pas de biais visible pour les 450 images analysées. Cependant, ceci a permis d’identifier deux cas pour lesquels les analyses divergent. Le premier correspond au cas des images prise sans filtre: Muphoten et STDpipe traitent ces images différemment créant un biais pour celles-ci. Le second cas correspond aux images en bandes B : ce biais est principalement dû aux images d’un

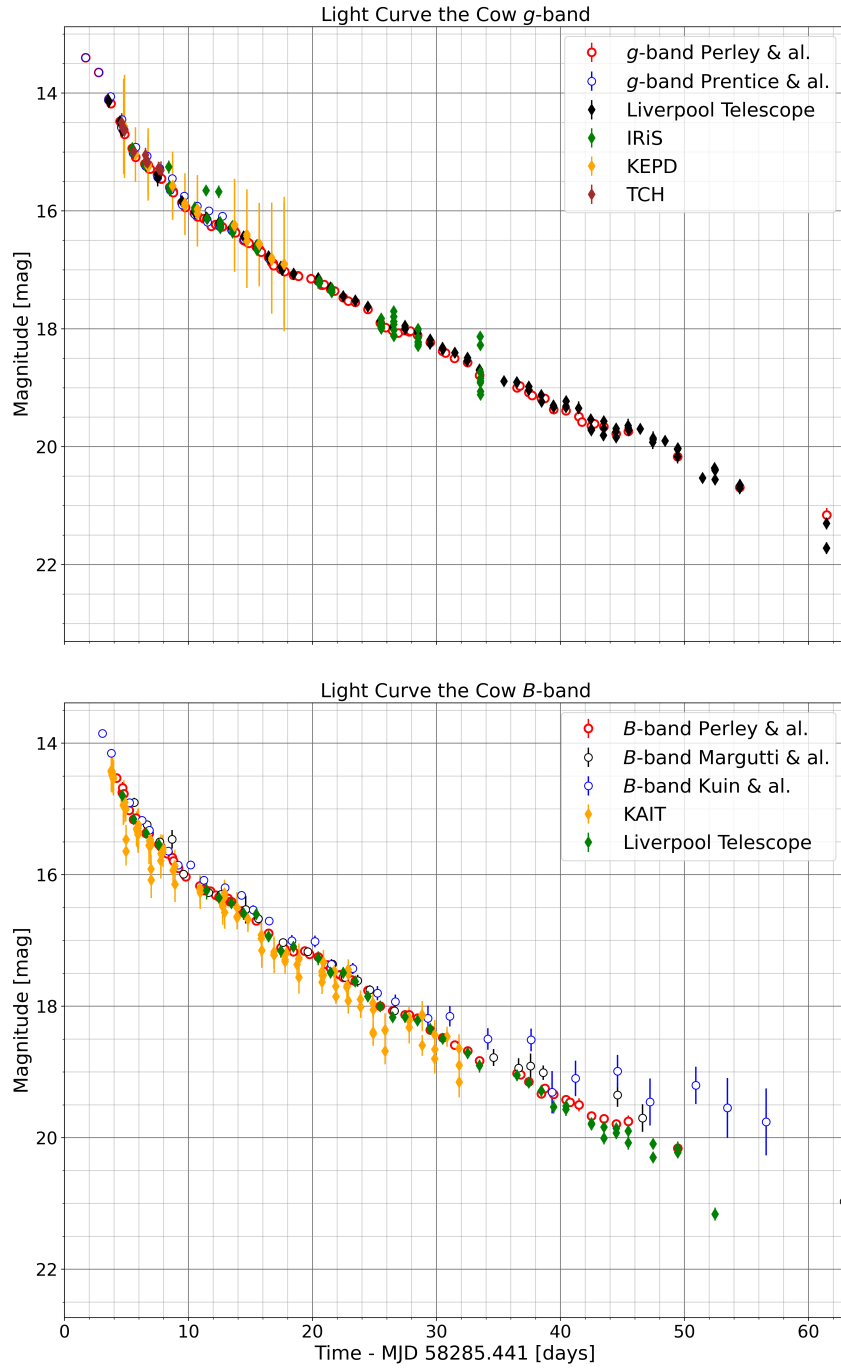


Figure 4: Courbes de lumière de SN2018cow obtenues avec Muphoten. La bande g est présentée sur la partie supérieure, et la bande B sur le graphe inférieur. Sur les deux graphes, les ronds correspondent aux point obtenus depuis la littérature sur la supernova SN2018cow, les losanges correspondent aux point obtenus par Muphoten.

amateur en particulier, dont le filtre B ne correspondait pas au filtre B standard.

L'astronomie multi-messagers est une révolution en Astrophysique, de part la quantité de données à analyser, la rapidité des observations et le potentiel de découvertes majeures dans de nombreux domaines. Cette thèse couvre ces différents aspects dans le domaine des ondes gravitationnelles et le domaine électromagnétique en proposant une approche transversale et en participant à l'émergence de nouvelles méthodes de recherche.

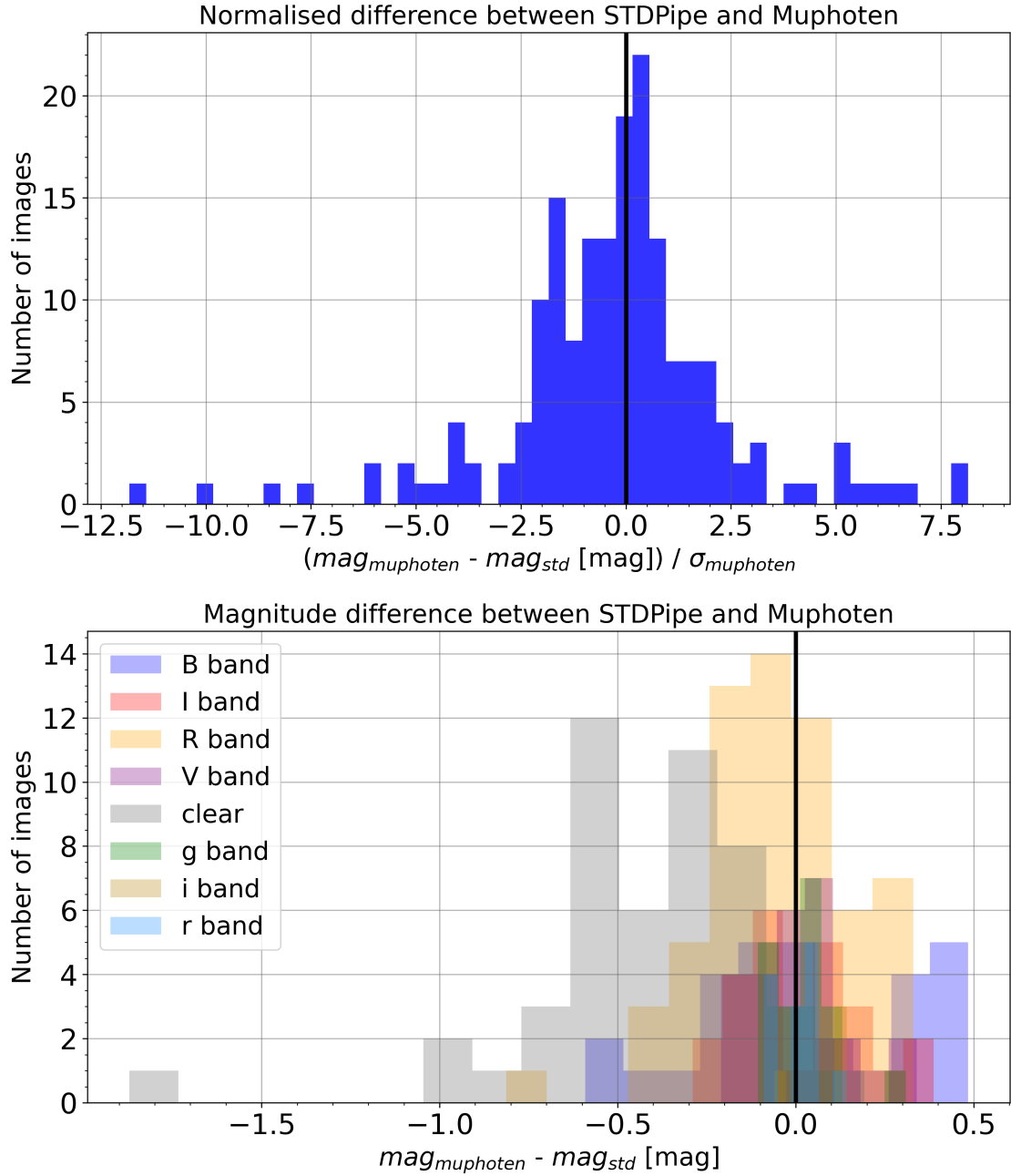


Figure 5: Comparaison des magnitudes estimées par les deux codes STDpipe et Muphoten. Le graphe supérieur présente la distribution des différences normalisées. Pour cette analyse globale, les résultats sont consistants et ne présentent pas de biais. Le graphe inférieur montre les différences absolues des magnitudes pour chacune des bandes utilisées pendant la campagne.

INTRODUCTION

Multi-messenger astronomy (MMA) aims at combining observations made with different signals ("messengers") of the same astrophysical source. Combining these signals allows us to draw a complete picture of the source and understand the underlying physical processes.

So far, four possible messengers are used in MMA analysis:

- Neutrinos: These particles are emitted in large amounts during cataclysmic events as supernovae or binary neutron star mergers and bring information about the thermal cooling of the source. The Ice-Cube (for the TeV domain) [110] and ANTARES (10 GeV - 100 TeV range) [12] instruments detect the high-energy astrophysical neutrinos. The lower energy neutrinos emitted by supernovae (~ 10 MeV) are detected by the Super Kamiokande detector [88].
- Ultra High Energy Cosmic Rays (UHECR): Charged particles, usually protons, reach energies up to the exa-electronVolt domain. UHECR sources are not known yet but are likely extra-galactic. They are detected by the Pierre Auger observatory [54], the HESS telescopes [52] and the recent CTA instruments [120].
- Gravitational waves (GW): These are ripples of space-time emitted by accelerating masses. They are extremely weak signals, only detectable during cataclysmic events such as binary black hole mergers. They are currently detected by the Laser Interferometer Gravitational wave Observatory (LIGO) [53] and Virgo [5] detectors. The Kamioka Gravitational Wave Detector (KAGRA) [8] joined the network in 2020, at the end of the last observing run.
- Photons: by far the most common way to observe the sky, astrophysical photons are observed on the whole electromagnetic spectrum, from gamma to radio. The instruments depend on the energy domain: Fermi for the gammas [18], Chandra for X-rays [259], Hubble space telescope for optical [126], and James Webb Space Telescope [89] for the infrared are examples of observing satellites. The Very Large Array (VLA) [57] or the Very Large Telescope (VLT) [39] are examples of ground-based facilities.

Multi-messenger astronomy is a vast topic that can be separated into various sub-domains. An important separation is made between continuous follow-up of stable objects and observations of transient phenomena. The only object continuously observed via different messengers so far is the Sun. It has been observed with neutrinos via various detectors [55, 190, 33], charged particles - the polar auroras are manifestations of these particles interacting with the Earth magnetic fields, for example - and of course, photons. There are expectations for a joint observation of galactic neutron stars as continuous signals in GW detectors in the near future, which are objects that we already observed via

photons over the whole electromagnetic spectrum. On the other hand, multi-messenger observations of the transient sky can be triggered by any of the four currently known messengers. However, their are privileged combination of observations for time-domain astronomy: the combination of photons with neutrinos and of photons with gravitational waves (GW) seems to be the most promising. To this day, only three examples of multi-messenger observations of transient events are known. The first detection happened in 1987 with the joint observation of neutrinos detected by the Kamiokande II, Baskan, and IMB instruments emitted by the supernova SN1987A [104]. The explosion occurred in a the Large Magellanic Cloud and was visible by human eyes and consequently by all the ground and space-based facilities. The second multi-messenger observation happened on August 17th, 2017, when a GW signal emitted by a binary neutron star (BNS) merger was associated with photons from the whole electromagnetic spectrum. This event is described in detail later in this thesis. The last event occurred on August 22nd, 2017, and consisted of the joint detection of high-energy neutrinos by Ice-Cube in coincidence with high-energy photons by the Fermi satellite and the ground-based gamma observatory MAGIC [100]. The source was consistent with a distant gamma-ray blazar, TXS 0506+056, experiencing a flaring episode.

The present work is focused on the multi-messengers observations of transient events, triggered by gravitational waves detection. In particular we focus on the optical follow-up of gravitational waves candidate events.

In the first chapter we present the GW astronomy, starting from theory to the description of the current ground-based interferometric detector design. Then we discuss the electromagnetic counterparts that we can expect to observe during a binary neutron stars merger, with focus on the kilonova counterpart. We also present in detail the joint observation of the GW170817 signal, and its counterparts over the whole electromagnetic spectrum. We finally discuss the scientific outcome of the August, 17th 2017 event, from the inferences made on the merger itself to the more fundamental results and the impact on the landscape of MMA.

In the second chapter, we present the rapid searches of GW candidate events along with their rapid localisation. We start by presenting the online GW search `PyCBC Live`, then the `Bayestar` algorithm which localises the detected GW events. We finally present a study we performed on `Bayestar`'s accuracy that point toward a careful tuning of the pipeline before the next acquisition run of LIGO and Virgo (O4).

The last chapter overviews the optical follow-up of GW events. We introduce the GRANDMA collaboration and its infrastructure, its strategy to find and follow the optical counterparts to GW event. We summarise the collaboration's optical follow-up results after the third data acquisition run of LIGO and Virgo. Then we present `Muphoten`, the photometry pipeline we developed for the collaboration. And we finally present the results of a GRANDMA campaign for which `Muphoten` produced the photometric datasets. This campaign was part of a broader preparation plan for the follow-up of events produced during the upcoming O4 run and consisted into the follow-up of kilonova candidates found by the Zwicky Transient Facility survey telescope.

DAWN AND RISE OF THE MULTI-MESSENGER ASTRONOMY

This chapter aims to overview the current gravitational-wave-based multi-messenger astronomy domain. We start with a description of GW astronomy, from the theory to the current ground-based detectors and future missions. Then we will describe the various electromagnetic counterparts expected for a BNS merger. After that, we will describe the August 17th, 2017 event. Eventually, we will discuss its influence in the current multi-messenger domain and its limitations.

1.1 Gravitational waves

General Relativity (GR) is a description of the gravitation interaction first proposed in 1915 by Albert Einstein [82]. It relates the curvature of space-time and its content in matter-energy within a geometric framework. One of the earliest predictions of GR, published in 1916, was gravitational waves [83]. They are emitted by accelerating masses and emerge from Einstein's equations as a propagating perturbation of the space-time metric. After a century-long quest, they were first detected in 2015 by the two Laser Interferometer Gravitational-Wave Observatory (LIGO) instruments [137]. The next section gives some basic theoretical background for GW and describes the detectors and the known sources of detectable GW.

1.1.1 Theory

Einstein's equations

General relativity (GR) is a relativistic description of gravitation relying on a geometric approach of space-time and some principles. The latter were formalised by Einstein in 1905 and state:

- The laws of physics are independent of an inertial frame choice.
- The speed of light in vacuum is the same for the frames.

In addition, GR adds the equivalence principle stating that the gravitational and inertial mass are equivalent. This can be reformulated as: "There is no distinction between an accelerating frame and a rest-frame in a gravitational field".

GR uses a non-Euclidean description of space-time, based on the four dimensions vector

space \mathbb{R}^4 equipped with a pseudo-scalar product with signature $(-, +, +, +)$. For a local system of coordinates $\{x^\mu\} = \{x^0, x^1, x^2, x^3\} = \{ct, x, y, z\}$, the pseudo-scalar product between two vectors $\mathbf{X} = x^\mu e_\mu$ and $\mathbf{Y} = y^\mu e_\mu$ described in the basis $\{e_\mu\}$ is written as:

$$\mathbf{g}(\mathbf{X}, \mathbf{Y}) = g_{\mu\nu} x^\mu y^\nu, \quad (1.1)$$

where we used Einstein summation convention, and $g_{\mu\nu}$ is the metric tensor. Einstein translated these principles into a set of equations:

$$R_{\mu\nu} - \frac{1}{2} g_{\mu\nu} R = \frac{8\pi G}{c^4} T_{\mu\nu}, \quad (1.2)$$

where $R_{\mu\nu}$ is the Ricci tensor, R is the Ricci scalar, and $T_{\mu\nu}$ is the stress-energy tensor. The left-hand side describes the space-time curvature, and the right-hand side describes the content in energy-matter. In the GR framework, the matter curves the space-time. In return, the latter influences the motion of matter. Einstein's equations are highly non-linear and not solvable analytically in general. However, they may become solvable under some assumptions and approximations.

Linearized General Relativity

To simplify Einstein's Equations, a usual approximation consists in considering a weak field situation, where the space-time metric is close to flatness. This approximation holds as long as the observer is far away from the gravitational field source. With this approximation, the metric $g_{\mu\nu}$ can be linearised and written as:

$$g_{\mu\nu} = \eta_{\mu\nu} + h_{\mu\nu}, \quad (1.3)$$

where $\eta_{\mu\nu}$ is the usual Minkowsky metric describing a flat empty space:

$$\begin{pmatrix} -1 & 0 & 0 & 0 \\ 0 & 1 & 0 & 0 \\ 0 & 0 & 1 & 0 \\ 0 & 0 & 0 & 1 \end{pmatrix} \quad (1.4)$$

and $h_{\mu\nu}$ is a small perturbation of the flat metric such that $|h_{\mu\nu}| \ll 1$. As one of the axioms of GR states that physics does not depend on the coordinates system, one can choose the Lorenz Gauge without any loss of generality. Keeping Equation 1.2 to linear order and in the Lorenz gauge, Einstein's equations simplify to:

$$\left(\nabla^2 - \frac{1}{c^2} \frac{\partial}{\partial t^2} \right) \bar{h}_{\mu\nu} = -\frac{16\pi G}{c^4} \left(T_{\mu\nu} - \frac{1}{2} g_{\mu\nu} T_k^k \right). \quad (1.5)$$

with:

$$\bar{h}_{\mu\nu} = h_{\mu\nu} - \frac{1}{2} h^{\alpha\beta} \eta_{\alpha\beta} \eta_{\mu\nu}. \quad (1.6)$$

Far away from the source, in an empty space, the right-hand side of Equation 1.5 becomes zero leading to:

$$\square \bar{h}_{\mu\nu} = 0, \quad (1.7)$$

the usual D'Alembert equation. Plane waves propagating at the speed of light are one type of solution for this equation, which can be written as:

$$h_{\mu\nu} = A_{\mu\nu} e^{ik_\sigma x^\sigma}, \quad (1.8)$$

with $A_{\mu\nu}$ is a symmetric tensor describing the effect of the GW on matter. Based on an adequate choice of coordinates called *traceless-transverse* gauge, denoted $h_{\mu\nu}^{TT}$. This results in:

$$h^{TT} = 0, \quad \partial^\mu h_{\mu\nu}^{TT} = 0, \quad \text{and} \quad h_{0i}^{TT} = 0. \quad (1.9)$$

For this gauge, the 10 degrees of freedom of a symmetric 4x4 tensor are reduced to two: h_+ and h_\times . Then, a plane wave that propagates in the z-axis direction, Equation 1.8 is written as:

$$h_{\mu\nu}^{TT} = \begin{pmatrix} 0 & 0 & 0 & 0 \\ 0 & h_+ & h_\times & 0 \\ 0 & h_\times & -h_+ & 0 \\ 0 & 0 & 0 & 0 \end{pmatrix} e^{-i(\omega t - kz)} \quad (1.10)$$

The quantities h_+ and h_\times represent the two polarisations of the GW that are illustrated in Figure 1.1.

Effect of GW on matter

After Einstein predicted GW, their existence was debated for a long time. The controversy stopped in 1957 at the Chapel Hill conference when F.Pirani and others demonstrated that GW was not a GR artefact but had an effect on matter measurable with an experiment [205]. The energy carried away by GW modifies the relative distance of a set of test masses. A situation helping to understand the effect of GW on matter is to consider two test masses A(x_a, y_a, z_a)=(0,0,0) and B(x_b, y_b, z_b) initially separated by a distance L_0 affected by a GW. In the weak field approximation and the TT gauge, the distance that separates them is:

$$L^2 = g_{\mu\nu}(x_B^\mu - x_A^\mu)(x_B^\nu - x_A^\nu) = (\delta_{ij} + h_{ij}^{TT})x^i x^j, \quad (1.11)$$

where $x^i = L_0 n^i$, with \vec{n} the usual unit vector. This last equation is equivalent to:

$$L = L_0 \sqrt{(1 + h_{ij}^{TT})n^i n^j}. \quad (1.12)$$

Using the weak field approximation $|h_{\mu\nu}^{TT}| \ll 1$, at first order, Equation 1.12 reduces to:

$$L \simeq L_0 \left(1 + \frac{1}{2} h_{ij}^{TT} n^i n^j\right). \quad (1.13)$$

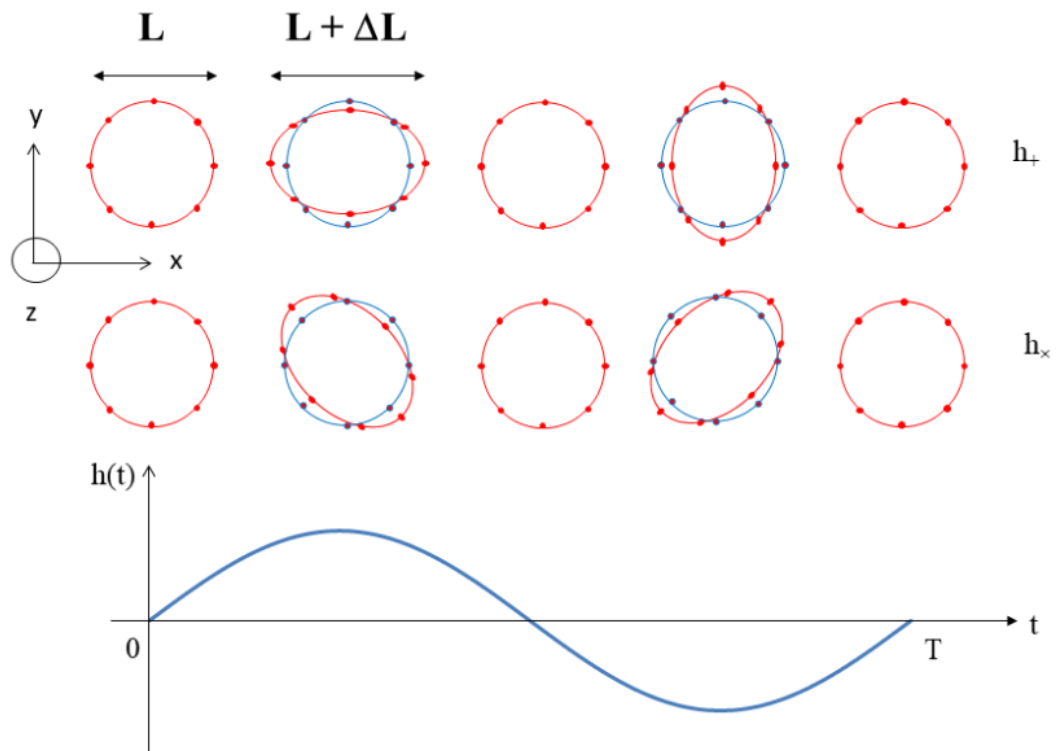


Figure 1.1: Effect of the h_+ and h_\times polarisations of a monochromatic gravitational wave propagating along the z -axis on a ring of free test masses according to the evolution with time of the amplitude of the gravitational wave h .

Defining $L - L_0 = \delta L$, we have the evolution of the relative distance:

$$\frac{\delta L}{L_0} = \frac{1}{2} h_{ij}^{TT} n^i n^j, \quad (1.14)$$

where the scalar $h = h_{ij}^{TT} n^i n^j$ is called the GW *strain amplitude*. This expression demonstrates that the passing GW changes the relative distance between the two test masses proportionally to the GW amplitude h . We illustrate this effect on a ring of test masses in Figure 1.1.

1.1.2 Sources

Emitted power

So far, we only saw what was happening far from the source, in an empty space. To understand how the GW is produced, we need to go back to Equation 1.6 and keep a non-zero right-hand side. At that point, an analogy with electromagnetism can help to understand how GW are emitted. As the electric charge is conserved, electromagnetic waves production requires at least time-varying dipole moments. Similarly, for gravity, the energy conservation prevents emission by the monopolar term, and the momentum conservation prevents emission by the dipolar term. Consequently, GW emission requires at least a time-varying quadrupole moments to be emitted.

Using retarded potential solutions of Equation 1.6, with quadrupole radiation approximation, the metric perturbation in the TT gauge is written as:

$$h_{ij}^{TT} = \frac{2G}{rc^4} \ddot{I}_{ij}^{TT} \left(t - \frac{r}{c} \right), \quad (1.15)$$

with I_{ij}^{TT} is the quadrupole moment of the source. This Equation is known as the Einstein quadrupole formula, and from it, one can evaluate the power emitted by a GW at a distance r :

$$P_{GW} = \frac{G}{5c^5} \langle \dot{I}_{ij} \dot{I}^{ij} \rangle, \quad (1.16)$$

where $\langle \cdot \rangle$ is the time average operator over several periods of time.

Order of Magnitudes

Using dimensional analysis for estimating orders of magnitudes, we can write the quadrupole moment as:

$$\ddot{I} \sim \varepsilon \frac{MR^2}{T^3}, \quad (1.17)$$

where ε is a dimensionless factor describing the source asymmetry, R and T are the source characteristic length and time scales, and M is the source mass. Similarly, the metric perturbation at a distance r can be estimated as:

$$h \sim \varepsilon \frac{GML^2\omega^2}{c^4 r}. \quad (1.18)$$

Introducing the typical speed of the source $v = \frac{R}{T}$ and its Schwarzschild radius $R_s = \frac{2GM}{c^2}$, we can re-write the emitted power as:

$$P_{GW} = \varepsilon^2 \frac{c^5}{G} \left(\frac{R_s}{R} \right)^2 \left(\frac{v}{c} \right)^6. \quad (1.19)$$

From this equation, we can guess the characteristics a detectable GW source should have:

- Asymmetric: the ε parameter should be as large as possible
- Compact: the typical size of the source should be close to its Schwarzschild radius
- Relativistic: the characteristic speed of the source must be close to the speed of light.

In the following paragraphs, we will review GW sources already observed and some other putative ones. The two first paragraphs correspond to continuous sources of GW, and the following two are transient sources.

Continuous waves

Continuous waves in LIGO and Virgo are emitted by rotating non-axisymmetric neutron stars (NS) at twice the pulsar rotational frequency [268]. The pulsars emit radio pulses at a period precisely measured by ground-based radio-telescopes. Consequently, their observations with gravitational waves would constitute an example of continuous MMA, in opposition to transient MMA.

Pulsars lose energy over time mainly via electromagnetic emission and GW but in smaller amounts, causing a process known as spin-down. Under the assumption that the spin-down is entirely caused by GW radiation, the spin-down limit, we can set an upper limit on the pulsar's eccentricity. No continuous GW emission has been detected so far, but using O2 and O3 data, the LIGO-Virgo collaborations have beat up the spin-down limit by a factor of ~ 100 for the Crab pulsar and a factor of ~ 20 for the Vela one. This demonstrates that EM emissions dominate the pulsar spin-down processes. In addition, the collaboration set upper limits on eccentricity for 234 other known pulsars [155].

Stochastic background

The stochastic background is constituted of an incoherent superposition of weak signals too weak to be resolved. The sources emit at similar frequencies and can be transient or continuous but indistinguishable. These unresolved signals are diverse and can originate from either astrophysical sources such as weak superimposed compact binary coalescences (CBC) [141]), or cosmological sources such as cosmic strings [140], early universe phase transitions [131] or quantum vacuum fluctuations during the inflation phase [96]. So far, no signature of such GW emissions has been detected, the latest upper limits on the strain emission are in the $(0.030 - 9.6)10^{-24}$ range and were set in the [20Hz, 1726Hz] band by LIGO, Virgo and KAGRA collaborations [149].

Burst sources

Burst GW emissions are defined by a short emission duration compared to the observing run duration. This definition covers many sources and emission processes, and consequently, bursts are difficult to model in general - except for compact binary coalescence, described in the next paragraph, or cosmic strings collisions [224]. The latter are promising sources of GW bursts [26], but the most prominent one we expect for burst-type events are core-collapse supernovae (CCSN). These events are produced by massive stars with $M \gtrsim 8 - 10M_{\odot}$ whose nuclear burning is not sufficient anymore for countering the gravitational collapse. This results in an explosion of the star superior layers and the formation of a compact remnant, a black hole or a neutron star. The GW emission occurs during or after the explosion and lasts for a few milliseconds up to seconds. However, the emission is weak and can only be detected for events in the Milky Way or its satellite galaxies as the Large Magellanic Cloud [200]. So far, no such emission has been observed by LIGO-Virgo, but it would constitute a major discovery for MMA, as we could expect to observe the supernova not only with GW but also with photons and neutrinos in a similar way as SN1987A. Such a triple coincidence could unveil processes occurring in CCSN, from asymmetry in the explosion with GW to cooling mechanisms with the neutrino and time evolution of the ejected external layers with photons. It may also bring constraints on more fundamental topics, such as the neutrinos mass.

Compact binary coalescence

Compact binary coalescences (CBC) are currently the only detected sources of GW in LIGO and Virgo. They are transient sources of GW and also belong to the burst-type sources but are precisely modelled via numerical relativity. Consequently, the distinction between CBC and other bursts is mainly due to how the searches are done within the LIGO-Virgo collaborations. CBC are produced when two compact objects, either two neutron stars, or two black holes or one neutron star and one black hole, orbit around each other and eventually merge because of GW radiation. This GW radiation causes energy losses that shrink the orbit until objects collide. As visible in Figure 1.2, there are three identified phases during a merger, the inspiral phase, during which the companions are orbiting around the centre of mass, then the merger phase and eventually the ring-down phase, when the remnant is dissipating energy.

Although the Newtonian description of the merger of two compact objects is not complete, it provides enlightening leading-order results. For a compact binary system with companions with masses m_1 and m_2 , orbiting at an angular velocity ω , and separated by a distance d , the mechanical energy of the binary is:

$$E = -\frac{GM\mu}{2d}, \quad (1.20)$$

where M is the total mass and $\mu = \frac{m_1 m_2}{M}$ is the reduced mass. We also have the third Kepler law:

$$\omega = \frac{(GM)^{\frac{1}{2}}}{d^{3/2}}. \quad (1.21)$$

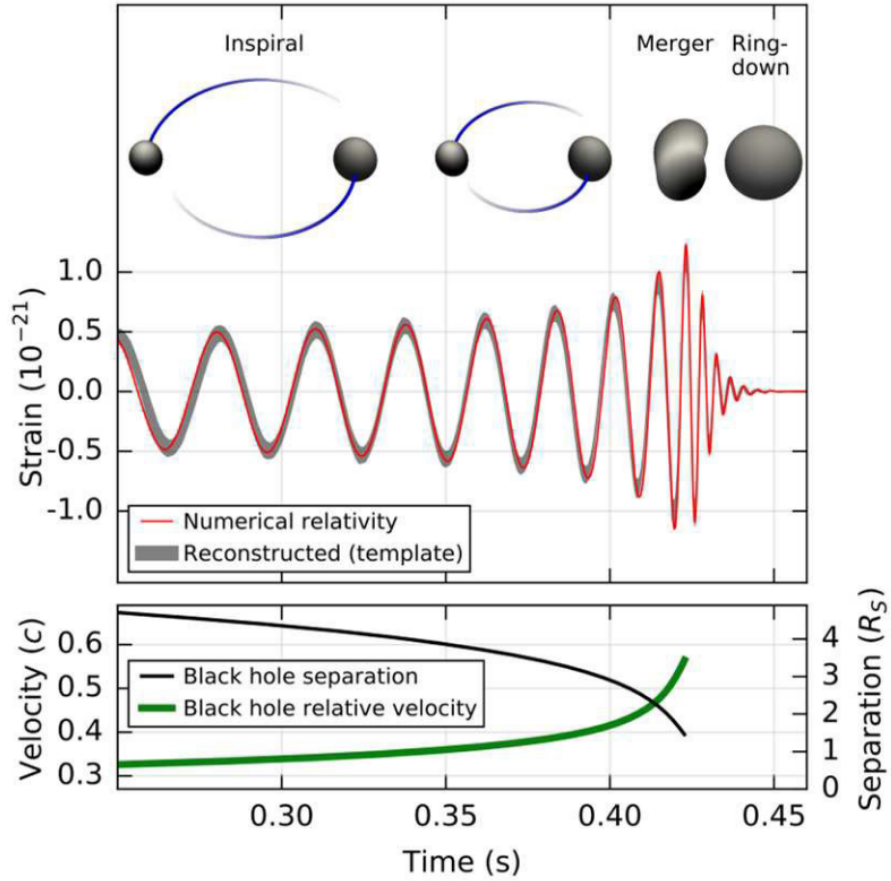


Figure 1.2: The upper plot shows the waveform of the GW strain amplitude $h(t)$, which experiences three phases during a CBC: the inspiral, the merger and the ring-down. These $h(t)$ waveforms are precisely reconstructed by numerical relativity, which allows searching for these signals within the detector data. The bottom panel shows the time evolution of the distance between the compact objects (in black) that decreases because of GW emission. The plot also shows the relative velocity of the compact objects (in green) that increases with time as the objects accelerate until they merge. This figure was taken from [189].

Combining and deriving the two previous equations, we have:

$$\frac{\dot{E}}{E} = -\frac{\dot{d}}{d} = -\frac{2\dot{T}}{3T}, \quad (1.22)$$

where T is the orbital period of the binary such that $T = \frac{2\pi}{\omega}$.

Using the equation of motion, we have:

$$\ddot{\vec{d}} = -\frac{GM}{d^3}\vec{d}. \quad (1.23)$$

Based on the motion of the two companions motion, we can estimate the GW emission starting by computing the quadrupole moment of the system:

$$I_{ij} = \int \rho x_i x_j d^3x = m_1(x_1)_i(x_1)_j + m_2(x_2)_i(x_2)_j. \quad (1.24)$$

The GW emission results in an energy loss for the system that is equal to the power in Equation 1.16:

$$\dot{E} = -P_{GW}. \quad (1.25)$$

And using Equations 1.16 and 1.24, we have:

$$P_{GW} = \frac{32}{5} \frac{G^4 \mu^2 M^3}{c^5 d^5}. \quad (1.26)$$

From these two results, we can evaluate the time evolution of the distance between the two objects:

$$\dot{d} = -\frac{64}{5} \frac{G^3 \mu M^2}{d^3}, \quad (1.27)$$

that gives, after time integration:

$$d^4 = \frac{256}{5} G^3 \mu M^2 (t_c - t). \quad (1.28)$$

These two quantities are plotted in the bottom panel of Figure 1.2 Here, t_c is the theoretical time when the objects collide. The GW emissions occur at twice the orbital frequency, consequently, it evolves with time as:

$$f_{GW} = 2 \frac{\omega}{2\pi} = \frac{2}{T}. \quad (1.29)$$

Hence, we deduce:

$$\frac{\dot{f}}{f} = -\frac{\dot{T}}{T}, \quad (1.30)$$

from which we have:

$$\dot{f} = \frac{96}{5} \pi^{8/3} G^{5/3} \mu M^{2/3} f^{11/3}. \quad (1.31)$$

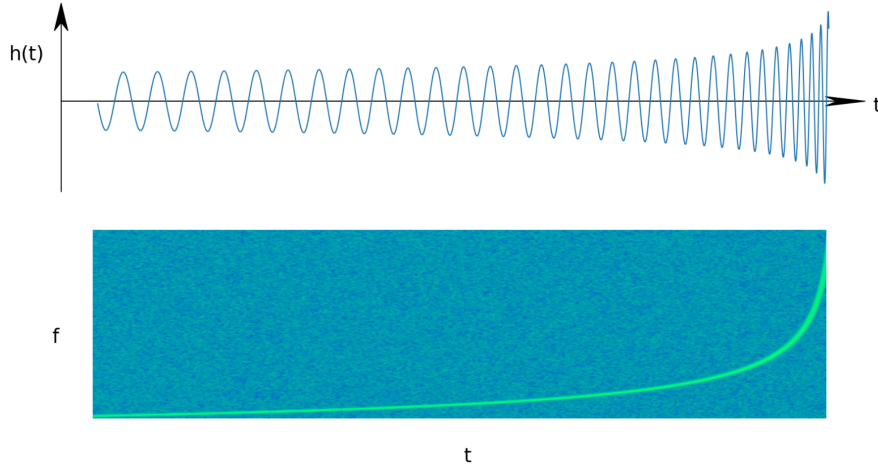


Figure 1.3: The upper panel represents the time evolution of the $h(t)$ GW strain amplitude, and the bottom panel is the spectrogram of this signal. This figure was taken from [78].

Based on this, we can deduce the time evolution of the GW frequency and strain amplitude:

$$f_{GW} \propto (t_c - t)^{-\frac{3}{8}} \quad (1.32)$$

$$h \propto \frac{1}{d} \propto (t_c - t)^{-\frac{1}{4}}. \quad (1.33)$$

Based on these, we can observe that the GW frequency and amplitude increase with time in a typical shape called *chirp* signal. Both quantities are shown in Figure 1.3 where the upper panel corresponds to the GW strain amplitude, and the bottom panel is the Time-Frequency representation of the signal.

1.1.3 Gravitational Waves Detectors Overview

After the Chapel Hill conference established the existence of gravitational waves, several proposals for experimental devices able to detect them. This section aims at giving a short overview of the various attempts to detect them. However, the current ground-based interferometers will be described in the next section.

Weber bars

Joseph Weber was one of the Chapel Hill conference attendants and was convinced that GW could be experimentally detected. Consequently, he designed one of the first GW detectors: the Weber bars. They consist of cylindrical bars acting as test masses. A passing GW could induce a quadrupole vibration exciting the longitudinal vibrational mode of the bar, creating an acoustic vibration within the detector. In the first designs,



Figure 1.4: A Weber bar, exposed at the LIGO Handford observatory. It consists of an aluminium bar with a piezo-electric readout on the top of the bar. Image taken from [81].

this acoustic vibration is turned into an electric signal via a piezo-electric apparatus [256]. One of these bars is pictured in Figure 1.4. These Weber bars can detect GWs at the kilohertz level in a ~ 100 Hz bandwidth, corresponding to the resonance frequency of the bar. In 1969, Weber claimed to have detected GW emission in coincidence in two bars [257], but the detected energy seemed too high to be real. In addition, several other independent groups conducted further searches with these devices and found no evidence for GW detections.

Pulsar Timing Array

Pulsars are highly magnetized rotating neutron stars emitting periodic radio pulses discovered by Jocelyn Bell in 1967. This radio emission is beamed and produces a regular train of pulse radiation. This regularity was used for various major discoveries in the latest decades. It includes the first detection of GW emission by Hulse and Taylor with the binary pulsar PSR 1913+16 [236], even before the LIGO and Virgo observations.

The Pulsar Timing Array (PTA) method relies on precise measurements of the time of arrival of pulsar pulses, using propagation models for the radio pulses in the interstellar medium. A passing GW would induce delays in the predicted arrival times on Earth. Consequently, based on the radio measurements, extracting information about the GW is possible. The expected typical time deviation created by a GW is ~ 100 ns. The actual searches with this technique are performed using the International Pulsar Timing Array (IPTA) [107], which combines the observations from different radio observatories

to detect very low-frequencies gravitational waves in the nHz band as it is plotted in Figure 1.6. The primary sources at these frequencies are binary supermassive black hole mergers. Despite no evidence of GW in IPTA, the latest results [263] show that the current decade could see the first detection of GW from supermassive black holes. In addition, the upcoming Vera C. Rubin Observatory will allow the rejection of false signals. Moreover, these observations would constitute an opportunity for multi-messenger observations.

Laser Interferometer Space Antenna

In the next decade, ESA and NASA plan to launch a space base GW observatory called Laser Interferometer Space Antenna (LISA) [73]. It will be able to observe and detect various sources, including supermassive binary black hole mergers or continuous waves emitted by galactic white dwarf binaries. In addition, LISA will also be able to detect compact object binary inspirals, including BNS, months before they merge and then allow an EM follow-up planning for having early observations of these events. LISA is sensitive in a low frequency band 10^{-4} - 10^0 Hz, as illustrated in Figure 1.6.

As it is visible in Figure 1.5, LISA is constituted of three spacecrafts, each of one containing two test masses. The spacecrafts are separated by 2.5×10^9 m distance and located at an astronomical unit from the Sun, 20° behind the Earth. Each spacecraft is linked to the two others via LASER interferometry, which evaluates the distances between the constellation elements.

A preparation mission called LISA Pathfinder has successfully tested several technologies planned to be implemented on the actual LISA mission [16].

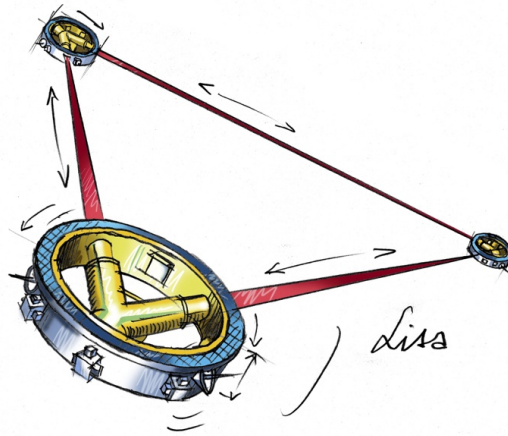


Figure 1.5: Scheme of the LISA instrument, planned to be launched by the 2030s. This illustration was taken from [37].

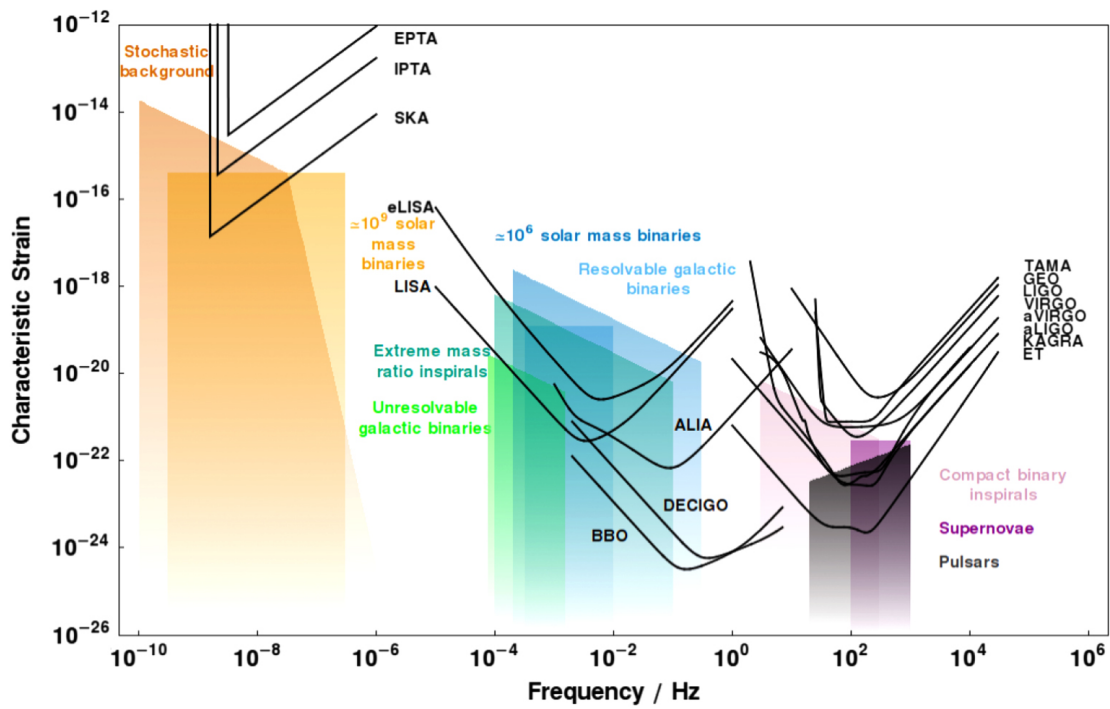


Figure 1.6: Sensitivity curves for various GW instruments - including PTA detectors (IPTA, EPTA, SKA), LISA and ground-based detectors (TAMA, GEO, LIGO, VIRGO, aVIRGO, aLIGO, KAGRA and ET). This image is extracted from [188].

1.1.4 Ground-Based GW Detectors

Principle

The current network of ground-based detectors consists of three main instruments: Ligo-Handford, LIGO-Livingston and Virgo. In addition, GEO-600 is a small version of the three first used to develop advanced technologies. KAGRA is a kilometric-size detector comparable to the LIGO and Virgo experiments that is still under development but ultimately aims at joining the main network.

These instruments rely on the same principle and are modified-kilometric Michelson interferometers - only KAGRA includes cryogenic technologies. These interferometers are made of two arms, "L"-shaped, and the leading idea of these instruments is to measure the small arms length variations induced by a passing GW.

A laser beam is sent onto a beam-splitter that separates it into both arms. In each arm, a Fabry-Perot cavity constituted of two mirrors - one at the beginning and one at the arm's end. This configuration allows for an increase of the optical path in the instruments and the light travel distance. Eventually, the beam from both arms is recombined onto the beam-splitter where they interfere. The interference pattern is tuned to be on the dark fringe and is observed on the end photodiode. By design, the optical path is the same for both arms until a GW passes and modifies it, as we presented in Figure 1.1 and Equation 2.2. This variation translates into an interferometer pattern and a signal in the diode that is no longer on the dark fringe for the GW signal duration. In this instrument, the cavity mirrors act as the free-falling test masses described in Figure 1.1, and consequently give access to the Riemann tensor. This whole principle is summarised in Figure 1.7, taken from the thesis [78].

In the previous section, we already saw that the effect on the distance between free falling masses translated into Equation 2.2. In the interferometer, these test masses correspond to the mirrors, δL corresponds to the differential distance between them induced by the GW and L_0 is the arms length when mirrors are at rest. The working point chosen by the operating team translates into a phase shift $\Delta\phi_0 = 2k_0\Delta L_0 = 2k_0(L_Y - L_X)$, where k_0 is the optical wave vector, and L_X and L_Y are the nominal arm lengths. A passing GW with amplitude h will create a variation in the optical path, inducing a phase difference $\delta\phi_{GW}$ in the diode readout signal such that:

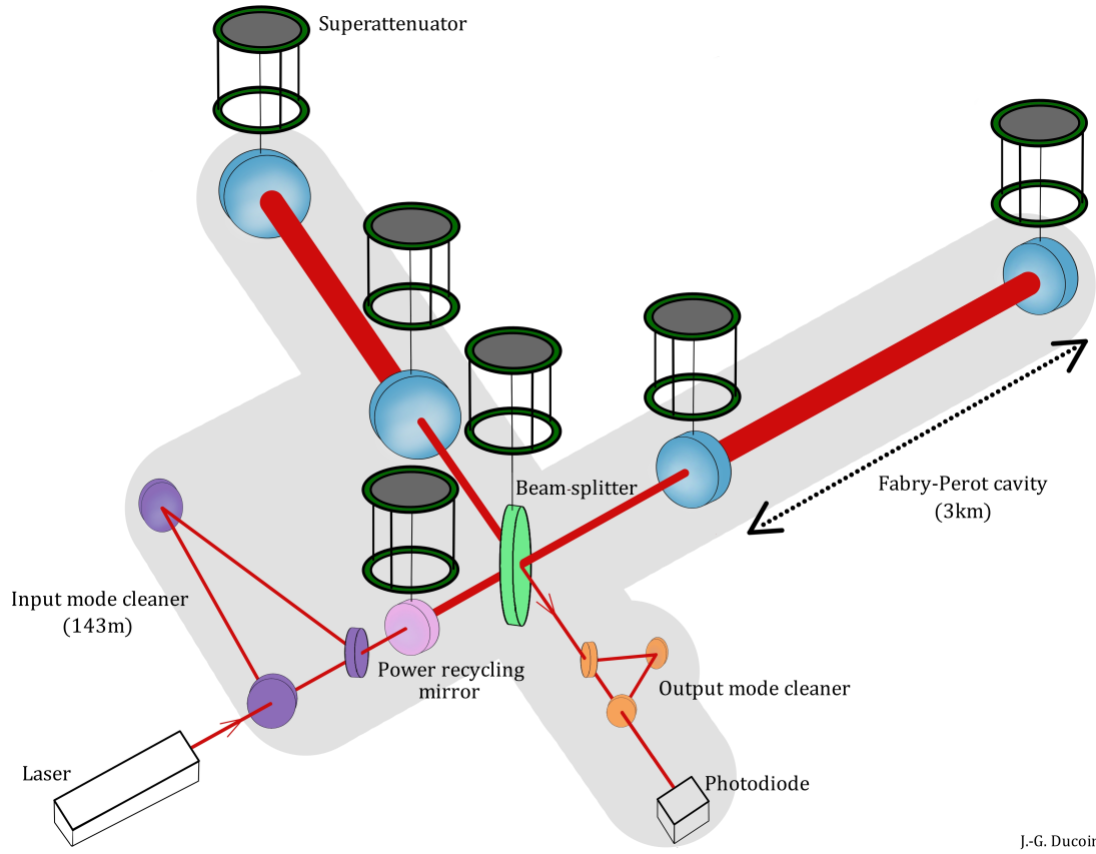
$$\delta\phi_{GW} = 2hk_0\delta L \ll \Delta\phi_0. \quad (1.34)$$

This leads to a total phase $\Delta\phi = \Delta\phi_0 + \delta\phi_{GW}$. This phase shift will lead to a readout power in the end photodiode that we can write at first order as:

$$P_{out} \approx \frac{P_{in}}{2}(1 - \cos(\Delta\phi_0) + \delta\phi_{GW} \sin(\Delta\phi_0)), \quad (1.35)$$

where P_{in} is the injected power of the laser [130]. Eventually, the passing GW effect will translate into a variation in the readout power that can be written as:

$$\delta P_{out}^{GW} = \frac{P_{in}}{2}\delta\phi_{GW} \sin(\Delta\phi_0). \quad (1.36)$$



J.-G. Ducoin

Figure 1.7: Scheme of the Virgo interferometer in its O3 design, the beam size reflects its power (not to scale), and the light blue background indicates that the system is in vacuum. This image is taken from [78].

The detector power variation is directly proportional to the phase shift induced by the GW: $\delta P_{out}^{GW} \propto \delta\phi_{GW}$. Based on Equation 1.34, we have $\delta P_{out}^{GW} \propto h(t)$. This last relation demonstrates how the GW amplitude can be related to the readout power of the detector. This power variation contains the information about the GW detected by the interferometer.

Detector Noises

Gravitational waves are extremely weak signals, and the detectors must be highly sensitive to detect them. It implies that the noise sources of the instruments must be understood and mitigated to increase the sensitivity. The latter is defined over a frequency band based on a quantity called *amplitude spectral density* (ASD) expressed in $1/\text{Hz}^{\frac{1}{2}}$. To estimate the ASD, we need to estimate the *power spectral density* (PSD) $S(f)$ [233]. For a generic function $s(t)$, its PSD is evaluated using the Wiener-Khintchine theorem [261] by computing the Fourier transform of its auto-correlation function. The latter is defined as:

$$s * s(\tau) = \lim_{T \rightarrow +\infty} \frac{1}{2T} \int_{-T}^T s(t)s(t+\tau) dt. \quad (1.37)$$

Then the PSD is extracted with the following relation:

$$S(f) = \frac{1}{\sqrt{2\pi}} \int_{-\infty}^{+\infty} s * s(\tau) e^{-i2\pi\tau} d\tau. \quad (1.38)$$

With the PSD, we estimate the ASD $\tilde{S}(f)$, which gives a direct estimation of the detector sensitivity:

$$\tilde{S}(f) = \sqrt{S(f)}. \quad (1.39)$$

The next chapter will describe a computation of the ASD and PSD with the discrete data produced by the instrument. The sensitivities of current and future detectors are shown in Figure 1.6.

The sensitivity reached by an interferometer depends on several noise sources that we describe in the following paragraphs.

Seismic Noise: Ground-based detectors suffer from ground motion that can perturb the measurements. The seismic noise above 1 Hz is mainly due to human activity, and below this value, the motions are produced by natural events such as earthquakes, wind or ocean tides. Attenuating these vibrations on the GW detector optical devices is done by isolating them from the ground. This is illustrated in Figure 1.7 with the cylinders above the mirrors and beam-splitter. The optics are suspended with silica wires in a so-called *superattenuator* [4]. It consists of a chain of five dampers gathered in an inverted pendulum. It isolates the optics by damping ground motions. By neglecting the mechanical losses, one damper of a *superattenuator* can be described by a transfer function:

$$|\tilde{H}(\omega)| \simeq \frac{\omega_0^2}{\omega_0^2 - \omega^2}, \quad (1.40)$$

where ω_0 is the resonance frequency of the damper. For $\omega \gg \omega_0$:

$$\left| \tilde{H}(\omega) \right| \simeq \frac{\omega_0^2}{\omega^2}, \quad (1.41)$$

hence, the transfer function of an individual damper tends toward zero, suppressing any transmission at high frequencies. The chain of five dampers of the *superattenuator* yields this final transfer function:

$$\left| \tilde{H}_{chain}(\omega) \right| \simeq \left(\frac{\omega_0^2}{\omega^2} \right)^5, \quad (1.42)$$

For the current Virgo configuration, the resonance frequency of the individual dampers is 0.6 Hz, and in the 40-80mHz band for the inverted pendulum. This leads to a seismic strain noise of:

$$\tilde{n}(f) \sim 10^{-29} / \sqrt{\text{Hz}}, \quad (1.43)$$

at 10Hz, the low bound of the sensitivity band of the interferometers [3].

Thermal Noise: The thermal noise is produced by thermal dissipation inside the mirrors and their suspensions. It results in a deformation of the mirrors and excitation of their pendular modes via the suspensions. The pendulum thermal noise has a resonance frequency at 0.6Hz linked to the suspensions described in the previous paragraph. This noise also contributes to the 50-200Hz frequency band in the Virgo detector. In addition, the silica wires are creating resonances at 450Hz, and its multiples frequencies, called the violin modes [130].

Shot noise: A passing GW will induce a power variation in the photodiode, as we have seen in the previous section. Hence, the detector sensitivity is limited by the smallest power variation the photodiode can observe. Considering that each photon carries an energy $E = h\nu_0$ according to the Planck-Einstein relation and that the number of detected photon N follows a Poisson distribution, we have after an integration time τ :

$$N = \langle N \rangle \pm \sqrt{N} = \frac{P_{out}\tau}{h\nu_0} \pm \sqrt{N}, \quad (1.44)$$

where P_{out} is the readout power of the detector. This induces on the detected power a standard deviation around P_{out} of:

$$\sigma_p = \sqrt{N} \frac{h\nu_0}{\tau}. \quad (1.45)$$

On the other hand, we can re-write Equation 1.35 as:

$$P_{out} \approx P_{in} \left(\sin^2 \left(\frac{\Delta\phi_0}{2} \right) + \delta\phi_{GW} \sin \left(\frac{\Delta\phi_0}{2} \right) \cos \left(\frac{\Delta\phi_0}{2} \right) \right), \quad (1.46)$$

where the power has a component due to the noise P_{noise} , and a signal component P_{signal} :

$$P_{noise} = P_{in} \sin^2 \left(\frac{\Delta\phi_0}{2} \right) \quad (1.47)$$

$$P_{signal} = P_{in} \left(\delta\phi_{GW} \sin \left(\frac{\Delta\phi_0}{2} \right) \cos \left(\frac{\Delta\phi_0}{2} \right) \right). \quad (1.48)$$

When there is no signal in the data, $P_{out} = P_{noise} = P_{in} \sin^2\left(\frac{\Delta\phi_0}{2}\right)$ and based on Equation 1.46, the output power fluctuation can be interpreted as a phase shift such that:

$$\sigma_\phi = \frac{2\sigma_p}{P_{in} \sin(\Delta\phi_0)} = \frac{1}{\cos\left(\frac{\Delta\phi_0}{2}\right)} \sqrt{\frac{h\nu_0}{\tau P_0}}. \quad (1.49)$$

To minimise the phase fluctuation, the detector is placed on the dark fringe, then $\Delta\phi_0 = 0$. Using that $\Delta\phi = \frac{4\pi L_0 \nu}{c} s(t)$, it is possible to re-write the phase noise as a contribution to the ASD:

$$n_{shot} = \frac{1}{L_0} \sqrt{\frac{c^2 h}{8\pi^2 \nu_0 P_{in}}}. \quad (1.50)$$

This derivation is extracted from [130] It can be noted that the shot noise is independent of the frequency and depends only on the interferometer characteristics. Using the Virgo parameters - arm length of $L = 3\text{km}$, injected laser power of 50W at $\nu_0 = 1064\text{ nm}$ wavelength - we find: $\tilde{n}_{shot} \sim 2.5 \times 10^{-21} \frac{1}{\sqrt{\text{Hz}}}$.

Radiation pressure noise: Photons hitting the mirrors will transfer a small fraction of their momentum and create a slight displacement. This creates a random radiation pressure force, inducing noise in the detector. In a similar procedure as the shot noise, we can write the noise created by this effect as [130]:

$$\tilde{n}_{rp} = \frac{1}{2\pi^2 m L_0 f^2} \sqrt{\frac{P_{in} h \nu_0}{c^2}}, \quad (1.51)$$

where m is the mirror masses. Hence, increasing their mass reduces the contribution of this noise to the total budget. The dependence of n_{rp} on the $1/f^2$ makes this noise dominating at low frequencies and negligible at high frequencies.

Standard quantum limit: The two previous contributions to the noise constitute total quantum noise in the interferometer, that is: $\tilde{n}_q = n_{shot} + n_{rp}(f)$. However, these two contributions have antagonist dependence on P_{in} : increasing it will reduce the shot noise but rise the radiation pressure noise. Consequently, we can compute the optimal laser power: $P_{opt} = \frac{\pi c^2}{2\nu_0} m f^2$ to estimate the standard quantum limit where the two contributions are equivalent for each GW frequency f :

$$\tilde{n}_{SQL} \sim \frac{1}{\pi L_0 f} \sqrt{\frac{h}{4\pi m}}. \quad (1.52)$$

This constitutes the fundamental limits the interferometers face to increase their sensitivity. All the contributions to the noise budget are illustrated in Figure 1.8 for the LIGO interferometers during the latest GW observing run O3 [45].

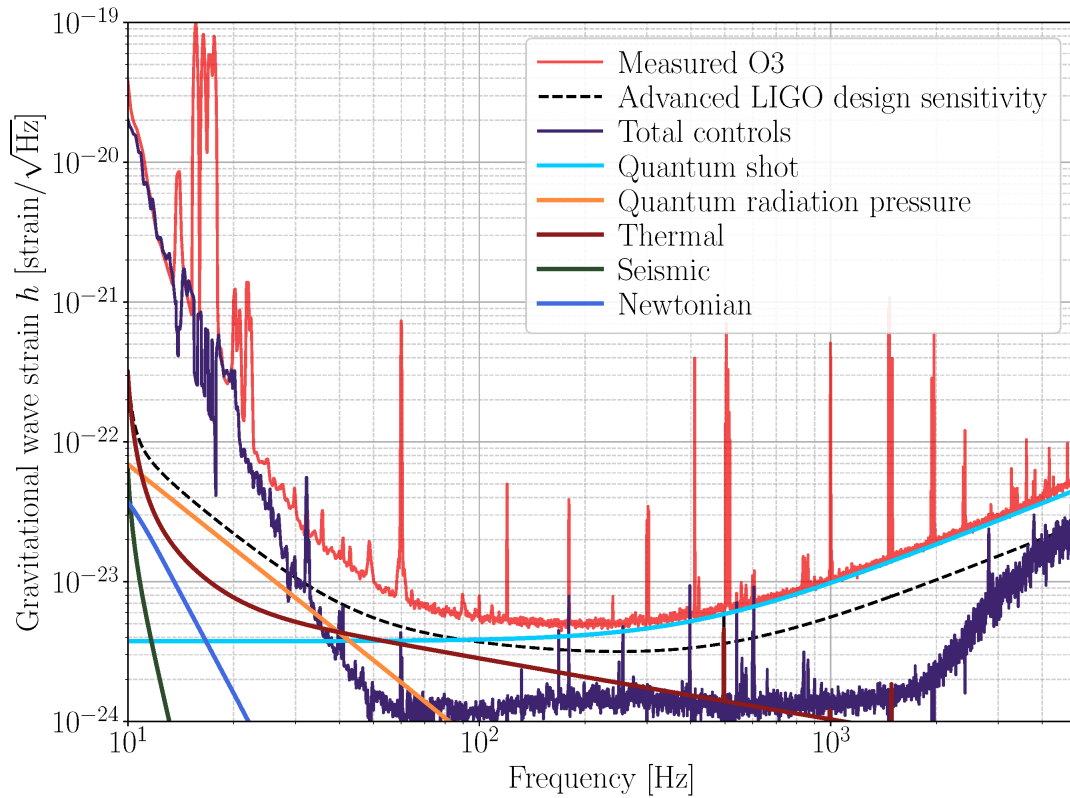


Figure 1.8: O3 LIGO Hanford gravitational wave noise budget. The measured curve in red represents the calibrated sensitivity to GWs. The dashed black curve is the Advanced LIGO design sensitivity curve [45].

1.1.5 Gravitational waves searches

Overview of the past searches

The advanced versions of the LIGO and Virgo interferometers were finalised in 2015. Since then, there have been three data takings, with improvements between two successive runs:

- O1 : 2015 September 12th - 2016 January 19th
During this run, the first GW signal has been detected [137], produced by the coalescence of two black holes (BBH). In addition, two other BBH were detected as well.
- O2 : 2016 Nov 30th - 2017 August 25th
During this run, seven additional BBH were detected, and GW170817 has been detected with the whole MMA follow-up [142].
- O3 : 2019 November 1st - 2020 March 27th
During this period, tens of BBHs were identified [151], one binary neutron star (BNS) - GW190425 [150] - and the two first neutron star-black hole mergers (NSBH) [153]. The run was split between O3a and O3b to improve the detectors during a month's stop.

During these runs, low latency searches were conducted and played a significant role, especially in GW170817 discovery by providing early information on the source, such as the coalescence time or the sky localization. The details about these searches will be given in the next Chapter.

Plan for the O4 run

The current configuration of the GW network involves four instruments: the two LIGO, Virgo and KAGRA. The LIGO interferometers are located in the USA, one in Livingston, the other in Handford, Virgo is in Cascina, Italy. KAGRA is located underground in the former Japanese mine of Kamioka. All of them are being upgraded for the next observing run O4. The latter will start in March 2023 and will last for one year plus two interruptions for improvement commissioning.

The sensitivities of an instrument can be summarised using the *horizon distance*. It is defined as the maximum distance at which the interferometer would detect a sky and inclination averaged fiducial 1.4-1.4 M_{\odot} BNS with a signal-to-noise ratio of 8. These are the quantities in Figure 1.9, summarising the plan for the LIGO-Virgo-KAGRA (LVK) collaboration. For O4, the LIGO are planned to have an horizon distance above 160 Mpc and above 80 Mpc for Virgo. KAGRA will likely be significantly less sensitive, with an horizon of 10 Mpc at best, but it will be improved along the run. This is due to its significantly different design compared to LIGO and Virgo, which involves cryogenics suspensions.

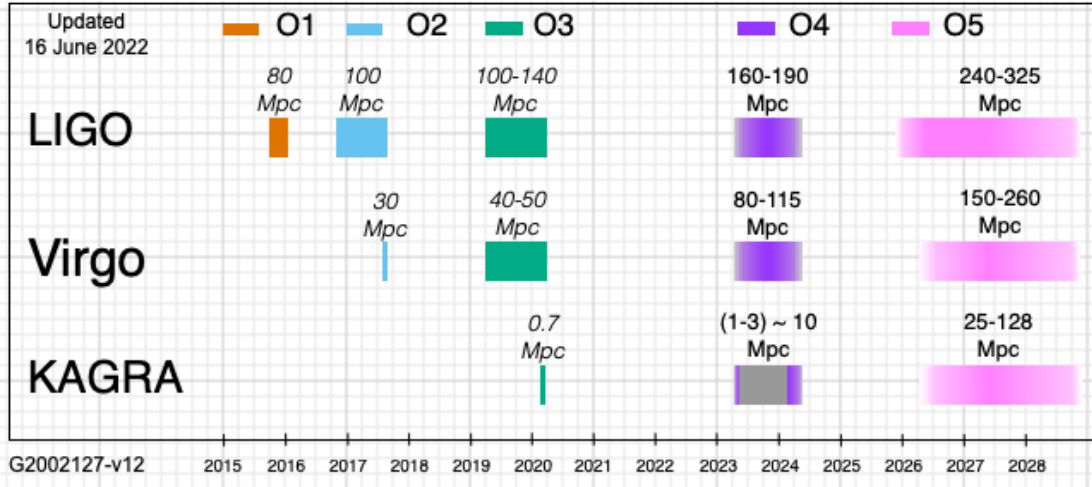


Figure 1.9: Current plan of observations for the LIGO-Virgo-KAGRA collaboration. The next observing run O4 is planned to start by March 2023 and to be split into three parts. The expected horizon distances are planned to be above 160 Mpc for the LIGO interferometers and above 80 Mpc for Virgo. This Figure is extracted from [156].

1.2 Electromagnetic counterparts to GW

In Section 1.1, we presented an overview of GW astronomy, but MMA requires counterparts in at least one other domain: electromagnetic, neutrinos or charged particles. Based on the GW170817 event described in Section 1.4, we already observed a gamma-ray burst, along with its X-rays optical and radio afterglows and a kilonova in the optical domain associated with a GW event. However, other types of emissions are predicted for such events, including neutrino and fast radio bursts (FRB). For the GW events emitting in the electromagnetic regime, the most promising are compact binary coalescences for which at least one of the companions is a neutron star, i.e. BNS or NSBH. BBH mergers are not expected to emit photons, although some models predict EM emissions for mergers occurring in the surrounding of a supermassive black hole or an active galactic nucleus (AGN) [264]. In addition, a supernova happening in a ~ 1 Mpc radius would be detected in the GW as a burst-type event, in the EM domain and by neutrino detectors. This section aims at presenting the known and predicted counterpart to GW events.

1.2.1 Gamma-ray Bursts

GRB prompt emission

Gamma-ray bursts (GRB) are transient emissions of high-energy photons. They are short-lived and last for a few milliseconds up to minutes. The duration and hardness of the spectrum lead to the separation of the GRB into two categories: long and short [27]. Long GRB last for at least 2 seconds and have a softer spectrum. The identified host galaxies of such GRB are usually young ones with star formation regions, however,

this is not a systematic rule. Short GRB last less than 2s, with a hard spectrum and are emitted in hosts that tend to be older, with the same mitigations as for the long GRB hosts. This separation suggested different progenitors for the two categories. Long GRB are supposed to be emitted by core-collapse supernova, and GW170817/GRB170817 confirmed the long suspected BNS origin of at least some short GRB. Based on this, short GRB are the privileged gamma counterparts to GW detected events.

The gamma-ray prompt emission is produced by an ultra-relativistic jet containing large quantities of kinetic energy - up to $\sim 10^{50}$ erg - as illustrated in Figure 1.10. In the current understanding of short GRB produced by a BNS, the jet is powered by the accretion of material on the central engine (neutron star or black hole) resulting from the neutron stars merger. Large amounts of energy are deposited in the polar region of the merger via a process that remains unclear to this day. This launches an ultra-relativistic fireball collimated to form the jet by the accretion disk surrounding material and intense magnetic fields. This emission is observable by observers within a half-opening angle θ_j such that $\theta_j \sim \frac{1}{\Gamma}$, where Γ is the Lorentz factor. Half-opening angles are usually below 15° , with visibility limited to regions where the bulk Lorentz factor has typical values of ~ 100 [103].

GRB afterglows

After the prompt emission of the GRB, a broadband emission occur when the jet collides with the surrounding interstellar medium, the so-called afterglow. In the case of GW170817, the afterglow has been observed in the X-ray and radio domains. In the optical domain, the kilonova dominated the emission during the first weeks. Although, post-170817 reviews of previously detected optical short-GRB afterglow lightcurves lead to the identification of kilonova emission [93, 245, 243].

1.2.2 Kilonovae

Emission processes

Kilonovae are optical-NIR thermal transients powered by the radioactive heating of the BNS expanding ejecta. These transients were theorised in the 1990's [132] as regions of heavy elements synthesis via rapid capture of neutrons by seed nuclei - the so-called r-process, that is described in Section 1.3.2. The models were refined in 2010 through simulations[181]. In the current understanding, a kilonova is well described by a two components model: a lanthanide-free one in the polar region, emitting in the UV-optical blue wavelengths - the "blue kilonova". A second lanthanide-rich component in the equatorial plane emitting in the red-NIR wavelengths, called the "red kilonova". An overview of the kilonova transients is done in [175] and references therein.

To describe a kilonova transient, we need the electron fraction Y_e to characterise the material in a BNS merger, defined as:

$$Y_e = \frac{n_p}{n_p + n_n}, \tag{1.53}$$

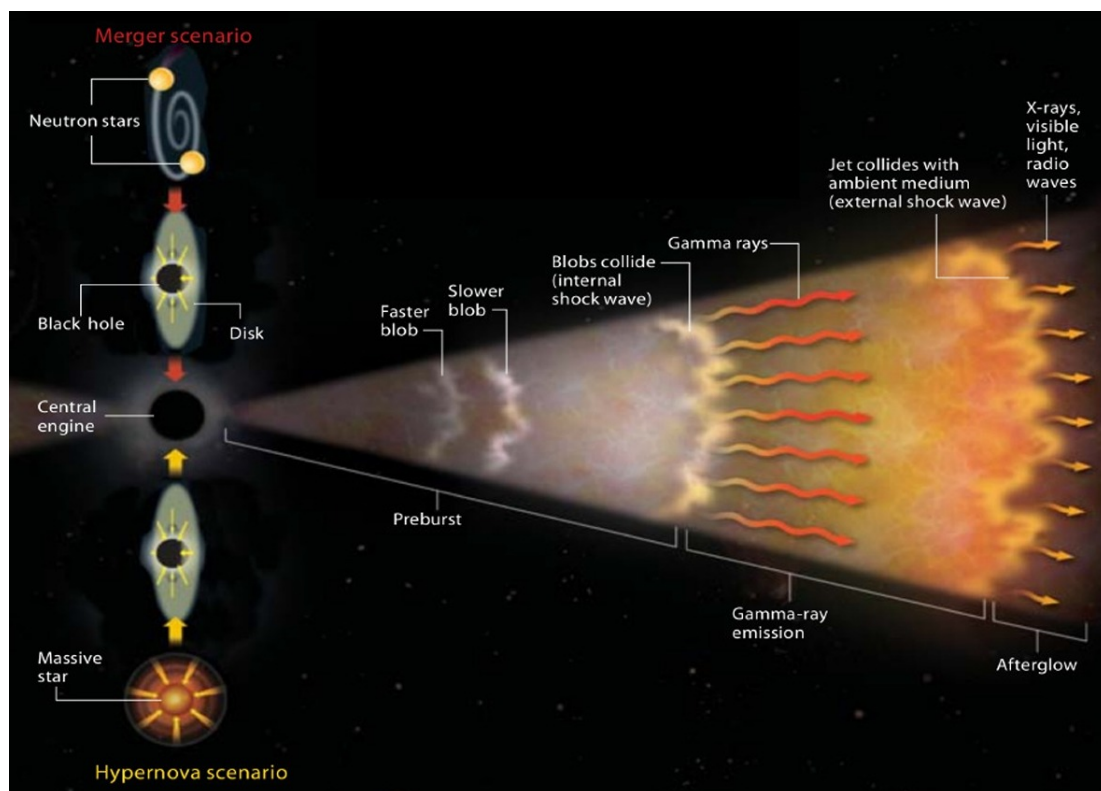


Figure 1.10: Illustration of the GRB prompt and afterglow emissions. This figure is extracted from [202].

where n_p and n_n are the proton and neutron densities, respectively. Usually, Y_e is close to 0.5 in stellar matter, although some BNS regions are neutron-rich, and the location of r-process, translating into Y_e smaller than 0.5.

During a BNS merger, when the two stars collide, part of the matter is ejected and expands in the surrounding medium at a mildly relativistic speed in the $\sim 0.1-0.3c$ range. In the first moments, the ejecta has a typical $\sim 10\text{km}$ size and is extremely hot, typically 10^9-10^{10}K . The ejecta cools by adiabatic expansion, although it is continuously heated by various sources. The dominant one is the radioactive heating by r-process, but the central engine, the emergence of the GRB jet or the rotational energy of a magnetar remnant at late times are suspected heating sources [175].

Two ejecta sources in BNS mergers produce the kilonova emissions: a dynamical ejecta and the accretion disk outflow.

Dynamical ejecta

The material unbound in the first milliseconds of the merger constitutes the dynamical ejecta, and its mass depends on the characteristics of the merging objects (mass ratio q , total mass), the equation of state of nuclear matter (EoS) and the nature of the post-merger remnant. The expected mass range is $10^{-4}-10^{-2} M_\odot$ for BNS mergers.

The equatorial material is neutron-rich with electron fraction Y_e , whose order of magnitude is typically 0.1, as expected with Equation 1.53. This implies intense r-process production and the synthesis of the heaviest nuclei ($A \gtrsim 130$) [172]. In these regions of intense r-process, the lanthanides elements are produced in large quantities, and their decays are responsible for the red kilonova emissions. The material at the contact interface of the two merging stars is compressed and expelled by hydro-dynamical forces from the remnant fairly isotropically. On the other hand, tidal forces create spiral arms in the equatorial plan that expands outward. The dominant ejection mechanism depends on the EoS and the mass ratio q . The isotropic ejecta has higher electron fraction $Y_e \sim 0.1-0.4$, and has lower r-process and lighter nuclei ($90 \lesssim A \lesssim 130$).

Disk outflow ejecta

The matter that has not been dynamically ejected or fell on the central remnant during the merger is circularised into an accretion disk. Its mass is in the $10^{-2}-0.3 M_\odot$ range, depending on the binary characteristics and the neutron stars EoS [198]. The disk creates an outflow that can dominate the dynamical ejecta on a timescale $\gtrsim 1\text{s}$. Part of the ejecta occurs as thermal neutrino winds are created in the disk [209]. Another contribution to the outflow comes from angular momentum transport via magneto-hydrodynamic instabilities [178]. The electron fraction depends greatly on the post-merger remnant, although it is in the 0.2 - 0.4 range. This allows to r-process to happen for light nuclei synthesis.

Electromagnetic emission

Most of the electromagnetic flux of the kilonova is emitted in the optical-NIR domain when the merger ejecta becomes transparent to its own radiation. The optical opacity of the merger is due to a dense forest of bound-bound transition lines. The ejecta composition will influence the luminosity of the transient. If the chemical elements within the material have a simple valence structure, the ejecta is relatively transparent. However, the presence of lanthanides and other elements with an incomplete f-shell will make the medium more opaque and less luminous. The peak emission occurs when the ejecta is cooled down to $\sim 10^3\text{K}$. Higher frequencies emissions - UV and above - are cut by a bound-free continuum as the ejecta is partly neutral.

Blue and red components

As stated at the beginning of this section, the kilonova transient is well described by two components - red and blue [175, 253]. The first is emitted in neutron-rich regions of the merger where $Y_e \lesssim 0.25$. It is emitted in the equatorial region by the tidal tail resulting from the merger or spherical outflow from the accretion disk. The red kilonova peaks in the infrared, in the J and K bands at $1.2\mu\text{m}$ and $2.2\mu\text{m}$. For a merger happening at 100 Mpc, the emission absolute magnitude will peak at ~ -16 mag.

The blue kilonova is emitted in regions with fewer neutrons, $Y_e \gtrsim 0.30$, and consequently fewer lanthanides elements. This emission occurs in the polar regions from isotropic outflows from the disk or merging stars interface ejecta. The peak emission occurs in bluer bands, at ~ 20 mag for a source at ~ 100 Mpc.

In addition to the two components we described, it is possible to observe a combination of the red and blue kilonova resulting in a "purple" component. It is visible for merger with viewing angles, allowing the neutron-rich and neutron-poor ejecta to be seen. The orientation of the merger can influence the observed color evolution. If the viewer is in the equatorial plane, the optically thick lanthanide medium blocks the blue emission.

Case of the Neutron star-Black hole merger

Neutron star-Black hole mergers (NSBH) are a known source of GW that can also produce EM counterparts. However, unlike BNS, which always emits EM radiations, NSBH requires favourable conditions to launch a kilonova. For cases where the mass ratio is small, i.e. when the black hole is heavy, the neutron star directly falls into the horizon before any EM emission occurs. Ideally, for EM emission to occur, the black hole mass should be less than $5M_\odot$. The black hole must also be rapidly spinning, with spin parameters $\chi_s \geq 0.70$, to enhance the chances of launching a kilonova [85, 86, 175]. These conditions allow a tidal disruption of the neutron star outside the black hole horizon allowing the ejection of matter in sufficient quantity for kilonova to happen.

The black holes observed by LIGO-Virgo are slowly spinning, reducing the chances of detecting an EM counterpart. This is also in agreement with the two clearly identified NSBH observed during O3 [153], that had slowly spinning black holes with $\chi = 0.09_{-0.08}^{+0.18}$

for GW200105 and $\chi = 0.31_{-0.29}^{+0.52}$ for GW200115. Their masses also disfavored the EM radiation with $m_1 = 8.9_{-1.3}^{+1.1}M_\odot$ for GW200105 and $m_1 = 5.9_{-2.1}^{+1.4}M_\odot$ for GW200115. Additional potential NSBH candidates are provided in [151], however none of them can be confidently associated to an electromagnetic counterpart.

1.2.3 Other counterparts

Fast Radio Burst

Fast radio bursts (FRB) are millisecond radio pulses detected at cosmological distances, [58]. Figure 1.11 corresponds to the first detection, that occurred in 2007 in the Parkes 64m instrument [163]. Now, FRB are detected on a daily basis by various radio-telescopes. Their progenitors and the emission mechanisms are still largely unknown, though some FRBs are confidently associated with magnetars, such as SGR 1935+2154 [239]. Things that are not yet explained are the repeating nature of some FRBs and whether the repeating and non-repeating classes have different progenitors.

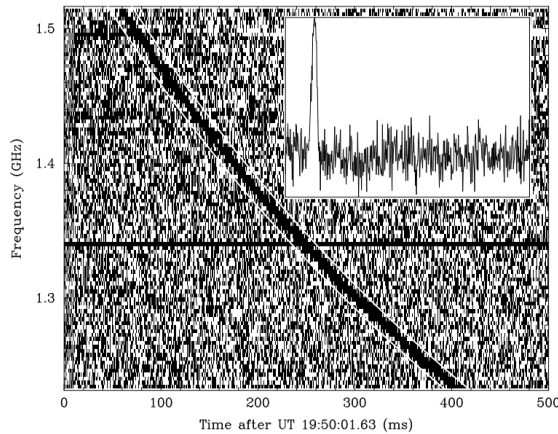


Figure 1.11: First fast radio burst discovered in 2007, with a typical "anti-chirp" shape in the Time-Frequency domain. These figures are extracted from [163].

Their mysterious nature leads to models linking repeating and non-repeating FRBs to GW. In particular, BNS mergers are expected to produce radio pulses near the merger time through magnetic braking or magnetic reconnections when the neutron stars are approaching each other. On the other hand, some BBHs with a charged companion are also thought to be potential FRB progenitors. An overview of various models predicting radio pulses as GW events counterparts is given in [160] and the references therein.

Neutrinos

Neutrinos are expected to be emitted in large quantities during a BNS or NSBH merger as part of the cooling mechanisms [209]. Part of the neutrinos is emitted in the accretion disk created shortly after the merger and participates in its stabilisation at early times by cooling it [234, 179]. Thermal neutrinos are also produced at the surface of the remnant if the latter is a neutron star [75]. For both cases, the peak neutrino luminosity can reach 10^{53} erg, with particle energy in the MeV range. These neutrino winds are responsible for the quantity of matter in the outflow. Detecting them would help understand it along with the cooling processes occurring in the merger.

There are various neutrino observatories, including ANTARES, Ice-Cube and the Pierre-Auger Observatory looking for high-energy astrophysical neutrinos that could be related to GW. As they continuously monitor the sky, they can perform low-latency or off-line coincident searches for counterparts.

1.3 Combining GW and EM observations

Performing multi-messenger observations brings information that would have been out of reach with individual messengers, enriching the understanding of the events. This section gives an overview of the outcome of the joint observations of a GW with an EM counterpart. We focus particularly on the kilonova observations and their potential for understanding the merger and for more fundamental topics. We finally present some searches of coincident EM and GW candidate events.

1.3.1 GW-GRB joint observations

GRB information on a merger

Detecting the prompt emission of a GRB in coincidence with a GW provides numerous information about the merger in its earliest stages. It carries information about the properties of the early ejecta of the merger and the timing of the jet formation compared to the coalescence time given by GW. The latter may enlighten the post-merger remnant nature as we expect a longer time delay from the GW-inferred merger time to the jet launching [265]. These joint observations could also constrain jet formation mechanisms, which are not entirely understood. For example, future joint detections will benefit from the GW-inferred masses and spins of a black hole remnant to understand the leading mechanisms to power a GRB with a BH. Furthermore, an early jet interacts with less polar material, potentially providing less collimation and would be more likely to breakout [44]. In addition to this physical information, the GRB prompt emission can narrow down the spatial localisation, in particular with observatories such as Swift, which is briefly described in the following paragraph. Such joint observations would pin down the localisation to a few arcminutes region, greatly facilitating the follow-up in longer wavelengths.

After the jet interacts with the surrounding medium, it produces an afterglow emission

that constrains the physical parameters of the merger [214]. An important one is the source orientation, which is difficult to estimate only with GW, as this quantity is degenerated with the source distance. Moreover, the afterglow break in the light curve can help constrain the jet half-opening angle θ_j . This can give access to the jet structure, whether the uniform top hat jet description does not hold and if the jet successfully pierced the ejecta [244, 127]. As the afterglow is produced by the interaction of the jet with the surrounding medium, we can extract information about the latter.

GRB Observatories

During the O3 run, several high-energy space-based facilities tried to detect the signals coincident with the GW alert distributed by the LVC. It includes instruments in the X-ray domain such as NuSTAR, Chandra or XMM-Newton (among others) and the gamma-ray domain such as Fermi. For multi-messenger purposes, two satellites are of particular interest: Fermi and Swift. The first has already proven its utility as it was responsible for the GRB counterpart to GW170817 detection with the GBM instrument. Moreover, it is the observatory with the highest number of detected GRBs. Fermi consists of two main instruments: Gamma-ray Burst monitor (GBM) [171] that probes the 8keV-30MeV energy range with 12 NaI scintillators and 2 BGO plastic detectors and the Large Array Telescope (LAT) [18], a pair-conversion telescope that observes from ~ 100 MeV-100 GeV. However, the localisation for the Fermi events is large (≥ 100 deg²), which complicates afterglow detection.

The Swift satellite can detect GRB with the Burst Alert Detector (BAT) [22] in the 15-150keV range. It consists of a detector array behind a coded mask that allows localising the source with a typical 4 arc-minutes error disk. Then the gamma-ray prompt emission is followed-up on shorter wavelengths from X-rays with the XRT detector and the UV-optical with the UVOT telescope. Despite Swift did not detect the GW1790817 GRB, its capabilities to reach arcminutes localisation based on the prompt emission and to have early observations of a potential afterglow make Swift a good candidate for future MMA observations.

In the upcoming year, the SVOM mission will be launched [258]. It will have similar capabilities as Swift, with the ECLAIR instrument equipped with a coded mask for prompt emission in the 4-150 keV band, allowing an arcminutes localisation and the GRM. The satellite will also be equipped with GRM, a gamma spectrometer for photons in the [15, 5000]keV range. In addition, there will be two telescopes, MTX in the X-ray domain and the VT for the optical/near-infrared capabilities. SVOM is planned to be launched in 2023, allowing a probable overlap with the O4 run of LIGO-Virgo, as illustrated in Figure 1.9.

1.3.2 GW-Kilonova joint observations

Kilonova follow-up

Kilonova observations can bring decisive information about the merger that GW alone would not. In addition, they can also lead to breakthroughs in fundamental physics topics such as cosmology or nuclear matter behaviour in a dense medium. In addition, this section described the kilonova in its most usual understanding. However, other possible emissions could be observed during a BNS merger. Decompressed neutrons ejected rapidly at the early stages of the collision may not be captured and decay in the layers outside the merger producing an early UV emission [24, 182]. However, finding this emission would require very early detection of the kilonova within hours after the GW detection. Another early emission possibly observed is due to the re-heating of the merger. At a later time, X-ray re-brightening could be emitted by the central compact remnant. Fall-back accretion could also be responsible for X-ray emissions, as it is detailed in [175] and references therein.

All these considerations indicate the importance of constituting a large and diverse kilonova sample. Using GW-based MMA follow-up is the most promising method, considering the lack of kilonova associated with short GRB. Constraining observations require early detection, and late follow-up, especially in the NIR, well-sampled light curves and spectroscopic observations. It will help evaluate the merger characteristics, from the ejecta mass to the nature of the post-merger remnant object, and bring constraints on important fundamental topics. Although there are many observational constraints in the kilonova follow-up, this will be detailed in Chapter 3.

Post-merger information

There are four possible outcomes after the merger of two neutron stars. For heavy binaries, the merger remnant promptly collapses into a black hole in less than a millisecond. This happens for mergers of total mass above 2.6 - 3.9 M_{\odot} depending on the EoS of neutron stars [175]. If there is no prompt collapse, the remnant is a neutron star whose fate depends on its mass and the mechanism opposing gravity. If the neutron star is stabilised by differential rotation, the remnant is called *hypermassive neutron star* (HMNS). Energy is dissipated efficiently by the differential rotation, matter accretion, and GW emission [222, 223]. Consequently, an HMNS will not last for more than ten to hundreds of milliseconds before collapsing into a black hole. A neutron star stabilised by solid rotation is called *supermassive neutron star* (SMNS). The SMNS will spin down by angular momentum losses until it collapses into a black hole. The energy is dissipated via less efficient processes than the HMNS, such as magnetic dipole radiation or GW emission via non-axisymmetric deformations. These mechanisms are less efficient for energy dissipation, hence, the SMNS last longer than an HMNS. The lifetime of an SMNS is in the hundreds of milliseconds to several minutes range. The last outcome of a BNS merger is a stable neutron star that will remain indefinitely and never form a black hole. This happens for low mass BNS mergers and in likely rare occurrences - less than 3% of the cases [165, 175].

The nature of the post-merger remnant is encoded in the GW signal at frequencies superior to kHz. Although, the current GW detectors are not sensitive enough in this domain to determine the post-merger nature. On the contrary, kilonova emission contains signatures of the resulting compact object that are observable via the transient color evolution. Consequently, kilonova observation in the MMA context is a privileged way to determine the post-merger remnant nature. For a BNS leading to a prompt collapse to a black hole, the ejecta will be lighter ($\ll 10^{-2} M_{\odot}$) and lanthanide-rich [84, 115]. Consequently, the merger will result in a red and relatively faint kilonova, peaking in the NIR at 23-24 mag at 100 Mpc [21]. Such a case would be difficult to detect considering the few instruments able to reach this depth in the NIR domain. In a merger with an HMNS transient remnant, the colliding stars interface produces heated and neutrons poor matter in the ejecta, which emits a bright blue component in the UV-optical domain for ~ 1 day, reaching 20 mag at 100 Mpc. In addition, a redder emission is followed at latter times, lasting for ~ 1 week [180, 175]. A longer-lived remnant - an SMNS or a stable neutron star - produces heating of the ejecta via the central engine spin-down [177]. It raises the luminosity of the blue component, although the energy injection mechanisms parameters or the collapse time are unknown, leading to high uncertainties about the transient brightness. The different emission scenarii are summarized in Figure 1.12 extracted from [175].

In addition to the post-merger nature, detecting a kilonova in coincidence with the GW could help to distinguish between BNS and NSBH mergers. As EM counterparts are more likely to be emitted for low-mass black holes, the nature of the binary companions can be difficult to distinguish using GW signal only. In the case of an NSBH producing a kilonova, the ejecta mass can be significantly larger than for a BNS [216], producing a kilonova brighter by ~ 1 magnitude [175]. As the ejecta is produced by the tidal disruption of the neutron star, the main contribution to the emission comes from the accretion disk. Consequently, the blue component emitted by the disk outflow is located behind and obscured by the tidal outflow, producing a redder kilonova compared to a BNS-powered one.

Nuclear physics

Kilonovae are the location of intense r-process, responsible for heavy elements synthesis. Consequently, a large kilonova sample could bring constraints to various topics in nuclear physics. In particular, it could explain the observed abundances of heavy elements in the stellar matter and constrain the EoS of neutron stars, which is currently an open question.

r-process

The r-process consists of rapid capture of neutrons by seed nuclei. Both ingredients are emitted by the neutron star ejected and decompressed matter. A neutron-rich material surrounds the seed nuclei, which capture the neutrons on a timescale τ_r much smaller

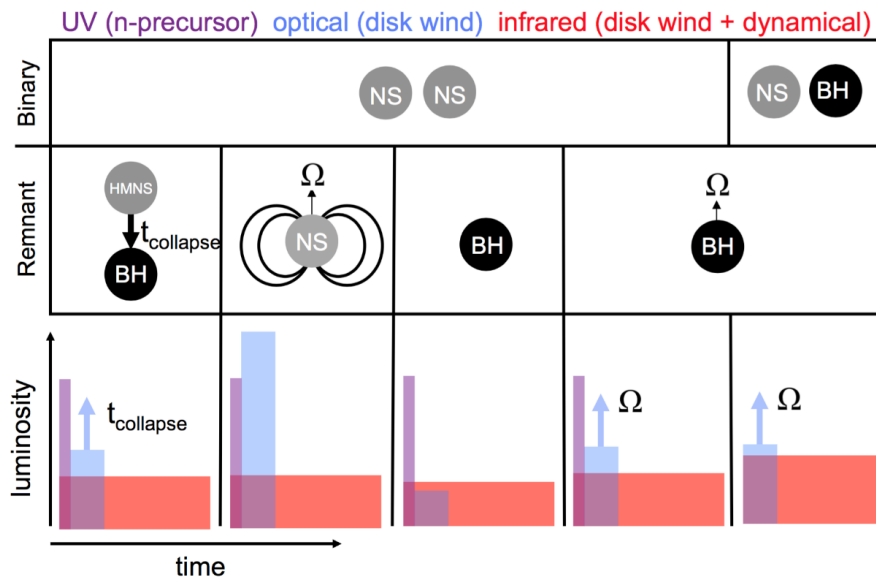


Figure 1.12: Overview illustration of the various outcome remnants for BNS mergers (middle row) and their corresponding kilonova emissions (bottom row). The blue component of the kilonova is materialised in blue, the red kilonova in red and the purple corresponds to the putative UV precursor due to free neutron decaying in the outer layer of the ejecta. For spinning remnants, the angular momentum is denoted Ω . This figure is extracted from [118, 175].

than the β -decay typical time τ_β [43, 17]. The seed nuclei are enriched by numerous neutrons, making them highly unstable, and then a β -decay occurs before more neutrons can be captured. This process requires neutron density $n_n \sim 10^{20} \text{cm}^{-3}$, high temperature $\sim 10^9 \text{K}$ and starts after $\sim 1 \text{s}$ in the ejecta.

Heavy Elements Nucleosynthesis

Originally, kilonovae were proposed to explain the abundances of heavy nuclei synthesised via r-process. The estimated mass of heavy elements produced via r-process per merger is estimated to be [175]:

$$\langle M_r \rangle \sim 10^{-2} M_\odot \left(\frac{R_{BNS}}{10 \text{yr}^{-1}} \right)^{-1}, \quad (1.54)$$

to explain the galactic abundances. Here R_{BNS} is the rate of BNS detection by LIGO and Virgo at design sensitivity. This makes the BNS merger a major source of heavy element synthesis. Consequently, it was proposed to use kilonova as a probe for heavy elements synthesis [181].

The quantity of r-process occurring in the merger can be estimated via the color evolution. The red kilonova traces the abundance of lanthanides and actinides. Although, estimating the quantities of the heaviest synthesised elements, beyond $A = 195$, requires ultra-late times observations, at least several weeks after the merger. At this point, the radioactive decays are due to specific nuclei such as ^{225}Ac , ^{225}Ra and ^{254}Cf . These elements can be identified as they produce un-ambiguous decay features in the bolometric lightcurve [173, 267]. Although this will require deep observations as the kilonova luminosity decay rapidly, making these events accessible only to the largest facilities. The recently launched James Webb Telescope could fulfil these requirements for future kilonova detections.

Constraining the neutron star equation of state

Quantum chromodynamics (QCD) is a quantum field description of the interactions between quarks and gluons and constitutes the relevant framework for describing dense matter in neutron stars [262]. Quarks are the elementary particles bound into hadrons via the exchanges of gluons. Protons and neutrons are made of three valence quarks and are the building blocks of nuclei. Although QCD is well tested, it is extremely complicated to describe large-scale structures such as neutron stars. The latter reach extreme densities close to nuclear saturation, where the baryons start to overlap. This starts at density $\rho_0 \sim 10^{14} \text{g.cm}^{-3}$. Beyond this density, nuclear matter starts to reach complex states. In particular, beyond $10\rho_0$, quarks are de-confined, creating the quark-gluon plasma, well described by perturbative QCD. On the other hand, between $2\rho_0$ and $10\rho_0$, the dense matter is not understood. These densities are found in the internal structure of neutron stars, making them natural laboratories for studying the dense nuclear matter.

The crucial quantity to measure for unveiling the neutron star structure is the equation of state (EoS) that describes the relation pressure-density of the star. As there is an antagonist effect between the gravitational force and the degeneracy pressure stabilising

the star, this EoS is measured via the mass-radius relation.

The GW signal emitted by a BNS merger can contain signatures of tidal deformation of the neutron star, informing about the neutron star EoS. In addition, the EoS drives the ejecta mass, consequently, detecting a kilonova, whose brightness is closely related to the ejecta, also constrains the EoS. Moreover, the post-merger remnant information also depends on the EoS, consequently, using the colour evolution is essential for estimating the EoS. Eventually, the use of MMA to combine the information from the GW and the EM emissions provides tight constraints on the EoS [59].

Cosmology

The Hubble constant H_0 is a measure of the expansion rate of the local Universe. It is linked to the luminosity distance D_L at first order:

$$v_H = H_0 D_L = cz, \tag{1.55}$$

where V_H is the Hubble flow and z is the redshift [41]. The Hubble constant is a fundamental quantity for cosmology estimated using various experiments and methods. Although a tension has emerged between some of these methods, in particular between the estimation via the cosmic microwave background (CMB) [206], and the estimation using of type Ia supernova as standard candles [215]. This tension between early probe (CMB) and late universe probes (SN Ia) is either due to systematic effects yet to be discovered or the smoking gun of new physics. In that context, multi-messenger observations could help to solve this tension. There are various ways to estimate H_0 with GW and their electromagnetic counterparts. The GW detection gives an estimation of the luminosity distance as the strain amplitude h is inversely proportional to D_L . Even without detecting an EM emission, using galaxy catalogs to cluster galaxies to have a statistical estimation of the redshift and extract H_0 [199]. However, finding a counterpart in the EM domain improves the H_0 estimation. In particular, finding an optical domain, either a kilonova or an afterglow, allows to precisely localise the source and identify a host galaxy to evaluate the source redshift and compute the Hubble constant. Moreover, detecting the GRB afterglow also allows estimating the source inclination. Otherwise, there is a degeneracy between the luminosity distance and the inclination ι of the source [248] as, at small angles, the GW strain amplitude is:

$$h \propto \frac{\cos \iota}{D_L}. \tag{1.56}$$

1.3.3 Multi-messenger searches during O3

During the last O3 run of LIGO and Virgo, several MMA searches were performed with various messenger and through the whole EM spectrum. We give a rapid overview of some of them in the gamma and radio domain and a search of coincident neutrino. For the optical domain, kilonova searches are treated in detail in Chapter 3.

GRB-GW searches

The LIGO-Virgo collaboration used candidate events produced by Fermi-GBM and Swift-BAT published through GCN¹ with complementary information from the Swift GRB archive², the Swift/BAT catalog³[134] and the GBM catalog to make targeted GW searches around the GRB trigger times [154, 157]. Two searches were conducted, an un-modelled search, looking for generic GW transients, and a modelled search, looking specifically for CBC.

The modelled analysis aims at searching for GW170817/GRB170817A-like association with the PyGRB pipeline [102]. Therefore only short and ambiguous GRBs were analysed this way. Six seconds of GW data are isolated around the GRB time trigger to create an on-source window of -5s to +1s. This choice was guided by the GW170817 event, for which the GW emission and the jet launching were separated by 1.7s.

The generic transient search is performed with X-pipeline [112] and aims at finding GW-GRB associations produced by sources that are not necessarily CBCs, using time-frequency maps. It includes core-collapse supernovae known as long GRB precursors or instabilities in accretion disks (ADI) of rapidly spinning black holes. As there is a large variety of possible sources, compared to the modelled search, the on-source time window starts 600s before and ends 60s after the GRB trigger time. The width is chosen in order to take into account different gamma emission mechanisms associated with a GW.

The distances probed by the two searches were estimated using GW signals injections of the various astrophysical populations. For the modelled search, the typical exclusion distance is 100-200 Mpc depending on the used model. On the other hand, the un-modelled search rejected events up to ~ 90 Mpc for supernova-linked associations [157]. Despite no joint detection of a GRB and a GW during O3, the LVK collaboration used the results from O1, O2 and O3 to constrain the rate of Fermi/GBM-GW associations for the next O4 run using a Bayesian approach [157]. The prior is built using a cumulative distribution rate $C_R^{obs}(z, \gamma_L, L_0)$ and P_{obs}^{GRB} , the probability of observing a short GRB, γ_L is the low-luminosity power index and L_0 the low-luminosity cutoff. The likelihood is constructed using the fact that one GW-GRB coincidence was detected during O2 and none during O1 and O3. This provided a rate R_{GW-GRB}^{O4} of 170817-like joint Fermi-GW detection for an O4 GW network with a 150 Mpc horizon for the LIGOs and 80 Mpc for Virgo:

$$R_{GW-GRB}^{O4} = 1.04_{-0.27}^{+0.26} yr^{-1}. \quad (1.57)$$

Other GW counterparts searches

The LIGO and Virgo collaborations have analysed some FRB triggers produced by the Canadian Hydrogen Intensity Mapping Experiment (CHIME) [160]. This instrument is a recent radio telescope commissioned in 2018, located in Canada, made of four 20 m x 100 m cylindrical parabolical reflectors. It is sensitive in the 400 - 800 Hz frequency

¹ https://gcn.gsfc.nasa.gov/gcn3_archive.html

² https://swift.gsfc.nasa.gov/archive/grb_table/

³ <https://swift.gsfc.nasa.gov/results/batgrbcat/>

band in a ~ 200 deg². The CHIME sample analysed by LIGO and Virgo comprises 34 non-repeating bursts and 11 bursts produced by the three closest repeating sources, all detected during O3a. This sample is based on the requirement of available data in at least one interferometer, distance estimation and good data quality in CHIME. The search methods are the same as for the GRB, an un-modelled search with **X-pipeline** and a modelled search with **PyGBR**. The choice of the on-source windows are [-10, 2]s for **PyGBR** and [-600, 120] for **X-pipeline**. They are larger than for GRB to account for the lack of constraints on the FRB-GW association. Moreover, using injections, exclusion distances were set on the tested models.

None of the p-value distributions shows any statistically significant coincidence, consequently, no significant association between FRB-GW can be established. For the modelled search, the median exclusion distances for BNS and NSBH with generic spins models are 192 Mpc and 257 Mpc. The various injections span exclusion distances from 1 to 80 Mpc for the generic transient search, depending on the parameters used. Due to the difficulty in estimating the FRB distance, the uncertainties span several orders of magnitudes. Eventually, it prevented ruling out any models tested with this analysis.

On the LVK collaboration side, a search pipeline called LLAMA has been developed to analyse Ice-Cube triggers [23]. For the O3a run, the Super-Kamiokande collaboration conducted an independent search for high-energy neutrino coincident with GW signals [2]. The method uses a 1000s on-source window centred on the GW triggers and searches for spatially and temporally compatible particles. However, no confident association has been established by the collaboration.

1.4 August 17th, 2017

August 17th, 2017, marks a milestone for MMA: the first joint detection of a gravitational wave (GW) produced by the merger of two neutron stars and its electromagnetic counterpart on the whole spectrum. The event is described from different perspectives in the following Section.

1.4.1 Gravitational wave signal: GW170817

At 12:41:04 UTC, the network of gravitational waves detectors composed of LIGO Handford (H1) and LIGO Livingston (L1) and Advanced Virgo (V1) detected a ~ 100 s long GW signal compatible with a binary neutron stars (BNS) merger, later named GW170817. At first, the low latency searches detected the signal only in the LIGO Handford data. The LIGO Livingston data had a large noise transient, also called "glitch", on top of the signal that had to be estimated and subtracted prior to the signal analysis. This treatment is visible in the left panel of Figure 1.13 and the resulting signal represented in the Time-Frequency domain for the three detectors (LIGO+Virgo) is visible on the right panel; these figures are extracted from the detection paper [139]. This event was

the loudest ever detected at the time, with signal-to-noise ratios (SNR) of $\rho_{H1} = 18.8$, $\rho_{L1} = 26.4$ and $\rho_{V1} = 2.0$ for Handford, Livingston and Virgo, respectively, after noise mitigation, for a total network SNR $\rho_{net} = \sqrt{\rho_{H1}^2 + \rho_{L1}^2 + \rho_{V1}^2} = 32.4$.

After the data cleaning, the source parameters were estimated, including the compact objects' component masses. They were evaluated to lie within $[1.36, 2.26] M_{\odot}$ for the heaviest and within $[0.86, 1.36] M_{\odot}$ for the lightest. The inferred masses, combined with the longer duration of the signal compared to the $\leq 1s$ duration of the binary black hole mergers signals previously detected, were strong evidence for GW170817 being a binary neutron stars merger (BNS) before any electromagnetic detection confirmation. The source of the signal has been rapidly localised using only the LIGO data to a region of 190 deg^2 , then reduced to a 31 deg^2 using the data from the whole network. These estimations are summarised in Figure 1.14, which was extracted from [159]. The estimated distance was $40_{-14}^{+8} \text{ Mpc}$, making this event the closest compact binary coalescence to this day. This information was rapidly made public to astronomers as the likely presence of neutron stars made observing an electromagnetic counterpart possible. It eventually led to the detection of the electromagnetic transients produced by the merger, covering the whole spectrum. Figure 1.13 summarises the various localisations by the instruments from both gravitational waves and electromagnetic sides.

1.4.2 Gamma-ray counterpart: GRB170817A

In coincidence with the GW signal, the GBM instrument onboard Fermi satellite detected a weak gamma-ray burst (GRB). The GBM instrument observed a 5σ excess in three of its twelve NaI scintillators 1.74 ± 0.05 second after the GW trigger. According to [92], the GRB seemed made of two components, a first hard one lasting for half a second and a second softer one lasting for several seconds. Despite this, based on the signal's duration and hardness, the GRB was three times more likely to be a short GRB than a long GRB [92]. The localisation of the signal returned a 50% and 90% credible localisation of respectively $\sim 350 \text{ deg}^2$ and $\sim 1100 \text{ deg}^2$ [148]. These results are summarised in Figure 1.14. This detection was done by an automatic search and outreached through a GCN notice [237]. On the other hand, the INTEGRAL satellite, through its SPI-ACS instrument, detected an excess with a SNR of 4.6, 1.88s after the GW trigger. Eventually, the chances of a GW signal and a GRB signal with both these spatial and temporal coincidences were evaluated as $p_{unrelated} = 5.0 \times 10^{-8}$ [148]. This unambiguous association between the two signals led to a worldwide observational campaign to find the electromagnetic counterpart in the other domain of the spectrum.

1.4.3 Optical counterpart: AT170817gfo

The joint announcement of the GW and GRB discovery started a broadband search for the UV/Optical/IR counterpart by ground and space-based instruments [159, 235, 15, 228]. The One-Meter, Two-Hemisphere was the first team to report the identification of a new bright transient in the *i*-band: AT2017gfo [65]. The detection image is visible in Figure 1.14, on the upper-right frame. It was taken on August 17 at 23:33 UTC,

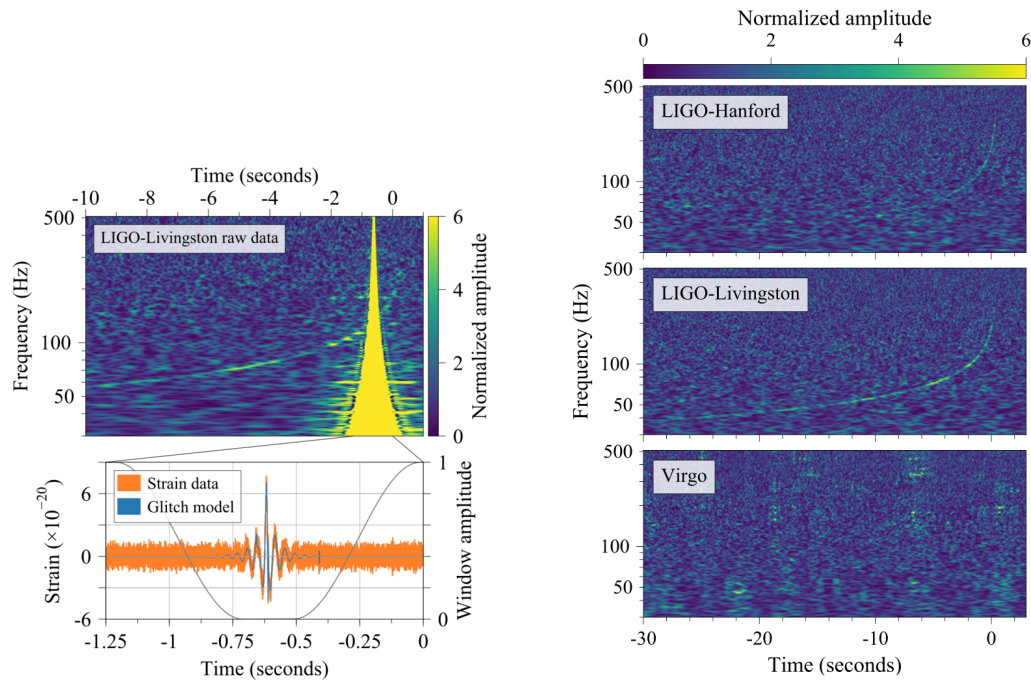


Figure 1.13: Summary of the gravitational wave detection. The left panel shows the raw data from the LIGO-Livingston interferometer exhibiting a large glitch on top of the GW170817 that delayed the identification of the signal as being of astrophysical origin. It also shows the transient noise model that has been subtracted to improve the parameters estimation and the sky localisation in particular. The right panel shows the GW signal in the three interferometers. The chirp is clearly visible in both LIGO but not in Virgo, the BNS being localised in one of Virgo less sensitive regions. These Figures were extracted from the GW170817 discovery paper [139]

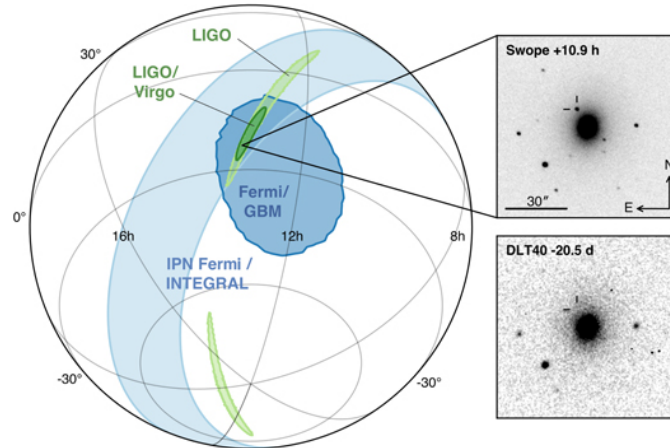


Figure 1.14: Localisation of the gravitational wave signal GW170817 (extracted from [159]). The light green region is given by the LIGO data only. The dark green area is obtained when Virgo data are used and span a 31deg^2 . The blue region corresponds to the IPN triangulation of GRB170817A detected by both the FERMI-GBM instrument and the INTEGRAL-Anti-coincidence Shield (SPI-ACS). The two right panels show the images of the Swope telescope that led to the discovery of the optical signal linked to the BNS 10.9h after the trigger (top) and the latest pre-discovery image of the field of view acquired by DLT40 20.5 days prior to the detection (bottom).

10.87h after the GW trigger. The astronomers used the 3D spatial information to list the known galaxy in the volume, ranked according to their stellar mass and star formation rate. The optical transient was detected with a magnitude $i = 17.057 \pm 0.018$ mag. Located at $\alpha(J2000) = 13^{\text{h}}09^{\text{m}}48^{\text{s}}.085 \pm 0.018$, $\delta(J2000) = -23^{\circ}22'53''.343 \pm 0.218$, in the galaxy NGC4993 at a luminosity distance of 40Mpc. Five other teams independently reported the detection of AT2017gfo, and they are visible in Figure 1.15 bottom panels. Over the following weeks, the transient was observed by telescopes ranging from 0.4m to 10m covering UV, optical and near-infrared with photometry and spectroscopy. Observations exposed a significant magnitude difference between daily image acquisition, indicating a rapid luminosity decline with a fading of 0.6 mag per day in the i , y and z bands according to [49]. Along with the photometric measurements, spectra of the newly discovered transient were acquired 30 minutes after the first image with the LDDS-3 spectrograph mounted on the *Magellan*-Clay 6.5m telescope and the MagE spectrograph on the 6.5m *Magellan*-Baade telescope. The spectrum revealed an unusual, though not unprecedented blue, featureless continuum within the 4000-10000 Å band. In the following days, various instruments acquired additional spectra. They showed a rapid flux decay in the blue wavelengths and a lack of absorption lines that would be observed for a supernova. Moreover, daily observations by the VLT/X-shooter showed r-process nucleosynthesis signatures. The Hubble Space Telescope spectrum contained signatures of lanthanides production within the ejecta. These characteristics were strong evidence that this transient was the first identified kilonova.

1.4.4 X-ray counterpart

Along with the follow-up of the UV, optical, and IR searches, several instruments performed X-ray observations to find the GRB afterglow. The first upper-limits on the X-ray flux was $8.6 \times 10^{-9} \text{erg.cm}^{-2}$ in the 2-10keV band, provided by MAXI 0.19 days after the GW trigger. No detection either for the Super-*AGILE* detector down to $3.0 \times 10^{-9} \text{erg.cm}^{-2}$ in the 18-60 keV band after 0.53 days. Some deep pointed observations were rapidly performed by *NuSTAR* and *Swift* down to $2.6 \times 10^{-14} \text{erg.cm}^{-2}$ 0.70 days after the GW emission, without any detection of the afterglow. *INTEGRAL* and *Chandra* started their observations nearby the optical transient 6 and 2.2 days after the trigger, respectively, without any detection. The discovery of the afterglow occurred nine days post trigger by *Chandra* [242] in a 50ks exposure where an X-ray source is visible at the previously detected UV/optical/IR source location as illustrated in the bottom panels in Figure 1.15.

1.4.5 Radio counterpart

After the merger, the fast-moving ejecta collided with the surrounding medium, creating a radio emission that gave information about the geometry of the ejecta and the interstellar medium. Despite the early observations by radio surveys such as the Australian Telescope Compact Array (ATCA) one day after the BNS signal or the Long Wavelength Array (LWA1) 6.5 hours, 6 days and 13 days after the GW170817 detection, no confident observations of a radio counterpart could be associated to the event down to 200 Jy at the 25MHz and 100Jy at 45MHz. The radio afterglow discovery occurred on 2017 September 2 and 3 (16 days after the GW trigger) by the Very Large Array (VLA) at 3 GHz and 6 GHz [99, 9] via two independent observations as visible in Figure 1.15, bottom panels. Radio observations are still ongoing to monitor the evolution of the afterglow as it is still visible for the largest instruments such as ATCA and brought information about the jet structure emitted by the neutron stars coalescence. The monitoring of the X-ray and radio afterglow is still ongoing [164, 208, 20, 246, 98, 69].

1.4.6 Neutrino emission

BNS coalescences are predicted to emit neutrinos at different energy bands from MeV to TeV-EeV. The Ice-Cube detector has searched the lower energy range. A supernova-like neutrino burst targeted search has been performed in a $\pm 500s$ time window around the trigger time. In addition, a follow-up search was extended to 14 days after the merger without any detection from Ice-Cube. On the other hand, the ANTARES collaboration probing for higher energy neutrinos (GeV-TeV) conducted a similar analysis without any detection. The same results stand for the Pierre Auger observatory that searched for Ultra-High Energy (UHE) neutrinos - with energies superior to 10^{17}eV [159].

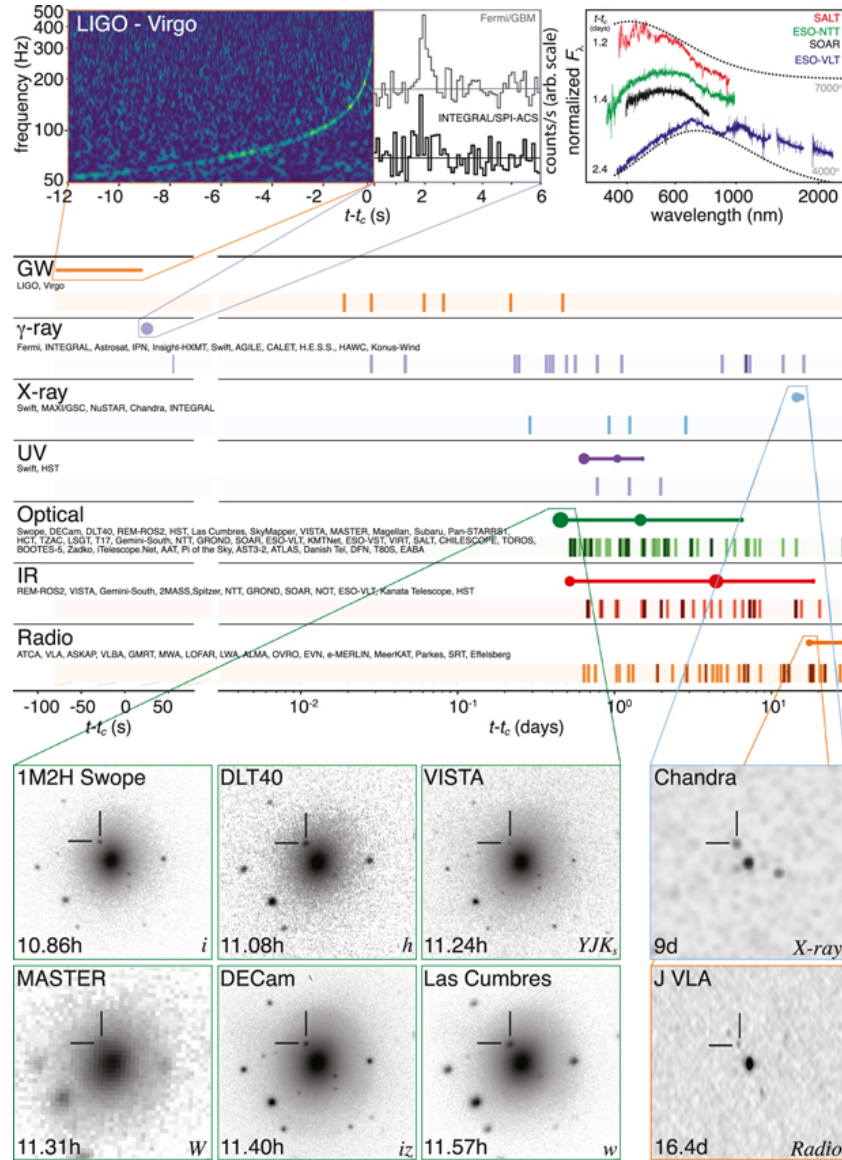


Figure 1.15: Summary of the 170817 observations. The upper left panels show the GW chirp; the middle corresponds to the GRB lightcurves from FERMI-GBM and INTEGRAL; the right one exposes the spectrum acquired by different optical ground-based spectrographs. The middle panel gives detailed timelines of observations and discovery of the different counterparts to the gravitational signal. The dots correspond to typical observation of the source, with areas scaled by source brightness. The solid lines correspond to the time when the source was detectable by at least one facility in the corresponding band. The bottom panels show the optical images of the discovery images acquired by the different facilities that independently observed AT2017gfo. On the right are the images of the X-ray counterpart detection (upper) and the radio afterglow (bottom). Figure extracted from [159].

1.5 Scientific outcomes of GW170817

The GW170817 event was a major discovery for many domains of astrophysics. The multi-messenger and multi-wavelengths observation not only allowed us to evaluate many physical properties of the merger itself but also allowed insights into several fundamental topics.

1.5.1 Inferences on the merger

The BNS merger has been widely studied via multi-messenger observations, and a summary of the results gathered from them is presented in Table 1.1 extracted from [175]. After the GW signal detection, the EM counterparts detection confirmed that at least one of the binary companions was a neutron star and allowed to reach a point localisation for the source. The GRB detection, along with the X-ray and radio afterglows, constrained the viewing angle and the jet structure. At first, several scenarii were considered for the jet: either a top hat jet, which was the usual way to model a jet, a structured jet viewed off-axis or a jet surrounded by a cocoon, a wide-angle outflow expanding quasi-spherically with radial velocity stratification [148, 191]. However, the very late times afterglow observation showed a peak luminosity at ~ 150 days post-merger, which ruled out the top-hat hypothesis. Later, the detection of an apparent superluminal motion of the radio flux centroid [187], together with the compact size of the radio image ~ 2 mas [90], strongly favoured the structured jet model. This structured jet was estimated to have a relativistic core with an opening angle $\theta_{core} = 3 - 5^\circ$ and a wider component with $\theta_{jet} \geq 10^\circ$ [247, 191]. These observations also constrained the GRB viewing angle of the jet, confirming the jet was off-axis with an angle $\theta_{view}^{GRB} \sim 21^\circ$ [247, 187, 191] or $\theta_{view}^{GRB} \sim 30^\circ$ [97], depending on the used model. The off-axis jet conclusion was a privileged explanation of the burst faintness.

For the optical emissions, the kilonova showed a two components behaviour as described in [175]. This is visible in Figure 1.16, extracted from [253], that collated all the images acquired during the AT2017gfo follow-up in the UV-optical-NIR bands. During the first days, the blue bands (B , V , g) dominated the apparent magnitudes. After ~ 2 days, the redder bands (from r to K) were brighter and completely dominated after 5 days. The kilonova follow-up returned a merger viewed from an angle of $\theta_{view} \sim 30^\circ$ [76, 192], which was consistent with the results obtained with the GRB emission and the constraints from the GW signal [145]. The spectrum of the kilonova in the $1.5\mu\text{m}$ and $2.5\mu\text{m}$ showed typical features from Cs, Te, and I presence, indicating nuclear synthesis via light r-process. The bolometric luminosity L_{bol} could be explained by the synthesis of many isotopes. The fit of the two components model yielded an ejecta mass in the $[0.02, 0.06]M_\odot$ and an electron fraction Y_e within $[0.15, 0.35]$ [175]. The three components (blue, red, purple) fit in Figure 1.16 from [253] yielded $M_{ej} \sim (0.02, 0.047, 0.011)M_\odot$ for each component, and velocity of $v_{ej} \sim (0.27, 0.15, 0.14)c$. The electron fraction was in the $[0.25, 0.35]$ range in addition to regions with $Y_e \leq 0.25$ where the r-process synthesised lanthanide elements with $A \geq 140$ up to $A \sim 195$.

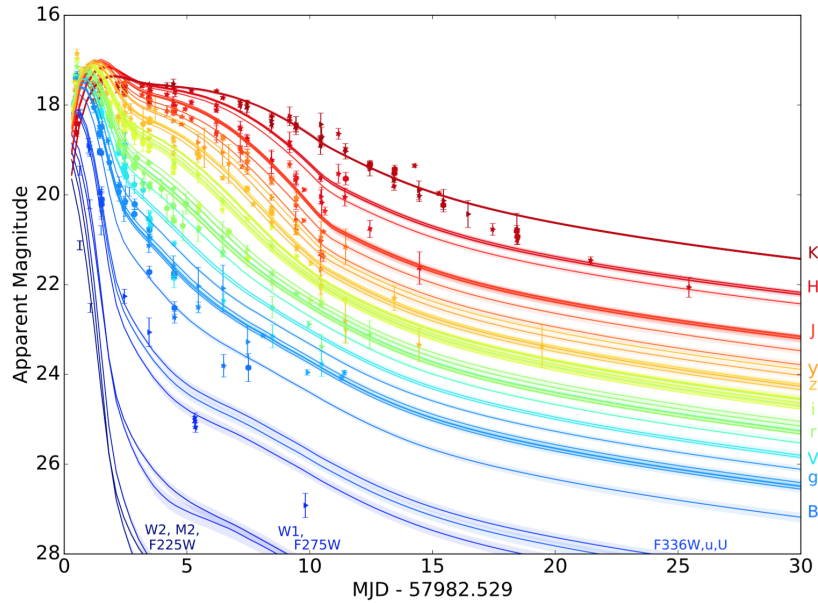


Figure 1.16: UV-optical-IR lightcurve of AT2017gfo based on data gathered by [253], along with the best fit model of three component kilonova (red-purple-blue). This figure is extracted from [253].

As the total ejecta mass was superior to $0.02M_{\odot}$, it required more than just a dynamical component, based on the predictions by simulation of BNS merger [175]. Moreover, the red kilonova required to have a disk outflow to appear. The blue kilonova origin was less clear, the current explanation involved a shock heated dynamical ejecta with high velocities $V_{ej} \sim 0.2-0.3 c$ and $Y_e \geq 0.25$. However, the relatively high mass of this ejecta $M_{blue} \sim 0.01 M_{\odot}$ was disfavored by numerical simulations. Another hypothesis for the blue component was that a wind emerged from an HMNS remnant before the collapse. Simulation of a magnetar with $B \sim 1-3 \times 10^{14} \text{G}$ could explain the ejecta mass and velocity. The latest explanation for the blue kilonova involved an HMNS remnant producing spiral density waves explaining the ejecta parameters [193].

The GW detection allowed to evaluate the size to $R_{1.6} = 10.8^{+2}_{-1.7} \text{km}$, assuming a $1.6M_{\odot}$.

1.5.2 Fundamental physics

Beyond the merger characterisation, the multi-messenger observations of GW170817 gave insights on several topics. It was the first detection of a binary neutron star merger and consequently was a significant discovery for GW astronomy. By itself, the GW observation gave essential results in various domains. For compact object astrophysics, it gave information about the population of extra-galactic neutron stars and the rate of BNS in the local universe. The BNS rate was estimated to be $R_{BNS} \sim 100 \text{Gpc}^{-1} \text{yr}^{-1}$ which implied that BNS mergers are a significant source of r-process, according

Table 1.1: Key Properties of GW170817. This Table is extracted from [175] and references therein.

Property	Value
Chirp mass, \mathcal{M}_c (rest frame)	$1.188^{+0.004}_{-0.002} M_\odot$
First NS mass, M_1	$1.36 - 1.60 M_\odot$ (90%)
Second NS mass, M_2	$1.17 - 1.36 M_\odot$ (90%)
Total mass, $M_{\text{tot}} = M_1 + M_2$	$\approx 2.74^{0.04}_{-0.01} M_\odot$
Observer angle to orbital axis, θ_{obs}	$19 - 42^\circ$ (90%)
Blue KN ejecta ($A_{\text{max}} \lesssim 140$)	$\approx 0.01 - 0.02 M_\odot$
Red KN ejecta ($A_{\text{max}} \gtrsim 140$)	$\approx 0.03 - 0.06 M_\odot$
Light r -process yield ($A \lesssim 140$)	$\approx 0.04 - 0.07 M_\odot$
Heavy r -process yield ($A \gtrsim 140$)	$\approx 0.01 M_\odot$
Energy of GRB jet	$\sim 10^{49} - 10^{50}$ erg
ISM density	$\sim 10^{-5} - 10^{-3}$ cm $^{-3}$

to Equation 1.54. However, the uncertainties on R_{BNS} did not allow us to determine whether BNS are the dominant source of r -process. The GW signal constrained the tidal deformability of the neutron stars using a set of EoS models. It was estimated to be in the [280, 310] range, depending on the GW model used for the parameter estimation [145]. This signal allowed several tests of the General Relativity. Constraints on the GR dynamics of the source, in particular the post-Newtonian coefficients used to produce GR waveforms, are set based on the GW170817 signal [135].

The confident association of the GW signal and the GRB170817A confirmed the long-suspected link of the binary neutron star mergers with at least part of the short GRB population. The observed delay between the GW and GRB emissions gave unprecedented occasion for fundamental physics tests and jet formation. In the former case, the 1.7s delay set tight constraints the speed of gravity:

$$-3 \times 10^{-15} \leq \frac{\Delta v}{c_f} \leq +7 \times 10^{-16}. \quad (1.58)$$

The GRB-GW association placed new bounds on the violation of Lorentz invariance. In an effective field theory, the relative group velocity of GWs and EM waves are described by differences in coefficients for Lorentz violation in the gravitational sector and the photon sector at each mass dimension d . The analysis did not show any violation and tightened the constraints previously obtained by other tests of the Lorentz invariance. It was also shown that the result of the GRB and GW combination was better than the previous limits based on BBH observations [148]. The equivalence principle has been tested using the Shapiro effect, which predicts that the propagation time of massless particles in a spacetime curved by a gravitational field is slightly increased compared to the flat spacetime case. The deviation from the Einstein-Maxwell theory was parametrised by a

parameter γ , which takes a value γ_{EM} for the electromagnetism and γ_{GW} for gravity in case of a deviation. The GW170817 event set the following upper limits:

$$-2.6^{-6} \leq \gamma_{GW} - \gamma_{EM} \leq 1.2^{-6}, \quad (1.59)$$

indicating no violation of the equivalence principle. This was an improvement compared to the previous tests performed with the Cassini probe [148].

A cosmology study based on the coincident observation of the kilonova and the GW signal evaluated the Hubble constant H_0 and evaluated it to be $H_0 = 70_{-8}^{+12} \text{ km s}^{-1} \text{ Mpc}^{-1}$. The posterior distribution leading to this value is plotted in Figure 1.17, extracted from [56]. This value was compatible with the values estimated by the SHOES and Planck collaborations. However, this study did not solve the tension between the two previous values, but future observations will help reduce the uncertainties. In particular, increasing the kilonova sample will give results precise enough to arrive at the SHOES or Planck levels [64].

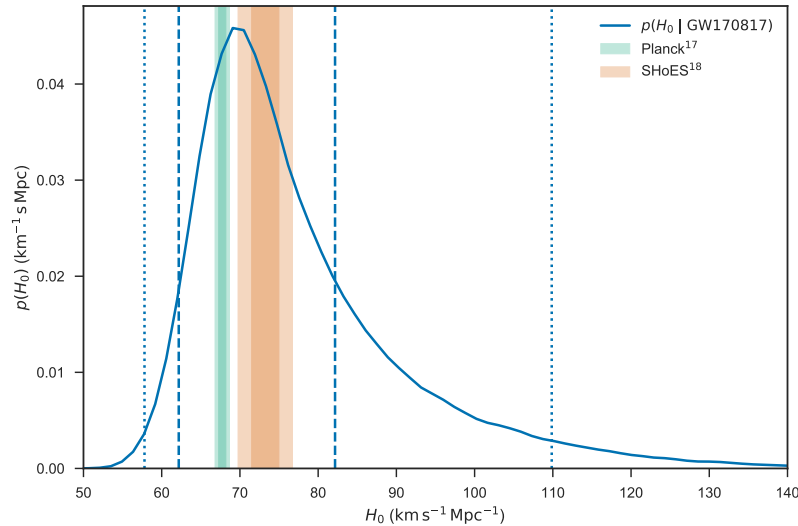


Figure 1.17: The solid blue line is the posterior distribution for H_0 based on the kilonova detection in coincidence with the GW170817 signal. The dashed vertical line is for the 68% interval and the dotted one represent the 95% interval. The green area is the H_0 estimation made by the SHOES collaboration, and in orange is the estimation from the Planck collaboration. This figure extracted from [56].

1.6 Was GW170817 a lucky event?

As we have seen, the multi-messenger observation of GW170817 was a significant success and raised high expectations for the following O3 observing run. However, several properties indicated that GW170817-like observations would be much rarer than expected.

The closeness of the BNS - 40 Mpc - is unusual, especially considering the distance of the LIGO-Virgo BNS alerts published during O3 [14]. The median distance was 200 Mpc, significantly reducing the optical emission and the amount of time during which the transient is observable. In addition, the O3 BNS event skymaps size was much larger - 100 up to 10000 deg² - than the ~ 30 deg² of GW170817. This introduced new observational difficulties compared to the 2017 event. Based on the O2 results and the GW network configuration of the first half of the third observing run, the rate of 2017-like kilonova observation is set to one per 12 year [184].

Moreover, the binary orientation allowed the detection of the gamma emission, indicating a slight viewing angle. This condition is also necessary to detect the X-ray and radio afterglow. The latter could also be dominant in the optical domain and prevent the observation of the kilonova.

Overall, the estimated rate for a complete MMA observation as GW170817 is larger than one every 100 years. Consequently, GW70817 is considered a really lucky event, unlikely to happen again in years.

GW-BASED MULTI-MESSENGER ASTRONOMY

Following what happened in 2017, gravitational waves will likely be the first messenger received for the next transient multi-messenger event. Maximising the chances of having another 170817-like event requires a rapid analysis of the gravitational waves (GW) data to have early information to plan the follow-up observations. The information extracted from the GW signal, such as the sky localisation, needs to be as precise and reliable as possible so that astronomer community can use them for their observations. Hence, the LIGO-Virgo collaborations play a crucial role in transient multi-messenger astronomy. This chapter will present the methods used to find signals rapidly in the interferometer data and the early sky localisation of the GW signal, with a focus on the localisation algorithm's accuracy.

2.1 Searching for GW in low latency

The searches for transient GW are separated into two main categories: modelled and unmodelled. Moreover, both types can be done online or offline, however, as we are interested in the follow-up of transient GW events, we only describe online searches. They are performed in low latency, with efforts made so that an alert is distributed within minutes once a candidate is identified. The expected timing is similar or better to what was achieved for GW170817, which is visible in the middle panel of Figure 1.15.

2.1.1 Unmodelled searches

Unmodelled searches look for generic transient signals in the data that create power excesses in the Time-Frequency plane. The common pipeline used by the LVC is **Coherent Wave Burst**¹ (cWB) [119]. It creates a Time-Frequency map with a data segment and uses a wavelet basis to find pixels containing energy in excess. If they fulfil some neighbourhood criterion, the pixels are clustered. Each cluster is assigned a ranking statistic based on a maximum-likelihood computation, a signal-to-noise ratio and a significance. Various types of signals can be found with cWB, and some of these, such as Supernova or binary black holes (BBH) mergers, can launch multi-messenger observations. A nearby supernova would emit a GW burst and be observable by neutrino detectors and ground and space-based telescopes. Long-duration GW signals produced for example by instabilities

¹ <https://gwburst.gitlab.io>

in a rapidly spinning black hole accretion disk. Short signals produced by cosmic string events are also sources expected to be detectable by the current detectors. `cWB` can also detect short BBH signals, and was responsible for the discovery of GW150914, the first GW ever detected [138, 137]. During O3, `cWB` detected 10 CBC events confirmed by other pipelines. It also produced online alerts for GW bursts, however, they were all retracted [151].

2.1.2 CBC searches

Compact binary coalescences are currently the only sources of GW detected by the LIGO-Virgo collaboration (LVC). They were expected to be a significant GW source, consequently, the LVC designed dedicated pipelines to search for them. These algorithms are based on matched-filtering techniques and a set of CBC waveforms, a so-called template bank, and both are described in the following sections. The collaboration uses several pipelines for collaborative online analysis, each one using a specific approach to matched-filtering:

- `GSTLAL`² uses matched-filtering in the time domain. The potential GW signals are ranked using their log-likelihood ratio. Their significance is estimated with Monte Carlo methods [46].
- `PyCBC Live`³ is a low latency adaptation of the `PyCBC` algorithm [35, 249], using matched-filtering in the frequency domain to produce triggers and a coincident analysis between them to identify candidate events. `PyCBC Live` constructs a buffer of false coincidences with time slides of the past five hours of data. The GW candidates are assigned a rank and a false alarm rate (FAR) by counting the number of fake coincidences with a higher ranking than the candidate [194, 71].
- `MBTAOnline` uses matched-filtering in the frequency domain but splits its analysis into a low-frequency band and a high-frequency one. The typical frequency cut is $f_C \sim 100\text{Hz}$ and allows reducing computational costs by shortening template duration in both bands at the expense of lower sensitivity. Separating the analysis into bands has two main advantages: (i) reducing the template bank size, (ii) reducing the cost of Fast Fourier Transform (FFT) thanks to down-sampled data. `MBTAOnline` constructs a background of coincidences with time slides of the triggers of the past three hours. The significance of a candidate is estimated with this background [6].
- `SPIIR` uses a time-domain matched-filtering but decomposes the waveforms of the template bank into a series of exponentially increasing monochromatic sinusoids to approximate the signal and filter the data and generate candidate events. Triggers from the previous week are time-shifted a hundred times to create a background distribution and assign significance to the candidates [108].

² <https://git.ligo.org/lscsoft/gstlal>

³ <https://pycbc.org/>

In the following section, we will focus on the example of PyCBC Live as it is used for this thesis.

2.2 PyCBC Live

PyCBC Live is an on-line adaptation of the PyCBC algorithm [35, 249], designed to find CBC signals within interferometers data. It is based on matched-filtering that allows finding signals whose shapes are known. As we described in Section 1.1.2, CBC signals have a typical shape called *chirp*, which is visible in Figure 1.3. For BBH, the chirp can be simulated with analytical models for the inspiral and ringdown phases and numerical relativity computations for the merger phase. For BNS, only the inspiral phase is simulated via analytical models, the merger and ringdown phases happen at frequencies that are too high to be detected by the current detectors. This section describes the implementation of the PyCBC Live search for CBC signals. We describe the template waveforms generation, the matched-filtering principle, the design of the set of waveforms used for the search and the identification of the credible candidates distributed as public GW alerts.

2.2.1 Waveform

A CBC signal can be described by a set of parameters that gives a template waveform $h_{template}$. The parameters used for the description can be separated into two categories: intrinsic parameters that are linked to the objects producing the signal and are independent of the observer, such as the masses m_1 and m_2 and the component spins S_1 and S_2 . On the other hand, the extrinsic parameters are observer-dependent, including the inclination or distance, for example. Some parameters are summarised in the following equation:

$$\boldsymbol{\theta} = \left[\begin{array}{l} \alpha \\ \delta \\ D \\ t_0 \\ \iota \\ \psi \\ \varphi_c \\ \hline m_1 \\ m_2 \\ \mathbf{S}_1 \\ \mathbf{S}_2 \end{array} \right] \left. \begin{array}{l} \text{right ascension} \\ \text{declination} \\ \text{distance} \\ \text{arrival time} \\ \text{inclination angle} \\ \text{polarization angle} \\ \text{coalescence phase} \\ \hline \text{first component's mass} \\ \text{second component's mass} \\ \text{first component's spin} \\ \text{second component's spin} \end{array} \right\} \begin{array}{l} \text{extrinsic} \\ \text{parameters,} \\ \boldsymbol{\theta}_{\text{ex}} \\ \\ \text{intrinsic} \\ \text{parameters,} \\ \boldsymbol{\theta}_{\text{in}}. \end{array} \quad (2.1)$$

Only the intrinsic parameters are used for generating the waveforms for the current searches. Similarly, this parameter space could be enlarged by adding more parameters affecting the signal, such as the tidal deformations of neutron stars or the binary eccentricity. However, including extrinsic parameters from Equation 2.1 or others would make

the search much more computationally expensive without a significant gain in detection efficiency for a search [225] and would require many more resources to achieve low latency performances.

PyCBC Live uses waveforms simulated with two different approximants. BNS and low-mass NSBH are described with the TaylorF2 model [174], that is a post-Newtonian approximants (based on the weak field and slow motion approximations) in the frequency domain for point masses with aligned spin in quasi-circular orbits. The high masses NSBH and BBH are simulated with the SEOBNRv4 [38] model, based on an effective one-body approximation for spinning point masses in quasi-circular, non-precessing orbits.

For both types of models, the *chirp* GW strain amplitude $h(t)$ in a given detector can be written as [11]:

$$h(t) = \left(\frac{1\text{Mpc}}{D_{eff}} \right) \mathcal{A}_{1\text{Mpc}}(M, \mu) (t - t_0)^{-\frac{1}{4}} e^{-i\Psi(t-t_0, M, \mu)}, \quad (2.2)$$

where M and μ are respectively the total and reduced mass of the binary. $\Psi(f, M, \mu)$ is the GW phase that depends on the time $t - t_0$ and $\mathcal{A}_{1\text{Mpc}}(M, \mu)$ is a normalised amplitude that only depends on the binary intrinsic parameters.

For a post-newtonian model the previous equation is written as :

$$h(t) = - \left(\frac{GM}{c^2 D_{eff}} \right) \left(\frac{t_0 - t}{5GM/c^3} \right)^{-\frac{1}{4}} \times \cos[2\varphi_0 + 2\varphi(t_0 - t, M, \mu)], \quad (2.3)$$

where:

$$\mathcal{M} = \mu^{3/5} M^{2/5} \quad (2.4)$$

is the chirp mass. t_0 is the binary merger time that is defined as the time when the GW frequency becomes infinite in the TaylorF2 approximation. $\varphi_0 + \varphi(t_0 - t, M, \mu)$ is the orbital phase of the binary and φ_0 is the termination phase, that is related to the phase at coalescence φ_c in Equation 2.1:

$$2\varphi_0 = 2\varphi_c - \arctan \frac{F_{\times}}{F_{+}} \frac{2 \cos \iota}{1 + \cos^2 \iota}, \quad (2.5)$$

where $F_{\times,+}$ are functions of the sky position (α, δ) called the antenna patterns of the interferometer that we describe in Section 2.3.1. The quantity D_{eff} acts as an effective distance of the binary to the interferometer defined as:

$$D_{eff} = D \left[F_{+}^2 \left(\frac{1 + \cos^2 \iota}{2} \right)^2 + F_{\times}^2 \cos^2 \iota \right]. \quad (2.6)$$

It is related to the luminosity distance D of the binary and to geometrical factors of the binary, the inclination ι in particular. For an optimally oriented source, directly overhead and orbiting in the plane of the sky (i.e. face-on and $\iota = 0$), the effective distance $D_{eff} = D$. Otherwise, $D_{eff} > D$ and a degeneracy between the distance and inclination emerges that makes the source appear further away than it really is when the signal is observed by a single interferometer.

2.2.2 Matched-filtering

Principle

Matched-filtering (MF) is an efficient method for finding a known signal hidden in noise implemented by correlating the detector output with a template representing the expected signal. MF aims at constructing the time series of the *signal-to-noise ratio* (SNR), which is defined in Equation 2.13. Local SNR peaks correspond to potential GW candidates at the point $\vec{\vartheta}$ in the search space defined in Equation 2.1. However, finding all the local maxima of $\text{SNR}(\vec{\vartheta})$ is too difficult considering the number of parameters and various tricks are used to deal with this large space and are described in the next paragraph.

PyCBC Live is based on the FINDCHIRP algorithm [11], a frequency domain filtering that correlates the data and the template filter via Fast Fourier Transform (FFT). This algorithm (i) computes the matched-filter response, (ii) discriminates the astrophysical signal and the transient noises using a chi-squared test and (iii) selects the candidate events using chi-square and filtering outputs.

The GW detector strain data are denoted here $s(t)$, and they are either made of noise only $s(t) = n(t)$ or of a signal on inside the noise $s(t) = n(t) + h(t)$. The matched-filter technique is based on the following inner product:

$$\langle s, h \rangle = 4 \int_0^\infty \frac{\tilde{s}(f)\tilde{h}^*(f)}{S_n(f)} df \quad (2.7)$$

where $S_n(f)$ is the one-sided power spectral density (PSD) of the noise, which is a measure of the detector sensitivity. It allows to define the output of the correlation of the data with a filter template $h_{\text{template}}(t)$:

$$x(t_0) = 4\Re \int_0^\infty \frac{\tilde{s}(f)[\tilde{h}_{\text{template}}^*(f)]_{t_0=0}}{S_n(f)} e^{2\pi i f t_0} df, \quad (2.8)$$

where t_0 is the termination time. Using FFT in the FINDCHIRP algorithm allows scanning for all possible t_0 termination times as a change in t_0 will translate into a phase shift in the MF output. The remaining unknown parameters are the amplitude of the GW strain data, the intrinsic parameters of the binary and the termination phase φ_0 .

The amplitude is directly related to the effective distance, and thus the MF output can be normalised. Under the stationary phase approximation, the FFT of Equation 2.2 is given by [220, 67, 207]:

$$\tilde{h}(f) = \left(\frac{1\text{Mpc}}{D_{\text{eff}}} \right) \mathcal{A}_{1\text{Mpc}}(M, \mu) f^{-7/6} e^{-i\Psi(f, M, \mu)}, \quad (2.9)$$

where $\mathcal{A}_{1\text{Mpc}}(M, \mu)$ is a normalised amplitude that only depends on the binary intrinsic parameters. By convention all the templates used by PyCBC Live are normalised at $D_{\text{eff}} = 1$ Mpc. For the post-newtonian approximation, the waveform in the frequency

domain is written as the FFT of Equation 2.3:

$$\tilde{h}(f) = - \left(\frac{5\pi}{24} \right)^{1/2} \left(\frac{GM}{c^3} \right) \left(\frac{GM}{c^2 D_{eff}} \right) \left(\frac{GM}{c^3} \pi f \right)^{-7/6} e^{-i\Psi(f, M, \mu)}, \quad (2.10)$$

where $\Psi(f, M, \mu)$ is the GW phase that depends on the frequency f and the total and reduced masses of the binary.

The filtering depends on the intrinsic parameters of the binary, which are explored by constructing a template bank. The method for designing the PyCBC Live bank is described in Section 2.2.3.

The unknown phase φ_0 is found by maximising the MF output $x(t_0)$ over φ_0 . Rewriting $x(t_0)$ as $x(t_0) = x_{re}(t_0) \cos(2\varphi_0) + x_{im}(t_0) \sin(2\varphi_0)$, with $x_{re,im}(t_0)$ are respectively Equation 2.8 evaluated at $\varphi_0 = 0$ and $\varphi_0 = \frac{\pi}{2}$. Deriving $x(t_0)$ with respect to φ_0 and evaluating at maximum $2\hat{\varphi}_0 = \arg(x_{re} + ix_{im})$, we find: $x^2(t_0)|_{\hat{\varphi}_0} = x_{re}^2(t_0) + x_{im}^2(t_0)$. This can be summarised by a complex MF output such that:

$$z(t_0) = x_{re}(t_0) + ix_{im}(t_0) = 4 \int_0^\infty \frac{\tilde{s}(f)[\tilde{h}_{template}^*(f)]_{t_0=0, \varphi_0=0}}{S_n(f)} e^{2\pi i f t_0} df. \quad (2.11)$$

Using Equation 2.9 evaluated at $D_{eff} = 1$ Mpc, a normalisation constant is computed for each template of the bank, indexed with m , such that:

$$\sigma_m^2 = 4 \int \frac{|\tilde{h}_{1\text{Mpc},m}(f)|^2}{S_n(f)} df = \langle \tilde{h}_{1\text{Mpc},m} | \tilde{h}_{1\text{Mpc},m} \rangle. \quad (2.12)$$

This allows to build the SNR time series $\rho_m^2(t)$ for a given template h_m , with m its label in the bank:

$$\rho_m^2(t) = \frac{|z_m|^2}{\sigma_m^2} = \frac{1}{\langle h_m | h_m \rangle} \left| 4 \int_0^\infty \frac{\tilde{s}(f)\tilde{h}_m^*(f)}{S_n(f)} e^{2\pi i f t} df \right|^2 = \frac{|\langle s | h_m \rangle|^2}{\langle h_m | h_m \rangle}. \quad (2.13)$$

Computing the SNR time series and identifying peaks above a defined threshold allows us to find the GW candidate signals. This quantity follows a χ^2 distribution with two degrees of freedom, corresponding to the two phase quadrature and non-centrality parameter that corresponds to the optimal SNR ρ_{opt}^2 :

$$\rho_{opt}^2 = 4 \int_0^\infty \frac{|\tilde{h}(f)|^2}{S_n(f)} df. \quad (2.14)$$

It approximately corresponds to the average SNR a binary would have in a detector if the template waveform used for the detection is the same as the signal waveform. The ρ^2 following a $\chi^2(dof = 2, \rho_{opt}^2)$ distribution gives $\langle \rho^2 \rangle = 2 + \rho_{opt}^2$. This is represented in Figure 2.1, and we can distinguish three regimes for this function. The first regime corresponds to $\rho_{opt}^2 \ll 2$, which correspond to undetectable signal. The second regime with $\rho_{opt}^2 \sim 2$ where signals are present in the data, but are weak and not confidently detectable. And a third regime where $2 \ll \rho_{opt}^2$, which is equivalent to $\rho^2 \sim \rho_{opt}^2$ for which the signals are strong and clearly detectable in the data.

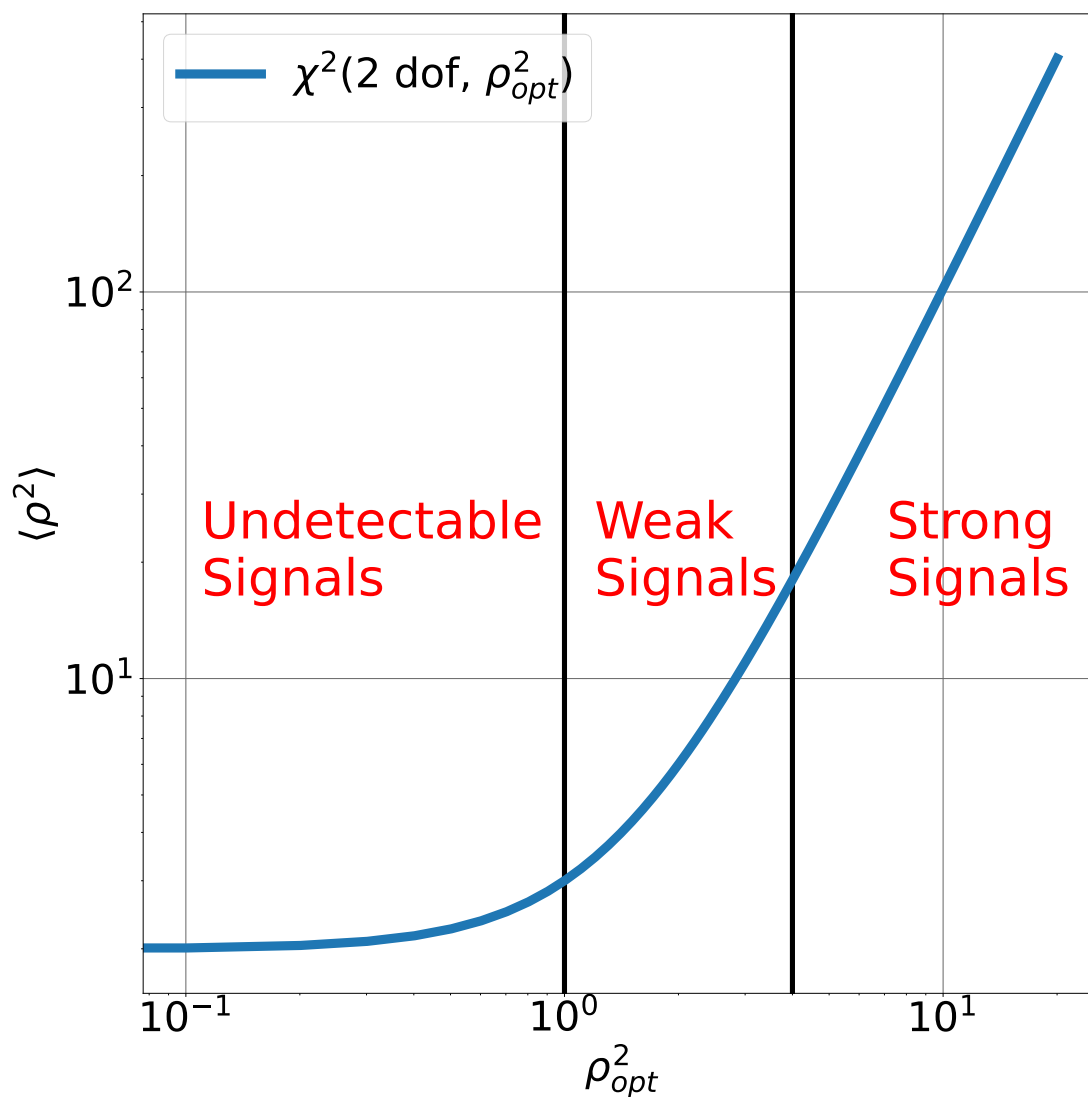


Figure 2.1: χ^2 distribution of the SNR amplitude returned by the MF computation. There are three regime identified: no signal visible, weakly detected signals and strong signals detection.

Estimating the PSD

A detector's power spectral density (PSD) $S_n(f)$ is a measure of its sensitivity. As such, it weights the matched filtering output of Equation 2.7. PyCBC Live estimates the PSD with Welch's method [260]. The PSD is computed by taking the last minute of data, dividing it into N_s 4s intervals that overlap by 50%. These segments are passed through a Hann window and converted to the frequency domain. For each segment, an average periodogram of the windowed data is computed:

$$P_n[k] = \frac{2\Delta f}{\frac{1}{N} \sum_{j=0}^{N-1} w^2[j]} \left| \Delta t \sum_{j=0}^{N-1} s_n[j] w[j] e^{-2\pi i j k / N} \right|^2, \quad (2.15)$$

where The PSD is extracted by median averaging the N_s P_n to remove the outliers:

$$S[k] = \text{median}\{P_0[k], P_1[k], \dots, P_{N_s-1}[k]\} \quad (2.16)$$

2.2.3 Template bank

Matched filtering requires templates covering the space of the intrinsic parameters of the binary to find GW signals. For computational efficiency purposes, the template placement is such that it optimally covers the search parameter space. The leading idea is to keep the total number of templates as low as possible without missing signals because of the mismatch between the model and the GW signal. The match between a template $h(\vec{\theta})$ with parameters $\vec{\theta}$ and a close neighbour $h(\vec{\theta} + d\vec{\theta})$ with parameters $\vec{\theta} + d\vec{\theta}$ is [201]:

$$M(\vec{\theta}, d\vec{\theta}) = \langle h(\vec{\theta}) | h(\vec{\theta} + d\vec{\theta}) \rangle. \quad (2.17)$$

At leading order, it can be written as:

$$M(\vec{\theta}, d\vec{\theta}) \simeq 1 - \frac{1}{2} \left(\frac{\partial^2 M}{\partial \theta^\mu \partial \theta^\nu} \right) d\theta^\mu d\theta^\nu, \quad (2.18)$$

where $\mu, \nu \in [0, p-1]$ and p is the number of intrinsic parameters describing the template. Here $\frac{\partial^2 M}{\partial \theta^\mu \partial \theta^\nu}$ can be seen as the parameter space metric denoted as $g_{\mu\nu}$ and the previous equation becomes:

$$M(\vec{\theta}, d\vec{\theta}) \simeq 1 - \frac{1}{2} g_{\mu\nu} d\theta^\mu d\theta^\nu. \quad (2.19)$$

It is then possible to define a parameter called *minimal match* (MM) which controls the spacing between the models such that $M \geq MM$. The MM fixes the acceptable SNR loss when changing from one template to one of its neighbours. The usual value is 97%, and this was the value chosen for the O3 template bank used by PyCBC Live. According to [50], a bank is optimally designed if the number of templates N_b is minimal and if, for any signal, there always exists at least one template in the bank such that:

$$\min_{\theta'^\mu} \max_i \langle \hat{s}(\theta'^\mu), \hat{h}(\theta_i^\mu) \rangle \geq MM, \quad (2.20)$$

where θ_i^μ is the set of p parameters describing a template, $\mu \in [0, p - 1]$, i is the index of the template in the bank $i \in [0, N_b]$. For `PyCBC Live`, there are four parameters for constructing the bank: the two binary companions masses and spins, which correspond to the intrinsic parameters of Equation 2.1. Then using the minimal match value, the templates are placed in the parameter space covered by the template bank.

There are three methods for bank placement. The first one is purely geometric and takes advantage of the fact that the coordinate system based on the chirp times τ_0, τ_3 , defined in Equation 2.21 is flat [50]. For a binary system with component objects of masses m_1 and m_2 , the chirp times are:

$$\tau_0 = \frac{5}{256\pi f_L \eta} (\pi M f_L)^{-\frac{5}{3}} \tag{2.21}$$

$$\tau_3 = \frac{1}{8f_L \eta} (\pi M f_L)^{-\frac{2}{3}},$$

where f_L is the lower frequency cutoff the template, $M = m_1 + m_2$ is the total mass of the binary and $\eta = m_1 m_2 / M$. For a flat 2D space, the optimal way of placing the templates to cover the plane is a hexagonal lattice similar to Figure 2.2. For cases where the templates include the merger and ringdown phases, the parameter space is no longer necessarily flat, and the templates are placed in a stochastic way [101]. This procedure works by randomly generating positions in the parameter space and discarding them if the overlap with the other templates is too large - i.e. if it is larger than the MM. The last method is a hybridisation of the geometric and stochastic methods. The first step is to generate a seed template following the geometric algorithm and then complete the holes with stochastic processes.

During the O3 run, the bank included the component objects spin projections along \vec{L} [71] for a total of $\sim 400\,000$ templates. Thus, the template placement requires a hybrid geometric-stochastic method described in [218, 217] with a minimal match of 97%. The parameter space explored by `PyCBC Live` includes BNS, BBH and NSBH. For BNS and NSBH binaries, the neutron stars have masses between 1 and $2 M_\odot$ and a dimensionless aligned-spin parameter ≤ 0.05 . These bounds account for the masses, and largest spins observed in pulsars [162]. For black holes, the magnitude of the spin is ≤ 0.998 , accounting for the spins observed in X-ray binaries [169]. The total mass of the binaries is $\leq 100 M_\odot$ for equal mass, weakly spinning templates and $\leq 500 M_\odot$ for templates of high-mass-ratio, high-aligned-spins binaries.

2.2.4 Identifying Gravitational Wave candidates

`PyCBC Live` splits the data into 8s-analysis strides for which the PSD is computed and the SNR time series is estimated for the whole template bank. To do so, `PyCBC Live` distributes the template bank over ~ 150 computational nodes to parallelise the computation and meet the low-latency requirements. In the O3 configuration, a node identifies a

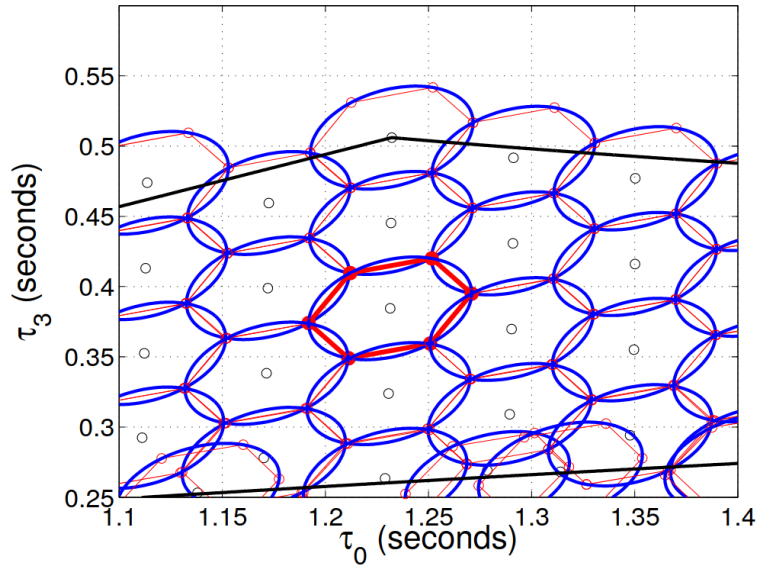


Figure 2.2: Hexagonal lattice in the τ_0, τ_3 plane, where each point is a template waveform location in the plane. The ellipses represent the iso-match for a minimal match of 95%, smaller than the currently usual 97% MM. This Figure is extracted from [50].

single-detector trigger every time the SNR time series rises above a 4.5 threshold. Each computational node keeps the 30 triggers with the highest SNR found in an 8s data segment. The nodes send them in a *head node*, which receives $O(10^3)$ triggers per detector per 8s data stride.

The data produced by a detector can be considered Gaussian at first order, however, it also contains transient non-gaussianities that may produce high SNR peaks. They are called *glitches*, and they can originate from various sources such as scattered light as visible in the upper-central panel of Figure 2.3 [238]. Another glitch example is visible in Figure 1.13, on the upper-left panel, as a large spike on top of the GW170817 signal. This glitch complicated the analysis of the GW170817 at first and had to be subtracted before further analysis of the LIGO Livingston data.

Glitches in the data produce high SNR peaks but do not fit a GW waveform. Thereby, PyCBC Live performs a goodness-of-fit test by computing the following quantity:

$$\chi_r^2 = \frac{1}{2(p-1)} \sum_{i=1}^{i=p} \|\langle s|h_i \rangle - \langle h_i|h_i \rangle\|, \quad (2.22)$$

where a template h is split into p frequency bands. χ_r^2 follows a reduced χ^2 distribution with $2p-2$ degrees of freedom and a non-centrality parameter that is large for transients that do not match the template waveform h . Based on this goodness-of-fit, the SNR is

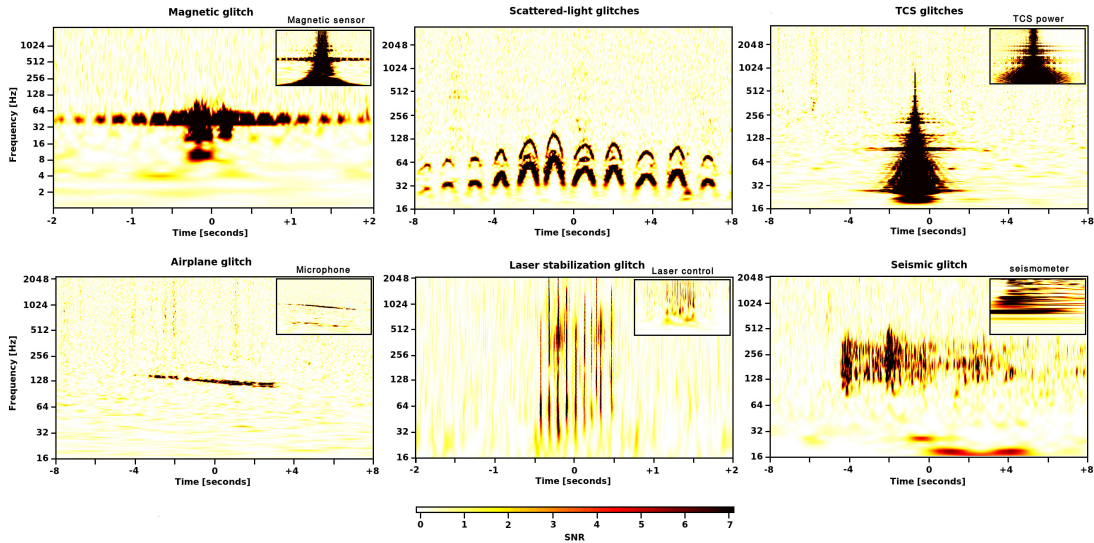


Figure 2.3: Time-frequency maps of six examples of glitches observed in Virgo data. Glitches are gathered by family based on their time -Frequency morphology. The first plot shows a power-line glitch also detected by Virgo internal magnetometers. The second map shows a series of glitches caused by scattered light induced by seismic activity. A thermal compensation system instability causes the third glitch. This system is used in Virgo to prevent mirror deformations due to the high-powered laser. The fourth plot presents an airplane event with a clear Doppler effect. The fifth event is due to a glitch in the laser stabilisation loop. The last glitch with an undefined shape is due to a seismic event up-converted to higher frequencies. This Figure is extracted from [238] and is based on an anterior version of Virgo, with data from the VSR2 observing run.

re-scaled to $\tilde{\rho}$, according to χ_r^2 [19, 10]:

$$\tilde{\rho} = \begin{cases} \rho & \text{for } \chi_r^2 \leq 1 \\ \rho \left[\frac{1}{2} (1 + (\chi_r^2)^3) \right]^{-\frac{1}{6}} & \text{otherwise} \end{cases}. \quad (2.23)$$

The re-weighting is design to remove any significance from glitches based on the chi-squared test. Then, when different detectors have acquired data, a coincident analysis is done for each pair of observing detectors (H-L, L-V and H-V with H: LIGO Hanford, L: LIGO Livingston and V: Virgo) based on the two detector ranking statistics developed in [195]:

$$\tilde{\rho}_c^2 = \tilde{\rho}_i^2 + \tilde{\rho}_{j \neq i}^2 + 2 \ln \left(p^S(\vec{\theta}) \right), \quad (2.24)$$

where (i, j) is one of the detector pairs, and $p^S(\vec{\theta})$ is the prior probability of a trigger with a set of parameters $\vec{\theta}$ to be of astrophysical origin. $p^S(\vec{\theta})$ has been constructed with Monte-Carlo simulations and is based on the phase difference $\Delta\varphi$ and the arrival time difference Δt agreement between two interferometers detecting a signal. Noise events are expected to be uniformly spread in the $(\Delta\varphi, \Delta t)$ in the but not a real signal, allowing for discriminate between them [195].

2.2.5 Significance of a GW candidate event

After identifying a trigger coincident in a detector pair, **PyCBC Live** estimates its significance compared to background noise for consideration by astronomers. **PyCBC Live** empirically computes a background distribution with times slides. For a given pair of instruments, the data from a detector are time-shifted by a delay superior to the light time-of-flight between the two instruments to create un-physical trigger associations. Then the ranking statistics in Equation 2.24 are computed for these associations. This procedure is repeated with steps of 100ms to generate a background sample as large as possible. The background created by the past 5 hours is kept in a rolling buffer stored on the computational head node. Each time slides with the past five hours allows to create five hours of coincident triggers artificially, leading to a total artificial observing time $T_{coinc} \sim 100$ yr. It enables finding triggers with a false alarm rate (FAR) down to 1 in 100 years. Keeping a five hours buffer allows adapting to changes in the detector state on this time scale. Then, the algorithm computes the number $n_b(\tilde{\rho}_c)$ of triggers in the background with a higher ranking statistic $\tilde{\rho}_c$ than the candidate. This gives an estimation of the false-alarm rate:

$$\mathcal{F} = \frac{1 + n_b}{T_{coinc}}. \quad (2.25)$$

When there are triggers coincident in more than two instruments, the FAR are combined to evaluate the significance of the candidate event by constructing a p-value for each other detectors and turning it into a FAR [71]. The triggers passing a FAR threshold of 1 per 2 hours are sent to the Gravitational-wave candidate DataBase⁴ (**GracedB**) and

⁴ <https://gracedb.ligo.org/>

used to construct public alerts.

During O3, the total amount of time between detection of a binary coalescence and its submission to the database was ~ 10 s, from which ten additional seconds comes from the data calibration and distribution to the computing cluster, and another ten seconds after the submission for the computation of critical information such as the spatial localisation [194, 71]. The whole PyCBC Live procedure is summarized in Figure 2.4 which is extracted from the O2 description of the pipeline [194].

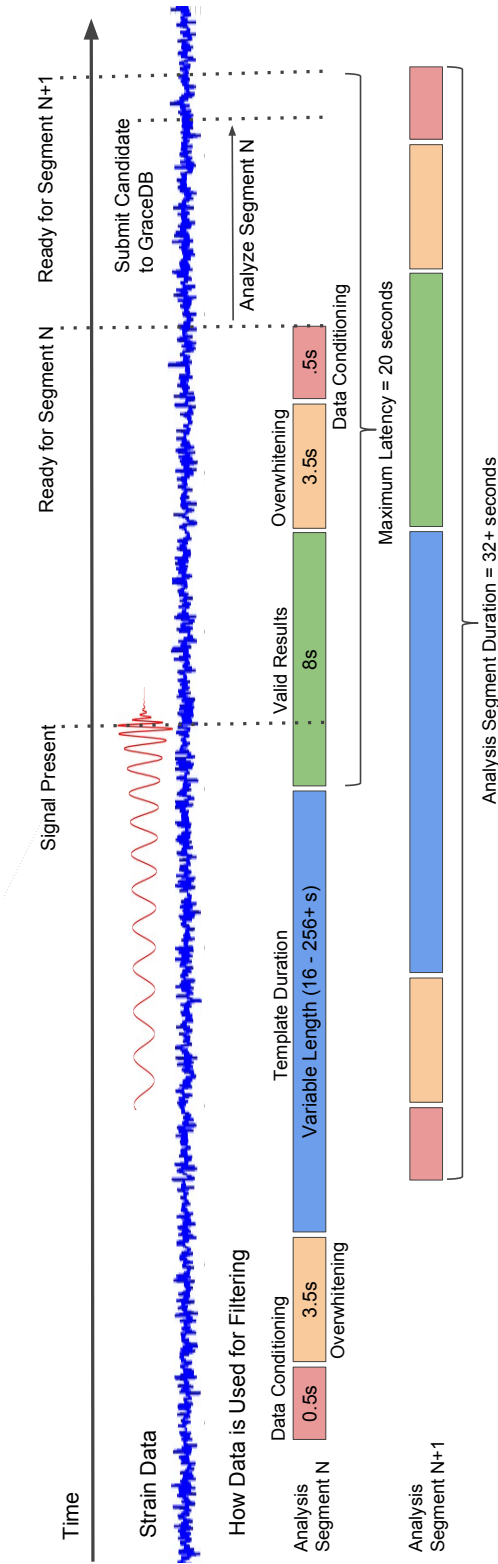


Figure 2.4: Summary of the data processing within PyCBC Live. The data are analysed in discrete analysis segments with an 8s stride between them. For the O2 configuration of this diagram, the average latency between the merger and its identification is 16s. Ten additional seconds are required to calibrate and distribute the data to the computing cluster. Furthermore, critical information, such as the sky localisation, nearly takes an additional 10s to be generated after an event is initially identified and uploaded to the Gravitational-wave Candidate Database (GraceDB). This Figure is extracted from [194].

2.3 Low latency spatial localisation

2.3.1 Localising a GW

Detector angular response

As we described in Section 1.1.1, in the traceless and transverse gauge, a plane GW is described by a tensor with two polarisations h_+ and h_\times . For a GW whose incident direction is \hat{n} , its strain amplitude h_{ij}^{TT} can be written in the polarization basis $(e_{ij}^+, e_{ij}^\times)$ as:

$$h_{ij}^{TT} = h_+ e_{ij}^+ + h_\times e_{ij}^\times, \quad (2.26)$$

where:

$$\begin{aligned} e_{ij}^+ &= l_i l_j - m_i m_j \\ e_{ij}^\times &= l_i m_j - l_j m_i. \end{aligned} \quad (2.27)$$

The unit vector \hat{l} and \hat{m} are chosen to form an orthonormal, right-handed basis with \hat{n} . Considering now a basis (\hat{a}, \hat{b}) , aligned with the detector arms, the signal $s(t)$ observed in the instrument is written as [212]:

$$s(t) = F_+(\hat{n})h_+(t) + F_\times(\hat{n})h_\times(t), \quad (2.28)$$

where $F_{+,\times}$ are the antenna pattern of the detector and are written as:

$$\begin{aligned} F_+(\hat{n}) &= \frac{1}{2}(a_i a_j - b_i b_j) e_+^{ij} \\ F_\times(\hat{n}) &= \frac{1}{2}(a_i a_j - b_i b_j) e_\times^{ij}. \end{aligned} \quad (2.29)$$

These two functions describe the angular response of the detector. Based on them, we see that the tensor of the metric perturbation h^{TT} is projected onto the detector arms. The antenna patterns are represented in Figure 2.5 in the usual spherical coordinates (θ, ϕ) , with $\theta \in [0, \pi]$ and $\phi \in [0, 2\pi]$, with the vertical axis is taken to be orthogonal to the detector plan. For unpolarised GW, the directional function F_{rms} of the detector can be computed as:

$$F_{rms} = \sqrt{F_+^2 + F_\times^2}. \quad (2.30)$$

This function is represented on the right-hand side plot of Figure 2.5. It results in a detector whose response is almost uniform on the sky but contains four blind spots. They are visible on the representation of F_{rms} in a Mollweide projection as the blue regions in Figure 2.6. They correspond to the two bisectors of the detector, where it is completely insensitive. However, this response also implies that a detector alone has no possibility of precisely localising the GW source. The antenna patterns are normally time-dependant, but as the typical duration of a transient GW signal, which is of the order of 0.1-10s at most for a BBH, is much shorter than the time scale to have a significant change in

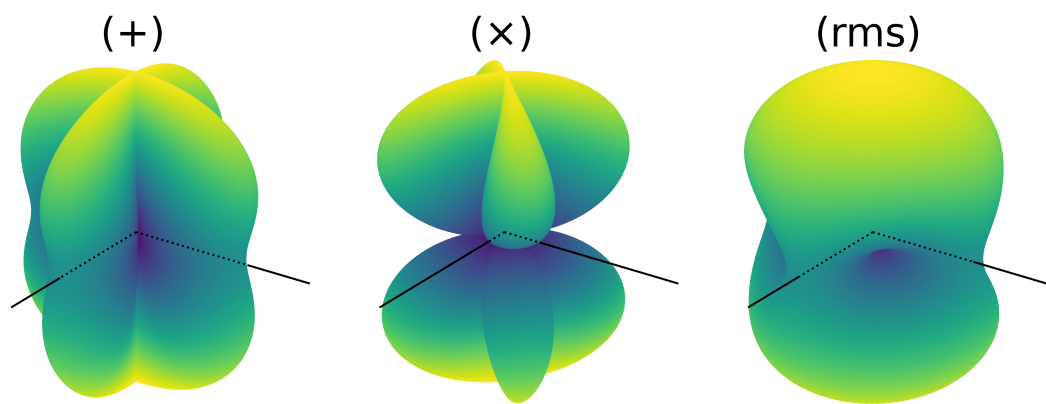


Figure 2.5: Antenna pattern of a GW detector, with F_+ on the left, F_\times in the centre and F_{rms} on the right. The more yellow the contour, the stronger the response of the detector. The black lines represent the instrument arms. This Figure has been reproduced from [78].

the angular response of the detector that is around $\sim 1\text{h}$. However, this will not be true anymore for future detector such as LISA.

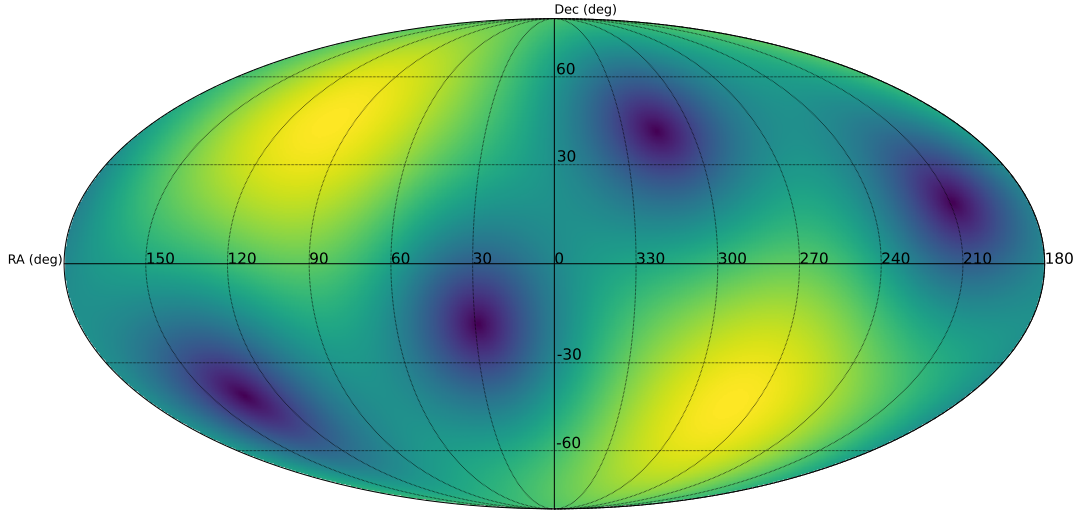


Figure 2.6: Mollweide projection of the antenna pattern of the Virgo interferometer on the 2022/07/22 at 10:00 UTC.

Source localisation

Although it is not possible to localise a short transient with only one detector, as there is a network of three detectors, four when KAGRA will start acquiring data, it is possible to use triangulation to identify the source position. As illustrated in Figure 2.7, the time delay between two sites creates an annulus of possible source position on the sky. The more instruments detect the signal, the better the constraint. For a triple coincidence, the credible region is reduced to two regions in mirror of each other with respect to the plane containing the three instruments corresponding to the intersections of the three annuli. Adding the constraints on signal amplitude and phase consistency reduces localisation to only one of these regions. The typical size of a localisation regions depends on various parameters, including the source distance and orientation and the number of detectors that detected the event. We used the O3 skymaps produced for the GSTLAL, MBTA and PyCBC Live pipelines as a by-product of this work to show the variety of the localisation regions area. The results are presented in Appendix A and for confident events detected during O3b, the typical 50% area $\sim 400 \text{ deg}^2$ (1500 deg^2) according to TableA.1. **Bayestar** is the algorithm responsible for the low latency sky localisation using a Bayesian approach. It estimates the credible region from where the source originates, along with its distance, to create *skymaps* distributed to other observing communities. This information is of utmost importance for any follow-up in the electromagnetic domain.

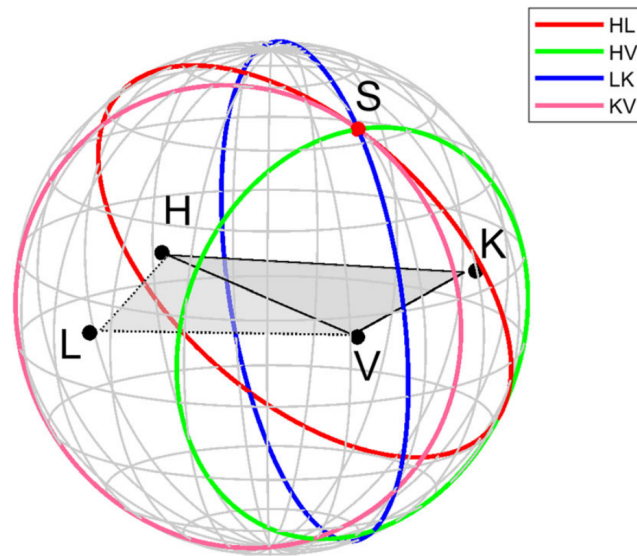


Figure 2.7: Source localisation based on timing triangulation for the network composed of LIGO-Hanford (H), LIGO-Livingston (L), Virgo (V) and KAGRA (K). Each circle represents the region of constant time delay between two network instruments. For clarity, the HK and LV combinations are omitted. For a four-detectors observation, there is a unique intersection region denoted S on the plot. This figure has been extracted from [158].

2.3.2 Bayestar

After the identification of a candidate event by `PyCBC Live` (or any other pipeline), an estimation of source sky-localisation, a so-called skymap, is produced via the `Bayestar` algorithm [225] and publicly distributed. `Bayestar` uses a Bayesian framework to produce a prompt estimate of the probability distribution of the luminosity distance, right ascension and declination parameters and turn it into a skymap. The algorithm has been designed with two main constraints, (i) being rapid to allow a quick outreach of the information, (ii) being accurate. `Bayestar` computes a skymap within ~ 1 -10s depending on the computational resources, with results comparable to a full joint parameter estimation that takes hours up to weeks to complete.

Bayes Theorem

In a Bayesian framework, the parameters $\boldsymbol{\theta}$ are inferred from the data \mathbf{y} to create a posterior distribution $p(\boldsymbol{\theta}|\mathbf{y})$ describing the probability distribution of the parameters, given the observations. The Bayes theorem provides the relation between the posterior and a likelihood $p(\mathbf{y}|\boldsymbol{\theta})$:

$$p(\boldsymbol{\theta}|\mathbf{y}) = \frac{p(\mathbf{y}|\boldsymbol{\theta})p(\boldsymbol{\theta})}{p(\mathbf{y})}, \quad (2.31)$$

where $p(\boldsymbol{\theta})$ is the prior distribution that describes the previous information about the parameters, either based on previous observations or known constraints on the parameters. The $p(\mathbf{y})$ can be seen as a normalisation factor.

For Bayesian inference, when only a subset $\boldsymbol{\beta}$ of the $\boldsymbol{\theta}$ model's parameters are relevant for the analysis, the $\boldsymbol{\lambda}$ remaining ones are being integrated over. The marginal posterior distribution is computed as:

$$p(\boldsymbol{\beta}|\mathbf{y}) = \int \frac{p(\mathbf{y}|\boldsymbol{\beta}, \boldsymbol{\lambda})p(\boldsymbol{\beta}, \boldsymbol{\lambda})}{p(\mathbf{y})} d\boldsymbol{\lambda}. \quad (2.32)$$

This is what is done within `Bayestar` as it estimates the spatial parameter α, δ and D from Equation 2.1, and considers the other parameters, such as masses or spins, for example, as nuisance ones.

Constructing a likelihood

To achieve the computation rapidly, the algorithm takes advantage of several insights. First, as visible in Equation 2.1, the parameters describing a binary coalescence can be separated between intrinsic (masses, spins) and extrinsic parameters (distance, Ra, Dec, ...). Equation 2.9 can be re-written for a detector j as [225]:

$$\tilde{h}_j(f; \boldsymbol{\theta}) = e^{-2i\pi f(t_0 - \mathbf{d}_j \cdot \mathbf{n})} \frac{r_{1,j}}{D} e^{2i\varphi_c} \left[\frac{1}{2} (1 + \cos^2 \iota) \Re \{ \zeta \} - i (\cos \iota) \Im \{ \zeta \} \right] H(f; \boldsymbol{\theta}_{\text{in}}), \quad (2.33)$$

where $H(f; \boldsymbol{\theta}_{\text{in}})$ is the part of the waveform that only depends the intrinsic parameters and for $f \geq 0$:

$$\zeta = e^{-2i\psi} (F_{+,j}(\alpha, \delta, t_0) + iF_{\times,j}(\alpha, \delta, t_0)), \quad (2.34)$$

where \mathbf{d}_j is the position of the detector j in units of light time travel. The quantity $r_{1,j} = 1/\sigma_j$ is a fiducial distance at which a detector i would detect an optimally oriented binary with an SNR of 1. It is similar to Equation 2.12 as:

$$\sigma_j^2 = 4 \int_0^\infty \frac{|H(f; \hat{\boldsymbol{\theta}}_{\text{in}})|^2}{S_j(f)} df. \quad (2.35)$$

The waveform in Equation 2.33 can be separated into one part that depends only on the intrinsic parameters, denoted $H(f; \boldsymbol{\theta}_{\text{in}})$, and another part which only depends on the extrinsic parameters. This separation comes from the fact that the masses and localisation uncertainties are uncorrelated. This is because the relevant quantities for triangulating a GW signal are the arrival time differences and phases, along with the ratio of the amplitudes. Averaging these differences and ratio over the detectors remove the correlation between them and the intrinsic parameters. A rigorous demonstration of this is given in Appendix A of the *Bayestar* paper [225]. *Bayestar* takes advantage of this separation to avoid the inference of the intrinsic parameter set $\boldsymbol{\theta}_{\text{in}}$. Instead, it uses point estimates provided on the intrinsic parameters by the detection pipeline through the template waveform that produced the candidate signal, reducing the problem's dimensionality.

The search provides the SNR time series through matched-filtering, along with the template parameters, which are the main ingredients for the localisation. The whole SNR time series is used to extract the time of arrival $\hat{\tau}_j$, amplitude $\hat{\rho}_j$ and the phase $\hat{\gamma}_j$. The time series of each interferometer j can then be turned into a Gaussian likelihood to apply a Bayesian analysis:

$$p(\hat{\rho}_j, \hat{\gamma}_j, \hat{\tau}_j | \rho_j, \gamma_j, \tau_j) \propto \exp \left[-\frac{1}{2} \hat{\rho}_j^2 - \frac{1}{2} \rho_j^2 + \hat{\rho}_j \rho_j \Re \{ e^{i\tilde{\gamma}_j} a_j^*(\tilde{\tau}_j) \} \right], \quad (2.36)$$

where, $\tilde{\tau}_j = \hat{\tau}_j - \tau_j$, $\tilde{\gamma}_j = \hat{\gamma}_j - \gamma_j$ and $a_i(\tilde{\tau}_i)$ is the template $H(f; \boldsymbol{\theta}_{\text{in}})$ autocorrelation function defined as:

$$a_j(t; \boldsymbol{\theta}_{\text{in}}) \propto \frac{1}{\sigma_j^2} \int_0^\infty \frac{|H(f; \hat{\boldsymbol{\theta}}_{\text{in}})|^2}{S_j(f)} e^{2i\pi ft} df. \quad (2.37)$$

Priors

To construct the arrival time prior, *Bayestar* uses Earth-fixed coordinates of the detectors \mathbf{n}_j and arrival times $\hat{\tau}_j$, average-weight over the detectors by timing uncertainties to

obtain $\langle \mathbf{n} \rangle$ and $\langle \hat{\tau} \rangle$. Then, these means are subtracted to have weighted coordinates:

$$\mathbf{n}_j \leftarrow \mathbf{n}_j - \langle \mathbf{n} \rangle, \quad \hat{\tau}_j \leftarrow \hat{\tau}_j - \langle \hat{\tau} \rangle.$$

With those coordinates, the arrival time prior is chosen such that it is uniform in $[-T, T]$, with $T = \max_j(|\mathbf{n}_j|/c) + 5ms$. The other priors used for the localisation are the following:

- Polarisation: ψ is uniform in $[0, 2\pi]$
- Inclination: $\cos(\iota)$ is uniform in $[-1, 1]$
- Distance: D follows a power law D^m in $[0, D_{max}]$, the default $m = 2$ corresponds to a prior uniform in volume. The case $m = -1$ corresponds to a prior uniform in the logarithm of the distance.

$D_{max} = \frac{1}{4} \max_j(r_{1,j})$, where $r_{1,j}$ is the same fiducial distance as in Equation 2.33.

Using the priors and the Bayes Theorem of Equation 2.31, the marginal posterior is evaluated as:

$$f(\alpha, \delta) \propto \int_0^\pi \int_{-1}^1 \int_{-T}^T \int_{r_{\min}}^{r_{\max}} \int_0^{2\pi} \exp \left[-\frac{1}{2} \sum_j \rho_j^2 + \sum_i \hat{\rho}_j \rho_j \Re \{ e^{i\tilde{\tau}_j} a^*(\tilde{\tau}_j) \} \right] D^m d\varphi_c dD dt_0 d \cos \iota d\psi. \quad (2.38)$$

HEALPIX Sampling

After evaluating the posterior distribution, the skymap is encoded using HEALPIX [94], a data structure designed for all-sky mapping. This process is iterative and adaptive. First, the whole sky is divided into 3072 pixels of 13.4 deg^2 . The probability density is evaluated at the centre of each pixel, and then the pixels are ordered by growing probability. The top 25% of them are then subdivided into daughter pixels; then, the probability is evaluated at each centre of the new pixels, see Figure 2.8. This process is repeated seven times and ends up with a tree structure describing a mesh of pixels and pixel resolution, which is turned into a Flexible Image Transport System (FITS) image and distributed.



Figure 2.8: Illustration of BAYESTAR sampling process. This figure is extracted from [225].

Precision and Accuracy

Bayestar precision is estimated by computing the area of the localisation. Usually, the credible regions used for this estimation are the 50% and the 90% ones. The computation starts by sorting the pixels by decreasing probability, finding the pixel index that allows reaching the chosen cumulative probability, and multiplying this index by the area per pixel returns the credible region's area.

The accuracy of *Bayestar* is estimated by localising injected signals and finding the minimal area that contains its true position. The quantity built this way is called *search area*. The latter is estimated similarly to a credible area but uses the pixel index containing the true location. Along with the search area, *Bayestar* computes a quantity called *search probability*, defined as the cumulative probability held in the *search area*.

Self-Consistency

Considering the importance of *Bayestar* for low-latency follow-up observations, we tested its self-consistency to ensure the distributed skymaps are reliable. We did it by performing a Percentile-Percentile-plot (PP-plot) test. It consists in making a cumulative histogram of the *search probability* for a population of injections. In the case of a consistent localisation, the histogram is expected to be diagonal. In other words, for a consistent analysis, one should find $p\%$ of the injections to have their true location contained in the $p\%$ credible region.

Originally, *Bayestar* self-consistency was tested using GSTLAL injections and analysis. It turned out that the PP-plot histogram lay below the diagonal, which meant that the sky-localisation uncertainties were underestimated. Consequently, a hard-coded factor, later denoted ξ , has been implemented and tuned with GSTLAL injections [225]. Its value was and is still $\xi=0.83$ [225].

ξ acts as a Fudge Factor that pre-scales the SNR time series before performing the inference and allows *Bayestar* to pass the PP-plot test. The effect of ξ is to reduce the SNR by using only 83% of its amplitude - i.e., an SNR=10 GW will have an effective SNR=8.3 before the localisation.

After this implementation, the PP-plot of *Bayestar* was diagonal as visible in Figure 2.9, indicating a self-consistent analysis. However, why ξ was necessary has never been explained. In addition, the ξ value has been tuned with GSTLAL, but is ξ the same for other GW detection pipelines such as PyCBC Live? This question has never been addressed.

2.4 Testing *Bayestar*'s self-consistency

2.4.1 Motivation

Along with the timing information provided by the GW detection, the sky localisation produced by *Bayestar* is one of the most critical pieces of information available for electromagnetic follow-up. Hence having reliable skymaps is an absolute necessity. Based on

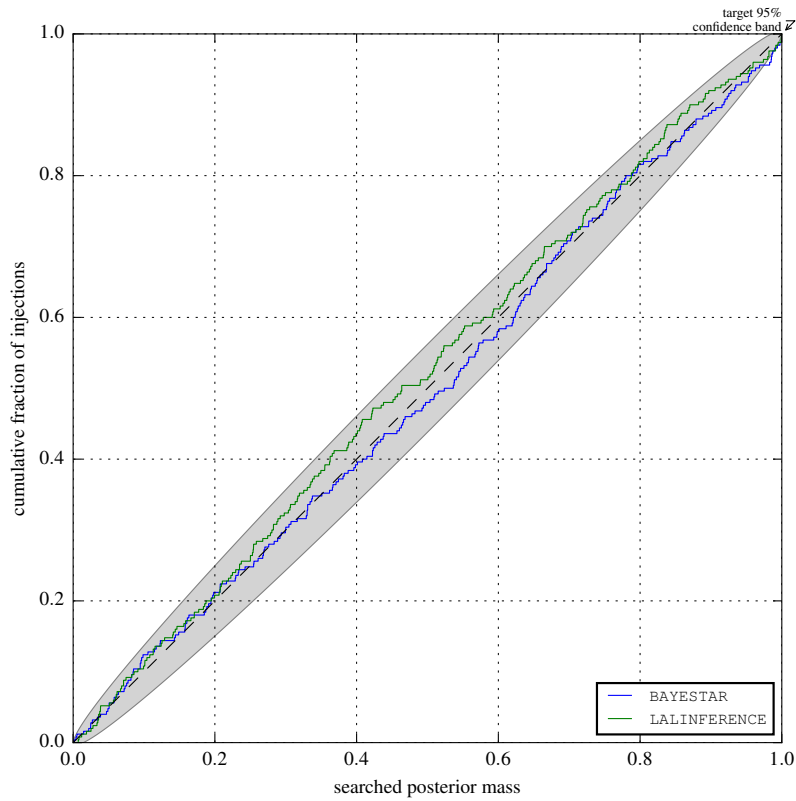


Figure 2.9: Percentile-Percentile plot for *Bayestar* for the 2016 network configuration. The green curve is the result of the PP-plot test for *LALINFERENCE* [252], the algorithm responsible for the whole parameter estimation in the LIGO-Virgo collaboration. The blue curve is the *Bayestar* results. Both curves are within the 95% statistical uncertainties given by the shaded grey band, indicating self-consistent results. This figure is extracted from [225].

Figure 2.9, the low-latency sky localization is self-consistent. However, another PP-plot test performed with **PyCBC Live** injections, showed a deviation as visible in Figure 2.10 taken from [194]. The green curve is the one that corresponds to the O2 and O3 configuration for both the interferometer network and **Bayestar**. The curve above the diagonal indicates an overestimation of the localisation uncertainties - i.e. the skymaps area is too large on average. Although it is in the direction of a conservative estimation of the uncertainties, it complicates the electromagnetic follow-up by increasing the chances of accidental coincidences with unrelated electromagnetic transient sources within the GW credible region. Furthermore, covering a significant part of the skymap will require more observing time for follow-up telescopes.

For the following sections, we propose to investigate this effect by using simulated GW signals and using PP-plot tests. We start by creating a controlled CBC population with realistic distribution for the merger parameters. Then we injected the resulting signals into noise samples and localised them with **Bayestar** to test its self-consistency under various hypotheses using PP-plot tests. However, we are interested in the 2D spatial reconstruction of **Bayestar** and we do not address the consistency of the 3D localisation that includes the luminosity distance of the source to Ra and Dec.

2.4.2 Simulated Astrophysical populations

For testing **Bayestar**'s accuracy, we simulated BBH, BNS and NSBH populations separately to test whether the CBC type influenced its consistency. Moreover, the BNS case is of particular attention as they are expected to systematically produce EM counterparts and lead to important follow-up observations. Regardless of their nature, the binary parameters are chosen as follows:

- 3D Position: Uniform in volume to match the default **Bayestar**'s prior on the spatial distribution.
- Polarisation: Uniform in $[0, 2\pi]$
- Coalescence Phase: Uniform in $[0, 2\pi]$
- Inclination: cosine uniform in $[-1, 1]$.

They are all chosen uniformly to match the observations that do not favour any behaviour for these parameters. For the coalescence time, unless something else is stated for the test, they are chosen such that they are separated by 500s starting from an arbitrary time. Along with these binary parameters, the component objects of the binaries are the following:

- Masses: Uniform in $[5, 100]M_{\odot}$ for BH and a Normal distribution with parameters ($\mu=1.4M_{\odot}$, $\sigma = 0.1 M_{\odot}$) for NS. The BH mass bounds are chosen to match the definition of LIGO-Virgo collaboration used during the O3 run. For NS, the mean of the distribution matches the Chandrasekhar mass of a NS.

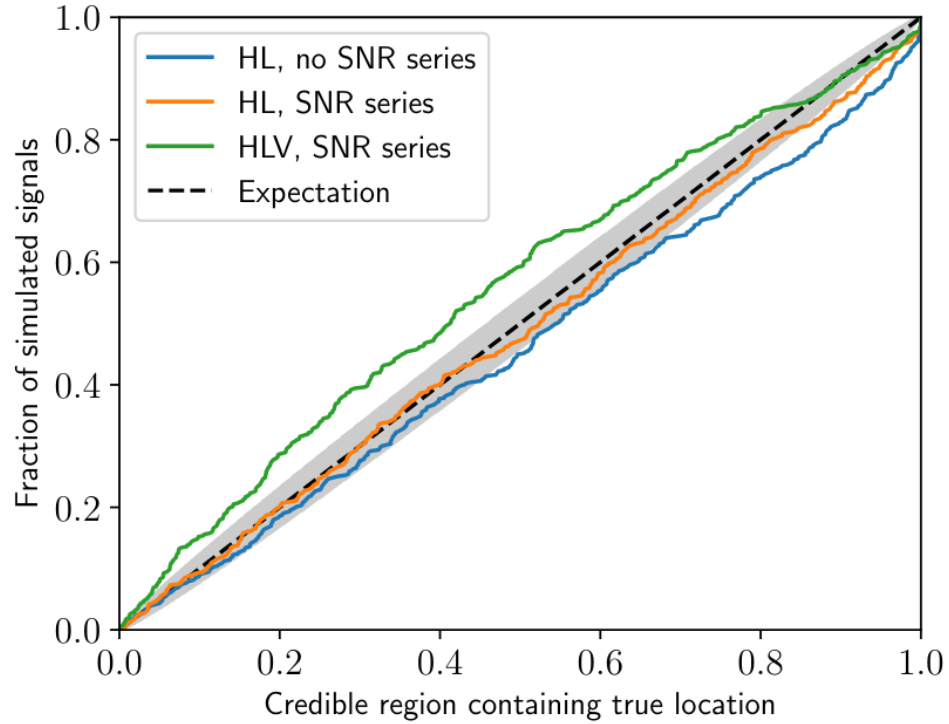


Figure 2.10: PP-plot used to test the self-consistency of *Bayestar* with PyCBC Live simulations. The blue curve represents the two-interferometer configuration and *Bayestar* using only the local maxima of the SNR time series to localise a candidate GW signal. The orange and green curves are made with different GW network configurations using the whole SNR time series for creating the skymap, which corresponds to the *Bayestar* configuration used during the O3 run. This figure is extracted from [194].

- Spin z component: for both BH and NS, the spins follow a Normal distribution, with $\mu = 0$. For BH, the deviation is $\sigma = 0.1$ and $\sigma = 0.01$ for NS, to follow the population of objects detected by the LIGO-Virgo instruments [240].

The BBH waveforms are generated using SEOBNv4 approximant, corresponding to a full inspiral-merger-ringdown simulation with an effective one-body model [38]. For BNS and NSBH, we used TaylorF4 approximant as waveform models, which correspond to a post-Newtonian waveform for the orbital phase of a merger [42]. After the generation of the binaries parameters, we computed the *optimal SNR*, defined in Equation 2.14 for each interferometer in the network (LIGO-Hanford, LIGO-Livingston and Virgo). We also computed the *optimal network SNR* by quadratically adding the *optimal SNR* for each detector.

2.4.3 Baseline Percentile-Percentile test

To verify whether the deviation observed in Figure 2.10 was reproducible, we simulated 500 BNSs and 500 BBHs to perform a PP-plot test.

Before the analysis, we computed the optimal SNR of the CBC population to only keep signals that had a *network optimal SNR* superior to 8 and an *optimal SNR* superior to 5.5 in at least one of the interferometers. Table 1 from [151] summarises the network SNR of the publicly distributed alerts during O3, and $\text{SNR} \sim 8$ is the lower bound for distributed online GW candidate events. This allowed having 500 signals loud enough to be detected and mimicking the selection effect a search would have on the triggers. Then every signal was injected in an independent 600s long sample of Gaussian and stationary noise, using simulated PSDs⁵ that are plotted in Figure 2.11. To have a configuration similar to O3, we chose to use the same PSD for the two LIGO interferometers and a significantly less sensitive PSD for Virgo. We used an internal PyCBC tool called `pycbc_make_skymap`⁶ to perform the localisation.

`pycbc_make_skymap` takes the merger parameters to create the template waveform, performs the matched-filtering to create the SNR time series, and passes it to *Bayestar* that computes the injection skymap. Then, we extracted the *search probability* for each injection and used the distribution for the PP-plot test. For this test, we considered that the Null hypothesis was that the localisation was self-consistent, i.e. the PP-plot is expected to be diagonal.

After having produced all the skymaps and established the *search probability* cumulative histogram, we performed a Kolmogorov-Smirnov test (KS-test) to compare the results to the Null hypothesis [122]. This test allowed us to compare two distributions and quantify their agreement thanks to two output values: the distance separating the two distributions and a p-value quantifying the statistical significance of a possible difference. Under the Null hypothesis, the *search probability* is uniformly distributed in $[0,1]$ and produces a diagonal cumulative distribution. Therefore, we compared the simulation results to a uniform distribution with the KS-test. Thus, the KS-test metric corresponds

⁵ <https://pycbc.org/pycbc/latest/html/pycbc.psd.html>

⁶ https://github.com/gwastro/pycbc/blob/master/bin/pycbc_make_skymap

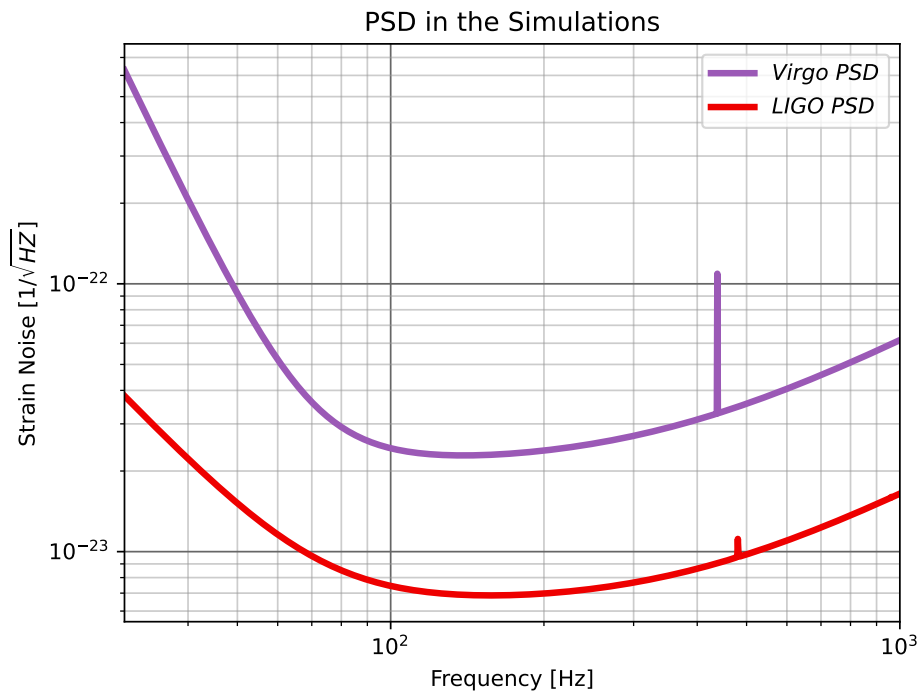


Figure 2.11: Simulated PSDs used for the injections. In red is the PSD for the LIGOs, and Virgo is in purple. In the the `lalsimulation` library [136], which gathers many LIGO and Virgo code, these models are named `aLIGOMidLowSensitivityP1200087` and `AdVEarlyLowSensitivityP1200087`, see note 5.

to the maximum distance of the PP-plot histogram to the diagonal. In the following sections, we consider that a KS-test p-value $\leq 3 \times 10^{-3}$, corresponding to a $\sim 3\text{-}\sigma$ deviation, is small enough to reject the Null hypothesis.

For the first batch of simulations, we used *Bayestar* in its O3 configuration, and we assumed the true parameters were known for computing the SNR time series with `pycbc_make_skymap` and for the localisation with *Bayestar*. Although this is not a realistic configuration, this test is easy to implement. The results for this configuration are visible in Figure 2.12 as a PP-plot with BBHs in orange and BNS in blue. In Table 2.1, the p-values and their corresponding σ deviation are presented. For both CBC types, the deviation is larger than $3\text{-}\sigma$, allowing us to reject the null hypothesis. The conclusion for this is that there is an overestimation of the sky-localisation uncertainties under the tested configuration confirming the results in [194].

CBC Type	p-value	Deviation
BBH	5×10^{-9}	5.8σ
BNS	2×10^{-11}	6.7σ

Table 2.1: Results for the 500 simulated BNS and 500 simulated BBHs. The p-values are computed with a KS test that compares the *search probability* with a uniform distribution. The deviation is based on the KS-test p-value and can be considered large enough to be statistically significant.

2.4.4 Finding bias origin

Figure 2.12 results were in the same direction as the results previously found in [194]. Consequently, we searched for the origin of *Bayestar* overestimation of the uncertainties. There were several possible causes, and we considered the following:

- **Network configuration:** *Bayestar* was created and tested before O2 when Virgo was not sensitive enough to bring spatial information about a GW detection, contrary to the O3 run, when there was a three detector network. As Figure 2.10 exhibits a deviation for the three instruments configuration with LIGO-Hanford (H1), LIGO-Livingston (L1) and Virgo (V1), but not for the H1-L1 one. Hence, we simulated several network configurations with only two instruments, different sensitivities and other Earth positions.
- **Selection Cut:** as explained in Section 2.4.2, a selection on the simulations based on the optimal SNR was used. The fact that signals above a certain loudness are localised could bias the estimation of the sky localisation uncertainties. Therefore we tested other selection cuts before the localisation.
- ***Bayestar* configuration:** as explained in Section 2.3.2, in order to pass the PP-plot test for simulations detected by GSTLAL, a hard-coded factor ξ was imple-

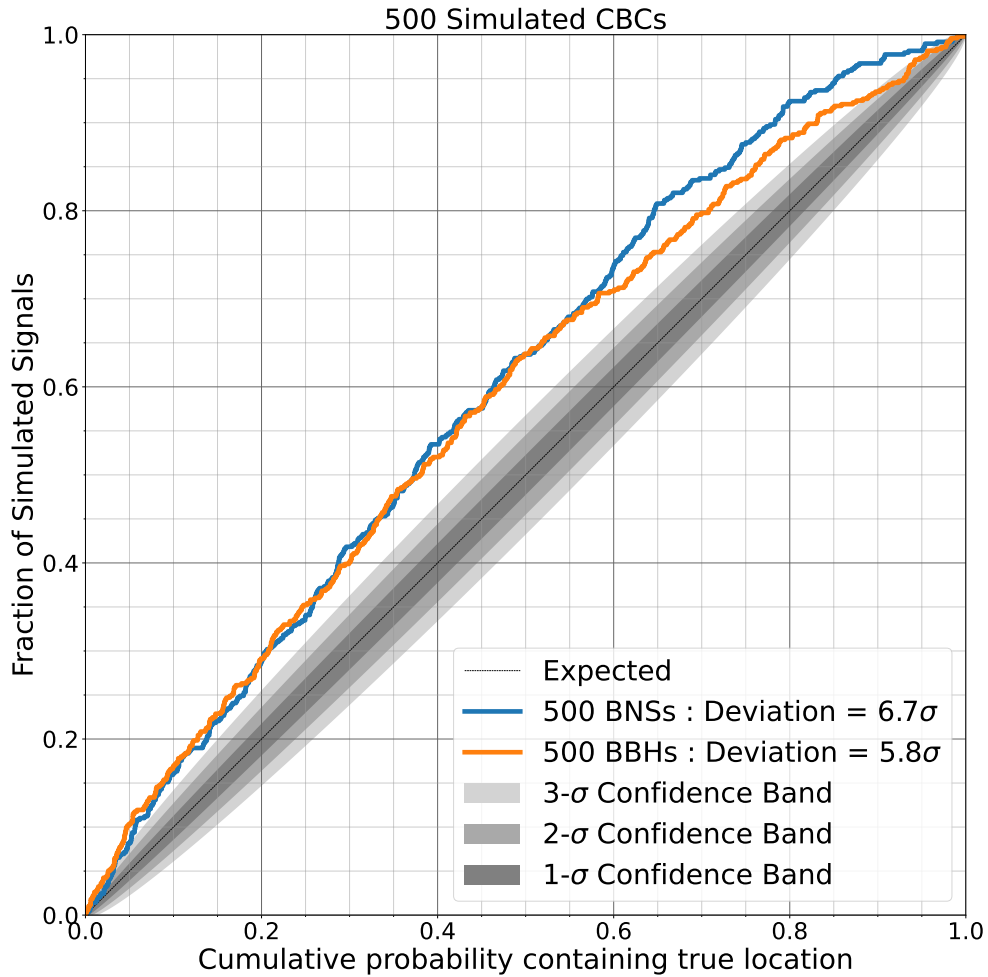


Figure 2.12: Baseline PP-plot for the simulated BNS and BBHs. The blue curve is the cumulative distribution of the *search probability* computed with the skymaps of 500 BNS. The orange one is for the 500 simulated BBHs. In the case of a self-consistent analysis, the curve is expected to be diagonal. The grey shaded areas around the diagonal are the 1, 2 and 3- σ confidence bands, showing the variability expected from the finite number of simulations.

mented in the algorithm to re-scale the likelihood used for the localisation and could bias the analysis.

We tested each hypothesis by simulating 500 BBH localised with `Bayestar` to perform the PP-plot test, and we used a KS-test to evaluate whether the tested hypothesis could explain the deviation in Figure 2.12. As for the first simulations, the template used for the injection and the SNR time series computation is the same.

Network Configuration

In order to test the influence of the number of instruments on the sky-localisation, we simulated two-interferometers network configurations with the same sensitivities as in the previous section, where Virgo is significantly less sensitive than the LIGO detectors, with the sensitivities of Figure 2.11. There are three possible pairs in this case: H1-L1, L1-V1 and H1-V1. The results for these tests are summarised in Table 2.2. As all the p-values returned by the KS-test allow us to reject the Null hypothesis, we concluded that the number of instruments responsible for the localisation was not responsible for the deviation previously observed. We notice that the p-value for the H1-L1 configuration is significantly larger than for the two others, however, considering that the deviation is still visible and that this is a relatively simple test, we did not investigate this more.

Network	p-value	deviation
H1-L1	4.10^{-4}	3.5σ
H1-V1	10^{-8}	5.7σ
L1-V1	4.10^{-7}	5.0σ

Table 2.2: 2-interferometers configurations results.

We also tested the influence of the sensitivity difference between detectors. Currently, Virgo is much less sensitive than the LIGO detectors. Consequently, we injected signals with the LIGO-like PSD in red in Figure 2.11 for all the instruments.

The possibility of a bias caused by the Earth location of the individual interferometer has also been evaluated. Indeed, as the antenna patterns of the two LIGO are almost aligned, the selection effects may bias the sky localisation by selecting events in a sky region where H1 and L1 are more sensitive than Virgo.

We used three network configurations to address these hypotheses: one with H1-L1-V1 equally sensitive and two configurations that include KAGRA (K1), the future Japanese GW detector. Although it has not taken part in the O3 run, its antenna pattern is neither aligned with H1 nor with L1 nor V1, allowing it to test the influence of the detector’s Earth location. It led to two simulated networks: H1-L1-K1 and H1-V1-K1, with equally sensitive instruments. The results for all those tests are summarised in Table 2.3. Again, the p-values are small enough to reject the Null hypothesis. Thus, we concluded that neither the sensitivity difference nor the detector location could explain the initial results.

Network	p-value	deviation
H1-L1-V1	10^{-10}	6.4σ
H1-L1-K1	3×10^{-9}	5.9σ
H1-K1-V1	5×10^{-12}	6.9σ

Table 2.3: 3-interferometers configurations Results.

Event Selection

Ruling out the hypothesis involving the different network configurations, another possibility we considered was the SNR cut described in Section 2.4.3. As only loud events are selected with this cut, one can imagine a more precise localisation on average, leading to overestimating the uncertainties.

To evaluate this hypothesis, we used two *optimal SNR* cuts, one looser and a tighter one.

- Tight cut: $SNR_{network} > 10$ and ($SNR > 8$ in H1 or L1 or $SNR > 5.5$ in V1).
- Loose cut: $SNR_{network} > 5.5$ and $SNR > 5.5$ in at least one interferometer.

The results for these tests are summarised in Table 2.4. The Null hypothesis is rejected, and we concluded that the event selection is not responsible for the results in Figure 2.12.

SNR cut	p-value	deviation
Tight	7×10^{-8}	5.4σ
Loose	10^{-9}	6.1σ

Table 2.4: Event Selection Results.

Bayestar ξ parameter

Initially, the *Bayestar* version presented in [225] mentioned a hard-coded fudge factor, denoted the ξ parameter. As described in Section 2.3.2, ξ allowed *Bayestar* to pass the PP-plot test. However, the deviation in the PP-plot was in the direction of underestimated uncertainties. Several hints made ξ a reasonable candidate to explain the bias observed in the simulations:

- The ξ tuning was made using the *GSTLAL* pipeline, whereas we made the previous simulations with *PyCBC*. As *Bayestar* takes the point estimates of the intrinsic parameters directly from the detection pipeline, in principle, ξ may have to be tuned differently from pipeline to pipeline.
- At the time of the publication, only the point estimates at the maximum of the SNR time series were used. On the contrary, the version used for these simulations and during O3 builds its likelihood with the whole SNR time series. Hence, this difference could also require a re-tuning of ξ .

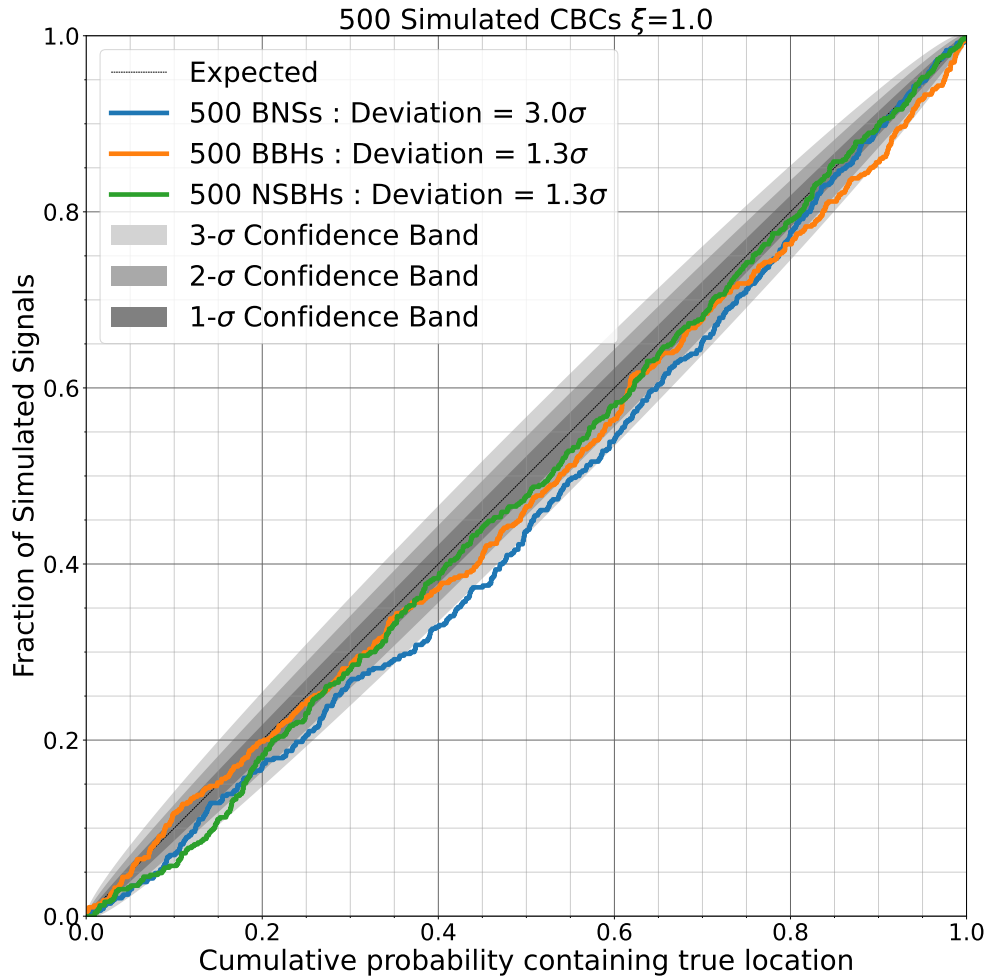


Figure 2.13: PP-plot for three separate populations of GW source after removing the ξ parameter effect in *Bayestar*. The BBHs are in orange, the BNS are in blue, and the NSBHs are in green. This time the deviations are inferior to or equal to $3\text{-}\sigma$, consequently, we can not reject the Null hypothesis. The BNS case is sort of borderline here, as it is just on the threshold we set.

In the current version of **Bayestar**, the ξ parameter has a value of 0.83. It has the effect of re-scaling the SNR time series to 83% of its value to construct **Bayestar**’s likelihood. We re-compiled the code after setting $\xi = 1$, which removed its influence on sky localisation. We generated three separate populations of 500 BBH, 500 BNS and 500 NSBH to test whether ξ influence could depend on the GW source type. The results for these simulations are summarized in Table 2.5, and the PP-plots are visible in Figure 2.13. For those three simulated populations, the p-values returned by the KS-test are not small enough to reject the Null hypothesis (i.e. the **Bayestar** analysis is self-consistent). Hence, we concluded that ξ explains the deviation observed in Figure 2.12.

CBC Type	p-value	Deviation
BBH	0.2	1.3σ
BNS	3×10^{-3}	3.0σ
NSBH	0.2	1.3σ

Table 2.5: Results of the KS-test for the simulations testing ξ influence.

Although these results explain the initial deviation, they also raised new questions that must be addressed to have reliable skymaps for the next observing runs. We can also notice that the simulated BNS show a p-value close to the threshold we set earlier. In the following sections, we investigate the ξ effect and origin, but not directly this BNS case as the deviation is not significant.

- *Why was ξ necessary in the first place?*
- *Is ξ still necessary with the current network configurations and Bayestar version?*
- *Is ξ still necessary with PyCBC? Or just with GSTLAL?*

2.4.5 ξ parameter effect

Intending to understand the effect of ξ on a skymap, we simulated a BNS signal with *optimal SNR* ~ 10 and injected it into a 600s fake Gaussian noise sample. Then **Bayestar** was run on this data segment changing the ξ value each time. The resulting skymaps are visible in Figure 2.14. The smaller ξ , the larger the credible region is dilated, but the credible region shape stays the same, and no systematic shift in the localisation is visible. The credible region area variation can be significant as the 50% and 90% regions area vary by a factor ~ 2 for ξ in the $[0.75, 1.0]$ range. The skymaps dilatation happens because ξ makes the effective SNR used for the localisation smaller than the SNR returned by the detection algorithm to correctly estimate the uncertainties. To fix the ideas, the GRANDMA network of optical telescopes, described in the next chapter, had a typical coverage of 200deg^2 per alert during O3. In comparison, the 50% credible regions move

from 551 deg² for a skymap produced with $\xi = 0.75$, to 190 deg² for $\xi = 1.0$, as it is presented in Figure 2.14. Consequently, the ξ tuning is important for follow-up observations of GW alerts.

2.4.6 Real Noise Influence on Localisation

Addressing why the reason ξ was necessary in the first place is crucial because it could hide a fundamental issue with *Bayestar* or with the search pipelines leading to significant corrections to the algorithm. The *Bayestar* paper [225] provides some hints in Section IX.D that could explain the ξ implementation. The template bank discreteness, an effect of the search or the correlation of the uncertainties with the intrinsic parameters are given possible explanations. In this section and the following, we will test some of these ideas.

This section describes the test performed to evaluate the influence on the localisation of the numerous glitches we described in Section 2.2.4 and the non-stationary character of the data produced by a GW detector. In the previous simulations, we simulated Gaussian and stationary noise. Thus, before going any further, it was necessary to verify if this was causing any significant bias in the localisation. If a glitch appears on top of a GW signal, the localisation will be ruined, as it happened for GW170817, where a loud glitch in Livingston data had to be removed before any analysis. However, the question addressed here is whether those glitches statistically affect localisation. We simulated populations of BBH and BNS in the same way as we described in Section 2.4.2 and injected them into publicly available data from both O3a and O3b. The main difference is the choice of the injection time made by picking a random time from O3 and keeping it if 600s of data were available in the three detectors around that time. As sensitivity and glitch rate between the two halves of O3 significantly improved, we did two separate batches.

We injected 1000 BBH signals and 1000 BNS for both O3a and O3b. Among them, 908/1000 BBH and 921/1000 BNS were loud enough to be localised with O3a data. For O3b it was 912/1000 BBHs and 940/1000 BNS. The results are summarised in Tables 2.6, and Figure 2.15 shows the PP-plots for the injected BNS and BBH for O3a data segments. For both O3a and O3b, we observed a deviation similar to Figure 2.13 for $\xi=0.83$, but not for $\xi=1.0$. These results are consistent with little to no effect on the PP-plots from the non-Gaussianities. Consequently, we concluded that ξ was not required because of the glitches in the data. Based on this conclusion, we only use simulated Gaussian noise for studying *Bayestar* for the next tests.

CBC	ξ	Deviation	CBC	ξ	Deviation
BBH	0.83	$\geq 10\sigma$	BBH	0.83	7.0σ
	1.0	1.0σ		1.0	3.3σ
BNS	0.83	$\geq 10\sigma$	BNS	0.83	$\geq 10\sigma$
	1.0	0.4σ		1.0	0.5σ

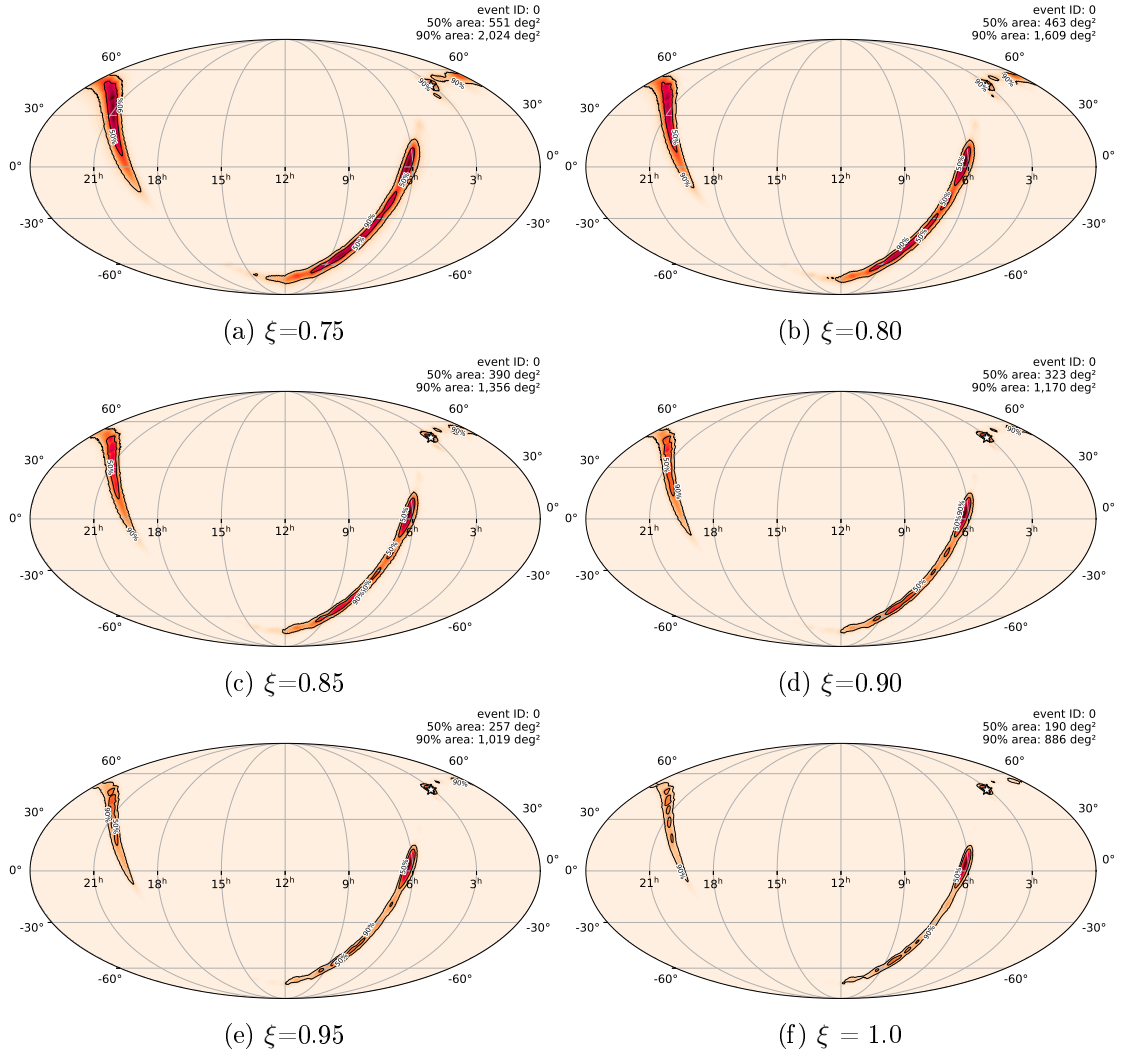


Figure 2.14: Skymaps of a BNS with SNR ~ 10 for various values of ξ . The star in the images corresponds to the true location of the GW source. The area of the skymaps corresponds to the 50% and 90% credible region.

Table 2.6: Results of the KS-test for the simulations testing glitches and non-stationarities in O3a data on the left and O3b on the right.

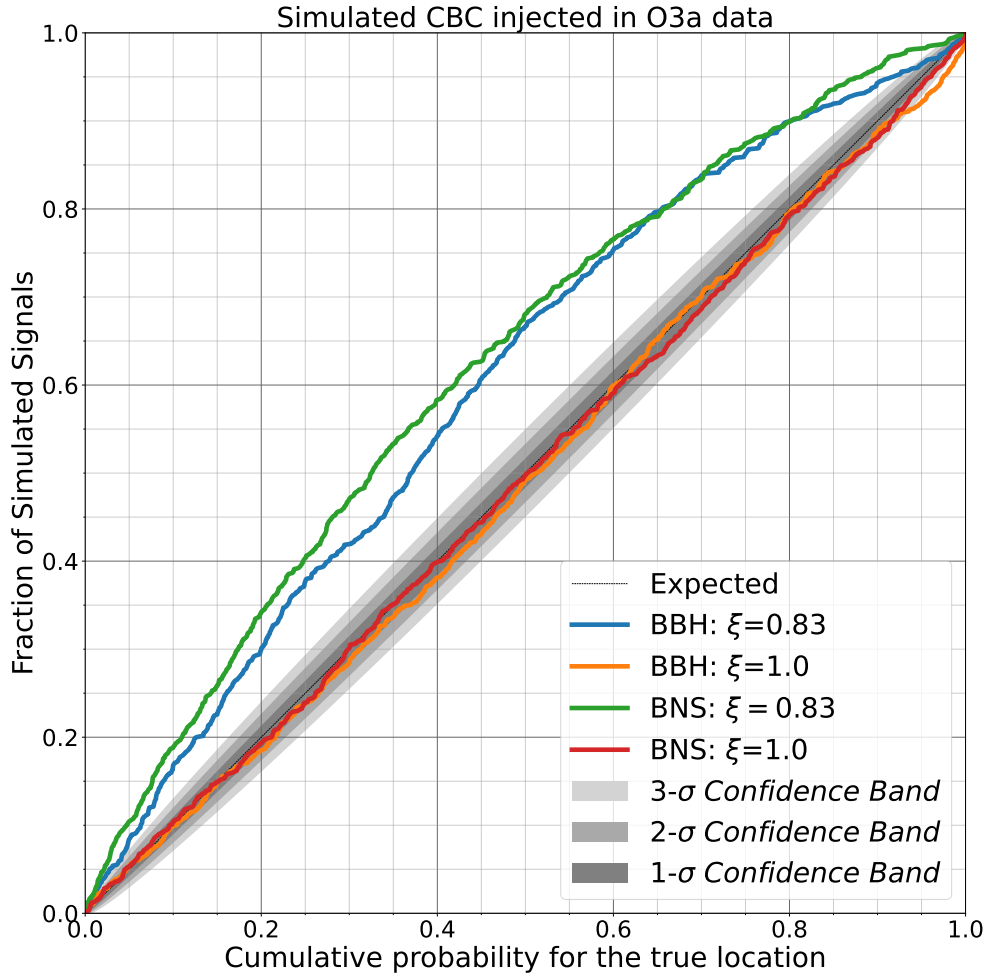


Figure 2.15: PP-plot BNS and BBH injection in O3a data. The blue and green histograms are for the default $\xi=0.83$ for BBH and BNS, respectively. The orange and red histograms are produced with a $\xi=1.0$ for BBH and BNS, respectively.

2.4.7 Jittering Localization Parameters

As stated in *Bayestar*'s paper, one of the explanations proposed to explain why ξ was initially necessary is the discrepancy between the simulated signals and the template waveform selected by the matched-filtering algorithm. In our previous simulations, we used the same waveform for both the injection and the localisation. To relax this, we performed additional simulations where we jittered the intrinsic parameters (masses and spins) before using *Bayestar* so that it would mimic the effect of an online low-latency

search. For this case, we simulated only BNS, for they are the most promising CBC for having EM counterparts, making their low-latency localisation critical. In addition, none of the previous tests showed any significant difference in behaviour between BNS and BBH localisation.

We injected simulated signals in 600s segments of Gaussian noise. Then, we randomised the component spins by using a number chosen uniformly in $[-1,1]$, under the assumption that an online search does not reconstruct the spins. For the component masses, we randomised the mass ratio q defined as:

$$q = \frac{m_1}{m_2}, m_1 \geq m_2, \quad (2.39)$$

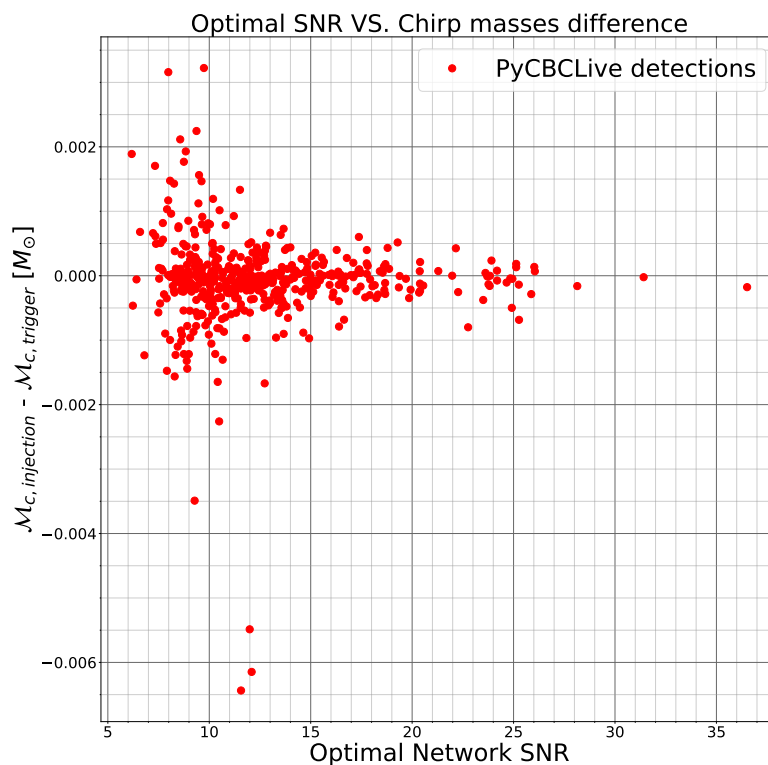


Figure 2.16: $\mathcal{M}_{c,injection} - \mathcal{M}_{c,trigger}$ distribution for triggers recovered by a PyCBC Live search on BNS simulations. These results were used to realistically randomise the \mathcal{M}_c .

where $m_{1,2}$ are the binary component masses, and the chirp mass \mathcal{M}_c , defined in Equation 2.4. Then we used them to compute the localisation template waveform component masses.

For the mass ratio q , we choose a value in $[1, 3]$ to stick to the LIGO-Virgo definition of neutron stars (i.e. objects with masses in $[1, 3]M_\odot$). Treating the chirp mass \mathcal{M}_c as more delicate as this is a parameter very well reconstructed by a search, in particular for

BNS, see [34]. To realistically jitter the chirp mass, we used the results obtained with an actual search performed on BNS injections described in Section 2.5. We used the results it produced to compute the standard deviation σ_{search} of the $\mathcal{M}_{c,injection} - \mathcal{M}_{c,trigger}$ distribution that is shown in Figure 2.16. Based on this, we added a random number to the injection chirp mass following a Normal distribution with parameters $\mu = 0$ and $\sigma = \sigma_{search}$. After that, we computed the skymap using several values for ξ evenly spread in $[0.70, 1.0]$, plus the default 0.83 value. For each ξ value, we ended up with a *search probability* distribution on which to apply a KS-test.

The PP-plots resulting from these simulations are shown in Figure 2.17, and contrary to previous results, here, ξ was necessary to have a diagonal PP-plot. The deviation was significant for $\xi=1$ and sagged below the diagonal, similarly to the original observation made in [225]. This result explained, at least partially, why the ξ was required in the first place. It compensated for the difference between the component objects true masses and spins and the template’s intrinsic parameters returned by a match-filtering algorithm. In addition, we noticed that the ξ value minimising the deviation to the diagonal is 0.85, close to its default value of 0.83, which also makes the plot diagonal. This indicated that the current ξ value still holds.

2.4.8 Jittering Chirp Mass

Continuing the investigations for understanding the ξ parameter role in the localisation, we next checked the influence of the masses uncertainties on the localisation. **Bayestar** is based on the assumption that the two are independent, though we observed that the uncertainties on intrinsic parameters influence the localisation. Hence, similar to the previous simulations, we randomised the chirp mass prior to localisation but kept the symmetric mas ratio fixed at the true value and used these two quantities to compute the component masses used for the template waveform. The template’s waveform was modified by adding a random number drawn from a normal law such that $\mathcal{N}(\mu = 0, \sigma = \sigma_{search} \times \alpha)$, where $\alpha \in [0, 0.5, 1.0, 1.5, 5, 10, 20]$. For each α value, the KS-test with the minimal deviation was estimated by testing the same values for ξ as in the previous section. The ξ value minimising the deviation was considered optimal.

The results are shown in Figure 2.18, and they show that ξ is not required for small values of α but becomes necessary for $\alpha \gtrsim 5$. Consequently, except for unrealistically large differences between the injected and reconstructed chirp masses, the assumption of the independence of mass and localisation uncertainties made by **Bayestar** holds. Moreover, we simulated only BNS whose chirp mass is reconstructed very precisely by matched-filtering techniques [34], making this assumption even more robust.

2.5 End-to-end simulation with PyCBC Live

The previous simulations have helped identify the ξ as a sensitive parameter for the self-consistency test. In particular, we observed that it was necessary to compensate for the

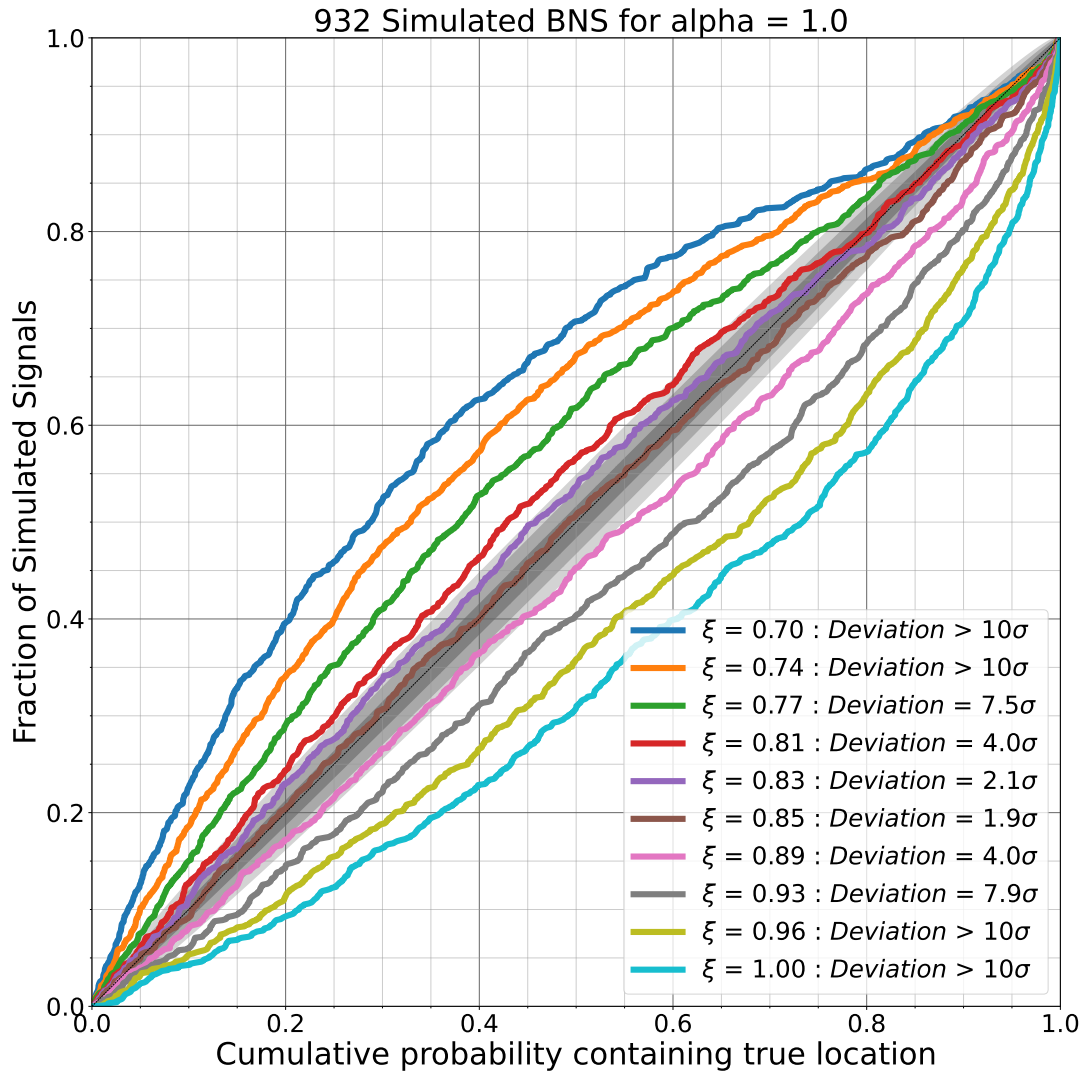


Figure 2.17: PP-plots obtained after randomising the template’s intrinsic parameters with respect to their true values prior to the signal localisation. The ξ value minimising the KS-test is 0.85, with a deviation similar to $\xi=0.83$.

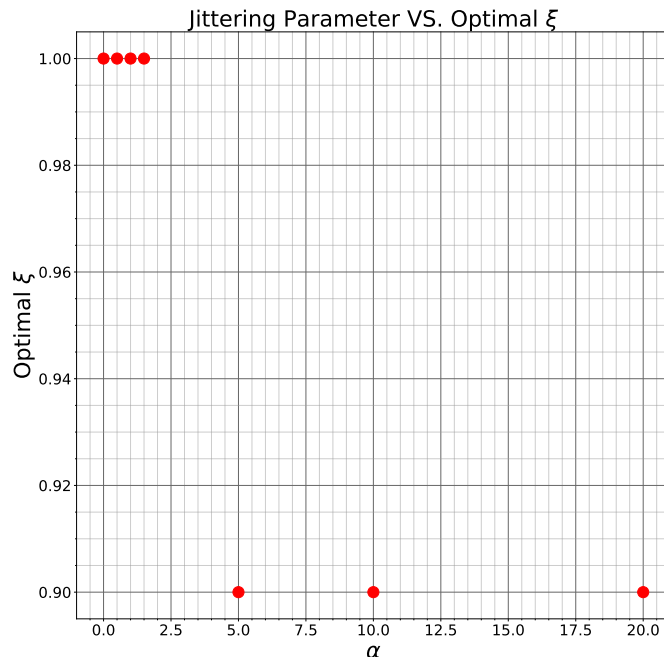


Figure 2.18: ξ minimising the KS-test deviation with respect to the α parameter controlling the chirp mass randomisation.

discrepancy between the injected waveforms and the template used for the localisation. During an actual observing run of LIGO and Virgo, this difference between the GW signal and the template returned by the search algorithm will inevitably arise because the true parameters of the binary are unknown. Hence, to prepare the incoming O4 run and have reliable skymaps available for low-latency multi-messenger follow-up, we set up an instance of `PyCBC Live` at a local cluster called `Virtual Data`. We used this instance to perform a more complete test of the influence of an online search on GW sky-localisation.

2.5.1 On-line search with the O3 bank

The instance locally set up was made of 170 worker nodes containing the template bank waveforms, performing the filtering of the data and finding the triggers. They were transmitted to the head node that clustered and ranked them to identify the candidate GW signals. Each node contained 4 GB of memory, half of which were filled by the assigned templates. The head node had 60GB of memory containing the background triggers constructed with the past five hours of data, used for a candidate GW signal false alarm rate estimation as presented in Section 2.2.5.

All the analyses performed with the local `PyCBC Live` instance were done using 1000 BNS signals injected in Gaussian noise, following the results from Section 2.4.6. The BNS were separated by 250s so that there is no possible overlap, and the injection rate

is not high enough to bias the PSD estimation. The total amount of simulated data represented ~ 3 days of data analysed with `PyCBC Live`.

First, we analysed the frames using the O3 bank generated using a mixed geometric-stochastic method as presented in Section 2.2.3. `PyCBC Live` produced 653 candidate events. We associated a trigger with an injection when its geo-centre time was less than 40ms apart from the injection time. We ended up with 493 confident associations. Then we used `Bayestar` to localise the detected injections, and we used the resulting skymaps for constructing the PP-plot in Figure 2.19. The triggers were used to compute the σ_{search} used in 2.4.7 along with the PP-plot.

The plot is diagonal for $\xi=0.83$ but lies below when $\xi=1$. This is consistent with results from both [225] and Sections 2.4.7. Moreover, we estimated the 50% and 90% credible region (CR) for each value of ξ and computed the cumulative distribution of the area, see Figure 2.20. The behaviour is similar to what was observed on a single injection in 2.4.5, the area of the CR grows when ξ decreases.

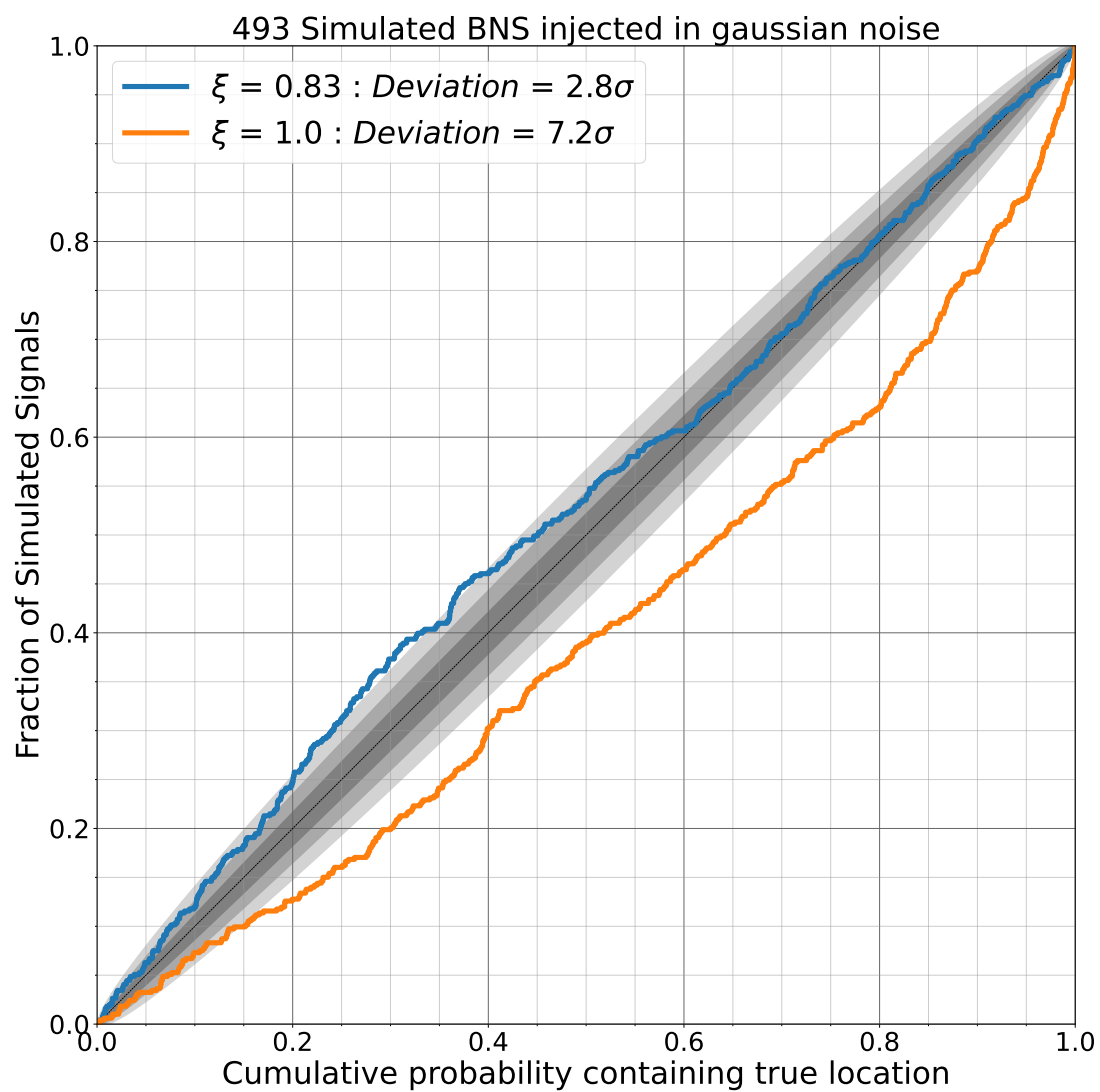


Figure 2.19: PP-plot distribution for the injections recovered by a complete run of PyCBC Live on simulated data. The blue curve corresponds to the usual 0.83 value for ξ , and the orange one is for $\xi = 1$.

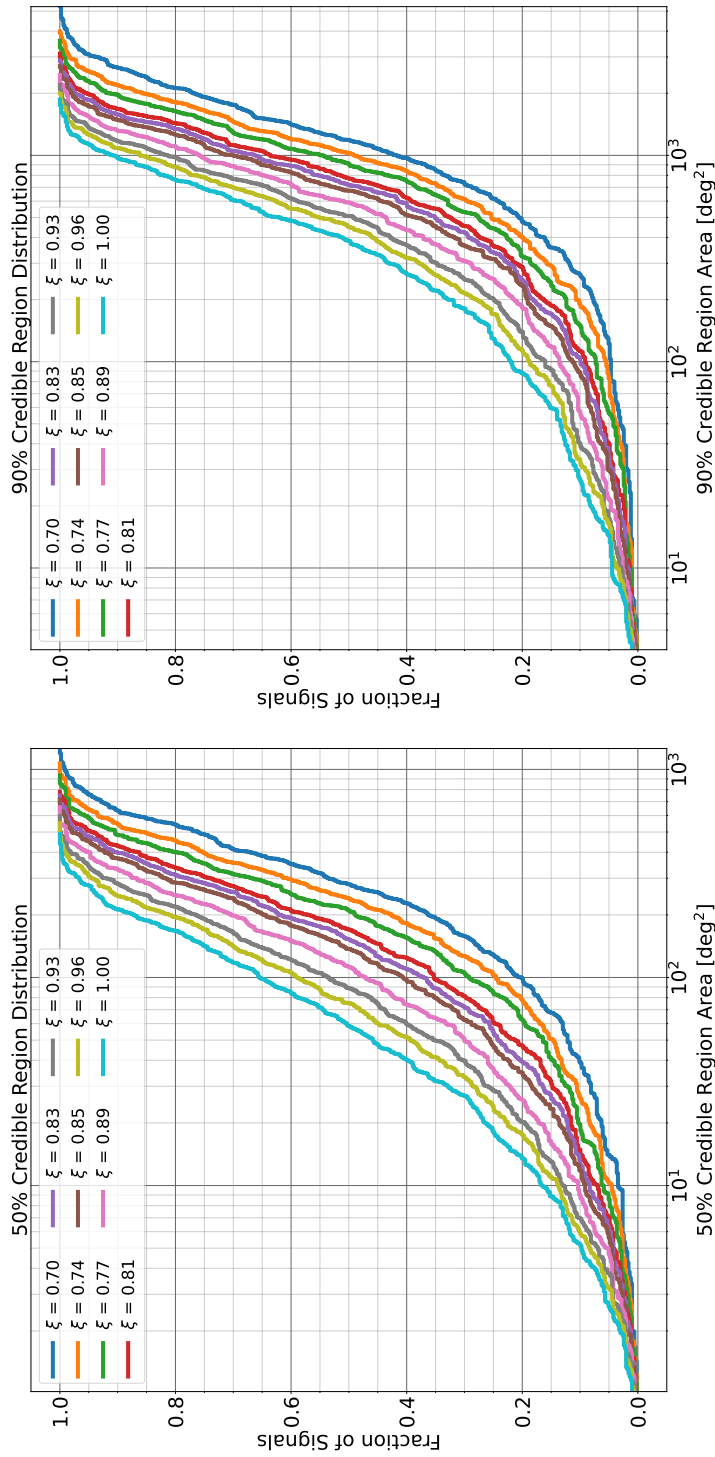


Figure 2.20: Credible Region area for the injections recovered by the search. The left plot is for the 50% credible region, the right plot is for the 90% credible region. Each curve corresponds to a given value of ξ .

2.5.2 Template bank influence on localization

As we described in the previous sections, the ξ parameter is necessary because of the discrepancy between the intrinsic waveform parameters and the true parameters of the binary. Consequently, one can consider that a sparser template bank would increase the discrepancy between the intrinsic waveform parameters and the binary ones. To test this hypothesis, we used the `PyCBC Live` instance to analyse the previous simulated data with other template banks to test their influence on localisation.s We only injected BNS and reduced the template bank explored parameter space to non-spinning BNS. We controlled the sparseness of the bank using the minimal match (MM) parameter described in Section 2.2.3. We generated three different banks, one much sparser than the O3 bank with MM=90%, one with the same MM of 97% and the last one finer with MM=98%. These banks were generated using the purely geometrical placement, described in Section 2.2.3 and presented in Figure 2.2, with a `PyCBC` tool called `pycbc_geom_nonspinbank`⁷. The template of these banks had both component masses in the $[1,12]M_{\odot}$ with 3.5 order post-Newtonian waveforms.

The candidate events recovered by `PyCBC Live` were associated with an injection in the same way as in Section 2.5.1 and localised with *Bayestar*. We performed the usual PP-plot test for several values of ξ and found the optimal one by minimising the KS-test deviation. The results for the different template banks are summarised in Table 2.7.

Minimal match	Optimal ξ	Deviation
90	0.89	0.9σ
97	0.89	0.7σ
98	0.89	1.2σ

Table 2.7: Template bank optimal ξ .

First observation, the optimal ξ does not vary with the MM, implying that the bank sparseness has little to no effect on the localisation.

Second observation: the optimal value is 0.89 for all the template banks, which differs from the usual 0.83. We suspect this difference is due to the parameter space covered by the banks. Compared to the O3 bank, these banks are not exploring spins for neutron stars. As seen in Section 2.4.7 and 2.4.8, ξ is compensating for the difference between the injection waveform and the template passed to *Bayestar*. Hence, the larger the parameter space, the larger the difference is, and the smaller ξ is.

2.6 Conclusion on *Bayestar* Accuracy

Previous work on `PyCBC Live` had shown that the *Bayestar* localisation may not be entirely self-consistent. We investigated the importance of the low-latency localisation

⁷ https://github.com/gwastro/pycbc/blob/master/bin/bank/pycbc_geom_nonspinbank

of the GW signal for follow-up observations. For this, we simulated CBC signals, used *Bayestar* to localised them, and tested various hypotheses with the pp-plot test.

We summarised the tested hypothesis in the following:

- Network configuration - Number of interferometers, the sensitivity of the detectors and Earth position
- Selection cut
- Effect off the ξ parameter
- Influence of the glitches and non-stationary effects of the interferometer data
- Influence of the template bank.

They allowed identifying the ξ parameter as a critical parameter for having self-consistent localisations.

Then we investigate the reason why this correction was necessary for *Bayestar* and by testing the following hypothesis:

- Discrepancy between the waveform template intrinsic parameters and the binary parameters
- Discrepancy between the waveform template component masses and the true binary masses.

We gathered evidences that ξ was necessary to compensate for the difference between the source parameters and the waveform parameters used for the localisation.

We also performed an end-to-end search with *PyCBC Live* to check whether the previous analysis was holding for a realistic search. We also tested the influence of the template bank design on GW localisation. We gathered evidence that the bank sparseness had little to no influence on the localisation uncertainties. The ξ tuning required to have a diagonal pp-plot appears to depend on the parameter space explored by the search. The larger this space is, the more the true GW and the template parameters reconstructed by the search can differ, and the smaller ξ must be to correct for this.

Perspectives

Future works on *Bayestar*'s accuracy would include a refined tuning of the ξ parameter, especially before the upcoming O4 run. A Mock Data Challenge (MDC) is ongoing within the LIGO Virgo Collaboration (LVC). It consists of the low-latency analysis of GW signal injections in Gaussian noise and a replay of the O3 data with injection within. These data are analysed by various detection pipelines, including *PyCBC Live*, for testing and development purposes. They are producing triggers that could be analysed in the same way as we did for our end-to-end analysis with *PyCBC Live*. These triggers would allow testing whether ξ must be tuned differently between pipelines with realistic production

conditions.

PyCBC Live will include new features for O4 that could potentially influence the template waveform choice during the low-latency production of triggers. As we already discussed, the template's agreement with the true parameters of the binary, and we should test the influence of these features on the localisation and check whether they do not require a re-tuning of ξ .

The last point we did not address is the 3D sky-localisation which is also influenced by ξ . A similar PP-plot test could be performed to evaluate its influence.

OPTICAL FOLLOW-UP OF GRAVITATIONAL WAVES

In the first chapter, we described the kilonova as thermal transients powered by r -process and why they are essential for gravitational waves-based multi-messenger astronomy (MMA). Although there are several kilonova sources, neutron star-black hole (NSBH) mergers or supernova, binary neutron star (BNS) mergers are the most promising source of MMA observations, according to the only example confidently identified so far: AT2017gfo. However, they are essential for multi-messenger astronomy, considering all the physics topics they could impact with more observations. This chapter starts with a description of the observational difficulties associated with kilonovae. Then we describe how the GRANDMA network tries to address these challenges. After this, we will describe the `Muphoten` photometry pipeline developed in this thesis work and currently used by the collaboration. Eventually, we will describe GRANDMA the various optical follow-up campaigns. The LIGO-Virgo third observing run O3 follow-up campaign and the two observing campaigns GRANDMA performed to prepare for the upcoming O4 run.

3.1 Kilonova observational difficulties

After the success of AT2017gfo follow-up observations, the GW and electromagnetic communities hopped for numerous new observations during the O3 run. Nevertheless, no discovery of a kilonova occurred during the O3 run, despite the tremendous efforts put by many optical facilities. This absence of new observation results from the numerous observational difficulties linked to kilonova, complicating their detection, identification and follow-up. These challenges can be classified into two categories: intrinsic difficulties arising from the physics of the transient itself, and extrinsic difficulties, coming from the methods available for detecting and characterising them.

3.1.1 Intrinsic difficulties

Kilonovae are very specific transients whose behaviour varies a lot compared to usual optical signals such as supernovae. The AT2017gfo counterpart to GW170817 can help us to understand the main constraints the emission mechanisms imposes on observations. First, despite being relatively close to Earth, 40Mpc, AT2017gfo peaked at a weak magnitude ~ 17 mag in the r -band. During the O3 run, the median distance for binary

neutron stars alerts was 200 Mpc [14]. Consequently, any kilonova emitted during these putative events would peak at ~ 21 mag, as illustrated in Figure 3.1, showing the r -band peak magnitude evolution with distance for an AT2017gfo-like transient. Similar magnitudes should be expected for the only clearly identified BNS of the O3 run, observed at 159^{+69}_{-72} Mpc [150]. This faintness imposes deep observations to detect the optical counterpart using large facilities (aperture ≥ 1 m).

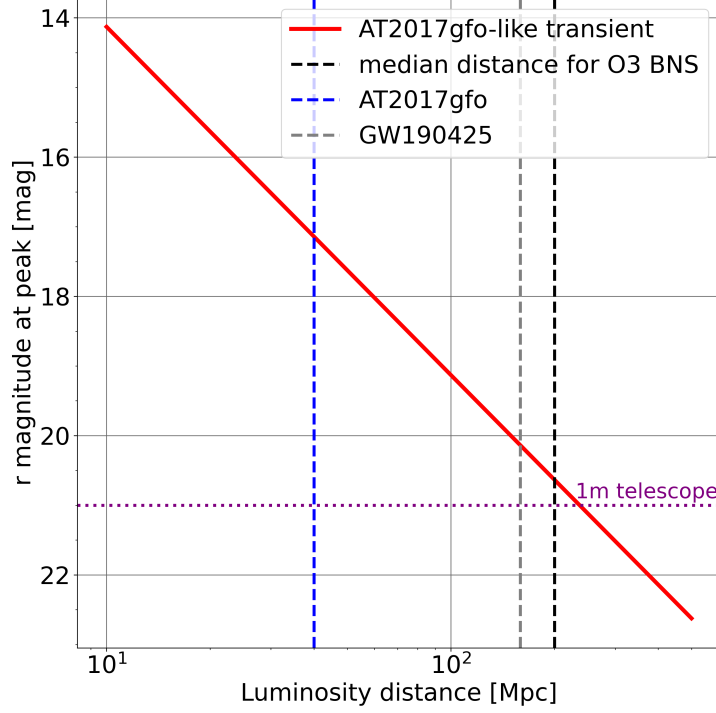


Figure 3.1: r -band peak magnitude of AT2017gfo for several distances based on the compiled data from [253]. The purple dashed line represents the typical magnitude reached by one-meter class telescopes in ~ 1 minutes exposure in good observing conditions.

Moreover, AT2017gfo luminosity decayed very rapidly, especially in the UV domain. It was visible for only one to three days with magnitudes less than 23 for the bluer bands, whereas in the near-infrared (NIR) - IR bands, the transient was observed for a month. This kilonova typical color evolution comes from the different ejecta components, as we presented in Chapter 1. However, based on Figure 3.2 showing AT2017gfo lightcurve in the r -band for several distances, a BNS occurring at 200 Mpc will produce a kilonova with a magnitude around 21 mag a day after the merger. Consequently, this only leaves chances for telescopes with apertures superior to 1 meter to detect the kilonova emission with usual exposure times ~ 1 minute. This rapid decay implies having a rapid reaction after the GW detection for the observing facilities. In addition, small aperture telescopes require longer exposure to reach 21 mag, reducing the number of frames they

can acquire in one night.

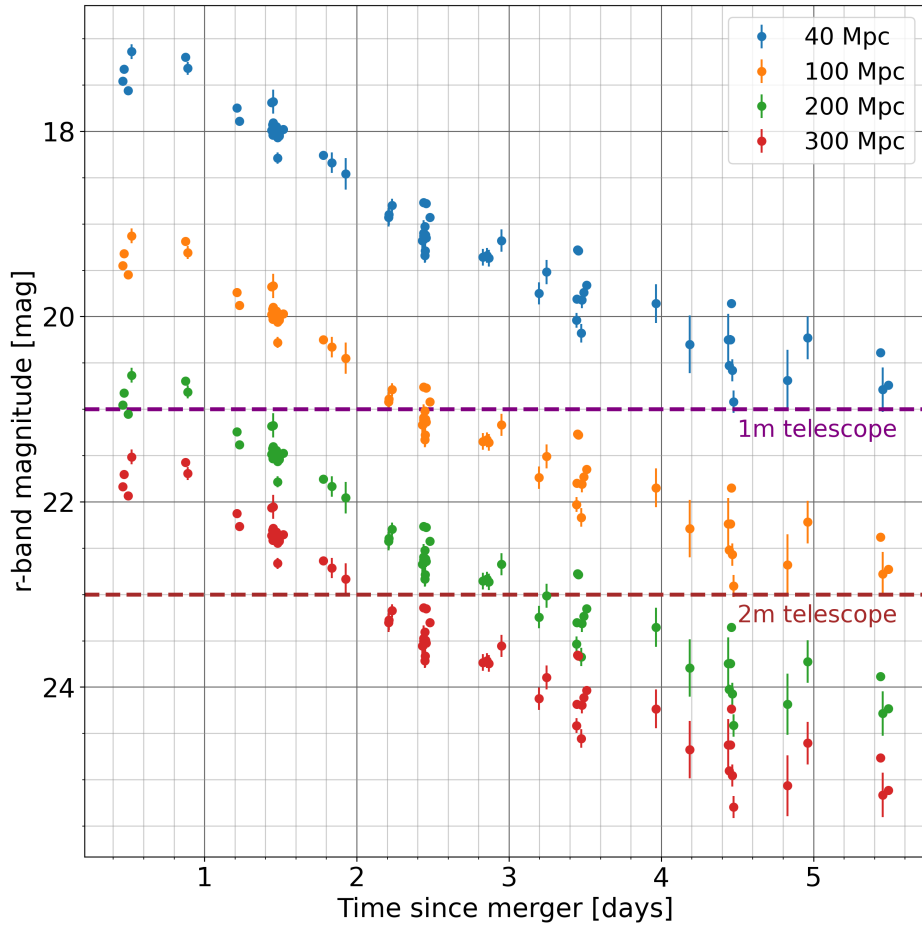


Figure 3.2: r -band magnitude of AT2017gfo for several distances based on the compiled data from [253]. The dashed line represents the typical magnitude reached by one (purple) and two-meter (brown) classes telescopes in ~ 1 minute exposure in good observing conditions.

The AT2017gfo transient had an unusual color evolution compared to commonly observed optical transients (Supernovae or GRB afterglows): during the first days, the kilonova was blue until it peaked in the red-infrared bands for several weeks. This evolution is visible in Figure 3.3 extracted from [235] where the spectral energy distribution starts with smaller magnitudes in the blue wavelengths ($0.5\text{-}1\ \mu\text{m}$) at 0.5 and 1.5 days post-merger, indicating a blue transient. Then, the redder wavelengths ($2\ \mu\text{m}$) start dominating the distribution after 3.5 days, indicating a reddening phase. After 8.5 days, the red wavelengths completely dominate the distribution, indicating a red transient and the extinction of the kilonova blue component. This specific color behaviour implies

that kilonova candidates must absolutely be followed with several bands. Simulated lightcurves of AT2017gfo-like transients observed with the ZTF facilities showed that the g and r filters best differentiate kilonovae from other candidate counterparts [229]. Adding a NIR band, such as i , to the two previous filters is even better but requires more observations.

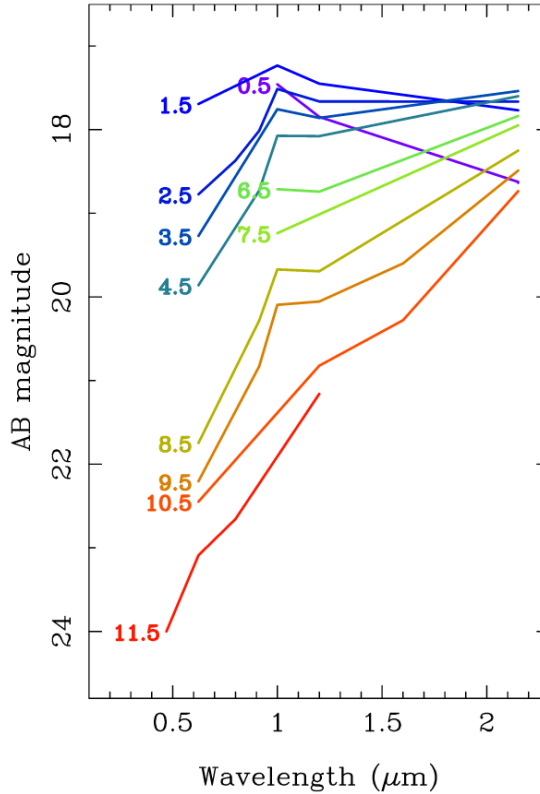


Figure 3.3: Spectral energy distribution (SED) of AT2017gfo for the ~ 12 first days of the transient follow-up. Each curve is the SED of the kilonova and is labelled by its corresponding time in days after the GW trigger. The curve color roughly corresponds to the kilonova color. The transient exposes a clear evolution from blue (0.5-1.5 days) to red color (after 3.5 days). This figure is extracted from [235].

These inferences have to be mitigated as kilonova are expected to be very diverse, depending on the viewing angle, the presence of a central engine or the source emitting it (BNS or NSBH) that could end up with a brighter transient than AT2017gfo- see [175] and chapter 1. In addition, a possible recent discovery of a kilonova associated with a long GRB could potentially add more input for constraining observations [213, 266]. However, as there is no GW data for this event, it is difficult to use it for constraining optical observations for the next O4 run. Overall, with only one kilonova example associated with a GW emission, these conclusions drive the design of follow-up infrastructures, as we will discuss in the following section.

3.1.2 Extrinsic difficulties

The previous arguments explain the kilonova elusiveness, but on top of these difficulties, observational challenges arise from our methods for detecting them. Currently, the best efforts are based on external triggers, particularly GW observations. They have the immense advantage of giving a precise time for the merger, a distance estimation and a sky localisation, although the latter can be crude, as we have discussed in chapter 2. Triggers from gamma-ray bursts satellites - Swift or Fermi, for example - may also lead to kilonova observations. However, some candidates were identified later [93, 245, 243], in light of AT2017gfo results, and a recent candidate has been associated with a long GRB detected by Swift [213, 266]. The latter still lacks GW observations that would have helped dissipate doubts about the emitting source. Moreover, this claimed kilonova is similar to AT2017gfo and does not inform much about their diversity. The last point is most likely related to the fact that we only have one example of such a transient. Consequently, we are looking for what we already know. Using GW could help solve this by allowing the discovery of new examples significantly different from AT2017gfo.

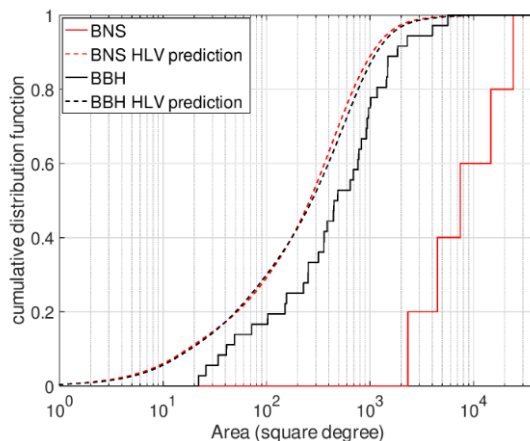


Figure 3.4: Cumulative distribution of the 90% credible region of the O3 GW event. The dashed lines correspond to the predictions made by LIGO and Virgo before O3 in [158]. This figure is extracted from [14].

However, with the use of GW comes specific issues complicating the observations. The most prominent is how poorly localised the GW sources are: a sky-localisation can cover hundreds up to thousands of square degrees. Figure 3.4 extracted from [14] shows the cumulative distributions of the 90% credible region for the GW triggers distributed during O3, resulting in a median area of $\sim 8000 \text{ deg}^2$ for BNS. These large uncertainties have several implications. First, they are difficult to cover, especially if no observing strategy is established before the run. Second, many unrelated optical transients will be spatially compatible with the neutron stars merger localisation. Most of the time, discarding the contaminants such as supernovae, novae or solar system objects must be

Constraint	Solutions
Faintness	Deep observations
Rapidly evolving	Rapid reaction between the trigger (GW or GRB) and first lights
Color Evolution	Multi-band observations (at least g and r for detection)
Localisation area	Coordination between telescopes Pre-established follow-up strategy to avoid duplication Important observing time
GW detection rate	Careful alert selection
Characterisation	Multi-band observations Spectroscopic observations Well sampled lightcurves

Table 3.1: Summary of the main observational constraints for kilonova observation based on GW triggers and their solutions.

done based only on photometric information as spectroscopic capabilities are much more limited. Indeed, considering the faintness and distance of the BNS we detect, only the largest optical facility can reach such depths and acquire spectrum. Consequently, only the most likely EM counterparts should and will be followed-up. In that case, it likely is context-dependent. If the GW is well localised or if a GRB is detected coincidentally, the number of candidates will be limited enough to be agnostic. If the GW is similar to O3 cases and poorly localised, the search will be limited to AT2017gfo-like candidates, compatible with it in terms of faintness, decay time and colour evolution.

During the upcoming O4 run of GW observations, the expected detection rate, including all types of sources, is one event per day. In particular, most events are predicted to be BBH that are not expected to produce EM counterparts. Consequently, the events have to be carefully selected, as trying to follow all of them would require too many resources. So far, we have described how to detect and identify a kilonova associated with a GW, but additional complications arrive after a detection. The characterisation of a kilonova requires well-sampled lightcurves to have significant constraints on the models. For example, in the case of AT2017gfo, despite the extensive follow-up campaign and the 714 images acquired, it is difficult to distinguish whether there are two (blue + red) or three (blue + purple + red) colour components [253]. We must expect fewer images taken for future detections considering the greater distances we observed for BNS candidates in O3, leading to fainter transients.

3.1.3 Addressing Observational Constraints

Table 3.1 summarises the different constraints arising from the kilonova searches. Between the O2 and O3 runs, astronomer communities addressed these two ways. On the

one hand, some individual facilities can do the follow-up by themselves. In this case, the optimal instrument design is a large field of view instrument - more than one square degree - that can rapidly cover a significant part of the GW sky localisation. However, it is difficult to have an instrument with both a large aperture and a large field of view (FoV) for technical and cost reasons. The Zwicky Transient Facility (ZTF [167]) is one of these instruments with a 47deg^2 FoV and a ~ 21 mag depth. It serendipitously followed-up several GW triggers during O3 and used archival data to identify candidate counterparts. The other way to address the challenges proposed by the GW EM searches is to use existing facilities and gather them into a network. This choice has been made by several collaborations such as GROWTH[60], MASTER[161] or GRANDMA [13, 14]. GOTO [230] is a network of identical telescope units with large FoV and a ~ 20 mag depth built to follow up GW.

In the next Section, we present GRANDMA, a network of telescopes aiming at following GW alerts to find and characterise EM counterparts, along with its infrastructures and strategies.

3.2 GRANDMA

3.2.1 Meet GRANDMA

In April 2018, the Global Rapid Advanced Network Devoted to the Multi-messenger Ad-dicts (GRANDMA) was created by gathering existing facilities, including robotic telescopes. It currently (Spring-Summer 2022) includes 33 telescopes spread in 23 observatories with photometric and spectroscopic capabilities. The collaboration regroups more than thirty groups and institutes worldwide that can start observations any time to find the EM counterparts.

The instruments of the consortium are highly heterogeneous and consist of both large and narrow fields of views telescopes mounted with filters covering near UV to NIR. GRANDMA has access to the TAROT network [196] with three small robotic telescopes (~ 18 mag in 60s), the two FRAM telescopes [1, 113, 211] (~ 17 mag in 120s) and the OAJ-T80 (~ 21 in 180s). They are large FoV instruments used to cover the area of the GW skymaps and find the counterpart as early as possible. There are also narrow FoV instruments with various apertures that can target specific galaxies or perform deep observations in case a confirmed counterpart is detected.

Another strength of the GRANDMA network is the various backgrounds of the ~ 100 scientists participating in it. It includes transient astronomy specialists knowing how to plan, perform the observations and interpret them, GW astronomers guiding the selection of the most interesting alerts and able to interpret the information distributed at low latency by LIGO and Virgo.

3.2.2 Observational strategy

As we have seen in Section 3.1, kilonovae are extremely challenging to observe, and meeting the requirements demands preparation and coordination between the instruments.

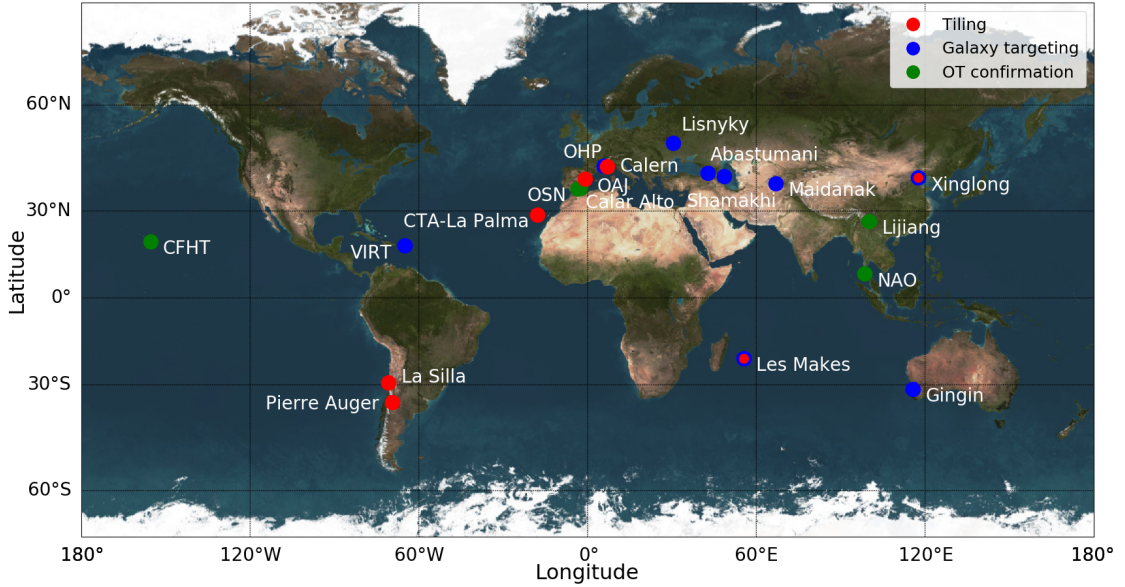


Figure 3.5: The O3b configuration of GRANDMA. The color indicates the observational strategy of the facility - see Section 3.2.2. This figure is extracted from [14]

Consequently, GRANDMA has two operational modes: a blind search when instruments observe to find the counterpart and a follow-up mode to characterise a confirmed counterpart. The latter is fairly simple: any available instrument that observes, regardless of the faintness of the counterpart. Effectively constraining models requires lightcurves sampling as fine as possible. Hence, monitoring the source as much as possible can help. Even a non-detection helps to constrain the merger parameter by setting upper limits on the ejecta mass or the lanthanide fraction based on the images limiting magnitude, for example.

For the blind search, GRANDMA uses two strategies to make the best use of its capabilities and optimise the chances of detecting a counterpart. The strategy adopted by individual telescopes highly depends on their FoV: large ones tile the GW sky-localisation, and narrower ones observe galaxies likely to be the GW source host.

Galaxy targeting

The idea driving the galaxy targeting strategy is to suppose that the merger occurs in a host galaxy that can be identified based on the distance and sky-localisation provided by the GW alert. Based on these, small FoV telescopes are assigned a list of spatially compatible galaxies to observe to check whether an unknown source appeared. This technique allowed the AT2017gfo discovery after the BNS signal was detected in LIGO and Virgo [159].

Within GRANDMA, the identification of potential hosts is made using the MANGROVE

catalog¹ [79], which is a refinement made after 2017. It identifies galaxies spatially compatible with the GW localisation and ranks them based on their position within the skymap and stellar mass. For the former, galaxies on a pixel of the GW skymap with a higher probability of containing the source are considered more likely to be the host. The second is implemented as identified short GRB host galaxies are known to be more massive than long GRB hosts as detailed in [78] and references therein. The galaxies stellar mass is estimated based on their NIR luminosity. MANGROVE is built on a crossmatch of the GLADE [72] and ALLWISE [68] catalogues. The first gives information in visible and NIR bands - *B*, *J*, *H* and *K*, and the second gives information in IR wavelengths. The $3.4\mu\text{m}$ band, in particular, is a known proxy for stellar mass and insensitive to dust extinction. This resulting ranking is illustrated in Figure 3.6, made on an *a posteriori* study of the GW170817 event spatial localisation.

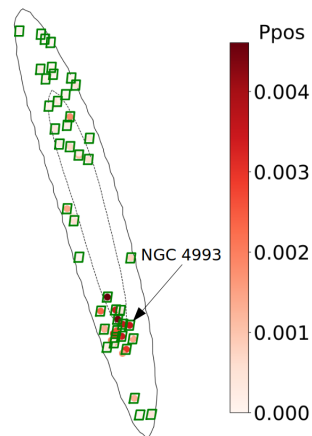


Figure 3.6: GW170817 skymaps with galaxies spatially compatible with the 50% (dashed line) and 90% (solid line) credible region. Green squares represent the FoV of $20'$ - typically the size for which galaxy targeting strategy is designed for. P_{pos} corresponds to the grade attributed to the host candidates based on the position only, NGC 4993 is AT2017gfo host. This figure is extracted from [79].

Tiling

For larger FoV instruments - typically more than one square degree - the best use of the observing time is called tiling. It consists of covering the GW sky localisation map with observations and looking into the frames to see whether a new transient appeared. The main difficulty here is to have coordinated scheduling of the observations to :

- Avoid multiple observations of the same region

¹<https://mangrove.lal.in2p3.fr>

- Give the regions with a higher probability of containing the source to the instruments with the best sensitivity

In GRANDMA, this scheduling was done with the `gwemopt`[61] algorithm during O3. It works by a hierarchical tile assignment to create individual observation plans distributed to the instruments. The best tiles are given to the most sensitive instruments and then removed to attribute the following tiles to the following instruments. Despite the overlap minimisation of the observations, this algorithm does not consider the observing conditions for its scheduling. Consequently, the most probable region may not be observed if a telescope can not perform any observations because of the weather or a technical issue. To address this issue, we define some *golden tiles*, corresponding to the few tens of per cent of the cumulative credible region. These tiles must be observed in priority and are attributed to several observing facilities to improve the observing cadence in case of counterpart detection. For the upcoming O4 run, the `gwemopt` algorithm will be replaced by a new upgraded algorithm.

3.2.3 The O3 infrastructure

Coordinating the observations requires a centralised infrastructure. In GRANDMA, this central system is called Interface and Communication for Addicts of the Rapid Follow-up in multi-messenger Era (ICARE). It fulfils several roles for the collaboration :

- Receive the GW alerts and produce the related observation plans sent to the different facilities.
- Send the observation plan to the collaboration rapidly via standard reports based on VOEvent.
- Monitor the status of the observatories to check the weather, technical issues or maintenance.
- Monitor the messages from other collaborations' GCN to know if candidates are identified or ruled out.
- Receive and store the images and results produced by the collaboration.
- Distribute the results of the collaboration via the GCN system.

These goals are addressed with various tools, all publicly available. We discussed MAN-GROVE and `gwemopt` in the previous sections. We used a web interface to monitor internal status and external information during the O3 run. For the incoming O4 run, these tasks will be done via a new, improved interface called Sky Portal² [255].

The data reduction - detection of transient and luminosity extraction - is done by multiple codes developed in parallel. For detection, we use `gmadet`³, a machine learning-based

²<https://skyportal.io/>

³<https://github.com/dcorre/gmadet>

algorithm. For O4, a new detection pipeline called `stdpipe`⁴, also able to perform photometry measurements, is developed. It will be described later in Section 3.5.1. For photometry analysis, we also developed the `Muphoten` pipeline⁵ that is described in the following section. It constitutes an important product of this thesis.

3.3 Muphoten

3.3.1 Motivation

Following-up rapid transients usually involved several optical facilities, allowing the production of finely sampled lightcurves. AT2017gfo is the epitome of this situation, for which tens of independent telescopes participated in one of the largest worldwide follow-up campaigns. However, as noted by [253], the photometry measurements performed by independent teams can eventually lead to discrepancies in the data set, not because of actual physical processes but because of the various methods used. Those lightcurves provide critical information for physical inferences on the mechanisms occurring in the kilonova, such as the number of optical components, transient viewing angle or the post-merger remnant nature. Consequently, reliable photometry datasets are necessary and require a homogeneous estimation of the transient magnitude.

GRANDMA network was in a similar situation before the O3 observing run of LIGO-Virgo: it required a method to deal with the diversity of instruments, in particular in case of a kilonova detection. Consequently, we decided to implement a photometry tool for the collaboration dealing with GRANDMA images in a consistent way, rapidly enough to bring information about the transient nature with good precision. Without spectroscopic information, we rely only on photometry to classify a candidate counterpart (supernova, kilonova, flaring variable star, etc.), which is crucial for deciding whether continuing the follow-up is necessary.

The tool we developed to meet the requirements imposed by the use of a heterogeneous network is called `Muphoten`. The following sections describe its main features and the tests we performed on a known transient followed by GRANDMA to assess for its performances. `Muphoten` constitutes a significant part of this work and is currently used as one of the official data reduction pipelines of the GRANDMA collaboration.

`Muphoten` is a Python based package using libraries such as `Photutils` [40] and `Astroquery` [91]. It also relies on external C codes: `SExtractor` [31], `Scamp` [28], `Swarp` [32], `PSFex` [29] and `HOTPANTS` [25]. The pipeline works on pre-processed images (dark or bias subtracted, flat-fielded) for which an astrometric solution is known. Although the results `Muphoten` yields are less precise than a code dedicated to a specific instrument, the process is generic enough to be used by any optical facility. In addition, the precision obtained in transient astronomy is mechanically poorer than for other domains, for the targets are observable for a short time. Hence, the precision reached by `Muphoten` is sufficient for its role in time domain astronomy.

⁴<https://gitlab.in2p3.fr/icare/stdpipe>

⁵<https://gitlab.in2p3.fr/icare/MUPHOTEN>

3.3.2 Pipeline Overview

Muphoten aims at extracting the magnitude from images acquired by optical instruments. This computation requires finding a relation between objects' magnitude in the image and their magnitude in a photometric band. This process is called the photometric calibration of an image. This section describes the main steps for calibrating images. For illustrating the different steps in this section, we used two images, one from KAIT taken in the Johnson-Cousins B -band and another by IRiS in the Sloan g -band.

Background subtraction

The first step for calibration is to estimate the image's background level to help detect image sources and improve photometry precision. To do it, we mesh the images in N square boxes Bo , whose size must be larger than the typical size of stars but small enough to catch the background variation across the image. The first criterion avoids star flux subtraction that would ruin the photometry. The last criterion allows a better estimation of the local background and then a better estimation of the stars' flux. The background estimation inside the boxes is done with one of the estimators available in the code. The default estimator is the one used in **Sextractor**, which is written as follows:

$$\begin{cases} 2.5 \tilde{Bo}_i^N - 1.5 \hat{Bo}_i^N & , \text{ if } \frac{(\hat{Bo}_i^N - \tilde{Bo}_i^N)}{\sigma_{Bo_i^N}} < 0.3 \\ \tilde{Bo}_i^N & , \text{ otherwise,} \end{cases} \quad (3.1)$$

where \tilde{Bo}_i^N and \hat{Bo}_i^N are respectively the median and mean pixels analog-to-digital units (ADU) counts in the i^{th} Bo box. For all the following sections, this is the estimator used for the analysis. With the estimation in all the Bo boxes, we create a background image that is eventually subtracted from the raw image. This process is illustrated in Figure 3.7 for the two test images with the background images in the central column and the background-subtracted image in the right column. Similarly to the background, the root mean square (RMS) is estimated in the Bo boxes to create an RMS map of the image.

Source Detection and Photometry

The next step for calibration is to identify sources - such as stars and galaxies - in the image and compute their magnitudes. **Muphoten** uses the background and RMS maps previously created to create a $2\text{-}\sigma$ threshold map following the equation: $background + 2 \times RMS$. Then, we flag the pixels with a count superior to the values in the threshold map. We cluster pixels above the threshold if they are contiguous in any of the eight directions. We consider that at least four contiguous pixels constitute a source.

For computing the source position and photometry for some methods, we require the source n^{th} -order raw moments. For a source S constructed with the previous method

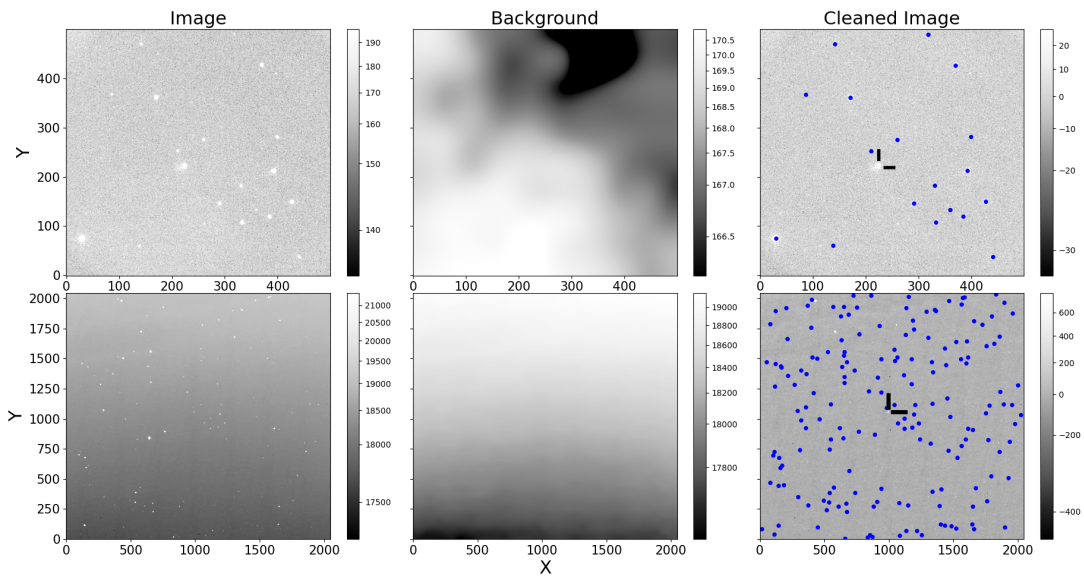


Figure 3.7: Images of the follow-up campaign of SN2018cow (see Section 3.3.5) taken by KAIT (upper row) and IRiS (bottom). The left column is for the raw images; the middle one is the background estimated with the method described in Section 3.3.2. The right column shows the background-subtracted images. The blue dots are stars detected by the algorithm and crossmatched with a reference catalogue - Pan-STARRS here. The black lines mark the SN2018cow location.

made of N pixels with positions (x_p, y_p) , $p \in [1, N]$, the n^{th} -order raw moments are defined as:

$$M_{ij} = \sum_{x_p} \sum_{y_p} x_p^i y_p^j I(x_p, y_p), \quad (3.2)$$

with $I(x_p, y_p)$ the ADU count of the pixel at position (x_p, y_p) and the moment's order $n = i + j$. Based on that definition, we can see that M_{00} corresponds to the total flux in the pixels associated with the source.

Computing the position of a source can be done with the zero (M_{00}) and first-order moments (M_{10} , M_{01}). This computation is analogous to the computation of the centre of mass of a physical system of total mass m . The i^{th} coordinates x_i , $i \in x, y, z$, of the latter is given by the formula: $x_i = \sum_{x_p} \frac{x_p m_p}{m}$. In that analogy, the total mass m of the system corresponds to the total flux M_{00} of the source, and the infinitesimal mass m_p corresponds to the ADU intensity of a pixel. Eventually, we have the following equations for the source position, or source centroids, in the image:

$$\begin{pmatrix} \bar{x} \\ \bar{y} \end{pmatrix} = \begin{pmatrix} M_{10}/M_{00} \\ M_{01}/M_{00} \end{pmatrix}. \quad (3.3)$$

Eventually, using the source centroid (\bar{x}, \bar{y}) of the source, we construct the central moments defined as :

$$\mu_{ij} = \sum_{x_p} \sum_{y_p} \frac{(x_p - \bar{x})^i (y_p - \bar{y})^j I(x_p, y_p)}{M_{00}}, \quad (3.4)$$

which are translational invariant.

Using only the flux computed with the pixels gathered at the previous step would lead to an underestimation of the total flux, especially for faint sources. Consequently, we use aperture photometry to compute the source flux. The user can choose a method among the three photometry methods available in the code:

- **Fixed aperture** : The point spread function (PSF) of the image is estimated in the image with `PSFex` [29]. We compute sources flux in circles centred on source centroids estimated following equations 3.3. The circle radius is the same for all the sources, and the PSF is multiplied by a user-selected value. The coefficient is chosen depending on how crowded the frame is: the radius can not be too large to avoid the presence of another source in the circle that would pollute the flux estimation.
- **Isophotal Photometry**: The fluxes are estimated in elliptic apertures whose semi-major and semi-minor axis lengths and orientations are computed using the second-order moments of the sources. Based on Equations 3.4, there are three of

them:

$$\overline{\mu_{20}} = \frac{M_{20}}{M_{00}} - \bar{x}^2, \quad (3.5)$$

$$\overline{\mu_{02}} = \frac{M_{02}}{M_{00}} - \bar{y}^2, \quad (3.6)$$

$$\overline{\mu_{11}} = \frac{M_{11}}{M_{00}} - \bar{x}\bar{y}. \quad (3.7)$$

They are then used to compute the covariance matrix:

$$\begin{pmatrix} \mu_{20} & \mu_{11} \\ \mu_{11} & \mu_{02} \end{pmatrix}. \quad (3.8)$$

The covariance matrix eigenvalues are computed as:

$$\lambda = \frac{\mu_{20} - \mu_{02}}{2} \pm \frac{\sqrt{\mu_{11}^2 + (\mu_{20} - \mu_{02})^2}}{2}, \quad (3.9)$$

from which we deduce the ellipse semi-major $a = \text{Max}(\lambda)$ and semi-minor axis $b = \text{min}(\lambda)$. In addition, the angle Θ between the eigenvector, associated with a , and a horizontal axis is written as:

$$\Theta = \frac{1}{2} \arctan \left(\frac{2\mu_{11}}{\mu_{20} - \mu_{02}} \right). \quad (3.10)$$

It corresponds to the ellipse orientation. To avoid underestimating the source flux, we multiply the semi-major and semi-minor axis a and b by a user-selected coefficient. These computations are illustrated in Figure 3.8, with a and b as red arrows and the extended ellipse in a blue-dashed line.

- **Kron photometry:** The fluxes are determined following the method described in [124]. The ellipses orientation, semi-major and semi-minor axis a and b are estimated with the second order moments in the same way as for Isophotal photometry. Then an elliptical aperture ε is defined by multiplying the parameters a and b by six that contain N pixels p . Then the unscaled Kron radius r_k is computed such that:

$$r_k = \frac{\sum_{p \in \varepsilon} r_p I(x_p, y_p)}{\sum_{p \in \varepsilon} I(x_p, y_p)}, \quad (3.11)$$

where r_p is the elliptical radius of the pixel p at position (x_p, y_p) in the image defined as:

$$r_p^2 = cxx(x_p - \bar{x})^2 + cxy(x_p - \bar{x})(y_p - \bar{y}) + cyy(y_p - \bar{y})^2. \quad (3.12)$$

The cxx , cxy and cyy parameters are the ellipse parameters defined as:

$$cxx = \frac{\cos^2 \Theta}{a^2} + \frac{\sin^2 \Theta}{b^2}, \quad (3.13)$$

$$cxy = 2 \cos(\Theta) \sin(\Theta) \left(\frac{1}{a^2} - \frac{1}{b^2} \right), \quad (3.14)$$

$$cyy = \frac{\sin^2 \Theta}{a^2} + \frac{\cos^2 \Theta}{b^2}. \quad (3.15)$$

The flux is integrated within an elliptical aperture with semi-major axis $A = a \times r_k$ and semi-minor axis $B = b \times r_k$.

The fluxes for all the sources are computed in analog-to-digital units (ADU) and turned into instrumental magnitudes :

$$m_{ins} = -2.5 \log_{10}(flux_{ADU}). \quad (3.16)$$

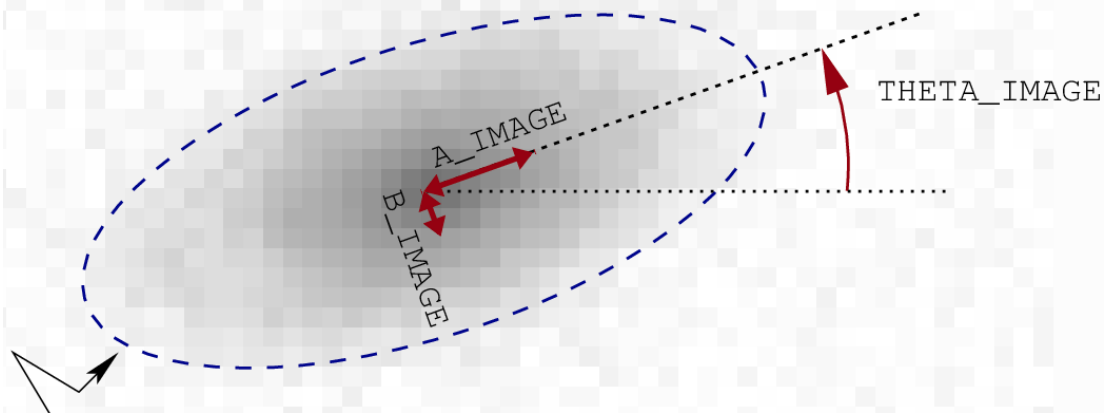


Figure 3.8: Extraction of the shape parameters of an elliptical source. In this figure, A_IMAGE corresponds to the semi-major axis a , B_IMAGE to the semi-minor axis b and THETA_IMAGE to Θ in the text. The a and b parameters are extended by a factor of 3 to have the dashed blue ellipse. This figure is extracted from the **SExtractor** documentation [30].

Photometric calibration

The instrumental magnitude m_{ins} is not a quantity one can use directly for computing a transient magnitude. It depends on the telescope characteristics (FoV, the telescope aperture), the exposure time and the observing conditions. Consequently, we use a reference catalogue for which the object magnitudes in the image are known. The relation between the reference and the instrumental magnitudes m_{ins} is used to create a model from which to deduce the final photometric calibration. For all the sources, we use the

centroids computed with Equation 3.3 and the image astrometry to find the sources sky positions and crossmatch them with a reference catalog. A detected source and a catalogued object are associated if their sky position differs by less than five arcseconds. This process is illustrated in the right column of Figure 3.7, where the detected sources that had a counterpart in the reference catalog are shown with blue dots. There are four catalogs available, whose choice depends on the filter used to take the frame and the observed sky portion. The references are:

- Pan-STARRS (PS) [48]: it is the default reference for any image in the northern hemisphere as it scans the whole sky above -30° in declination, in five bands covering visible to infrared - g_{PS} , r_{PS} , i_{PS} , z_{PS} and y_{PS}
- Sloan Digital Sky Survey (SDSS) [36]: is a survey scanning the sky in five bands covering UV to NIR: u' , g' , r' , i' , and z' . We use it to calibrate images acquired in a UV filter, usually u' or U , in the northern hemisphere, as Pan-STARRS does not cover this part of the spectrum.
- Gaia [219]: is an all-sky survey covering the visible wavelengths with three bands G , G_{BP} and G_{RP} . We use it to calibrate images in areas not covered by PS or SDSS.
- USNO-B1 [186]: is an all-sky catalogue with two bands, B1 and R1, covering the visible spectrum. We only use it for cases where the three others are not usable.

The PS, SDSS and Gaia filters transmission curves are visible in Appendix B. It happens that the filter used to take the image is not in the photometric system of the reference catalogue (i.e. the filters used by the survey), and then it is necessary to correct the calibration for this. The most common case is when we use PS or SDSS surveys to calibrate images acquired with the old, but still widely used, Johnson-Cousins (JC) photometric system: $UBVR_cI_c$. PS or SDSS catalogues both use the standard *Sloan* bands: u' , g' , r' , i' , z' , and y . In that case, we use the Landolt transformation equations to calibrate the JC bands. These equations were established by observing well-characterised, standard stars from the Landolt catalog [128], located around the equator so that any observer on Earth can observe them. The SDSS and PS surveys transformation equations are established with the extended and more recent Stetson catalog [123, 232, 114, 221]. If Gaia is used for calibration, as it does not have standard bands, we use equations provided by the collaboration to have magnitudes in the standard Sloan and JC system [47]. For USNO-B1, which does not use standard bands, we use equations given by the GROND collaboration, [95]. Nevertheless, the photometric results with USNO-B1 will not be very trustworthy because of the catalogue uncertainties. Thus, USNO-B1 is only used when none of the other catalogues can be used.

The last case happens when the image is acquired without any filter (also called *clear* band) or with the L -band that covers the whole visible spectrum with cuts in UV and NIR wavelengths. For unfiltered images the result will highly depend on the camera's quantum efficiency (QE) and will be challenging to interpret when QE is not well known.

Although using *clear* or broadband filters, such as *L*, observations are interesting for GRANDMA when the network is in search mode. As no filter narrows the flux, it increases and the chances of detecting a faint transient improve. For clear and *L*-band images, Muphoten adds the g_{PS} and r_{PS} -bands fluxes and then turns it into a magnitude for calibration:

$$M_{clear} = -2.5 \log_{10} (10^{-0.4 \times r_{PS}} + 10^{-0.4 \times g_{PS}}). \quad (3.17)$$

These two bands cover the visible spectrum, which gives an approximate transformation. If PS is not usable, we calibrate those images with the *G*-band of Gaia as it covers the visible wavelengths.

If the catalogue contains flags about the photometry quality of the objects or if there is an internal classifier of point source VS extended source, we use it to improve the final calibration. We only keep objects with reliable photometry and point-like sources as the transients we follow are point sources.

Eventually, the model implemented in Muphoten consists of a linear relation between the instrumental and the catalogue magnitude:

$$M_{calibrated} = a \times m_{instrumental} + zp \quad (3.18)$$

The two fitted parameters, the slope a and the zero-point zp , are the relevant quantities for photometric calibration as visible in Figure 3.9, showing the photometric calibration of the two test images. Based on them and given an instrumental magnitude of an unknown object, we can compute its calibrated magnitude. The model is rather simple, but it provides satisfying results, as it will be presented in Section 3.3.5. However, it only provides results in the natural system of the instrument that acquired the image, not in the standard Sloan or JC systems. A colour term must be added to the model if there is a significant discrepancy between the natural and standard filters. This improvement will be implemented in Muphoten in the future to improve the precision of the measurement.

Host Galaxy Subtraction and Transient magnitude Extraction

With the calibration we now have, we can compute the transient magnitude. There are two cases: if the transient is not inside a host galaxy, we can use the same photometry as for calibration and Equation 3.18 to find its magnitude. Otherwise, we use the HOTPANTS software [25] to subtract a *template* image without the transient inside. For Muphoten, the *template* can be either an archive image from the same instrument acquired before or after the detection after the transient disappeared. However, for the latter case, the transient must be completely invisible. Otherwise, too much flux is subtracted, which biases the magnitude estimation. According to [253], this happened in the analysis of the AT2017gfo kilonova in [109, 15, 226]. Another option implemented in Muphoten to create a *template* image is to download Pan-STARRS images covering the same FoV as the analysed image. Then we co-add them to create a mosaic image that we re-scale to the same pixel scale as the studied frame with the Swarp algorithm [32]. Eventually, we subtract this template with HOTPANTS to have a difference image.

After the subtraction, the transient is searched for in a radius of 10 pixels around its

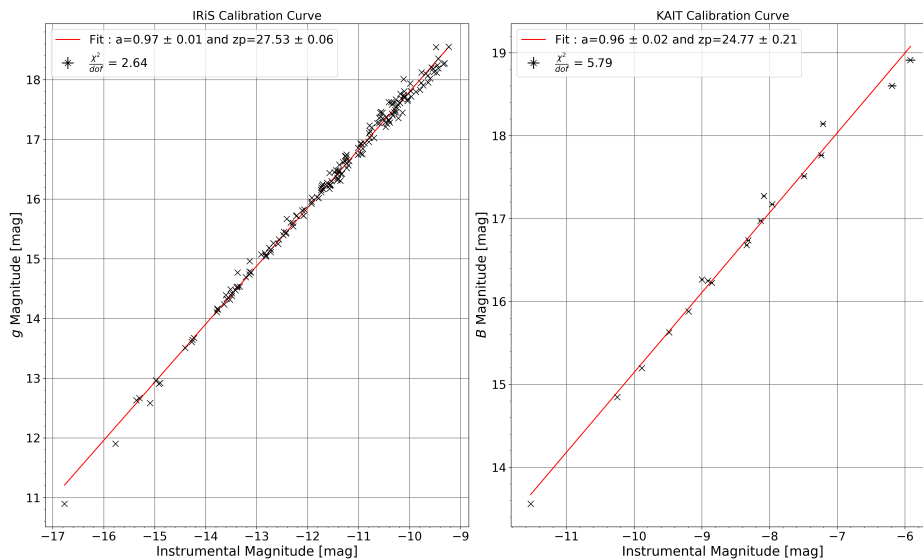


Figure 3.9: Calibration for the two test images from IRiS (left) and KAIT (right). Each point corresponds to a detected source in the image crossmatched with Pan-STARRS. The fit parameters used for the calibration are the slope a and the zero-point zp .

expected position with the same method as described in Section 3.3.2. Eventually, we use the instrumental magnitude and the calibration Equation 3.18 to have the transient magnitude.

3.3.3 Error Budget

For this thesis, Muphoten estimates the errors from the four effects described in the following list. However, late discussions led to the conclusion that the error estimations must be re-evaluated. As the following computations were used for all the analysis described below, there kept as it is for this work.

- **Poisson noise in the transient** : The uncertainties on the ADU count N_{count} are given by the Poisson distribution : $N_{count} \pm \sqrt{N_{count}}$. It results in an uncertainty on the instrumental magnitude :

$$\delta m_{ins} = \frac{2.5}{\ln 10 \sqrt{N_{count}}} . \quad (3.19)$$

- **Poisson noise in the background** : We compute the number of ADU $N_{background}$ in the background image computed in Section 3.3.2 at the transient location using same aperture as the one used for the transient itself. The uncertainty is also following the Poisson distribution, resulting in :

$$\sigma_{background} = \frac{2.5}{\ln 10 \sqrt{N_{background}}} . \quad (3.20)$$

- **Calibration** : We compute the calibrated magnitude using Equation 3.18, and a , zp and m_{ins} bears some uncertainties. The two fit parameters uncertainties are computed with the covariance matrix. We finally get :

$$\sigma_{calibration} = \sqrt{m_{ins}^2 \delta a^2 + \delta zp^2 + a^2 \delta m_{ins}^2} \quad (3.21)$$

- **Photometric transformation**: We propagate the error due to the photometric system conversion when this is required. They are given in [123] for PS, in [221, 114] for SDSS, in [47] for Gaia and in [95] for USNO-B1 and are denoted $\sigma_{transfo}$. For clear images, we propagate the catalogue magnitudes errors in the g' and r' bands in the following way:

$$\sigma_{transfo,clear} = \sqrt{\frac{\phi_r}{(\phi_r + \phi_g)^2} \delta m_r^2 + \frac{\phi_g}{(\phi_r + \phi_g)^2} \delta m_g^2}, \quad (3.22)$$

with $\phi_{r,g}$ the flux observed in the g' and r' bands.

Eventually, we quadratically add all the uncertainties :

$$\sigma_{tot} = \sqrt{\delta m_{ins}^2 + \sigma_{background}^2 + \sigma_{calibration}^2 + \sigma_{transfo}^2}. \quad (3.23)$$

3.3.4 Additional Features

Limiting Magnitude Estimation

In the case no transient is visible in the images, we implemented a limiting magnitude estimation method. A non-detection can occur in two cases: when the transient is too faint to be detected and when GRANDMA is in blind search mode seeking an EM counterpart to a GW. For the former, the limiting magnitude information helps set an upper limit on the flux emitted by a transient. In the latter, having these upper limits also helps constrain some parameters of the GW event, such as the ejecta mass or the lanthanide fraction in the equatorial plan, as we will describe in Section 3.4.2 and illustrate in Figure 3.18.

In *Muphoten*, the limiting magnitude is estimated using the Pan-STARRS survey. We start by detecting all the sources in the image using the same method as in Section 3.3.2. Then we search in the PS catalogue for all the known objects in the same FoV as the studied frame. Then, we build the ratio of detected objects in the frame to the object in PS per magnitude bin as illustrated by the vertical green line in Figure 3.10. When this ratio drops below a user-given threshold, we consider that the limiting magnitude is reached. The default value for this threshold is set to an arbitrary 50% value. However, internal discussions in GRANDMA during the last campaign (see Section C) led to the conclusion that this value was over-conservative. This is visible in Figure 3.10, where the red vertical line corresponds to the limiting magnitude estimated with a 10% threshold. For both images, setting the threshold to 10% shifts the estimation by ~ 2 mag, which is consistent with results from other images. Consequently, the future default value for

the threshold will be set at 10% of detected objects compared to PS to have the limiting magnitude.

The major drawback of this method is that it relies on PS. Hence it can be used as soon as PS is complete. The limiting magnitude of PS is around 21 mag in its bands. However, most GRANDMA instruments reach their limits in the [17,20]mag interval. Consequently, Muphoten’s method is adapted for the GRANDMA network. In particular, the instruments used for tiling strategies, such as the TAROT network [196] or FRAM [1, 113, 211] are in this magnitude range. Consequently, we can confidently use PS for those instruments during an observing run. In particular, as our method is easily implemented and automated, it fits well the large numbers of images that must be analysed from these large FoV telescopes observing large sky areas. In addition, prospects are ongoing to implement new methods for limiting magnitude estimations independent of the catalog depth.

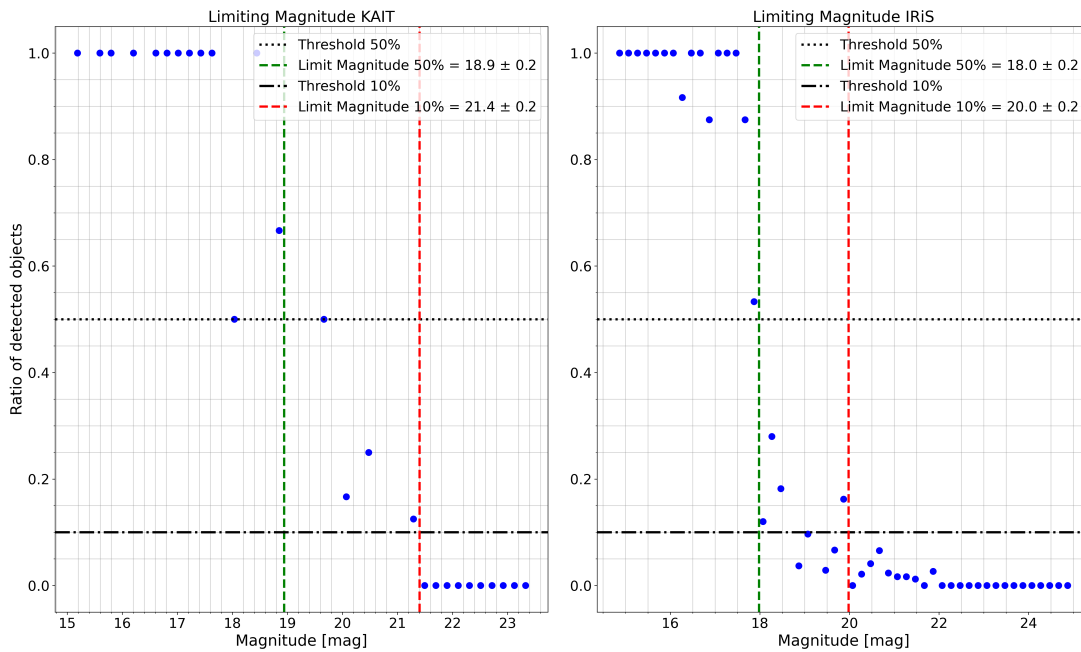


Figure 3.10: Limiting magnitude for KAIT (left) and IRiS (right). The bin width is 0.2 mag, and the threshold for estimating the limiting magnitude is materialised as a solid black line and the limiting magnitude by a vertical dashed grey line.

Quality Checks

A network following up a transient for weeks produces many images. Considering the heterogeneity among the instruments and observing conditions, we implemented two quality checks to reject poor-quality images.

- **PSF veto:** For a given telescope, we compute the full-width at half maximum (FWHM) of the PSF with `PSFex` for all the images acquired in a given filter of the same transient see Figure 3.11. Then we reject all the images that deviate by more than $3\text{-}\sigma$ from the median of the PSF distribution. This criterion allows keeping homogeneous datasets in terms of observing conditions. Moreover, it helps to reject images taken by robotic telescopes that had an issue with their tracking system. It usually leads to images where stars are not dot-shaped but form tracks in the frames. It makes the PSF FWHM very different from normal images and consequently rejected using this check.
- **Photometry veto:** To test our photometric calibration, we select a star in the vicinity of the transient. Then we use the calibration we computed in Equation 3.18 to compute its magnitude and compare it to the catalogued one. Whether the results are incompatible, we reject the image. Moreover, if the user can set a threshold on the error acceptable for the *check star* magnitude and reject the frames beyond this limit. It removes poor-quality images that would pass the first criterion. In Figure 3.12, for the KAIT telescope (upper plot), we used a 0.15 mag threshold but a 0.10mag one for the IRiS instrument (bottom plot).

3.3.5 First test and application: AT2018cow

Motivation

To test the processes implemented in `Muphoten`, we used a transient named AT2018cow - later called SN2018cow - also known as "Cow" [204, 210, 166, 125, 227, 121, 70, 203, 183, 105, 87]. We chose this one as it was observed by different GRANDMA instruments in various optical bands over several weeks. This test case was similar to what would happen if the collaboration was monitoring a confirmed GW optical counterpart. Moreover, the Cow belongs to an emergent category of transients: the Fast Blue Optical Transient (FBOT), and is considered the first and archetypal example. Since then, numerous others have been discovered, such as the "Koala" [106]. Their usual features are the brightness, the blue color, and a short rising time (\sim days) with a hot, blue and featureless spectrum. Although their origin is still unclear, their unusual properties are compatible with the tidal disruption of a star by a compact binary companion - a black hole or neutron star [176, 204]. Some of these observational properties are close to the kilonova ones, making FBOT good candidates for testing GRANDMA follow-up capabilities. Furthermore, the Cow was located in a host galaxy, whose luminosity was significant compared to the transient luminosity, especially at a late time, and had to be removed. This situation allowed us to test the `Muphoten` subtraction procedure.

We used images of the Cow acquired by five different telescopes, three belonging to the GRANDMA consortium. The latter are: TAROT-Chili (TCH), a 25cm robotic telescope that we already discussed in Section 3.4.2, Katzman Automatic Imaging Telescope (KAIT), a 76 cm telescope that usually studies supernova [133], and Initiation à la Recherche en astronomie pour Les Scolaires (IRiS), a 50cm instrument. The two other

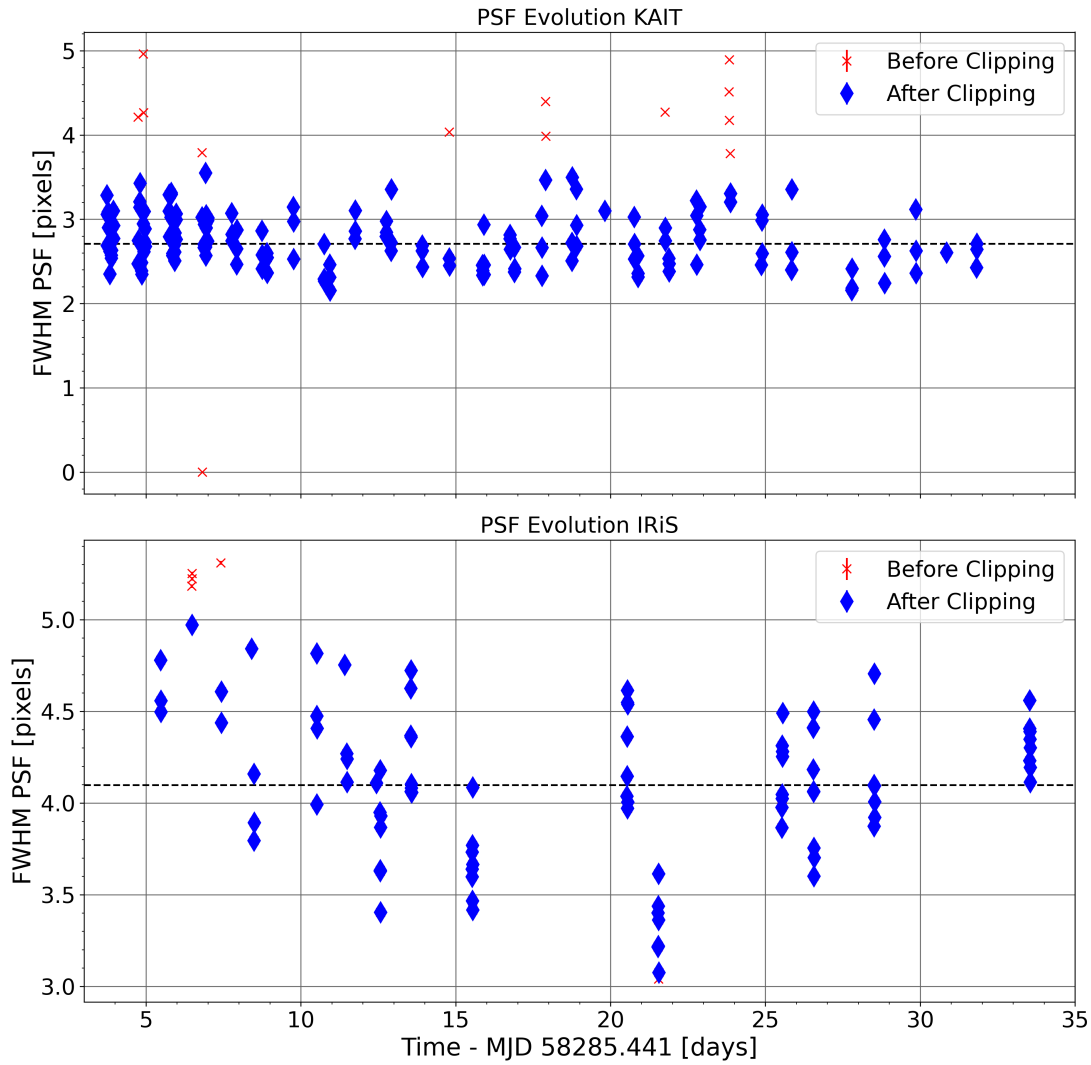


Figure 3.11: PSF FWHM time series for the KAIT B -band (upper plot) and IRiS g' -band (bottom plot) datasets produced during the follow-up of SN2018cow by GRANDMA. The black dashed line represents the PSF FWHM distribution median. Blue dots are for images passing the PSF quality check - i.e. images for which the mean FWHM differs by less than 3σ the median - and red crosses are the rejected images.

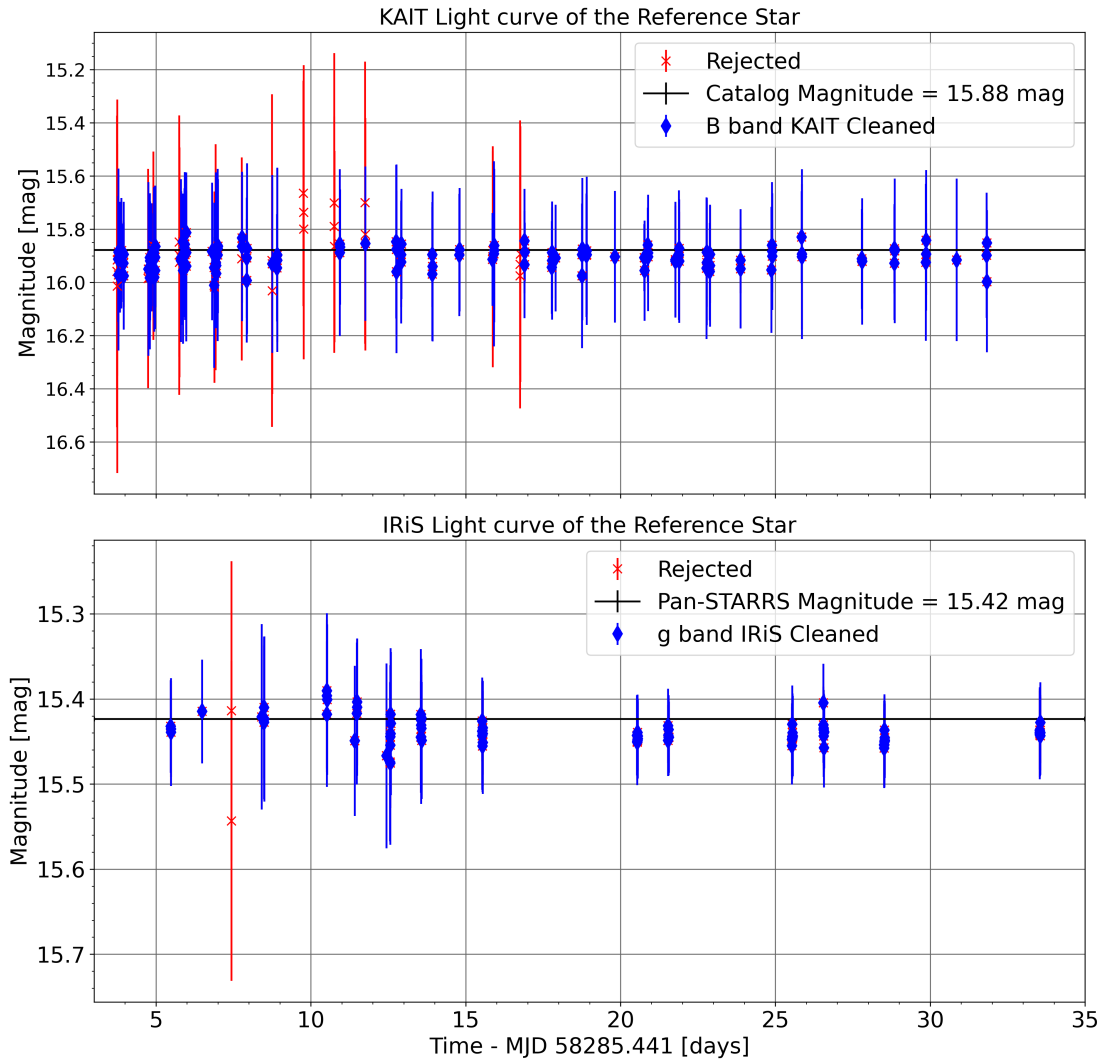


Figure 3.12: Lightcurve for a reference star located at $Ra=243.9749^\circ$, $Dec=22.2937^\circ$. The upper plot is for the B -band KAIT images set, and the bottom plot is for the g' -band of IRIS. The calibration was done with the Pan-STARRS catalogue. For KAIT, which is not equipped with the Sloan filter, we used the relations in [123] to get B -band values. The red crosses represent the rejected images in the plots.

Table 3.2: Summary table of the instruments that followed up the SN2018cow transient.

Telescope	Diameter	focal ratio	Field of View	Filter	Sampling
-	m	-	arcmin	-	arcsec/pixel
KAIT	0.76	f/8.2	6.67 x 6.67	clear, UBVRI	0.8
TCH	0.25	f/3.2	1,8 x 1.8 deg ²	clear, griz	3.2
IRiS	0.50	f/8.2	24	griz	0.7
LT	2.0	f/3	10 x10	BV, ugriz	0.15
KPED	2.1	f/4.864	4.4 x 4.4	UBVRI, gr	0.26

instruments used for this study are the Kitt Peak 84-inch Telescope equipped with the EMCCD demonstrator camera (KPED) [62] and the Liverpool telescope (LT), a 2m telescope whose data were publicly available [231]. We summarised all the characteristics Table 3.2.

We analysed data from those instruments and compared our results to published lightcurves to check that *Muphoten* behaves correctly and is able to retrieve them. In particular, as we had access to the same LT and KPED images as [204], we used them to check if the photometry was done correctly. On the other hand, as the GRANDMA instruments (TCE, KAIT and IRiS) data were not published, we used them to check that *Muphoten* can create independent, consistent photometric datasets with heterogeneous instruments. In particular, the field of view, diameter and sampling spanning values over an order of magnitude was one of the major complications in reducing GRANDMA data. In addition, we combined all the data produced by *Muphoten*, either based on images already analysed in the literature (LT and KPED instruments) or based on the new images brought by GRANDMA (KAIT, IRiS and TCH), to extract some temporal properties of the AT2018cow transient.

Overall, the Cow that was rapidly evolving, located in a host galaxy, and followed by several independent and heterogeneous instruments constituted a fairly general configuration, with many similarities with the AT2017gfo one. This generic configuration allowed us to test whether the pipeline met the requirements it was designed for.

AT2018cow discovery and properties

The Cow was detected by the ATLAS survey [241], a 0.5 m telescope aiming at detecting transients, on 2018-06-16 10:35:38 in an ATLAS-specific orange o -band with magnitude $o = 14.74 \pm 0.1$ mag and no previous detection on MJD = 58281.5 down to $o \approx 19.5$ mag. This indicated an unusually fast rise time, one of the FBOT principal characteristics. It is located at $\alpha(\text{J2000}) = 16^{\text{h}}16^{\text{m}}00.22^{\text{s}}$ and $\delta(\text{J2000}) = +22^{\circ}16'04.8''$. This position was coincident with the dwarf starburst galaxy CGCG 137-068, located at 66 ± 5 Mpc and with an offset of 1.7 kpc from the galaxy's centre.

At first, the Cow was announced as a cataclysmic variable (CV) by [227]. After 2.6 days, an LT spectrum [210, 204, 125] revealed a featureless, hot (3×10^5 K), blue

transient, ruling out the CV hypothesis. The Cow has been detected across the entire electromagnetic spectrum, except in gamma-rays [70, 121]. The optical flux peaked at $L = 4.10^{44} \text{erg.s}^{-1}$, to decline as t^{-2} . At later times - 15 days post-detection - the spectrum showed narrow He emission lines indicating shock interaction with the ejected material and the circumstellar environment [87, 74]. The X-ray light curve shows several episodes of re-brightening attributed to burst-type events rather than periodic activity [125] suggesting a central engine [166]. A recent study reported 225Hz quasi-periodic behaviour in the X-ray lightcurve [203]. The millimetric [105] and radio [183] counterparts of SN 2018cow were detected at early times and are relatively bright. They are emitted by the shock between a polar ejecta and a dense circumstellar medium.

Observations and Muphoten configuration

IRiS observations in the g band started on 2018-21-06 and lasted until early September 2018. We subtract a template frame taken by IRiS on 2018-09-07. It corresponds to one of the last images of the dataset in which the transient is not visible anymore. KAIT observed the Cow in the B -band from 2018-20-06 until 2018-08-08, and we used a template image acquired on 2018-08-07 for subtraction. The LT started its observations on 2018-19-06 until 2018-10-01 in the g -band and from 2018-20-06 until 2018-09-30 in the B -band. We used a Pan-STARRS frame as the template image as the transient can be visible even at late times. KPED observed the Cow from 2018-20-06 until 2018-07-07 in the g -band. The Cow was still very bright (~ 17 mag) when KPED took its last image, hence we used a Pan-STARRS template for subtraction. TCH observed from 2018-21-06 until 2018-06-24 in g , and a Pan-STARRS image was used for subtraction for a similar reason as KPED.

To perform our photometric analysis with `Muphoten`, we chose the `SExtractor` estimator for all the images used for this test. The calibration was done using Pan-STARRS stars for the five telescopes. We used the isophotal photometry of `Muphoten` with an extension factor of 5, see Section 3.3.2. As the B filter of KAIT and LT are not in the Sloan photometric system used by Pan-STARRS, we use equations from Table 2 in [123] for handling the conversion.

Vetoos

The number of images we analysed for the follow-up of SN2018cow is summarised in Table 3.3. We did not keep images without Cow detection for final results. KPED and TCH observed the Cow when it was still bright (≤ 17 mag) and detected it in all the reduced images. KAIT have 68 images without detection because of the small aperture and the short exposure time of 60s. There is no detection in IRiS images after 35 days due to its small aperture.

In addition, we also use the `Muphoten` quality checks to reject low-quality images to improve the final lightcurves. For the veto based on a reference star, we used the following threshold on the uncertainties to reject the images: 0.25 mag for TCH, 0.8 mag for KPED,

0.3 mag for KAIT, and 0.15 mag for IRiS and the LT - see Section 3.3.4. We reject between 1 and 5 images for the TCH, KPED, IRiS and LT instruments. On the contrary, for KAIT, the calibration was poorer as 50 images were rejected by this check. Most of them were because the uncertainties on the star magnitude exceeded the threshold we set to 0.3 mag. For TCH images, two had a star magnitude measurement incompatible with the Pan-STARRS value. Visual inspection confirmed that the quality of these images is poorer than the other TCH frames.

Based on the PSF FWHM time evolution, no images are rejected for TCH and KPED, and between one and six are rejected for the remaining instruments. A visual check confirmed that the images have poor seeing.

Table 3.3: Summary of the image used for the test of **Muphoten**. We also used the quality check implemented in **Muphoten** to reject poorer quality images - these images are counted in columns 4 and 5.

Telescope	Images Processed	Non- Detection	Rejected star Veto	Rejected PSF Veto	Images Left
TCH	17	0	4	0	13
KPED	39	0	5	0	34
IRiS	111	17	2	2	90
LT — g	161	42	1	6	112
LT — B	63	17	1	1	44
KAIT	239	68	50	6	115

Uncertainties Discussion

As described in Section 3.3.3, we consider three sources for the uncertainties in the pipeline: Poisson, calibration, and background errors. Except for KPED, the dominant uncertainties come from the calibration, as the signal-to-noise ratio is high enough to make both Poisson and background uncertainties negligible. The lower Poisson and background uncertainties of IRiS compared to the LT are due to the longer exposure time of the first (300 s) compared to the second (60 s). KAIT calibration errors are ~ 0.2 mag because of the few detected objects in its field of view (typically ~ 10 sources; see Figure 3.9), leading to higher uncertainties on the fit parameters. The latter argument also explains why the calibration errors are larger for the LT than IRiS. For KPED, the much larger error bars are due to a short exposure time (10 s) that leads to a low ADU count and thus to a large Poisson and background errors. Moreover, the lower number of detected sources ~ 20 increases the calibration errors.

Results

The final lightcurves are presented in Figure 3.13 for the B (bottom plot) and g (upper plot) bands along with the results published by Perley et al.[204], Margutti et al. [166],

Table 3.4: Mean errors for each component of the error budget discussed in Section 3.3.3. The values in that table are computed for images that passed the two vetoes described in Sec. 3.3.4.

Telescope	Poisson Error	Calibration Error	Background Error
-	[mag]	[mag]	[mag]
TCH	0.009	0.12	0.002
KPED	0.31	0.32	0.52
IRiS	0.008	0.06	0.002
LT — g	0.01	0.08	0.006
LT — B	0.02	0.08	0.01
KAIT	0.03	0.2	0.01

Kuin et al. [125], and Prentice et al. [210]. Our results are in very good agreement with results from various studies demonstrating the validity of the method implemented in the **Muphoten** pipeline. Even with data from highly heterogeneous instruments, our standardised method is able to produce self-consistent photometry datasets. In addition, **Muphoten** method can produce photometry consistent with external measurements of common images from the LT used in [204].

For the g -band in the last night IRiS detected the transient, the measurements show a large dispersion around ~ 18.5 mag, 32 days post detection. As these images passed our vetoes, this is neither a quality problem nor a calibration issue. Visual inspection of those images and the calibration fits do not reveal any issue. Consequently, we attribute this dispersion to the template subtraction at a time when the transient magnitude is close to the IRiS limiting magnitude. The faintness makes the measurements more sensitive to small variations in subtraction among images of the same night. The B -band in blue circles in Figure 3.13 comes from Kuin et al. and is based on Swift satellite observations. For these measurements, the galaxy flux was estimated in an image acquired 120 post-detection, then subtracted in the other frames. This process likely caused a host contamination as the measurements lie above the other lightcurves.

Based on **Muphoten** results, we also derived some basic properties of the Cow that we summarised in Table 3.5. We interpolated the results with splines shown in cyan for both lightcurves in Figure 3.13. We computed the decline in magnitude between the peak and 15 days after in both g bands and found $\Delta m \approx 3.5 \pm 0.5$ mag. We derived the interpolations to obtain decay rates in the B and g bands. The results are presented in Figure 3.14. They show a steep decay rate for ~ 30 days, followed by stabilisation to a $0.10 \text{ mag day}^{-1}$ rate. These two results are in agreement with those found by [210]. In particular, the decay rate for the blue bands was very rapid, between 0.2 mag day^{-1} and 0.4 mag day^{-1} during the first week. Moreover, the interpolations give a delay of $\sim 3 \pm 0.5$ days in both bands for the luminosity to decay to half its peak value, in agreement with [204].

We computed the colour evolution of the Cow ($B - g$) in the right-hand-side plot of Figure 3.14, with interpolations of both light curves. During the 40 first days, the colour

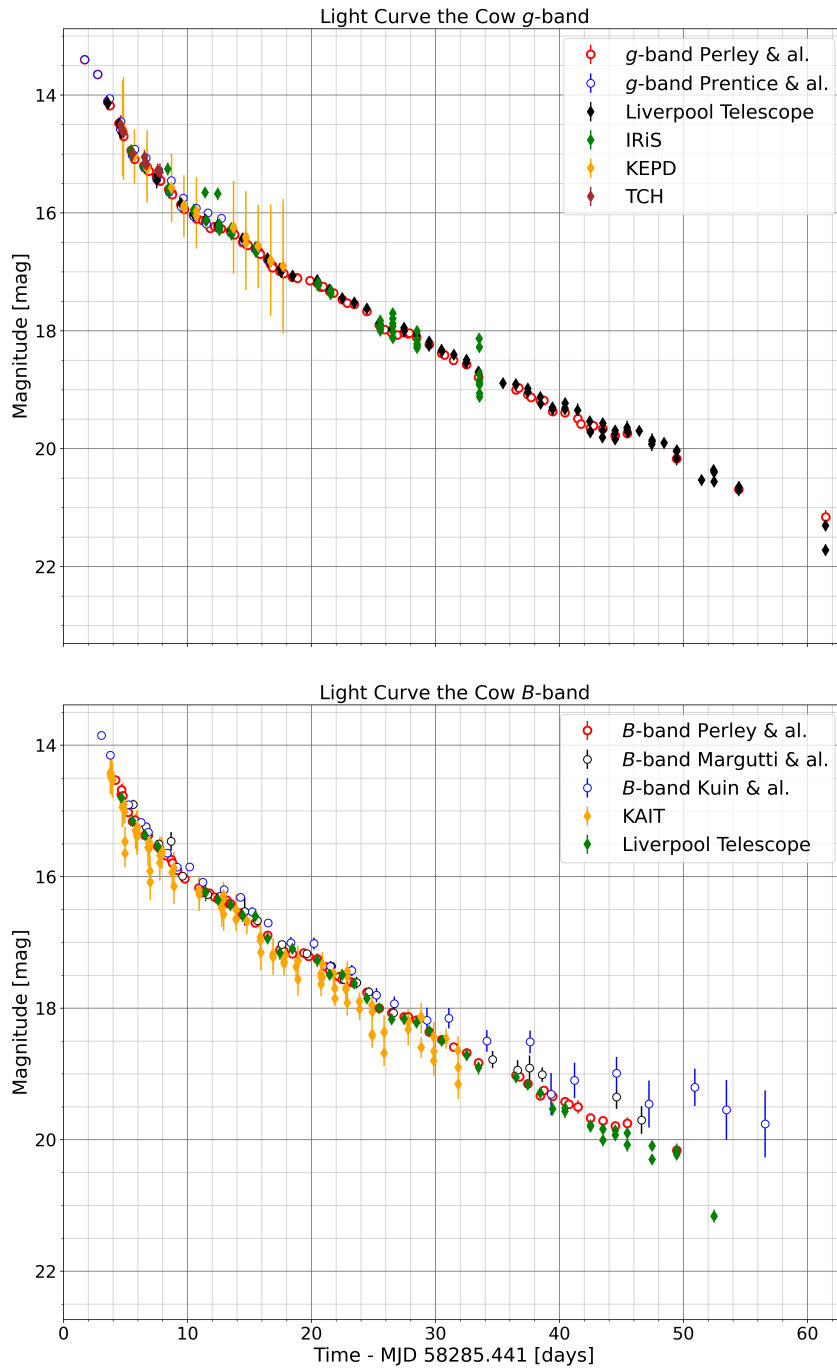


Figure 3.13: Lightcurves for the Cow in the g (top) and B bands (bottom) in the AB system. The circles are the points extracted from the literature about the Cow (Perley et al. [204], Margutti et al. [166], Kuin et al. [125], and Prentice et al. [210]). The diamonds are from this work.

Table 3.5: Temporal properties of the Cow derived with the data produced by **Muphoten**. All the values are consistent with the published literature about this transient.

Δm_g	3.5 ± 0.5 mag	Decline after 15 days rate for the g-band
Δm_B	3.5 ± 0.5 mag	Decline after 15 days rate for the B-band
T	30 days	Time for the decay rate to stabilize for both bands
τ_f	0.10 mag day ⁻¹	Final decay rate
τ_{1w}	$0.2-0.4$ mag day ⁻¹	Decay rates during the first week
$T_{1/2}$	3 ± 0.5 days	Time to reach half the peak luminosity in both bands
T_{RH}	18 ± 2 days	Time at which occurs the re-heating of the Cow

index decreases, except for two peaks at $\sim 18 \pm 2$ days and $\sim 31 \pm 2$ days. The peak at 18 days indicates an increase in the Cow’s temperature, consistent with the behaviour described in [204]. After 45 days, the increase is likely due to a lack of data in the B-band.

To understand its nature, we compared the Cow lightcurves computed with **Muphoten** analysis with other optical transients. The Figure 3.15 plots the Cow *g* light curve and different known typical events: The kilonova AT2017gfo [253], supernova templates of type Ia, Ibc, IIL and IIP (from Nugent templates⁶[197]) and a model of a short gamma-ray burst from [116]. The kilonova light curve is six magnitudes fainter than the Cow, and its decay is too fast compared to the Cow to be the observed transient. The short gamma burst model is too bright by five magnitudes, and the decay is too slow compared to the Cow. During the first ten days, the decay of the Cow is higher than 0.17 mag/day, which is not compatible with the ~ 0.1 mag/day rate observed for Nickel to Cobalt-based supernova (see [51]), with a half-life of 6.1 days. This lack of radioactive Nickel is consistent with what is currently known for the FBOT [176], whose SN2018cow is the epitome. Beyond ten days, supernovae luminosity decay rates decrease to ~ 0.01 mag/day (Cobalt to Iron), although the Cow maintains a decay rate higher than 0.1 mag/day. These comparisons show how singular the Cow is compared to typical cataclysmic events and must be considered an outlier among supernovae.

3.3.6 Conclusion on Muphoten

This section presented **Muphoten**, one of the GRANDMA photometry pipelines. **Muphoten** aims to produce homogeneous photometric datasets. We used images of SN2018cow from three GRANDMA and two external instruments to test our algorithm. The results demonstrate that **Muphoten** is able to retrieve results produced by other teams with the same set of images. In addition, the photometric measurements from GRANDMA instruments show that **Muphoten** returns homogeneous measurements. Based on this photometry, we can also derive some physical properties, summarised in Table 3.5, consistent with the literature. We concluded that the GRANDMA collabora-

⁶https://c3.lbl.gov/nugent/nugent_templates.html

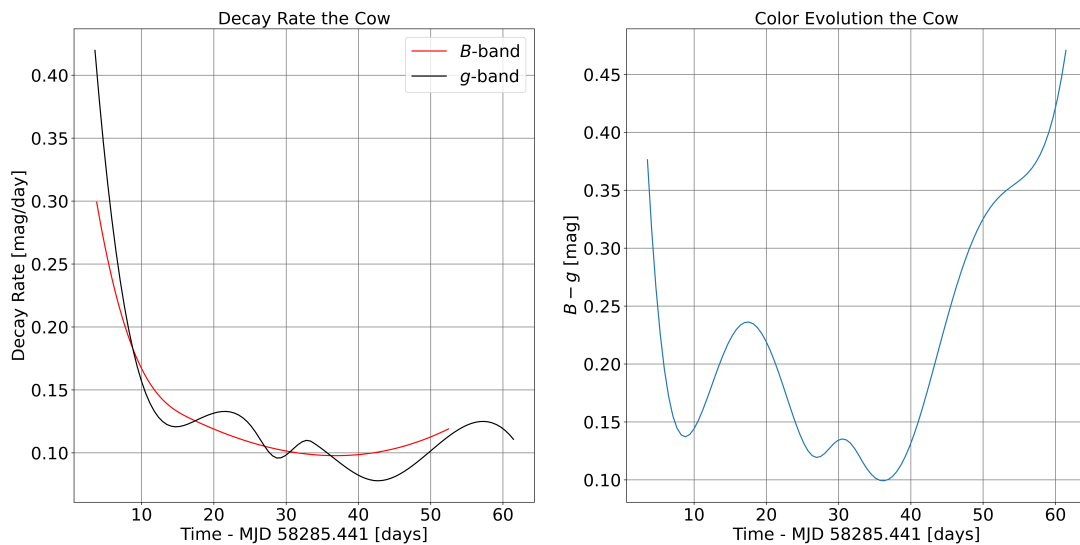


Figure 3.14: Left plot shows the decay rate of the B and g light curves only based on *Muphoten* results. The decay rates are between 0.25 and 0.05 mag day $^{-1}$, and compatible with values [210]. The right-hand side figure shows the color index $B - g$ evolution of the Cow.

tion’s results with *Muphoten* are confidently usable to characterise followed-up transients. Furthermore, some follow-up conditions of the Cow (the presence of a host galaxy, a blue rapidly evolving transient, large follow-up campaigns by many different telescopes) were close to what we expect for GW EM counterparts.

3.4 GRANDMA during O3

3.4.1 O3 overview

The O3 run of LIGO and Virgo took place between April 2019 and March 2020, and GRANDMA performed a massive follow-up of the GW alerts. Collaboration members participating in the campaign had to do monitoring shifts once a month. The sifter’s role was to monitor GW alerts and external collaborations reports, contact the telescope teams when a GW alert was received and report the results of the observations.

The run policy was to observe any possible alert, resulting in a 90% rate of follow-up for GRANDMA (49/56 alerts). The reaction time between the GW alert and the first images acquired was less than thirty minutes for 15% of the alerts and did not exceed 90 minutes for half of the alerts. The delay included the reception of the alert (~ 5 min) and its digestion by ICARE to compute the observation plan and its distribution (~ 5 min). These performances were possible thanks to the TAROT [196] and FRAM [1, 113, 211] networks composed of large FoV, robotic instruments with an automatic scheduler able to read the *gwemopt* plans. Moreover, the worldwide coverage of GRANDMA

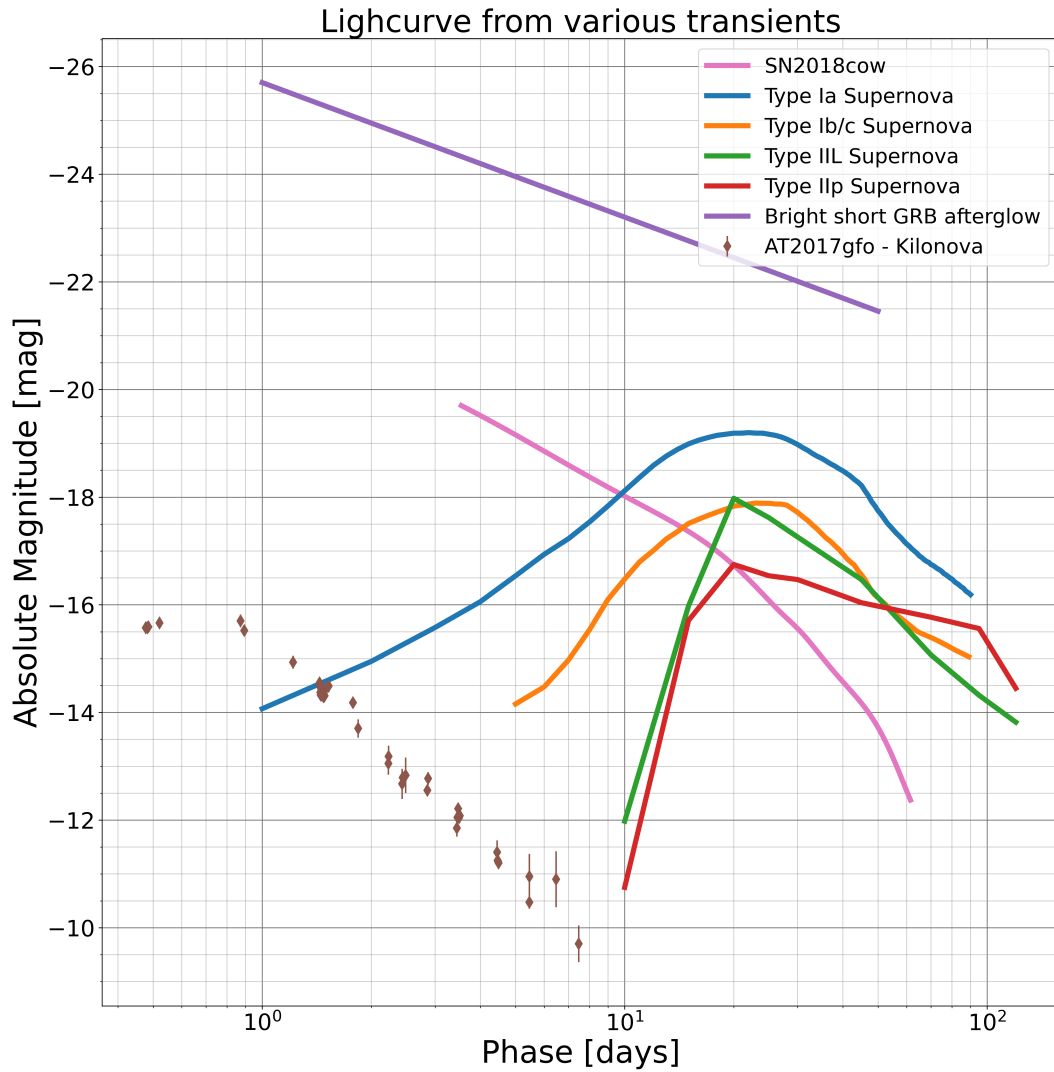


Figure 3.15: Comparison of the g -band lightcurve of AT2018cow with know archetypal transients. We used different types of supernova template lightcurves from P. Nugent, the AT2017gfo[253] and a bright short gamma-ray burst afterglow model taken from [116]. For the Cow lightcurve, we used the interpolation from Figure 3.13

allowed to always have facilities in a nighttime zone to perform observations. These results demonstrated GRANDMA's ability to have quick observations based on its coordination, addressing the timing constraint imposed by kilonova follow-up.

Concerning the sky coverage, over the whole run, GRANDMA observed 9000 deg^2 with an average $\sim 200 \text{ deg}^2$ per alert. Half of the alerts had more than 100 deg^2 covered by observations. Figure 3.16 summarises all the O3 observations based on the tiling technique. These results show that GRANDMA can handle the GW's large localisation uncertainties. Although, they also demonstrate the crucial importance of correctly estimated sky-localisation. In particular, we have seen in the previous chapter the effect of the ξ parameter that helps to have consistent localisation. However, the mean coverage of GRANDMA is also comparable to the difference of median between values of ξ around 0.83 - see Figure 2.20. This is another strong argument in favour of tuning this parameter before the next run and the others.

At the end of O3, no counterpart to any alert has been identified, neither by GRANDMA nor by other groups performing similar follow-ups. However, two GW candidates followed by GRANDMA instruments are particularly interesting: S200213t and S191213g. The following two sections are dedicated to the description of the related observations. Nevertheless, at that point, *Muphoten* was not entirely developed yet, and no centralised data reduction was available, even though some images were analysed with a primitive version.

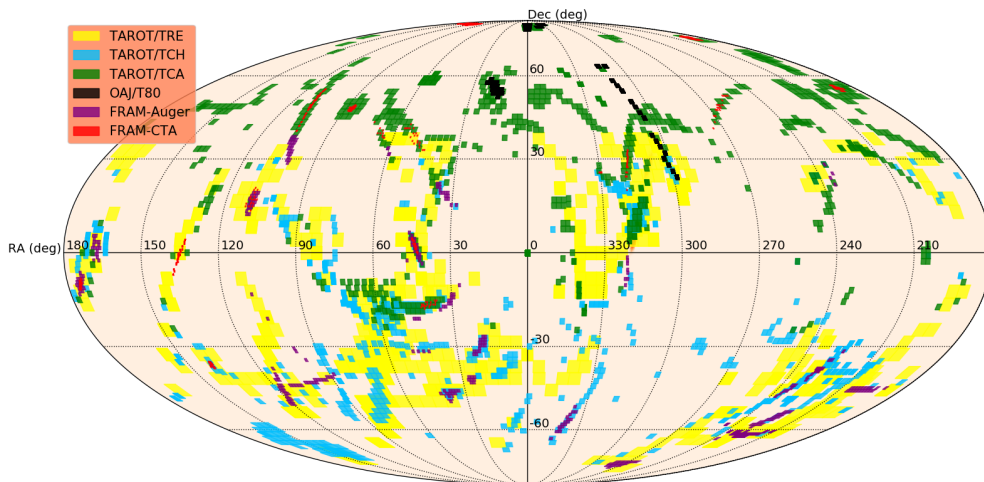


Figure 3.16: Summary of sky coverage by GRANDMA during the O3 run. The focus is on large FoV instruments: TAROT, FRAM networks and the OAJ-T80 telescope. The galaxy observations based on MANGROVE ranking are not shown here, but they also represent a significant part of the observations. This figure is extracted from [14].

3.4.2 Follow-up of S200213t

Among the 49 alerts followed by GRANDMA, S200213t was a weak BNS candidate detected by the GstLAL online search [146, 151]. However, it is not in the final list of the O3 GWTC-3 events, according to Table VII in [151], for it finally does not meet the false alarm rate threshold imposed by the LIGO-Virgo collaborations, even though the alert was never retracted. It was distributed as a BNS alert with a 90% credible region (CR) of 2587 deg^2 and a most probable luminosity distance of 240 Mpc according to the **Bayestar** algorithm. Later, a refined estimation revised the luminosity distance to 201 Mpc, and 2326 deg^2 for the 90% credible region [147].

Six of the GRANDMA large FoV instruments performed tiling observations: the three TAROT telescopes, the two FRAM and OAJ-T80. The first images were acquired by TAROT-Calern (TCA) 26 minutes after the alert. The others started observing $\sim 15\text{h}$ after the GW alert. Overall, GRANDMA instruments covered 33% of the revised CR. Along with the tiled coverage, three GRANDMA instruments - UBAI-T60S, UBAI-T60N and VIRT - observed galaxies that MANGROVE ranked. The frames were acquired in the R_c -band with a limiting magnitude of 17 mag ~ 6 days post-trigger. Moreover, several amateur astronomers participating in GRANDMA's citizen branch, **Kilonova-Catcher**, described in Section 3.5.2, observed 29 galaxies for this alert. All the observations are shown in Figure 3.17 with coloured squares for the TAROT, FRAM and OAJ tiled observations and coloured stars for the galaxies observed by UBAI instruments, VIRT and the **Kilonova-Catcher** amateurs. According to the analysis performed on OAJ images with **gmadet**, [14], no strong candidates were found within GRANDMA images.

Although no counterpart was discovered for S200213t, the early and deep observations allow us to evaluate the putative merging source parameters. Under the hypothesis that TAROT (30% of the CR covered) or OAJ (18% of the CR) observed the source position, it is possible to constrain the ejecta mass and velocity along with its lanthanide fraction. The OAJ telescope observed in the r' -band for down to 20.1 mag, and TAROT observed in the R_c -band down to 18 mag. The kilonova red color is dependent on the lanthanide fraction X_{lan} in the ejecta. Consequently, with red filters R_c and r' , we can evaluate X_{lan} . We analysed the ejecta properties (v_{ej} , M_{ej} and X_{lan}) using the non-detection of kilonovae in our observations and the known distance of the event. To do this, we employed a Bayesian toy model described in [63]. However, we are not able to set upper limits on the ejecta mass, even for cases largely disfavoured by BNS numerical simulations [77] where the ejecta mass is $\sim 0.4M_\odot$ (compared to the $0.05 M_\odot$ estimated for GW170817).

These non-constraining results were attributed to a luminosity distance five times larger than GW170817, reducing the flux by ~ 25 . Consequently, an AT2017gfo-like transient would have had a peak magnitude ~ 21 mag in the r -band. These results are summarised in Figure 3.18, where the 90% upper limits on the ejecta mass are materialised with horizontal dashed lines. They are likely prior-dominated, indicating non-constraining observations.

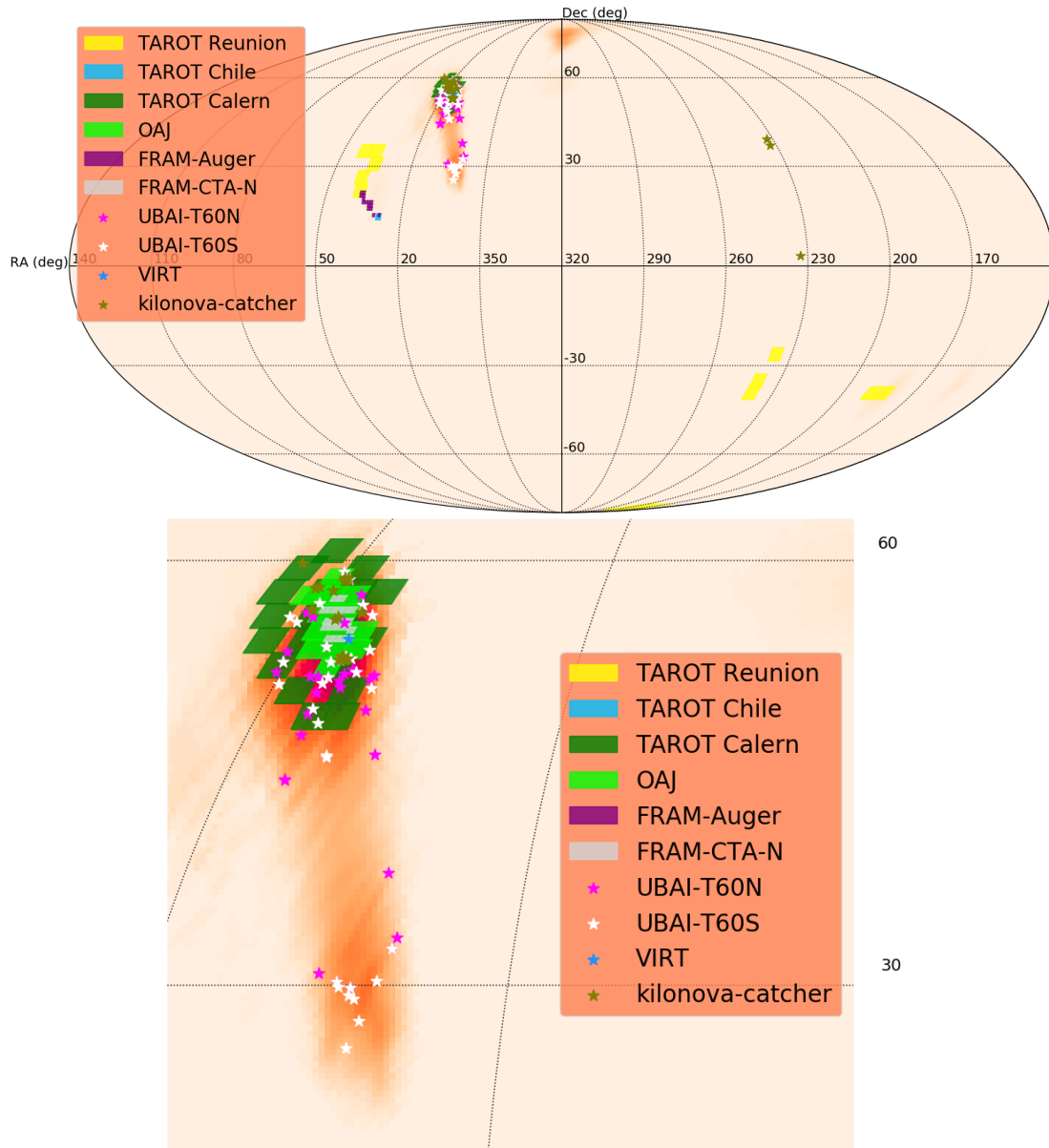


Figure 3.17: Summary of the observations of S200213tBNS by the GRANDMA network. The coloured square are the tile of the large FoV instruments : TAROT-Réunion (TRE), TAROT-Chili (TCH), TCH, FRAM-CTA and FRAM-Auger. The stars represent small FoV instruments observations of host galaxies candidates identified by MANGROVE. The upper plot shows all the observations performed by the network. The bottom plot shows a zoomed-in region of the sky representative of the network observation for this alert. This figure is extracted from [14]

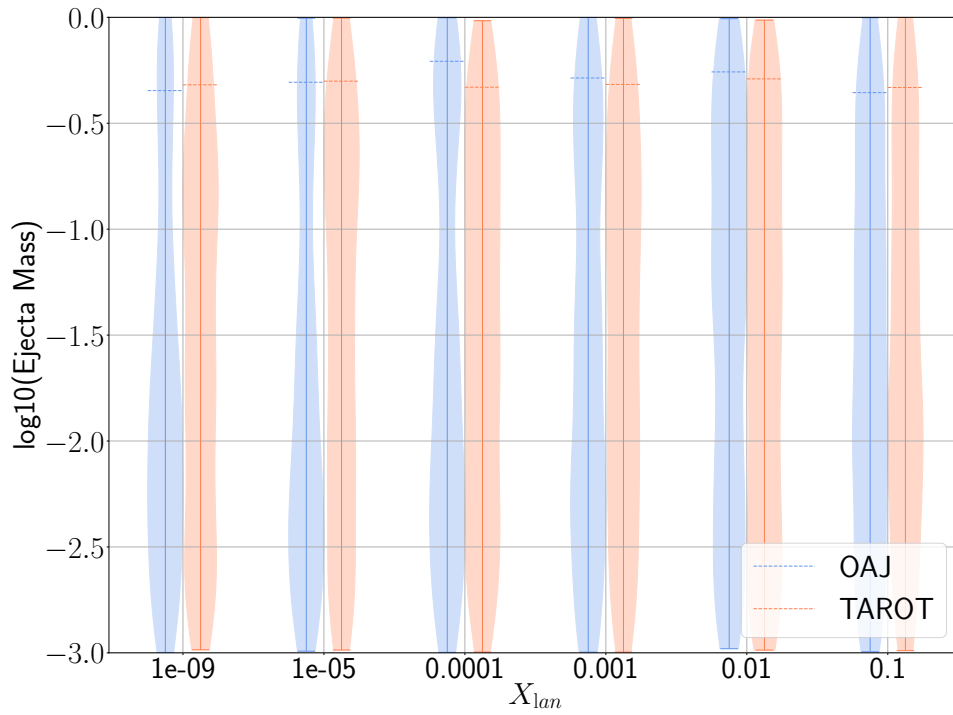


Figure 3.18: Constraints on the lanthanide fraction X_{lan} of the BNS alert S200213t. The thickness of the vertical bands represents the posterior distribution - the thicker, the more probable the ejecta mass is for a given region of the parameter space. Horizontal dashed lines represent the 90% upper limit on the ejecta mass. This figure is extracted from [14]

3.4.3 Follow-up of SN2019wxt

The weak GW candidate S191213g was detected on 2019-12-13 at 04:36:53 (UTC) as the first O3b potential BNS event [143, 144]. Offline analysis by LIGO-Virgo resulted in its absence in the final GWTC-3 catalogue for a similar reason as S200213t [151]. Nevertheless, at the time of its detection, this alert has been vastly follow-up by various groups, including GRANDMA. Seventeen instruments of the collaboration received observation plans. However, S191213g was detected at the end of the Western European night, with observations limited to the Northern hemisphere instruments, which limited the opportunities for early observations by GRANDMA. FRAM-CTA started observation 53 minutes after the alert in the R_c band. Overall, only 3% of the initial *Bayestar* sky localisation was covered by tiling observations. In addition, some galaxies were also observed by Kilonova-Catcher program participants. They observed 16 galaxies down to 17-18 mag without filter to maximise the chances of detection. No candidate counterparts were found within GRANDMA data.

On 2019-12-18, the Pan-STARRS survey detected a candidate counterpart PS19hgw - later named SN2019wxt - located in the galaxy KUG 0152+311 at a distance of 144 Mpc [168]. Initially, both the localisation and the blue-featureless spectrum of the transient made it a credible counterpart candidate. Eventually, a VLT-X-Shooter spectrum showing Helium emission lines classified it as a type Ib supernova, ruling out PS19hgw as a kilonova candidate [254]. Eventually, the LBT instruments later refined this classification to a type IIb supernova [250].

GRANDMA also observed this candidate, and we decided to give some details about it to demonstrate the network capabilities for candidate counterpart characterisation. The Lisnyky/AZT-8 instrument did the first observations in GRANDMA without detecting SN2019wxt down to 19 mag in the R_c -band. Along with AZT-8, The Tingshua-NAOC Telescope (TNT), the 2.16m telescope located in Xinglong and the Thai National Telescope observed it in the B , V , u' , g' , r' , i' and z' bands. Only the two last facilities detected the transient using their own photometry method. Moreover, one Kilonova-Catcher participant detected SN2019wxt in a Luminance filter with a magnitude of 18.80 ± 0.23 mag. This image was reduced with an early version of *Muphoten* using a template image for subtraction taken by the same instrument that took the first frame. Some observations from GRANDMA and other groups, whose data were collected in GCN, are gathered in Figure 3.19.

We compared these lightcurves to pre-computed kilonova lightcurves modelled with a full radiative-transfer Monte-Carlo algorithm, see [14] and references therein. Based on the host distance, this analysis returns a $0.1M_{\odot}$ ejecta mass, which is too large for a kilonova. Moreover, a two components-like model cannot reproduce u' and g' bands excesses observed for SN2019wxt. These two arguments disfavour the kilonova hypothesis, which is consistent with the final classification by the LBT instruments. However, our timely observations showed that SN2019wxt can originate from the explosion of a binary star.

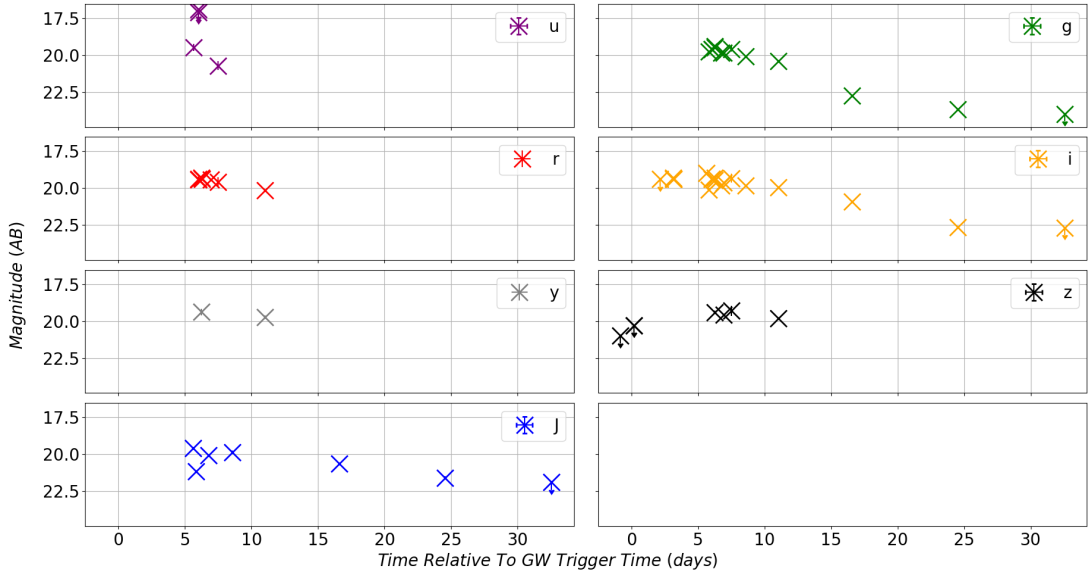


Figure 3.19: Light curves of SN 2019wxt for the seven bands used compared to kilonovae models. The start time T_0 corresponds to the GW trigger time 2019-12-13 04:33:36.000 UTC. This figure is extracted from [14]

3.5 Preparing O4 (I) : ZTF/Fink campaign

3.5.1 Motivation

The GRANDMA observational campaign during O3 is considered a success demonstrating the network’s ability to address the GW follow-up challenges. However, the run lacks convincing optical candidates to follow, and only SN2019wxt was observed by GRANDMA instruments, as we presented in Section 3.4.3. Consequently, the next data acquisition run of LIGO and Virgo requires training and experience on the optical side to maximise the chances of counterpart detection. On the other hand, the last years have seen the apparition of optical-NIR surveys, and they can be used as a powerful tool to detect more kilonova, either via GW triggers or by themselves. This include Pan-STARRS [48], ATLAS [241], GOTO [230] and ZTF [167]. The Vera C. Rubin Observatory’s Legacy Survey of Space and Time (LSST) will see its first light in a year from now [111]. Its cadence, depth and large FoV will allow for serendipitous kilonova discoveries. However, all those facilities work as surveys and transients characterisation can highly depend on their cadence. It causes a coarse lightcurve sampling, which is problematic for kilonova considering their fast decay. However, simulations demonstrated that developing a GW triggers target of opportunities (ToO) program for LSST would not significantly impact the survey and would raise the chances of kilonova detection [66]. Consequently, networks such as GRANDMA can play an essential role in kilonova identification and follow-up. Their observations allow for a more rapid classification, even without spectroscopic data and fill cadenced survey lightcurves gaps, resulting in finely sampled, constraining data.

These observations led to the organisation of a GRANDMA follow-up campaign of ZTF alerts selected with the FINK broker [185]. The objectives of this campaign are:

- Test the characterisation/follow-up mode of GRANDMA
- Improve coordination between instruments
- Test the capabilities of the amateur segment Kilonova-Catcher
- Find photometric criteria to classify transient nature
- Refine, test and characterise GRANDMA photometry pipelines: `Muphoten` and `STDpipe`, which described in Section 3.5.4

We chose to follow alerts provided by the ZTF survey for several reasons. First, it was involved in O3 follow-up and will be involved in O4 with important tiling capabilities thanks to its 47 deg^2 FoV. Consequently, it provides a lot of EM counterpart candidates that GRANDMA could help characterise and classify. Second, ZTF is a prototype for LSST that is expected to release ten million alerts per night whose classification and distribution will be done via brokers, including FINK, an official LSST broker. These brokers must be tuned and adapted by the users for selecting the relevant alerts. Consequently, this campaign is an opportunity for both FINK and GRANDMA to train finding kilonova candidates in optical surveys data. Tuning it to improve the kilonova classification will eventually benefit the astronomer communities when LSST is ready and for the O4 run.

This campaign is called `Ready for O4` [7], and lasted for six months, between 21 May 2021 and 21 September 2021.

3.5.2 The Kilonova-Catcher initiative

The `ReadyforO4` campaign heavily involved the citizen science program of GRANDMA called *Kilonova-Catcher* (KNC). This program was created in 2019 to take advantage of the vast amateur astronomer observing capabilities. They have an almost unlimited observing time, giving a great capability for GW alert coverage and transient characterisation. This program was also used during O3 to perform galaxy targeting observations, as detailed in section 3.4.1. No tiling was done due to the usual small FoV of amateur instruments. KNC uses a web portal⁷ for participant registration, alert distribution and image storage. The amateur network is illustrated in Figure 3.20 and currently gathers 77 instruments worldwide, although most are in Europe. A typical KNC instrument has a limiting magnitude of ~ 18 mag, and some can reach ~ 20 mag with long exposure images.

⁷<http://kilonovacatcher.in2p3.fr/> supported by the University of Paris and IJCLab

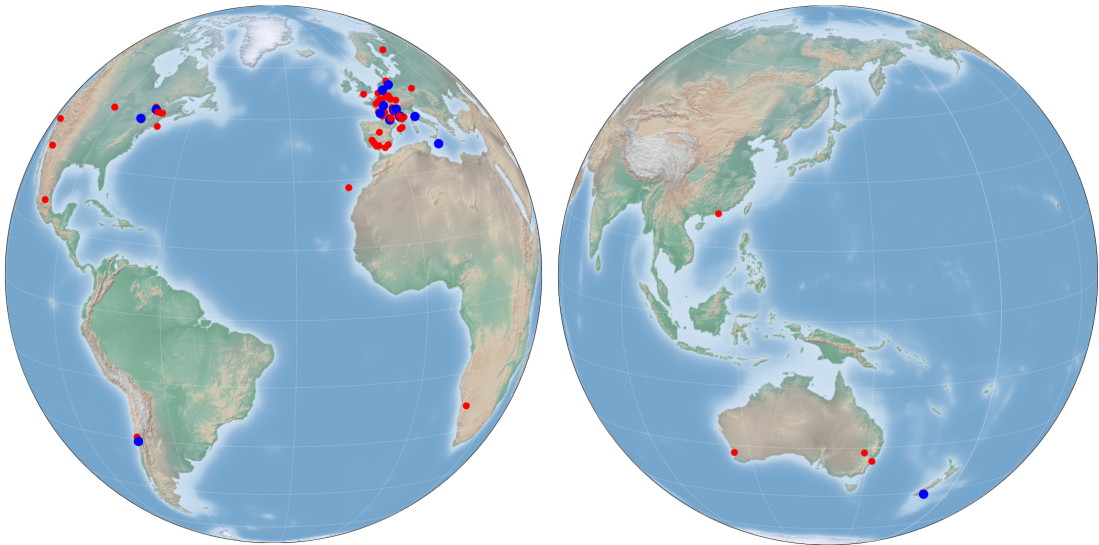


Figure 3.20: Locations of the 77 telescopes involved in the GRANDMA citizen science program *Kilonova-Catcher*. The blue dots represent the telescopes that participate in ReadyforO4. The red dots represent the rest of the network. This figure is extracted from [7].

3.5.3 FINK and the alert selection

FINK [185] is a community broker dealing with large alert streams for time-domain astronomy. It is designed for the incoming LSST and its ten million alerts per night and developed with the ZTF survey. It is community-developed and driven by numerous topics in transient sky physics, from solar system science to extra-galactic violent events. Currently, FINK listens and collects the data stream produced by the ZTF image reduction pipelines. An alert contains basic information: transient magnitude, sky positions, the timing of the detection and the information from the previous 30 days in case of prior observations. Between 21 May 2021 and 21 September 2021, FINK dealt with 35,387,098 alerts that were sent through three quality filters:

- Machine-learning-based cut removing image subtraction artefacts - we kept alerts with a RealBogus score superior to 0.55
- No bad pixels flagged in a 5×5 pixels cutout around the transient
- Difference between aperture magnitude and PSF magnitude less than 0.1 mag.

These filters removed $\sim 70\%$ of the alerts of the campaign, and the science modules of FINK processed the remaining ones. The broker had enough information to classify half of the alerts. Most were crossmatched with the SIMBAD database or corresponded to objects identified in the Minor Planet Center. The remaining alerts were associated with

Solar System Object (SSO), supernova, microlensing candidates, and alerts associated with several labels - called ambiguous alerts.

The filters are designed to be strict enough to avoid having tens of thousands of candidates, considering the alert flux, and select the most promising kilonova candidate. On the other hand, they are agnostic enough to explore the parameter space as we lacked constraining kilonova observations. The three filters we use are:

- KN-LC: A machine-learning-based filter that yielded 107 alerts during the period
- KN-Mangrove: A nearby galaxy criteria that yielded 68 alerts during the period
- KN-Slope: A luminosity decay rate that yielded 108 alerts - although this cut was not used during the campaign.

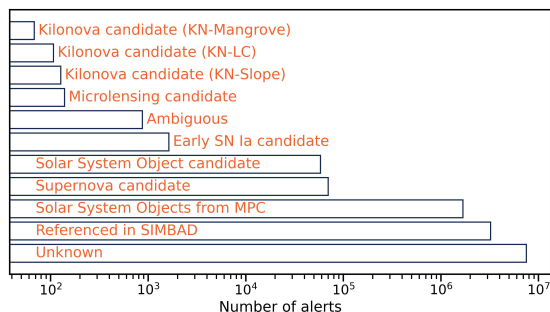


Figure 3.21: Summary of the alerts for ZTF filtered out by FINK. The broker could not conclude based on the available information for almost half of the alerts (Unknown label). Most of the remaining alerts are objects with a counterpart in the SIMBAD database (match within a 1.5 arc-seconds radius) and alerts associated with a known object from the Minor Planet Center database referencing moving objects from the Solar System). Other alerts are divided among supernova events, Solar System Object candidates, microlensing candidate events, or have an ambiguous classification - i.e. more than one label at a time. Concerning KN candidates, we report here the candidates from the three filters we implemented. This figure is extracted from [7].

KN-LC

As kilonova lightcurves are unusual compared to the usual optical transient, particularly in terms of color evolution, we used a filter based on a machine learning classification of the ZTF alerts. The lightcurves of the transient in the g' and r' bands were deconstructed in principal components to infer the kilonova nature probability. The number of components extracted was a trade-off between classification accuracy and the amount of time required to reach a classification - i.e. the more components, the more ZTF measurements were required. At the beginning of the campaign, we used the only first component, and after some time, we used two of them. This change allowed to reduce the

number of false-positive from 28 alerts per month at first to only ten alerts per month. The features extracted from the lightcurves were compared to kilonova models to assess the transient nature with a random forest classifier. However, this approach relied heavily on the models used to train the classifier, which may be biased, considering the poorly constrained kilonova diversity.

The ZTF online data analysis included a neural network-based classifier to automatically reject template subtraction artefacts or bogus [80]. Objects in the difference image were assigned a score by the network and rejected if it was lower than a 0.5 threshold.

- The score from the KN binary random forest classifier must be above 0.5.
- point-like object: the star/galaxy extractor score provided by ZTF must be above 0.4.
- Non-artifact: the deep real/bogus score provided by ZTF must be above 0.5.
- Object not referenced in the SIMBAD database (except extra-galactic origin).
- Young detection: less than 20 days. This threshold is loose but sufficient to filter long-trend or well-known objects.

This cut selected 107 alerts among the 12,556,539 processed during the six months of the campaign, corresponding to 70 unique objects on the sky. FINK eventually classified most of them as supernova after ZTF collected more data, even though some remained classified as kilonovae. When using only one component for the classification, a crossmatch with the Transient Name Server (TNS) that gathers information from various external facilities yielded most of the candidates as Type Ia candidates (41/71). After the classification changed, 29/36 of the candidates had no counterpart in the Transient Name Server as other observatories followed them.

KN-Mangrove

Although the KN-LC filter helped classify the alerts, the two days delay in concluding was too long for the kilonova timing constraints, as described in Section 3.1. An actual kilonova would have been far too faint to be observable. Consequently, we implemented a second filter to find early detection by associating a host galaxy to the transient, similar to the galaxy targeting technique used for GW follow-up. Then, the presumed host known luminosity distance was used to compute the transient absolute magnitude. Eventually, we checked that the luminosity was compatible with kilonova models. The filter works with the following criteria:

- point-like object: the star/galaxy extractor score must be above 0.4.
- Non-artifact: the deep real/bogus score must be above 0.5.
- Object not referenced in the SIMBAD database (except extra-galactic origin).

- Young detection: less than 6 hours.
- Galaxy association: the alert should be within 10 kpc of a galaxy from the MANGROVE catalogue. The 10 kpc offset was empirical and based on a discussion in [27]). We also tested different values: above a 10 kpc threshold, there were too many contaminants alerts, and below it, we would potentially have missed valid transients.
- Absolute magnitude: the absolute magnitude of the alert should be -16 ± 1 mag (in both g' and r' bands), based on the AT2017gfo kilonova.
- Non-Solar System Object: the alert must be at least 5 arcseconds away from any known Solar System objects referenced in the Minor Planet Center database at the time of emission.

The host association was done with MANGROVE galaxies up to 230 Mpc distance, for it was the current BNS detection range of the LIGO-Virgo network.

Out of the 68 alerts filtered out with this cut during the six months of the campaign, 59 corresponded to unique objects on the sky. Based on these criteria, most remained classified as kilonovae, although some were confirmed with the Transient Name Server as supernovae or solar system object candidates. Overall, we found 51/68 alerts without a counterpart (i.e., no follow-up results were reported), 7/68 confirmed as supernova type Ia, 4/68 as supernova type II, 3/68 as supernova type IIp, 1/68 as supernova type IIb, 1/68 as supernova type Ib, and 1/68 as supernova type Ic.

3.5.4 Readyfor04 overview

The Readyfor04 campaign took place between 21 May 2021 and 21 September 2021. We followed 12 ZTF alerts at a rate of one alert per week. Six of them were selected via the FINK filters, and the six remaining were chosen as early supernovae for practice. We sent the alert only to amateur astronomers during the campaign's first half. We invited them to observe for 72h to evaluate the response time of the community, the number of observers and the image quality. In addition, starting in July 2021, the professional GRANDMA observers joined the campaign to increase the data sample size for pipeline development purposes.

At first, we used the network in *classification mode* by observing the alerts to confirm the detection and improve the FINK classification based on the added photometric points. Then, we used a *monitoring mode* by following confirmed sources with as many bands as possible to have a fine understanding of the flux evolution. In total, we achieved participation by 26 amateurs and 11 different GRANDMA telescopes. The various filters used by professional and amateur observers are summarised in Figure 3.22. They gathered usual standard filters from the Johnson-Cousins and the Sloan systems, along with unfiltered images and non-standard filters from specific amateur setups.

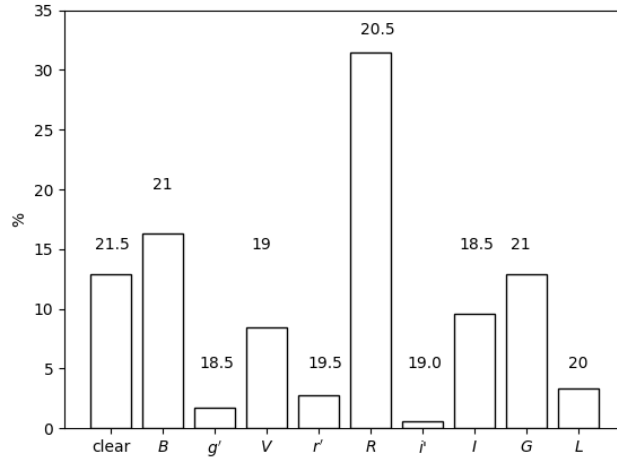


Figure 3.22: Filters used in the images taken during this observational campaign and when a source is detected. Above are mentioned the fainter upper limits reached during the campaign. The G -band here is not the usual g' Sloan band but a similar one used by one of the amateurs. We treated those G images as g' frames. The L -band corresponds to a broadband filter cutting NIR and near UV wavelengths, similar to an unfiltered image. This figure is extracted from [7].

Data Reduction

This campaign was also an opportunity to test the reduction processes. Consequently, `Muphoten` was used as an official pipeline of the GRANDMA collaboration with 37 telescopes, which was one order of magnitude larger than the six instruments used for the AT2018cow analysis. Although creating a consistent dataset for that number of instruments was challenging, it was a realistic test for a GW follow-up campaign. In addition to `Muphoten`, we also used another independent photometry pipeline called `STDPipe`. It allowed to search for potential systematic biases within the reduction process.

`STDPipe` [117] is a set of Python routines for astrometry, photometry and transient detection-related tasks. It is intended to quickly and easily implement custom pipelines and interactive data analysis. It is designed to operate on standard Python objects: NumPy arrays for images, Astropy Tables for catalogs and object lists, etc., and conveniently wraps external codes that do not have their own Python interfaces such as `SExtractor` [31], `Scamp` [28], `PSFex` [29], `HOTPANTS` [25] and `Astrometry.Net` [129]. It supports the following steps of processing and analysing the images:

- Object detection with `SExtractor` and simple PSF photometry using simple model from `PSFex` or aperture photometry with `SExtractor`.
- Astrometry with either `Astrometry.Net` for blind solution or `Scamp` for refining first solution.

- Photometric calibration using with any catalog available in Vizier - including photometric system transformation when relevant, see Section 3.3.2
- Image subtraction with HOTPANTS
- Transient detection based on noise model in the difference image
- Fake star injection for transient detection sensitivity estimation.
- Plotting routine for visualisation purpose.

Based on this, `STDPipe` starts by removing cosmic-rays with `astrocrappy` [170], an LA-Cosmic implementation [251], then detect the objects with `SExtractor` to perform aperture photometry. The aperture radius is equal to the median image FWHM. The background is locally estimated in an annulus between 5 and 7 FWHM units. The astrometric solution is found with the Astrometry.net solver applied to the list of detected objects. Pan-STARRS DR1 is used for both astrometric and photometric solutions. The latter is constructed using the closest filter for the PS filter set or Johnson-Cousins thanks to [123]. An instrumental colour term ($B - V$) or ($g_{PS} - r_{PS}$) is derived if the telescope is equipped with Sloan filters. The zero-point is either a constant value for all the stars if they are not too many or a second-order spatial polynomial if there are enough stars in the frame. The subtraction is done with `HOTPANTS` using a downloaded and mosaicked template from PS - similarly to what is done in `Muphoten` - in the closest filter. Forced aperture photometry at the transient position on the difference image and the magnitude is estimated with the calibration model previously estimated. The limiting magnitude is computed at the transient position by converting the background noise inside the aperture multiplied by 5 (so that it corresponds to 5σ), then to flux and then to magnitude. When the object is not detectable in the image, this value is adopted as an upper (detection) limit for its magnitude.

Converting the results of this analysis into a standard photometric system requires knowing the transient colour. This information is computed either by combining several simultaneous or quasi-simultaneous observations in different filters (and thus with different colour terms) and then regressing for the colour from them or using some external information. For this campaign, we interpolated the g' and r' bands of ZTF. Then, we estimated the transient colour at the image acquisition time. Then, we converted to $B - V$ or $g_{ps1} - r_{ps1}$, depending on the photometric system used to calibrate the frame.

On the `Muphoten` side, the data reduction was made following the description in Section 3.3. Although the template subtraction for both clear (i.e. image taken without any filter) and L -band see Figure 3.22 images was done with a PS template in the g_{PS} -band. Same for the B and V images. For R_c images, we subtracted r_{PS} template, and for I_C , we subtracted an i_{PS} template.

Consistency of the analysis

Having two independent analyses in the collaboration had the tasteful benefits of allowing the comparison of their respective results and finding systematic bias. As detailed above, **STDPipe** used an interpolation of ZTF lightcurves to estimate the transient colour, contrary to **Muphoten** that assumed that the colour of the transient was the same as the average colour of calibration stars used in the analysis. It constituted the principal difference between the algorithms and could have introduced a systematic colour-dependant bias in the photometric datasets. We tested this by comparing the pipelines magnitudes for all the images where the transient was detected. Eventually, we found that **Muphoten** and **STDPipe** were mostly consistent, as shown in the upper panel of Figure 3.23. The most important differences appeared for clear images (frames taken without filter) where the impact of atmospheric conditions or the instrumental photometric system are expected to be maximal. This effect is visible in the lower panel of Figure 3.23 where the clear images magnitude difference distribution is centred around ~ -0.5 mag.

Moreover, these images were treated differently between the two pipelines: in **Muphoten** a g -band image was subtracted contrary to **STDPipe** where it was a r -band image, in addition to the systematic different colour treatment. The B -band also had a significant systematic difference with a significant number of images in the $+0.5$ mag direction, according to the lower panel of Figure 3.23. This deviation was mostly due to one amateur telescope for which the B filter was not exactly the usual Johnson-Cousins B -band but a specific instrumental device that complicated the analysis. Overall, we may conclude that our pipelines had no significant bias.

3.5.5 Observation Summary

This section gives an overview of the observation we performed with both GRANDMA and Kilonova-Catcher networks. Figure 3.24 summarises the observations of the alerts followed by both professional and amateur astronomers. We gathered them by FINK filter that selected the alert. The upper limits given in this Section are estimated following the **Muphoten** method detailed in Section 3.3.4. Overall, **Muphoten** analysed 415 images, including the clear images, throughout the campaign. The transient being followed-up was detected in 153 images acquired with a filter, and the measurements by **Muphoten** and **STDPipe** were compatible for 150 of them. We did not include the unfiltered images in this count as they are treated in a significantly different way between the pipelines. Among the 415 images, only two were rejected by **Muphoten** vetoes. This rather low number is due to the fact that ~ 20 images were removed from the dataset, for it was impossible to launch the pipeline without having it crash due to data quality issues.

In order to constrain the transient nature, we used the **Muphoten** and **STDPipe** photometric measurements to measure the decay slope of the transient. It was done using the following procedure: we started by grouping the images with a 0.1 day precision. Then we applied a linear fit with a maximum likelihood estimation approach to estimate the slope between two different time bins. The slopes of the best fit, $a_r(t = n)$, were then computed using data taken with r or R filters in a given time bin. Here we took the de-

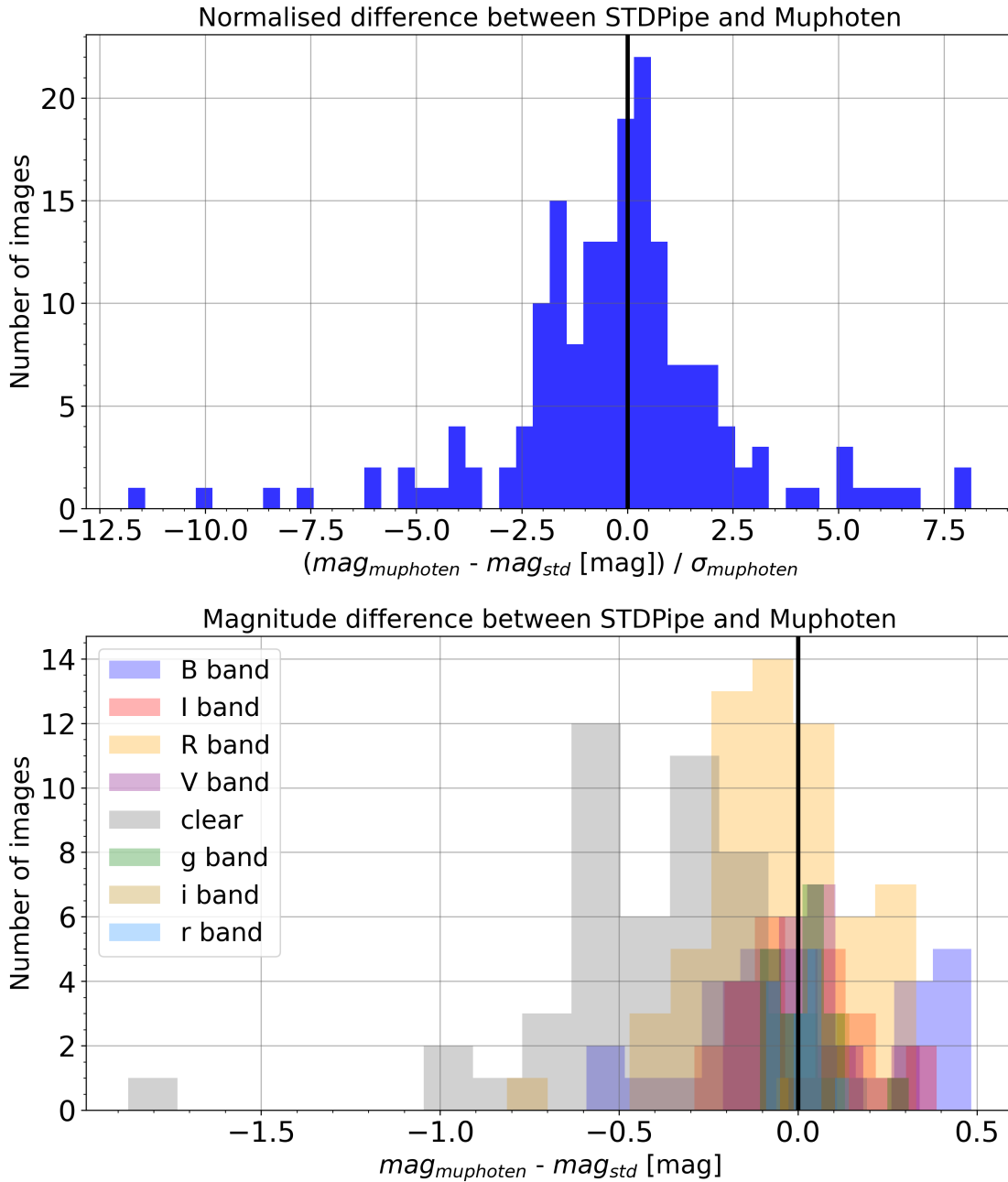


Figure 3.23: Comparison of the transient magnitudes estimated by two different pipelines. The upper panel shows the distribution of normalised differences, which is mostly consistent with the estimated error bars of individual measurements. The lower panel shows the absolute differences for individual photometric filters used. This figure is extracted from [7].

tection time as the first observation of the transient by ZTF, denoted T_0 . We computed three slopes as in [7]:

1. $a_{\text{STD},r}(t = n)$, the temporal slope of the transient light curve between the first detection by ZTF at T_0 and the time at which GRANDMA detected it by using `STDPipe`.
2. $a_{\text{MU},r}(t = n)$, the temporal slope of the transient light curve between the first detection by ZTF at T_0 and the time at which GRANDMA detected it by using `Muphoten`.
3. $a_{\text{ZTF},r}(t = n)$, the temporal slope of the transient light curve between the first detection by ZTF at T_0 and the next detections by ZTF.

KN-Mangrove alerts

- ZTF21abdwdwo: observed by eleven amateur telescopes for a total of 42 images taken between 0.7 days to 60 days after public detection (021-06-04 04:27:26 UTC). No GRANDMA or Kilonova-Catcher instruments detected the transient. We found a median upper limit of 17.9 ± 0.8 mag in the r' and R_c bands. A KNC instrument - T-CAT - acquired the deepest images 3.7 days post-trigger in the B and G bands down to ~ 21 mag. The GRANDMA telescope VIRT took the latest image with an upper limit of $R_c = 17.5$ mag. We concluded for this alert that the transient was a miss association of a Solar System Object to a MANGROVE galaxy in the background induced by the process described in Section 3.5.3.
- ZTF21abfbmbix - later renamed SN2021pkz, associated with the galaxy 2MASS-12551554253477 at 38 Mpc. It was observed by 13 different amateur telescopes and FRAM-Auger, for a total of 29 images taken between 0.7 and 50.8 days after T_0 (2021-06-11 05:14:49). Two days before detection, ZTF did not detect the source due to $g' > 20.5$. We detected the transient in 25/29 images taken in 6 distinct filters between 0.7 and 29.7 days post-trigger. 17/25 measurements were compatible for the two pipelines. From these measurements, we found a luminosity rising in the r' -band with : $a_{\text{STD},r}(t = 0.7) = -0.7 \pm 0.2$ mag/day and $a_{\text{MU},r}(t = 0.7) = -0.9 \pm 0.2$ mag/day. With later measurements, we found for $t = 1.7$: -0.5 ± 0.1 and -0.7 ± 0.1 mag/day for `STDPipe` and `Muphoten` respectively. This was compatible with public data from ZTF at $t = 2.0$ days $a_{\text{ZTF},r} = -0.5 \pm 0.1$ mag/day. This example demonstrated the benefit of early measurements during the rising phase of the transient, which is useful to guide the decision on spectroscopy observations before night-time on the American continent. Indeed, a two days long rising phase is not expected for a typical kilonova. The final classification of the source was a supernova Ia according to an independent spectroscopic measurement by the ZTF Spectral Energy Distribution Machine (SEDM).
- ZTF21abultbr was observed by three amateur telescopes and by the Abastumani-T70. It yields a total of 8 images between 0.6 day and 2.5 days post-trigger - $T_0 =$

2021-08-21 02:44:39.100 UTC. FINK KN-Mangrove filter associated the source to a galaxy at 89 Mpc HyperLEDA/UGC04104. We detected the source with both pipelines in 3 images in the R and G bands (here G is not the usual Sloan g' filter - see Figure 3.22) from two distinct telescopes. The measurements from both algorithms were consistent except for clear images. We found the following slopes at $t = 0.6$ day: $a_{\text{STD},r}(t = 0.6) = -0.3 \pm 0.4$ mag/day and $a_{\text{MU},r}(t = 0.6) = -0.0 \pm 0.4$ mag/day. The rate from ZTF public data at 3 days were $t = 3.0$ days ($a_{\text{ZTF},r'}(t = 3.0) = -0.0 \pm 0.1$ mag/day). We did not have enough data to conclude about the transient nature. The source was independently classified as a supernova II after 21 days by the ZTF SEDM.

- ZTF21abxkven was observed simultaneously by four GRANDMA instruments: Abastunami/T70, TRT-SRO, Lisnyky/Schmidt-Cassegrain, and FRAM-CTA. Nine more distinct amateur telescopes also observed the source location. It yielded 17 images taken between 0.5 and 11.7 days after $T_0 = 2021-09-03$ 08:28:07. The FINK KN-Mangrove filter associated the alert to HyperLEDA- UGC12816, located at 80 Mpc. As ZTF never detected the source again, FINK classified this transient independently as a Solar System object [185]. No instrument detected the source, and a clear image taken 0.7 day after T_0 by T-ST SOPHIE had a 20.6 mag upper limit. Eventually, the GRANDMA follow-up ruled out any possible existing KN within 80 Mpc at $T_0+0.7$ day.
- ZTF21abxlpdl was observed simultaneously by three GRANDMA instruments - Abastunami/T70, FRAM-CTA, and TRT-SRO - and seven amateur telescopes. We have 15 images for this alert, taken between 0.5 and 13.9 days after the first public detection. As the alert was sent the same day as ZTF21abxkven, the participation was limited for both targets. KN-Mangrove filter associated the source to NGC 105, located at 79 Mpc. No images show the transient, and a clear image acquired 1.7 days after the alert using the T40-A77DAU has an upper limit of 20.7 mag. In summary, GRANDMA follow-up ruled out any kilonova up to 80 Mpc with luminosity decay rate > 1 mag/day in the r' -band.

KN-LC alerts

Along with the KN-Mangrove, we followed up one alert selected by the KN-LC filter:

- ZTF21ablssud was observed simultaneously by four GRANDMA instruments: TRT-SRO, Lisnyky/Schmidt-Cassegrain, Tibet-50, and UBAI-NT60 telescopes. In addition, 17 distinct amateur telescopes also observed the source. It resulted in 141 images taken between 2.6 to 26.7 days after $T_0=2021-07-16$ 21:11:45. Due to how the KN-LC filter works, the alert was sent by FINK two days after the first observation by ZTF with a kilonova score of 53%. Other scores delivered by FINK were: Early SN (5%), Supernova SN Ia vs non-IA SN (73%) and SN Ia and Core-Collapse vs non-SN (39%).

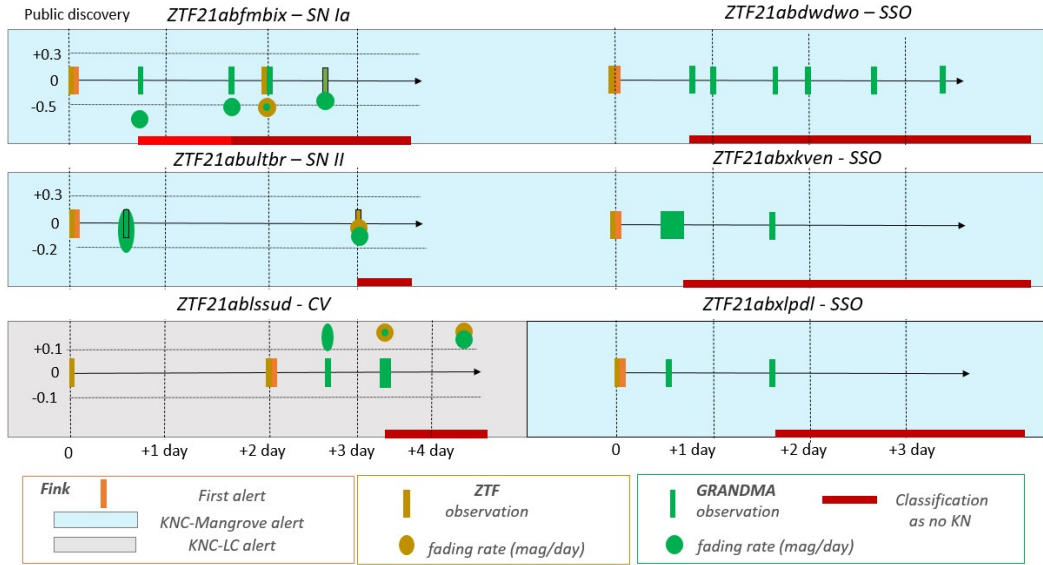


Figure 3.24: Overview of the GRANDMA observations of the six FINK alerts followed up by both professional and amateur astronomers. The FINK alerts come from two selection filters of the initial ZTF flux measurements: KN-LC and KN-Mangrove. The orange patches are the time-stamps for the alert sent by FINK for the source. Gold vertical bars represent the release time of ZTF public data. Green vertical bars represent the GRANDMA data analysed with `STDpipe` and `Muphoten`. The circles present our fading slope estimation using r'/R filters using only ZTF public data (gold) and ZTF+GRANDMA data (green). Horizontal red bars materialise when we consider the alert not a kilonova candidate anymore. SSO corresponds to Solar System Object, CV to cataclysmic variable, and SN to supernova given by our post-observation analysis months after - see figure 3.21). Figure extracted from [7].

Observations started 0.6 days after the FINK alert. Both pipelines detected the source in 66 images in various filters and in 17 clear images. With the GRANDMA photometry datasets, we found a slope of 0.15 ± 0.1 mag/day at $t = 3.7$ days for both **Muphoten** and **STDPipe**. Based on the ZTF public measurement of $r' = 17.2$ mag delivered five days after the first detection, we found $a_{\text{ZTF},r} = 0.15 \pm 0.1$ mag/day at $t = 2.0$ day and $t = 5.0$ day. Consequently, we ruled out a kilonova emission by a BNS merger. In addition, the ZTF lightcurve fitting ruled out the supernova and GRB afterglow hypothesis.

As this alert has been observed a lot with GRANDMA and KNC telescopes, we plotted the lightcurves for several bands in Figure 3.25. Considering the closeness with the galactic plane and the colour evolution, we estimate that ZTF21ablsud was a cataclysmic variable - see Table 3.6.

Practicing Alerts

The six remaining alerts were not selected via the FINK filters we implemented but are early supernova candidates we proposed to observe for training the network observers. This section summarises the results of those alerts.

- ZTF21abfaohe/SN2021pfs: classified as a supernova by external collaborations, see Transient Name Server reference.
- ZTF21abbzjeq/SN2021mwb: idem.
- ZTF21abotose/SN2021ugl is a supernova IIb. These three sources distributed via FINK were selected to test and improve data reduction GRANDMA capabilities.
- ZTF21abyplur was only observed by Tibet-50, a GRANDMA instrument. Four images were acquired, starting 9.5 days after the first public detection, on 2021-09-07 at 09:12:26. The KN-Mangrove filter associated the galaxy HyperLEDA-PGC1115282 to the source. It was located at a 10 arcseconds angular distance close to the limit of a positive association. However, FINK classified this object independently as a Solar System object, probably attached to Solar System object number 22327 [185]. The images taken by the Tibet-50 could not rule out the case of a fast transient with an upper limit of $g' > 18.3$ mag, at $t = T_0 + 9.5$ days.
- ZTF21absvlrr was observed by six amateur telescopes and four GRANDMA telescopes: Terskol/Zeiss-600, TRT-SBO, TRT-SRO, and Abastumani-T70. It resulted in a total of 24 images taken between 1 and 59 days post-detection - $T_0 = 2021-08-12$ 09:52:43. An associated alert from the KN-Mangrove filter was sent by FINK with a 2.3 h delay, but distributed to GRANDMA as a practical exercise about 0.9 days afterwards. HyperLEDA/ESO540-025 is the galaxy associated with the transient, located at 89 Mpc. Both pipelines detected the source in 19 images, acquired by seven telescopes in B , V , r' and R in addition to unfiltered frames. The ZTF survey released its next measurement, $g' = 17.6$ mag and $r' = 17.7$

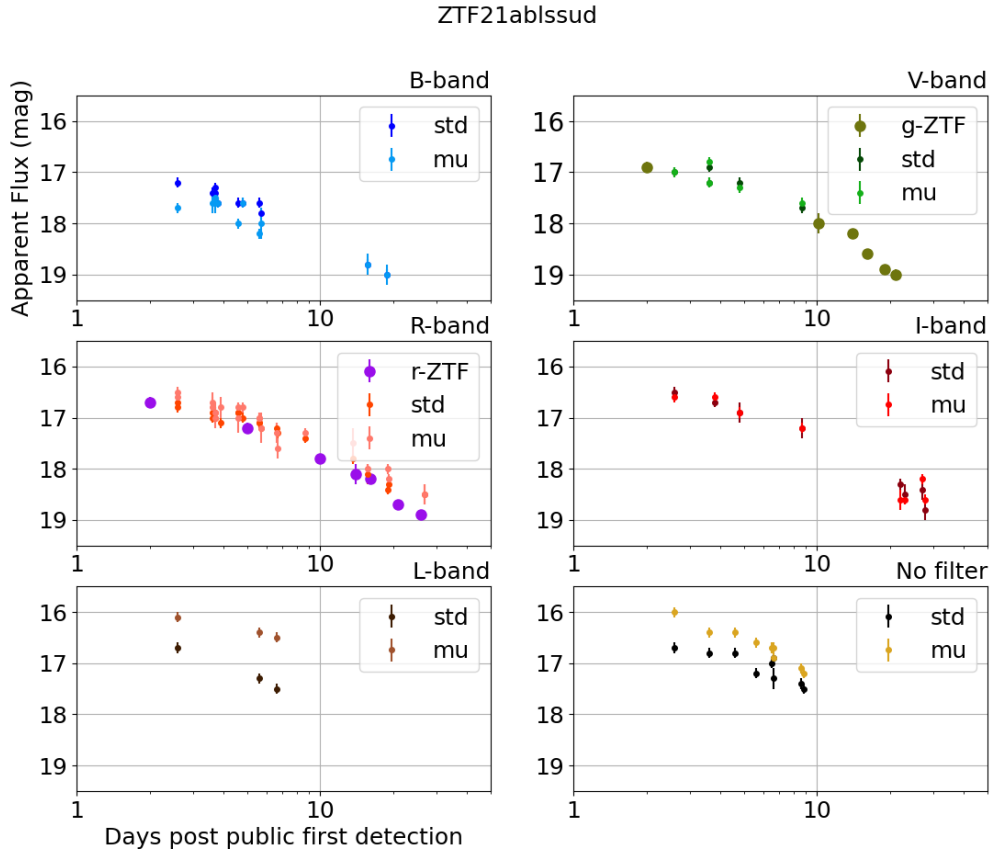


Figure 3.25: ZTF21ablssud lightcurves with observations from ZTF and the 17 GRANDMA instruments. Before $t = T_0 + 10$ days, data were mostly taken by amateur astronomers. For $t > T_0 + 10$ days the data comes from GRANDMA professionals. STDPipe and Muphoten measurements are in agreements for V , R_C , and I_C bands. We showed that the GRANDMA measurements are consistent with the ZTF ones, allowing for filling in the light curve gaps. However, the use of non-standard filters by some amateur astronomers (especially the B -band of the T-CAT instrument) can lead to discrepancies between measurements up to 0.5 mag. This figure is extracted from [7].

Table 3.6: Results of the simulations of transients with rapid evolution, in order to validate or reject the concordance of each transient using ZTF data with the four models: KNe (Ka2017), supernova (nugent-hyper), GRB afterglows (TrPi2018) and shock cooling (Piro2021). Note that the Bayes factors are evaluated logarithmically.

Transients	Ka2017	TrPi2018	nugent-hyper	Piro2021	light curve
ZTF21abfmbix	-12.38	-15.95	-9.18	-10.1	Supernova Ia
ZTF21absvlrr	-9.78	-16.73	-9.91	-11.07	Supernova Ia
ZTF21abultbr	-2.73	-9.14	-5.24	-4.76	Supernova II
ZTF21ablssud	-6.32	-11.58	-9.83	-9.41	Cataclysmic Variable
ZTF21abfaohe	-12.3	-10.98	-7.47	8.67	Supernova Ia
ZTF21abbzjeq	-8.22	-11.41	-7.49	-8.47	Supernova Ia
ZTF21acceboj	-16.52	-19.44	-14.52	-15.6	Supernova IIb
ZTF21abotose	-6.37	-10.62	-7.41	-7.49	Shock Cooling - Supernova IIp

mag, two days post trigger. These values were consistent with both GRANDMA pipelines. Based on these measurements, data showed a rising phase for the transient with a rate of -0.1 ± 0.2 mag/day at $t = 1.0$ and -0.5 ± 0.1 and -0.7 ± 0.1 mag/day at $t = 1.7$ days. This was consistent with ZTF rate at $t = 2.0$ days with a rate of $a_{ZTF,r} = -0.5 \pm 0.1$ mag/day.

This behaviour was not compatible with an AT2017gfo-like transient. External spectroscopic measurements by ZTF SEDM on $T_0 + 1$ day classified the source as a supernova Ia.

- ZTF21acceboj/SN 2021yyg was observed by two GRANDMA instruments: Tibet-50 and Terskol-600 telescopes. It yielded a total of 11 images taken after 1.4 days after the first public detection reported on 2021-09-14 11:04:25. We obtained $a_{STD,r}(t = 1.4) = -0.3 \pm 0.1$ mag/day, and $a_{MU,r}(t = 1.4) = -0.4 \pm 0.1$ mag/day, compatible with the ZTF measurement of $a_{ZTF,r}(t = 2.0) = -0.3 \pm 0.1$ mag/day. This two-day rise in the r' -band ruled out ZTF21acceboj as a kilonova emission from a BNS. The Global SN Project (with LCO) classified the source as a supernova IIp one day after the first public detection.

3.5.6 Offline source modeling

For constraining the transient nature, we used four lightcurve models [63]. Then we used a regression to compare our results with each model and estimate the ideal model thanks to the Bayes factor as visible in Table 3.6 taken from [7].

3.5.7 Conclusion and Lessons

For the **Readyfor04** campaign, we followed up twelve alerts from the ZTF survey filtered with the FINK broker to search for serendipitous kilonova with the GRANDMA network. Four of these alerts were classified as Solar System Objects; the eight others are supernovae or cataclysmic variables. 11 GRANDMA telescopes and 26 amateur instruments provided images we analysed with two independent pipelines for the campaign. We demonstrated the capabilities of both GRANDMA and its amateur branch to follow up and characterise optical transients.

This campaign was the first fully-fledged realistic test for **Muphoten**, and it allowed the identification of some issues but also some points of satisfaction.

One of the main issues identified with the campaign was the difficulty of reducing the images acquired in various non-standard filters used by amateur astronomers. Same for the unfiltered images that were complicated to analyse according to the results in Figure 3.23. However, these broadband observations could be important for detection as, when all other parameters are equal, they allow for deeper observations than filtered ones. This pointed toward using these images for detection purposes in future campaigns. On the other hand, based on Section 1.2.2 discussion about the importance of color evolution of kilonova, observations in various filters are crucial for GW follow-up to constrain the physical parameters of a potential kilonova. Consequently, even with non-standard filters, filtered observations will be used during the O4 run. For some amateurs, especially the observers that reach 20-21 mag, the collaboration is considering funding new, standard, narrow band filters.

The last point this campaign enlightens is the heterogeneity among observers on the data quality. Some images were clearly impossible to analyse, and both amateur and GRANDMA professionals need to gain experience in data quality checks before sending their images to the network repository. For this issue, **Muphoten** vetoes are not of any help as the code crashes because of the quality issues.

On the other hand, thanks to the amateur community, we achieved rapid follow-up with a 16h delay between the alert and the first lights. The major part of this delay happens since most amateur astronomers are located in France and ZTF in the USA. Future participants from other continents will help improve this. Moreover, some observers reached fairly deep observations down to 20.5 mag in clear images. These results met the kilonova observation requirements based on the AT2017gfo characteristics and O3 BNS event triggers estimated distance. In addition, many GRANDMA telescopes are equipped with red filters (r' and R_c), which is essential for late-time kilonova characterisation.

We also demonstrated our ability to produce consistent photometry datasets with independent methods. We showed that none of the algorithms contains a systematic bias due to transient colour. In addition, it allowed improving **Muphoten** parameters for GRANDMA instruments.

Our early observations also allowed for a more rapid transient classification than the classification based only on ZTF data. This rapidity will be crucial during the O4 run to guide the decision to trigger larger facilities and spectroscopic capabilities of the network, which are valuable but limited resources. Overall, we consider that **Readyfor04** was a suc-

cess, with promising GRANDMA and Kilonova-Catcher performances for the upcoming O4 observing run.

CONCLUSION

Multi-messenger astronomy (MMA) based on gravitational waves is a promising domain for producing new results in several fundamental topics. In particular, the joint observation of binary neutron stars merger in the gravitational regime and the optical electromagnetic wavelengths lead to a better understanding of the compact object merger. In addition it also bring further constrains in various fundamental topics such as dense nuclear matter and cosmology. However, such observations require preparation on both sides for having exploitable results.

We presented the **PyCBC Live** low-latency search that detects, characterises and distributes the GW candidate events. This pipeline and the others that do similar searches are of significant importance for MMA as they provide early and crucial information about the event, including indications on the source nature that helps to decide quickly whether rapid electromagnetic follow-up is necessary. In addition, the signal-to-noise ratio (SNR) time series the pipelines construct with matched filtering technique is used to perform a fast localisation with the **Bayestar** algorithm. The latter creates skymaps within seconds, which are distributed for allowing follow-up by other observers. This makes **Bayestar** a central tool for MMA, which has to produce reliable spatial information for maximising the chances of multi-messenger observations. However, we identified a potential bias in the localisation that we attribute to a hard-coded fudge factor we called ξ . It was initially implemented before the O2 observing run to make **Bayestar** self-consistent with the GSTLAL pipeline as otherwise, the localisation uncertainties are underestimated. ξ works by rescaling the SNR time series provided by the search pipeline, which dilates the area of the credible regions and makes the localisation self-consistent. However, the tuning of ξ has been made with GSTLAL with a network configuration different from the current one. More importantly, the **Bayestar** paper [225] has not provided a confident reason why ξ was necessary in the first place. Consequently, we investigated the ξ origin. We gathered evidences that ξ is required to compensate for the discrepancy between the intrinsic parameters of the template waveform used for the localisation and the parameters of the source binary. In addition, by doing an end-to-end test with **PyCBC Live**, we also tested the influence of the template bank used for the low-latency search on spatial localisation. We gathered evidence that the sparseness of the bank has little to no effect on the localisation with **Bayestar**, rather than the parameter space itself.

On the other hand, we also gave an overview of the optical follow-up of the GW landscape. We identified significant difficulties that are separated into two categories: intrinsic ones that are linked to the physics of this kind of transients (faintness, rapid evolution) and extrinsic challenges that are related to their observation that heavily relies on GW information (poor localisation, large number of observations for detection and characterisation). The GRANDMA collaboration was created before the O3 run of LIGO and

Virgo to address this difficulty. The collaboration has systematically followed up the candidate event publicly distributed by LIGO and Virgo to find counterparts and adopted two types of strategy. Although no counterpart has been discovered, GRANDMA has demonstrated that using an heterogeneous network of telescopes to search for kilonova was a promising solution for GW optical follow-up. However, it also demonstrated that specific difficulties arise with this type of network. In particular, the heterogeneity requires a dedicated treatment of the data for having reliable photometric datasets. This issue has also been identified with the observation of the AT2017gfo kilonova. The compilation of observations and data from various independent teams showed inconsistencies between groups datasets that could degrade the strength of the results based on them. To address this, we designed a generic photometry pipeline called `Muphoten` that produces a consistent photometry dataset based on heterogeneous observations. It has been tested with observations of SN2018cow, a supernova that belongs to an emerging class of transient, the Fast Blue Optical Transient (FBOT), that shares some characteristics with kilonova, especially the rapid timing evolution. The pipeline is publicly available and currently used for the researches within the collaboration.

GRANDMA set up two observing campaigns to prepare for the upcoming O4 run of LIGO and Virgo. The first was based on the follow-up of the Zwicky Transient Facility (ZTF) survey kilonova alerts with GRANDMA and its amateur branch, Kilonova-Catcher. `Muphoten`, along with another photometry pipeline called `STDpipe`, were used for the data reduction and using the results provided by the two codes, we demonstrated that there was no systematic bias in the analysis. This campaign also showed that the collaboration could observe within a few hours after detecting a transient. It helped for having a better sampling of the transient light curves, enabling a better discrimination of the transients nature. Most of the delay is due to the relative Earth positions of ZTF (USA) and the GRANDMA instruments (Europe-Asia). We also showed the interest of the amateur astronomer community for the follow-up of optical transient, despite the non-standard and unfiltered observations bringing new and important difficulties for data analysis. The other observing campaign was based on a follow-up of Swift GRB alerts in order to find and follow the GRB afterglow emission. The data analysis is currently ongoing.

Future works linked to this thesis would include developments on both sides of the analysis performed for this thesis. For the low-latency spatial localisation, it would be essential to check the behaviour of the ξ parameter for all the pipelines involved in low-latency searches for O4. This could be done using the results from the ongoing Mock Data Challenge (MDC) in the LIGO-Virgo collaboration that allows using simulated searches with various pipelines on shared data. It would also be necessary to investigate whether ξ has to be tuned or not for each pipelines. In particular, `PyCBC Live` will include a new feature that aims at improving the template waveform selection for the detected candidate events. Considering the influence of the agreement between the intrinsic parameters and the source ones, this may affect the localisation via ξ .

For the optical follow-up analysis, `Muphoten` will be continuously improved for preparing the O4 run. In particular, the GRB campaign has shown the importance of the limit-

ing magnitude estimation for setting upper limits on the source parameter, such as the ejecta mass. There is a review of the numerous methods used to estimate the limiting magnitude, and the most reliable will be implemented in the short term. The most likely direction of the benchmark of limiting magnitude estimation is to use fake stars injections, as it allows control of all the simulation parameters and does not depend on an external reference catalog, as is currently the case for **Muphoten**.

CONTRIBUTION TO THE GWTC-3 CATALOG

Producing O3b skymaps

The third observing run of the LVC took place between 2019, April 1st and 2020, March 27th, with a one-month stop after six months to upgrade the network. Despite no confident joint detection of a GW signal and an EM emission during the run, several studies were performed off-line within the collaboration to find sub-threshold multi-messenger events.

The GWTC-3 catalogue was created with the data of the three-run (O1, O2 and O3) [151]. It includes events with a probability of being of astrophysical origin of at least 50%. The O3b run corresponds to a list of 35 events plus seven marginal events. The data release also includes all the triggers that had a false alarm rate (FAR) of less than 2 per day, regardless of whether they had a probability of being of astrophysical origin superior to 50%.

As part of this thesis work, we produced the O3b skymaps for all the off-line triggers identified by the pipelines MBTA, GSTLAL and PyCBC. For the latter, there was two different analysis, a broad one that searches for various types of CBC and an analysis focused on BBH systems with total mass in the $[10, 500]M_{\odot}$, mass ratio q in the $[\frac{1}{3}, 1]$ range and component masses such that $5M_{\odot} \leq m_1 \leq 350 M_{\odot}$ and $m_2 \geq 5 M_{\odot}$. This analysis is designed for a better sensitivity to BBH mergers constituting the most frequently observed by the LIGO and Virgo interferometers.

The skymaps we produced were released as official products of the LIGO-Virgo collaboration [152]. For the MBTA and GSTLAL search algorithms we used **Bayestar** directly on the triggers stored on **GraceDB** to produce the skymaps. For PyCBC, we used `pycbc_make_skymap` that takes the masses and spins given by the search to generate a template waveform and create the SNR time series passed to **Bayestar**. All these skymaps were produced using a $\xi = 0.83$ value.

These skymaps are currently used for multi-messenger astronomy studies, in particular a joint search of coincidences between Fermi-GBM sub-threshold gamma-rays bursts and sub-threshold GW event in **Pillas et al.** (in preparation). Another study about to be published used these skymaps searching for coincidences between Ice-Cube high energy neutrinos and GW events - see **Marka et al.** (in preparation).

Summary of the skymaps

In Table A.1 we summarise the median area for the 50% and 90% credible region for the 35 probable candidates detected by the four CBC searches during the O3b run. These values give the typical localisation for the current GW detector generation and the area an optical instrument or network such as GRANDMA must cover during an efficient follow-up. We also present the cumulative distributions for these areas for these events in Figure A.1 and A.2.

Search	50% Credible Area	90% Credible Area
-	deg ²	deg ²
PyCBC	408	1670
PyCBC High mass	401	1656
MBTA	383	1520
GSTLAL	317	1336

Table A.1: Median credible area of the 35 confident events detected during the O3b observing run for the four CBC searches.

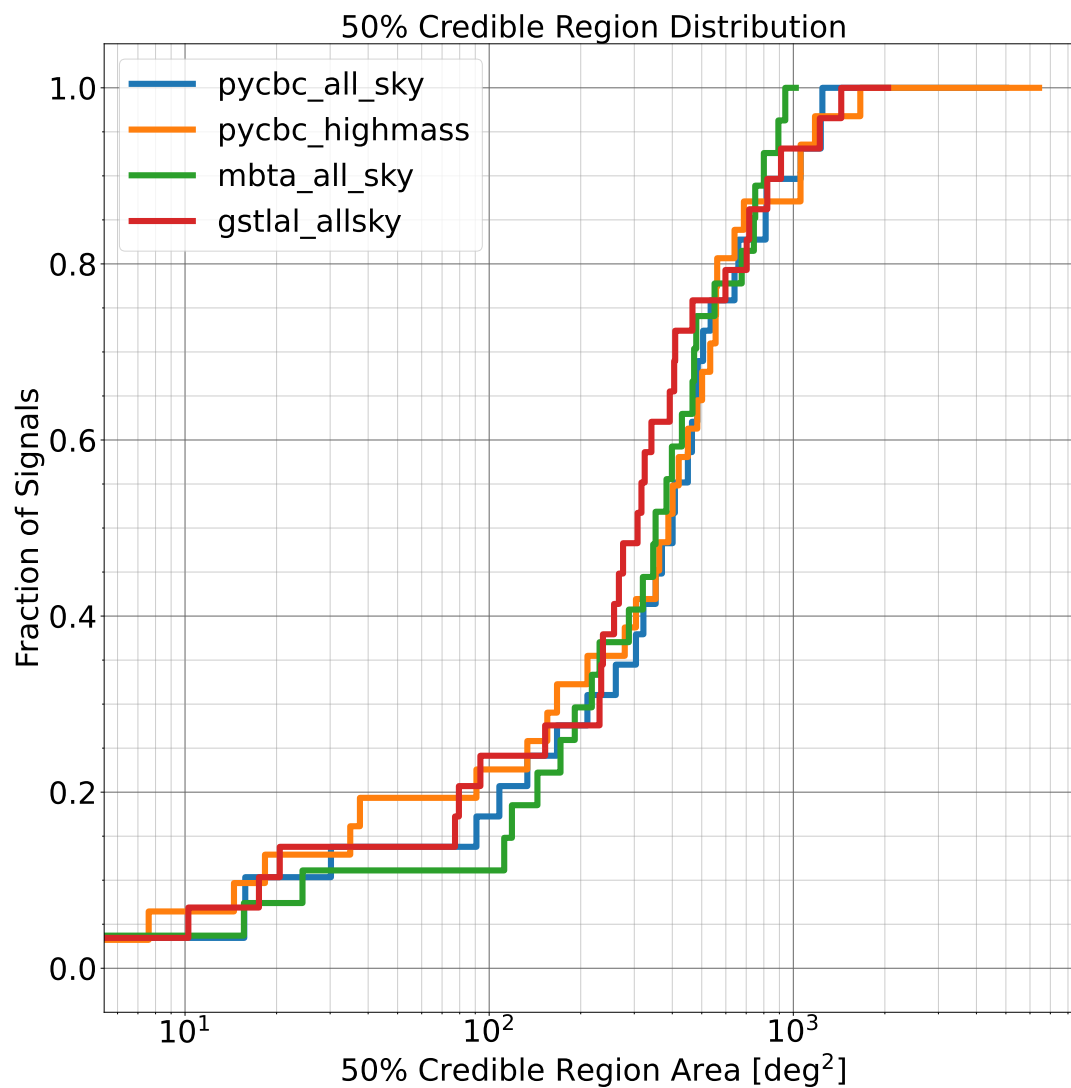


Figure A.1: Cumulative distribution for the 50% credible region of the skymaps produced for the GSTLAL, MBTA and PyCBC detection pipeline. The broad PyCBC analysis is plotted in red and the BBH-focused one is plotted in blue. The MBTA triggers credible regions are in green and GSTLAL ones are in orange.

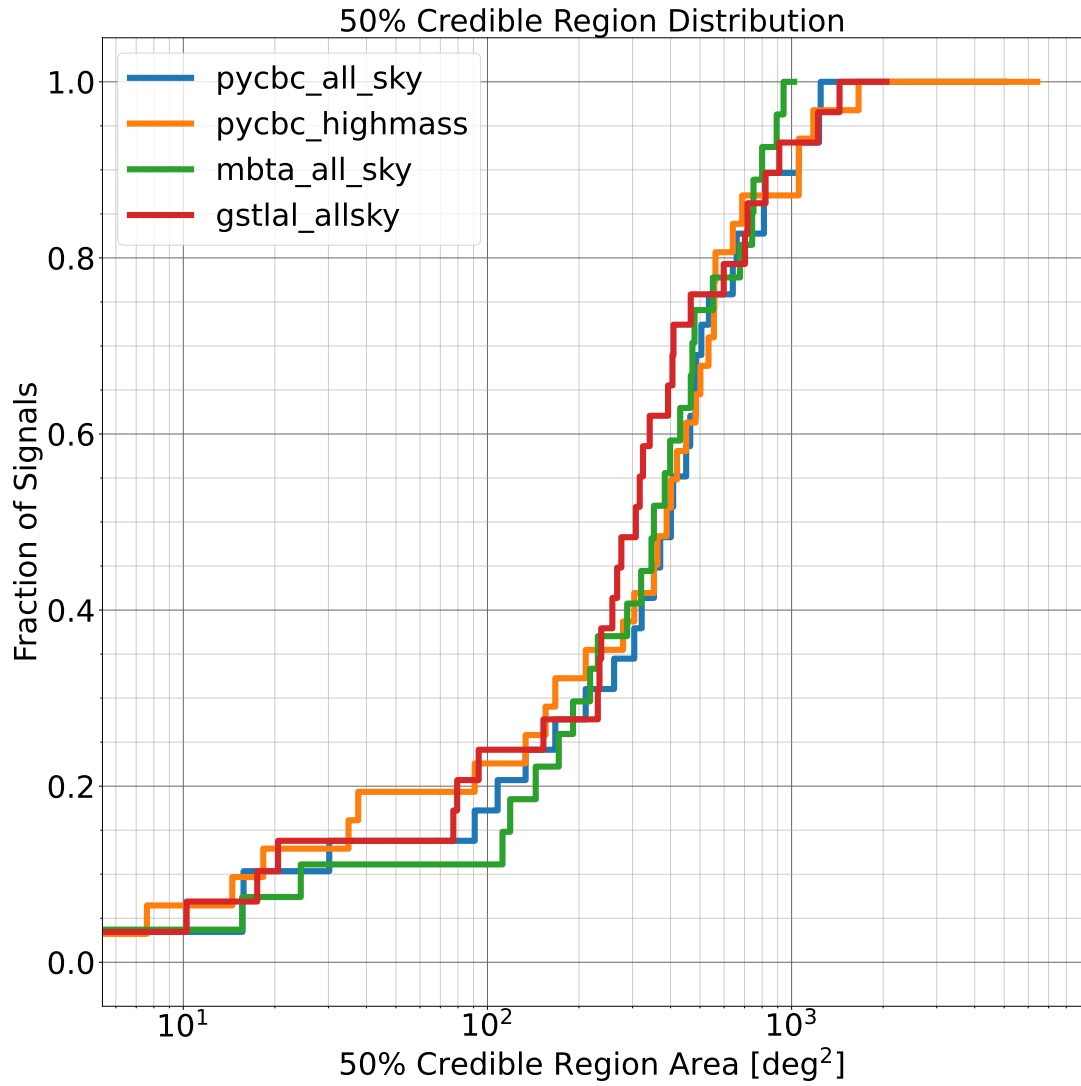


Figure A.2: Cumulative distribution for the 90% credible region of the skymaps produced for the GSTLAL, MBTA and PyCBC detection pipelines. The broad PyCBC analysis is plotted in red and the BBH-focused one is plotted in blue. The MBTA triggers credible regions are in green and GSTLAL ones are in orange.

PHOTOMETRIC SYSTEMS

Photometric Systems

It is usual for astronomical observations of astronomical to use filters to acquire images. There are various filters available, designed with specific purposes. However, fairly standard sets of filters, or photometric systems, are commonly used. Before the SDSS instrument started, the Johnson-Cousins System was very common. It is still widely used, and the transmission curves are presented in FigureB.1. It consists of five filters covering the near-UV to the NIR wavelengths: U , B , V , R_c and I_c . In the 1990s, the SDSS survey began, and a new photometric system was designed with the new use of CCD instead of photometric plates. It consists of five bands covering the same wavelengths as the Johnson-Cousins ones but with much less overlap between the filters' transmission curves: u' , g' , r' , i' , and z' . These filters are shown in FigureB.2. Many modern facilities use this photometric system. It includes Pan-STARRS, although this survey includes a band in the infrared called y and does not cover the EM spectrum's UV part. The PS filters are visible in FigureB.3. For this work, sometimes Gaia is used for calibration, although it has not the usual filter. Its photometric system contains only three bands; G , B_p and R_p and they are shown in FigureB.4. The last filter mentioned in this work is called Luminance and is shown in FigureB.5. It covers the whole Optical domain and is used to cut wavelengths above UV and below infrared. It is mainly used by amateurs for this work, as mentioned in Chapter 3.

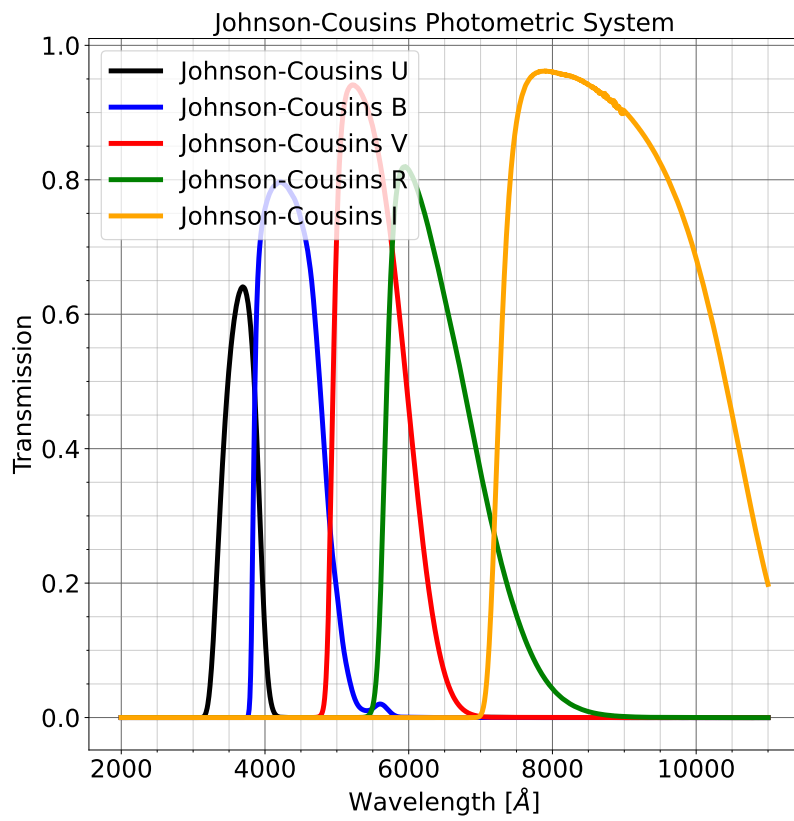


Figure B.1: Filter set Johnson-Cousins.

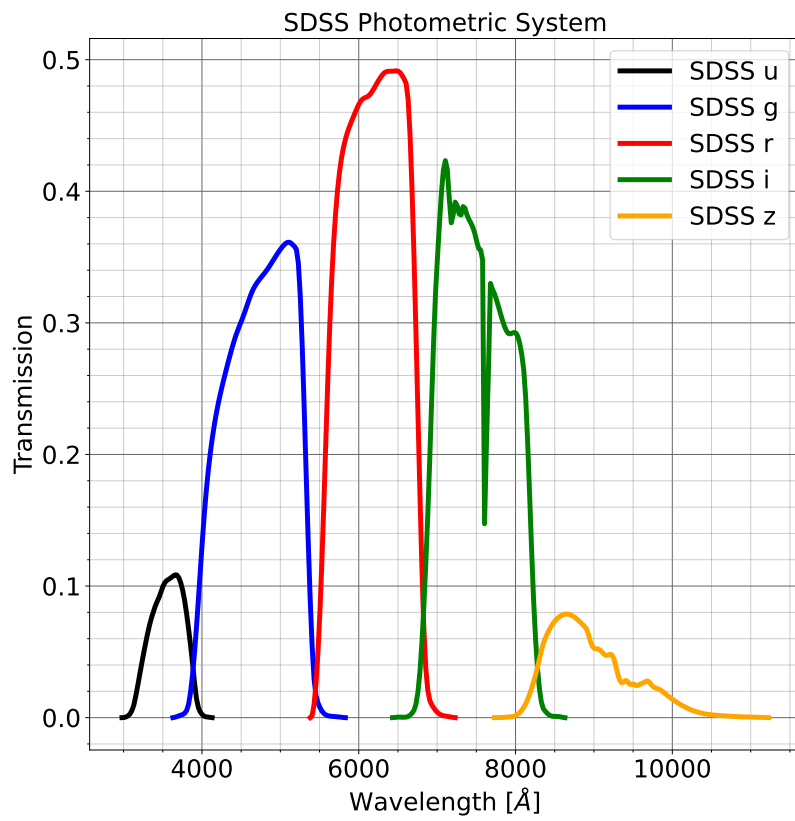


Figure B.2: Filter set for the Sloan Digital Sky Survey instrument.

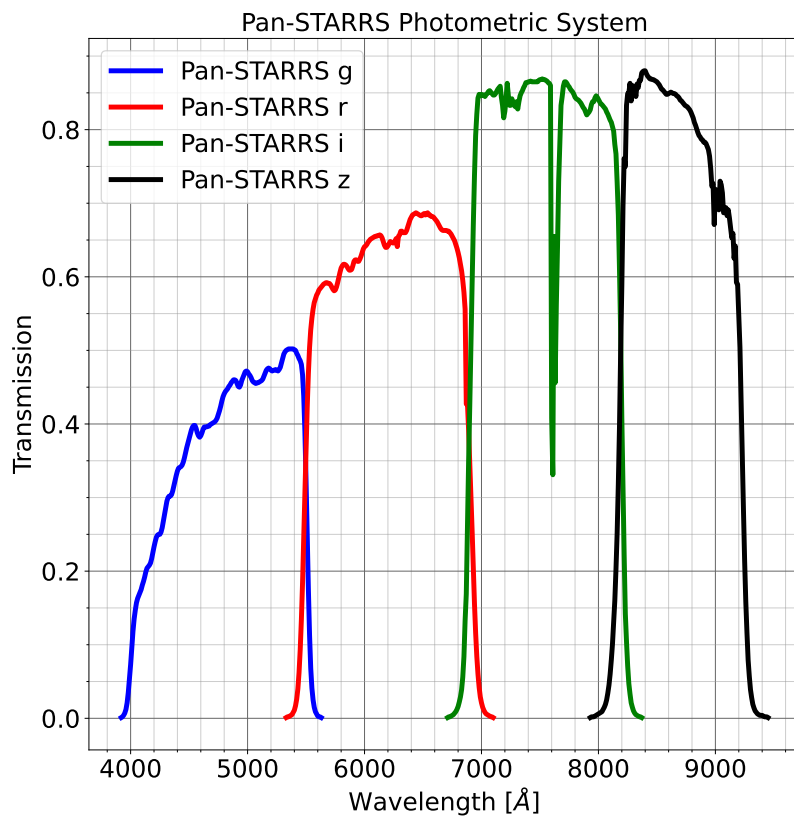


Figure B.3: Filter set for the Panoramic Survey Telescope And Rapid Response System instrument.

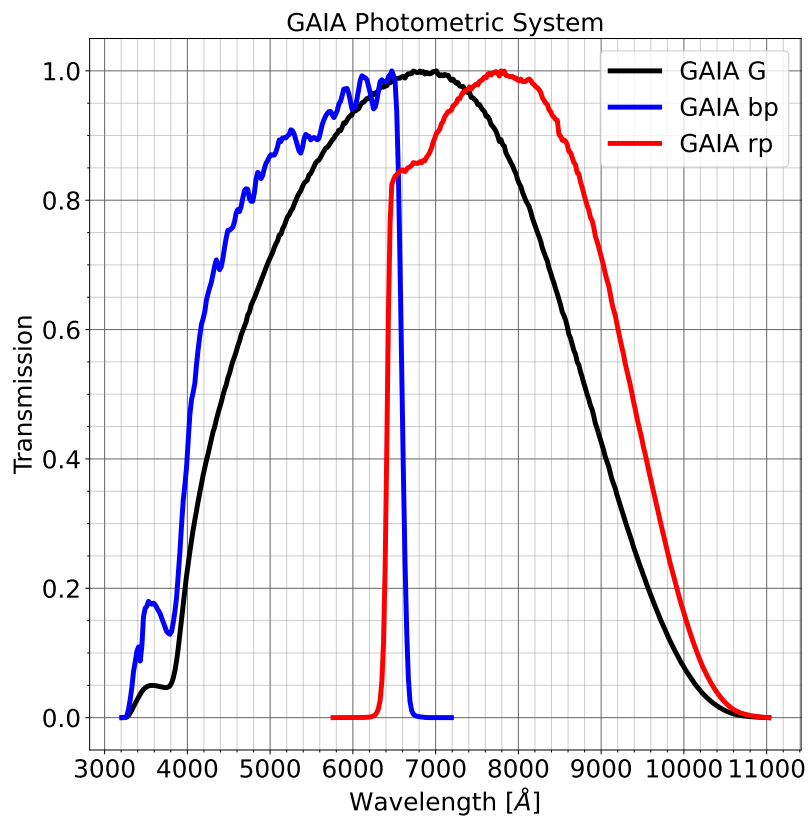


Figure B.4: Filter set for the Gaia satellite.

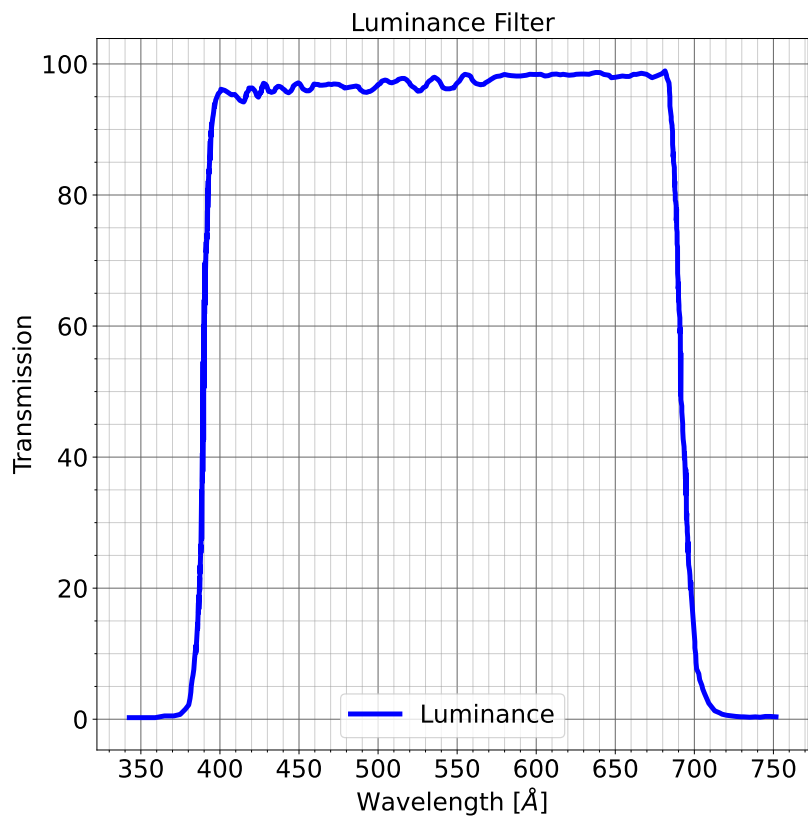


Figure B.5: Luminance filter transmission curve.

PREPARING O4 (II) : SWIFT GRB CAMPAIGN

Motivation

For an observing run of LIGO and Virgo, a possible way to trigger optical follow-up is to have a coincident GRB-GW detection - as happened during O2 for GW170817. Consequently, we decided to organise a follow-up campaign of GRB triggers produced by the Swift satellite. For this campaign, GRANDMA aims to:

- Train the network to external alerts with very low latency - considering the short lifetime of GRB afterglow.
- Test detection mode of the network: contrary to the ZTF campaign, there is not always an optical counterpart to GRB, and its position is not always known when it exists.

We chose the Swift satellite for this campaign - and not Fermi, which would also be another relevant choice for a similar campaign - for the following reason:

1. The source localisation of the Swift-BAT instrument is of the order of 5 arcminutes, which is small enough to be observed with only one observation by most of the GRANDMA instruments. It allows an easier search, contrary to Fermi localisation, whose size is similar to GW. In addition, Swift also does early observations in the X-ray domain with the XRT instrument and in the optical domain with the UVOT telescope to rapidly find the burst afterglow. When the latter is found, it reduces the localisation to arcseconds regions.
2. Swift has a good chance to discover a potential counterpart during O4 - following its alerts is a realistic test
3. Swift is designed to observe its localisation in the X-ray domain with the XRT instruments and the optical domain with the UVOT instrument immediately after the GRB detection. This allows early detection of afterglow. Hence GRANDMA can test whether it can respond and observe that candidate rapidly enough to follow up and characterise them.
4. The alert rate of ~ 1 per week is high enough for training but not too high to saturate the network with follow-up.

Overview of the campaign

The campaign happened between March 21st 2021 and May 15th 2021 and lasted six weeks. GRANDMA and Kilonova-Catcher followed 9 GRBs during this campaign and observed 4 afterglows.

Organisation

To be as close as possible to O4, we set up a shift calendar with one shifter team on duty each week. The weekly team is driven by a coordinator responsible for managing and guiding the shifters. The latter are divided into pairs in 6h slots - taking advantage of the worldwide spread of the members. On-duty shifters have a list of tasks to complete :

- Listen to the Swift alerts
- Control that the telescope teams received the alert and are able to observe
- Control that the images are correctly uploaded to the collaboration database
- Watch the GCN circular from external teams concerning the current alerts
- Write and distribute GRANDMA GCN once an alert is over

Telescope teams are asked to observe any alert they can reach and analyse their images - limiting magnitude estimation when nothing is detected or luminosity estimation for detected afterglows.

Data reduction

The data reduction is ongoing with both `Muphoten` and `SDTpipe` and is not complete yet. However, one observation made during the campaign is that the limiting magnitude estimation must be improved. The estimations made by the observing team and `Muphoten` differ significantly in the direction of an over-conservative estimation `Muphoten`, indicating a necessary pipeline tuning. Prospects are currently ongoing to implement new estimation methods. The preferred option is to use fake, injected sources whose magnitudes are known to estimate the sensitivity.

BIBLIOGRAPHY

- [1] A. Aab et al. “The FRAM robotic telescope for atmospheric monitoring at the Pierre Auger Observatory”. In: *Journal of Instrumentation* 16.06 (2021), P06027.
- [2] K. Abe et al. “Search for Neutrinos in Coincidence with Gravitational Wave Events from the LIGO-Virgo O3a Observing Run with the Super-Kamiokande Detector”. In: *The Astrophysical Journal* 918.2 (2021), p. 78.
- [3] F. Acernese et al. “Measurements of Superattenuator seismic isolation by Virgo interferometer”. In: *Astroparticle Physics* 33.3 (2010), pp. 182–189.
- [4] F. Acernese et al. “Advanced Virgo: a second-generation interferometric gravitational wave detector”. In: *Classical and Quantum Gravity* 32 (2014), p. 024001.
- [5] F. Acernese et al. “The Advanced Virgo detector”. In: *Journal of Physics: Conference Series* 610 (Apr. 2015), p. 012014.
- [6] T. Adams et al. “Low-latency analysis pipeline for compact binary coalescences in the advanced gravitational wave detector era”. In: *Classical and Quantum Gravity* 33.17 (2016), p. 175012.
- [7] V. Aivazyan et al. “GRANDMA Observations of ZTF/Fink Transients during Summer 2021”. In: *Monthly Notices of the Royal Astronomical Society* 515.4 (2022), pp. 6007–6022.
- [8] T Akutsu et al. “Overview of KAGRA: Detector design and construction history”. In: *Progress of Theoretical and Experimental Physics* 2021.5 (Aug. 2020).
- [9] K. D. Alexander et al. “The Electromagnetic Counterpart of the Binary Neutron Star Merger LIGO/Virgo GW170817. VI. Radio Constraints on a Relativistic Jet and Predictions for Late-time Emission from the Kilonova Ejecta”. In: *The Astrophysical Journal* 848.2 (2017), p. L21.
- [10] B. Allen. “ χ^2 time-frequency discriminator for gravitational wave detection”. In: *Phys. Rev. D* 71 (2005), p. 062001.
- [11] B. Allen et al. “FINDCHIRP: An algorithm for detection of gravitational waves from inspiraling compact binaries”. In: *Phys. Rev. D* 85 (2012), p. 122006.
- [12] ANTARES Collaboration. “ANTARES: the first undersea neutrino telescope”. In: *Nucl. Instrum. Meth. A* 656 (2011), pp. 11–38.
- [13] S. Antier et al. “The first six months of the Advanced LIGO’s and Advanced Virgo’s third observing run with GRANDMA”. In: *Monthly Notices of the Royal Astronomical Society* 492.3 (2019), pp. 3904–3927.
- [14] S. Antier et al. “GRANDMA observations of advanced LIGO’s and advanced Virgo’s third observational campaign”. In: *Monthly Notices of the Royal Astronomical Society* 497.4 (2020), pp. 5518–5539.

- [15] I. Arcavi et al. “Optical emission from a kilonova following a gravitational-wave-detected neutron-star merger”. In: *Nature* 551.7678 (2017), pp. 64–66.
- [16] M. Armano and H. Audley. “Sub-Femto- g Free Fall for Space-Based Gravitational Wave Observatories: LISA Pathfinder Results”. In: *Phys. Rev. Lett.* 116 (2016), p. 231101.
- [17] M. Arnould, S. Goriely, and K. Takahashi. “The r-process of stellar nucleosynthesis: Astrophysics and nuclear physics achievements and mysteries”. In: *Physics Reports* 450.4-6 (2007), pp. 97–213.
- [18] W. B. Atwood et al. “The Large Area Telescope on the Fermi gamma-ray space telescope mission”. In: *The Astrophysical Journal* 697.2 (2009), pp. 1071–1102.
- [19] S. Babak et al. “Searching for gravitational waves from binary coalescence”. In: *Phys. Rev. D* 87 (2013), p. 024033.
- [20] A. Balasubramanian et al. “GW170817 4.5 Yr After Merger: Dynamical Ejecta Afterglow Constraints”. In: *The Astrophysical Journal* 938.1 (2022), p. 12.
- [21] J. Barnes et al. “Radioactivity and thermalization in the ejecta of compact object mergers and their impact on kilonova light curves”. In: *Astrophys. J.* 829 (2016), p. 110.
- [22] S. D. Barthelmy et al. “The Burst Alert Telescope (BAT) on the SWIFT Midex Mission”. In: *Space Science Reviews* 120.3 (2005), pp. 143–164.
- [23] I. Bartos et al. “Bayesian multimessenger search method for common sources of gravitational waves and high-energy neutrinos”. In: *Phys. Rev. D* 100 (8 2019), p. 083017.
- [24] A. Bauswein, S. Goriely, and H. -T. Janka. “Systematics of Dynamical Mass Ejection, Nucleosynthesis, and Radioactively Powered Electromagnetic Signals from Neutron-star Mergers”. In: *The Astrophysical Journal* 773 (2013), p. 78.
- [25] A. Becker. *HOTPANTS: High Order Transform of PSF AND Template Subtraction*. 2015. eprint: 1504.004.
- [26] I. Belahcene. “Searching for gravitational waves produced by cosmic strings in LIGO-Virgo data”. PhD thesis. 2019.
- [27] E. Berger. “Short-Duration Gamma-Ray Bursts”. In: *Annual Review of Astronomy and Astrophysics* 52.1 (2014), pp. 43–105.
- [28] E. Bertin. “Automatic Astrometric and Photometric Calibration with SCAMP”. In: *Astronomical Data Analysis Software and Systems XV*. Ed. by C. Gabriel et al. Vol. 351. Astronomical Society of the Pacific Conference Series. 2006, p. 112.
- [29] E. Bertin. “Automated Morphometry with SExtractor and PSFEx”. In: *Astronomical Data Analysis Software and Systems XX*. Ed. by I. N. Evans et al. Vol. 442. Astronomical Society of the Pacific Conference Series. 2011.

- [30] E. Bertin. *SExtractor Documentation*. <https://sextractor.readthedocs.io/en/latest/Position.html#shape-iso-def>. [Online; accessed 05-July-2022]. 2017.
- [31] E. Bertin and S. Arnouts. “SExtractor: Software for source extraction.” In: *Astronomy and Astrophysics Supplement* 117 (1996), pp. 393–404.
- [32] E. Bertin et al. “The TERAPIX Pipeline”. In: *Astronomical Data Analysis Software and Systems XI*. Ed. by David A. Bohlender, Daniel Durand, and Thomas H. Handley. Vol. 281. Astronomical Society of the Pacific Conference Series. 2002, p. 228.
- [33] S. Bilenky. “Neutrino oscillations: From a historical perspective to the present status”. In: *Nuclear Physics B* 908 (2016), pp. 2–13.
- [34] S. Biscoveanu, S. Vitale, and C.-J. Haster. “The Reliability of the Low-latency Estimation of Binary Neutron Star Chirp Mass”. In: *The Astrophysical Journal* 884.2 (2019), p. L32.
- [35] C. M. Biwer et al. “PyCBC Inference: A Python-based Parameter Estimation Toolkit for Compact Binary Coalescence Signals”. In: *Publications of the Astronomical Society of the Pacific* 131.996 (2019), p. 024503.
- [36] M. R. Blanton et al. “Sloan Digital Sky Survey IV: Mapping the Milky Way, Nearby Galaxies, and the Distant Universe”. In: *The Astronomical Journal* 154.1 (2017), p. 28.
- [37] Blelly,A., Moutarde, H., and Bobin, J. *LISA Mission*. https://irfu.cea.fr/en/Phocea/Vie_des_labos/Ast/ast.php?t=fait_marquant&id_ast=4867. [Online; accessed 05-July-2022]. 2020.
- [38] A. Bohé et al. “Improved effective-one-body model of spinning, nonprecessing binary black holes for the era of gravitational-wave astrophysics with advanced detectors”. In: *Phys. Rev. D* (2017), p. 044028.
- [39] P.A. Boley. “The European Southern Observatory and VLT telescopes on Paranal”. In: *Physics of Space: the 41st Annual Student Scientific Conference*. 2012, pp. 7–18.
- [40] L. Bradley et al. *astropy/photutils: 1.1.0*. 2021.
- [41] M. Bulla et al. “Multi-Messenger Constraints on the Hubble Constant through Combination of Gravitational Waves, Gamma-Ray Bursts and Kilonovae from Neutron Star Mergers”. In: *Universe* 8.5 (2022).
- [42] A. Buonanno et al. “Comparison of post-Newtonian templates for compact binary inspiral signals in gravitational-wave detectors”. In: *Phys. Rev. D* 80 (2009), p. 084043.
- [43] E. M. Burbidge et al. “Synthesis of the Elements in Stars”. In: *Rev. Mod. Phys.* 29 (4 1957), pp. 547–650.

- [44] E. Burns. “Neutron Star Mergers and How to Study Them”. In: *Living Rev. Rel.* 23 (2020), p. 4.
- [45] C. Cahillane and G. Mansell. “Review of the Advanced LIGO Gravitational Wave Observatories Leading to Observing Run Four”. In: *Galaxies* 10.1 (2022).
- [46] K. Cannon et al. “GstLAL: A software framework for gravitational wave discovery”. In: *SoftwareX* 14 (2021), p. 100680.
- [47] J. M. Carrasco. *Photometric relationships with other photometric systems, GAIA DATA RELEASE DOCUMENTATION*. https://gea.esac.esa.int/archive/documentation/GDR2/Data_processing/chap_cu5pho/sec_cu5pho_calibr/ssec_cu5pho_PhotTransf.html. [Online; accessed 05-July-2022]. 2019.
- [48] K. C. Chambers et al. “The Pan-STARRS1 Surveys”. In: (2016). eprint: 1612.05560.
- [49] K. C. Chambers et al. “LIGO/Virgo G298048: Pan-STARRS 1z photometry monitoring of SSS17a/DLT17ck”. In: *GRB Coordinates Network* 21617 (2017).
- [50] T. Cokelaer. “Gravitational waves from inspiralling compact binaries: Hexagonal template placement and its efficiency in detecting physical signals”. In: *Phys. Rev. D* 76 (10 2007), p. 102004.
- [51] S. A. Colgate and C. McKee. “Early Supernova Luminosity”. In: *Astrophysical Journal* 157 (1969), p. 623.
- [52] H.E.S.S. Collaboration. “The H.E.S.S. Survey of the Inner Galaxy in Very High Energy Gamma Rays”. In: *The Astrophysical Journal* 636 (2006), p. 777.
- [53] LIGO Collaboration. “LIGO: the Laser Interferometer Gravitational-Wave Observatory”. In: *Reports on Progress in Physics* 72.7 (2009), p. 076901.
- [54] Pierre Auger Collaboration. “The Pierre Auger Cosmic Ray Observatory”. In: *Nuclear Instruments and Methods in Physics Research Section A: Accelerators, Spectrometers, Detectors and Associated Equipment* 798 (2015), pp. 172–213.
- [55] SNO Collaboration. “Direct Evidence for Neutrino Flavor Transformation from Neutral-Current Interactions in the Sudbury Neutrino Observatory”. In: *Phys. Rev. Lett.* 89 (2002), p. 011301.
- [56] The LIGO Collaboration and The Virgo Collaboration. “A gravitational-wave standard siren measurement of the Hubble constant”. In: *Nature* 551.7678 (2017), pp. 85–88.
- [57] J. J. Condon et al. “The NRAO VLA Sky Survey”. In: *The Astronomical Journal* 115 (1998), p. 1693.
- [58] James M. Cordes and Shami Chatterjee. “Fast Radio Bursts: An Extragalactic Enigma”. In: *Annual Review of Astronomy and Astrophysics* 57.1 (2019), pp. 417–465.

- [59] M. W. Coughlin et al. “Constraints on the neutron star equation of state from AT2017gfo using radiative transfer simulations”. In: *Monthly Notices of the Royal Astronomical Society* 480.3 (2018), pp. 3871–3878.
- [60] M. W. Coughlin et al. “GROWTH on S190425z: Searching Thousands of Square Degrees to Identify an Optical or Infrared Counterpart to a Binary Neutron Star Merger with the Zwicky Transient Facility and Palomar Gattini-IR”. In: *The Astrophysical Journal* 885.1 (2019), p. L19.
- [61] M. W. Coughlin et al. “Optimizing multitelescope observations of gravitational-wave counterparts”. In: *Monthly Notices of the Royal Astronomical Society* 489.4 (2019), pp. 5775–5783.
- [62] M. W. Coughlin et al. “The Kitt Peak Electron Multiplying CCD demonstrator”. In: *Monthly Notices of the Royal Astronomical Society* 485.1 (2019), pp. 1412–1419.
- [63] M. W. Coughlin et al. “Implications of the search for optical counterparts during the first six months of the Advanced LIGO’s and Advanced Virgo’s third observing run: possible limits on the ejecta mass and binary properties”. In: *Monthly Notices of the Royal Astronomical Society* 492.1 (2020), pp. 863–876.
- [64] M. W. Coughlin et al. “Measuring the Hubble constant with a sample of kilonovae”. In: *Nature Communications* 11.1 (2020), p. 4129.
- [65] D. A. Coulter et al. “Swope Supernova Survey 2017a (SSS17a), the optical counterpart to a gravitational wave source”. In: *Science* 358.6370 (2017), pp. 1556–1558.
- [66] P. S. Cowperthwaite et al. “LSST Target-of-opportunity Observations of Gravitational-wave Events: Essential and Efficient”. In: *The Astrophysical Journal* 874.1 (2019), p. 88.
- [67] C. Cutler and É. E. Flanagan. “Gravitational waves from merging compact binaries: How accurately can one extract the binary’s parameters from the inspiral waveform?” In: *Phys. Rev. D* 49 (1994), pp. 2658–2697.
- [68] R. M. Cutri et al. “VizieR Online Data Catalog: AllWISE Data Release (Cutri+ 2013)”. In: *VizieR Online Data Catalog* (2021), pp. II/328.
- [69] P. D’Avanzo et al. “The evolution of the X-ray afterglow emission of GW 170817/GRB 170817A in XMM-Newton observations”. In: *Astronomy & Astrophysics* 613 (2018), p. L1.
- [70] T. Dal Canton et al. “AT2018cow: Fermi/GBM Data Search”. In: *The Astronomer’s Telegram* 11793 (2018), p. 1.
- [71] T. Dal Canton et al. “Real-time Search for Compact Binary Mergers in Advanced LIGO and Virgo’s Third Observing Run Using PyCBC Live”. In: *The Astrophysical Journal* 923.2 (2021), p. 254.
- [72] G. Dályá et al. “GLADE: A galaxy catalogue for multimessenger searches in the advanced gravitational-wave detector era”. In: *MNRAS* 479 (2018), pp. 2374–2381.

- [73] K. Danzmann and Lisa Study Team. “LISA - An ESA Cornerstone Mission for the Detection and Observation of Gravitational Waves”. In: *Advances in Space Research* 32.7 (2003), pp. 1233–1242.
- [74] L. Dessart et al. “Nebular phase properties of supernova Ibc from He-star explosions”. In: *A&A* 656 (), A61.
- [75] L. Dessart et al. “Neutrino signatures and the neutrino-driven wind in Binary Neutron Star Mergers”. In: *Astrophys. J.* 690 (2009), p. 1681.
- [76] S. Dhawan et al. “Constraining the Observer Angle of the Kilonova AT2017gfo Associated with GW170817: Implications for the Hubble Constant”. In: *The Astrophysical Journal* 888.2 (2020), p. 67.
- [77] T. Dietrich and M. Ujevic. “Modeling dynamical ejecta from binary neutron star mergers and implications for electromagnetic counterparts”. In: *Class. Quant. Grav.* 34.10 (2017), p. 105014.
- [78] J.-G. Ducoin. “Multi-messenger astronomy : from the analysis of transient sources of gravitational waves to electromagnetic counterparts searches”. Thèse de doctorat dirigée par Leroy, Nicolas Astroparticules et cosmologie université Paris-Saclay 2021. PhD thesis. 2021.
- [79] J.-G. Ducoin et al. “Optimizing gravitational waves follow-up using galaxies stellar mass”. In: *Monthly Notices of the Royal Astronomical Society* 492.4 (2020), pp. 4768–4779.
- [80] D. A. Duev et al. “Real-bogus classification for the Zwicky Transient Facility using deep learning”. In: *Monthly Notices of the Royal Astronomical Society* 489.3 (2019), pp. 3582–3590.
- [81] Strang E. *LIGO Handford Weber bar*. <https://www.flickr.com/photos/cheneyseric/25313545489>. [Online; accessed 05-July-2022]. 2016.
- [82] Albert Einstein. “The Field Equations of Gravitation”. In: *Sitzungsber. Preuss. Akad. Wiss. Berlin (Math. Phys.)* 1915 (1915), pp. 844–847.
- [83] Albert Einstein. “Approximative Integration of the Field Equations of Gravitation”. In: *Sitzungsber. Preuss. Akad. Wiss. Berlin (Math. Phys.)* 1916 (1916), pp. 688–696.
- [84] R. Fernández and B. D. Metzger. “Delayed outflows from black hole accretion tori following neutron star binary coalescence”. In: *MNRAS* 435 (2013), pp. 502–517.
- [85] F. Foucart. “Black-hole-neutron-star mergers: Disk mass predictions”. In: *Physical Review D* 86, 124007 (2012), p. 124007.
- [86] F. Foucart, T. Hinderer, and S. Nissanke. “Remnant baryon mass in neutron star-black hole mergers: Predictions for binary neutron star mimickers and rapidly spinning black holes”. In: *Physical Review D* 98 (2018), p. 081501.
- [87] O. D. Fox and N. Smith. “Signatures of circumstellar interaction in the unusual transient AT 2018cow”. In: *Monthly Notices of the Royal Astronomical Society* 488.3 (2019), pp. 3772–3782.

- [88] S. Fukuda, Y. Fukuda, and T. Hayakawa. “The Super-Kamiokande detector”. In: *Nuclear Instruments and Methods in Physics Research Section A: Accelerators, Spectrometers, Detectors and Associated Equipment* 501.2 (2003), pp. 418–462.
- [89] J. P. Gardner, J. C. Mather, and M. Clampin. “The James Webb Space Telescope”. In: *Space Science Reviews* 123 (2006), pp. 485–606.
- [90] G. Ghirlanda et al. “Compact radio emission indicates a structured jet was produced by a binary neutron star merger”. In: *Science* 363.6430 (2019), pp. 968–971. DOI: 10.1126/science.aau8815. eprint: <https://www.science.org/doi/pdf/10.1126/science.aau8815>. URL: <https://www.science.org/doi/abs/10.1126/science.aau8815>.
- [91] A. Ginsburg et al. “astroquery: An Astronomical Web-querying Package in Python”. In: *Astrophysical Journal* 157.3 (2019), p. 98.
- [92] A. Goldstein et al. “An Ordinary Short Gamma-Ray Burst with Extraordinary Implications: Fermi-GBM Detection of GRB170817A”. In: *The Astrophysical Journal* 848.2 (2017), p. L14.
- [93] B. P. Gompertz et al. “The Diversity of Kilonova Emission in Short Gamma-Ray Bursts”. In: *The Astrophysical Journal* 860.1 (2018), p. 62.
- [94] K. M. Gorski et al. “HEALPix: A Framework for High-Resolution Discretization and Fast Analysis of Data Distributed on the Sphere”. In: *The Astrophysical Journal* 622.2 (2005), pp. 759–771.
- [95] J. Greaves. *Crude USNO B1.0 B1-R1 to B-V transformation*. http://www.aerith.net/astro/color_conversion/JG/USNO-B1.0.html. [Online; accessed 05-July-2022]. 2003.
- [96] L. P. Grishchuk. “Amplification of gravitational waves in an isotropic universe”. In: *Zh. Eksp. Teor. Fiz.* 67 (1974), pp. 825–838.
- [97] A. Hajela et al. “Two Years of Nonthermal Emission from the Binary Neutron Star Merger GW170817: Rapid Fading of the Jet Afterglow and First Constraints on the Kilonova Fastest Ejecta”. In: *The Astrophysical Journal* 886.1 (2019), p. L17.
- [98] A. Hajela et al. “Evidence for X-Ray Emission in Excess to the Jet-afterglow Decay 3.5 yr after the Binary Neutron Star Merger GW 170817: A New Emission Component”. In: *The Astrophysical Journal Letters* 927.1 (2022), p. L17.
- [99] G. Hallinan et al. “A radio counterpart to a neutron star merger”. In: *Science* 358.6370 (2017), pp. 1579–1583.
- [100] F. Halzen et al. “On the Neutrino Flares from the Direction of TXS 0506+056”. In: *The Astrophysical Journal* 874.1 (2019), p. L9.
- [101] I. W. Harry, B. Allen, and B. S. Sathyaprakash. “Stochastic template placement algorithm for gravitational wave data analysis”. In: *Phys. Rev. D* 80 (10 2009).
- [102] I. W. Harry and S. Fairhurst. “Targeted coherent search for gravitational waves from compact binary coalescences”. In: *Phys. Rev. D* 83 (2011), p. 084002.

- [103] R. Hascoët et al. “Do Fermi Large Area Telescope observations imply very large Lorentz factors in gamma-ray burst outflows?” In: *Monthly Notices of the Royal Astronomical Society* 421.1 (2012), pp. 525–545.
- [104] K. Hirata et al. “Observation of a neutrino burst from the supernova SN1987A”. In: *Phys. Rev. Lett.* 58 (1987), pp. 1490–1493.
- [105] A. Y. Q. Ho et al. “AT2018cow: A Luminous Millimeter Transient”. In: *The Astrophysical Journal* 871.1 (2019), p. 73.
- [106] A. Y. Q. Ho et al. “The Koala: A Fast Blue Optical Transient with Luminous Radio Emission from a Starburst Dwarf Galaxy at $z=0.27$ ”. In: *The Astrophysical Journal* 895.1 (2020), p. 49.
- [107] G. Hobbs et al. “The International Pulsar Timing Array project: using pulsars as a gravitational wave detector”. In: *Class. Quantum Gravity* 27.8 (2009), p. 084013.
- [108] S. Hooper et al. “Summed parallel infinite impulse response filters for low-latency detection of chirping gravitational waves”. In: *Phys. Rev. D* 86 (2 2012), p. 024012.
- [109] L. Hu et al. “Optical observations of LIGO source GW 170817 by the Antarctic Survey Telescopes at Dome A, Antarctica”. In: *Science Bulletin* 62.21 (2017), pp. 1433–1438.
- [110] IceCube Collaboration. “The IceCube Data Acquisition System: Signal Capture, Digitization, and Timestamping”. In: *Nucl. Instrum. Meth. A* 601 (2009), pp. 294–316.
- [111] Ž. Ivezić et al. “LSST: From Science Drivers to Reference Design and Anticipated Data Products”. In: *The Astrophysical Journal* 873.2 (2019), p. 111.
- [112] Sutton P. J. et al. “X-Pipeline: an analysis package for autonomous gravitational-wave burst searches”. In: *New Journal of Physics* 12.5 (2010), p. 053034.
- [113] P. Janeček et al. “FRAM telescopes and their measurements of aerosol content at the Pierre Auger Observatory and at future sites of the Cherenkov Telescope Array”. In: *European Physical Journal Web of Conferences*. Vol. 197. European Physical Journal Web of Conferences. 2019, p. 02008.
- [114] K. Jordi, E. K. Grebel, and K. Ammon. “Empirical color transformations between SDSS photometry and other photometric systems”. In: *A&A* 460.1 (2006), pp. 339–347.
- [115] O. Just et al. “Comprehensive nucleosynthesis analysis for ejecta of compact binary mergers”. In: *MNRAS* 448 (Feb. 2015), pp. 541–567.
- [116] N. Kanthanakorn. “Astronomie multi-messenger avec des télescopes à grand champ de vue : stratégies d’observation, analyse d’images, suivi de candidats, études et implications astrophysiques”. 2020TOU30120. PhD thesis. 2020.
- [117] S. Karpov. *STDPipe: Simple Transient Detection Pipeline*. 2021.

- [118] D. Kasen, R. Fernandez, and B. Metzger. “Kilonova light curves from the disc wind outflows of compact object mergers”. In: *MNRAS* 450 (2015), pp. 1777–1786.
- [119] S. Klimentenko et al. “Method for detection and reconstruction of gravitational wave transients with networks of advanced detectors”. In: *Phys. Rev. D* 93 (2016), p. 042004.
- [120] J. Knödseder. “The CTA Observatory”. In: *AIP Conference Proceedings* 1379 (2011), pp. 175–182.
- [121] D. Kocevski and C. C. Cheung. “Fermi-LAT Search for Gamma-ray Emission from AT2018cow”. In: *The Astronomer’s Telegram* 11808 (2018), p. 1.
- [122] “Kolmogorov–Smirnov Test”. In: *The Concise Encyclopedia of Statistics*. 2008, pp. 283–287.
- [123] A. Kostov and T. Bonev. “Transformation of Pan-STARRS1 gri to Stetson BVRI magnitudes. Photometry of small bodies observations.” In: *Bulgarian Astronomical Journal* 28 (2018), p. 3.
- [124] R. G. Kron. “Photometry of a complete sample of faint galaxies.” In: *The Astrophysical Journal Supplement Series* 43 (1980), pp. 305–325.
- [125] N. P. M. Kuin et al. “Swift spectra of AT2018cow: a white dwarf tidal disruption event?” In: *Monthly Notices of the Royal Astronomical Society* 487.2 (2019), pp. 2505–2521. ISSN: 0035-8711.
- [126] M. D. Lallo. “Experience with the Hubble Space Telescope: 20 years of an archetype”. In: *Optical Engineering* 51 (2012), p. 011011.
- [127] G. P. Lamb, I. Mandel, and L. Resmi. “Late-time evolution of afterglows from off-axis neutron star mergers”. In: *MNRAS* 481 (2018), pp. 2581–2589.
- [128] A. U. Landolt. “UBVRI Photometric Standard Stars in the Magnitude Range $11.5 < V < 16.0$ Around the Celestial Equator”. In: *The Astronomical Journal* 104 (1992), p. 340.
- [129] D. Lang et al. “Astrometry.net: Blind Astrometric Calibration of Arbitrary Astronomical Images”. In: *The Astronomical Journal* 139.5 (2010), pp. 1782–1800.
- [130] A. Lartaux-Vollard. “Beating the standard quantum limit for the gravitational wave detector Advanced Virgo”. 2020UPASP046. PhD thesis. 2020.
- [131] L. Leitao, A. Mégevand, and A. D. D. Sánchez. “Gravitational waves from the electroweak phase transition”. In: *Journal of Cosmology and Astroparticle Physics* 2012.10 (2012), pp. 024–024.
- [132] L.-X Li and B. Paczyński. “Transient Events from Neutron Star Mergers”. In: *The Astrophysical Journal* 507.1 (1998), pp. L59–L62.
- [133] W. Li et al. “The Katzman Automatic Imaging Telescope Gamma-Ray Burst Alert System, and Observations of GRB020813”. In: *Publications of the Astronomical Society of the Pacific* 115.809 (2003), pp. 844–853.

- [134] A. Lien et al. “The Swift Burst Alert Telescope gamma-ray burst catalog”. In: *The Astrophysical Journal* 829.1 (2016), p. 7.
- [135] LIGO Collaboration and Virgo Collaboration. “Tests of General Relativity with GW170817”. In: *Physical Review Letters* 123.1 (2019).
- [136] LIGO Scientific Collaboration. *LIGO Algorithm Library - LALSuite*. 2018.
- [137] LIGO Scientific Collaboration and Virgo Collaboration. “Observation of Gravitational Waves from a Binary Black Hole Merger”. In: *Phys. Rev. Lett.* 116 (2016), p. 061102.
- [138] LIGO Scientific Collaboration and Virgo Collaboration. “Observing gravitational-wave transient GW150914 with minimal assumptions”. In: *Phys. Rev. D* 93 (2016), p. 122004.
- [139] LIGO Scientific Collaboration and Virgo Collaboration. “GW170817: Observation of Gravitational Waves from a Binary Neutron Star Inspiral”. In: *Phys. Rev. Lett.* 119 (2017), p. 161101.
- [140] LIGO Scientific Collaboration and Virgo Collaboration. “Constraints on cosmic strings using data from the first Advanced LIGO observing run”. In: *Physical Review D* 97 (2018), p. 102002.
- [141] LIGO Scientific Collaboration and Virgo Collaboration. “GW170817: Implications for the Stochastic Gravitational-Wave Background from Compact Binary Coalescences”. In: *Phys. Rev. Lett.* 120 (2018), p. 091101.
- [142] LIGO Scientific Collaboration and Virgo Collaboration. “GWTC-1: A Gravitational-Wave Transient Catalog of Compact Binary Mergers Observed by LIGO and Virgo during the First and Second Observing Runs”. In: *Phys. Rev. X* 9 (2019), p. 031040.
- [143] LIGO Scientific Collaboration and Virgo Collaboration. “LIGO/Virgo S191213g: Identification of a GW compact binary merger candidate”. In: *GRB Coordinates Network* 26402 (2019).
- [144] LIGO Scientific Collaboration and Virgo Collaboration. “LIGO/Virgo S191213g: Updated Sky Localization”. In: *GRB Coordinates Network* 26417 (2019).
- [145] LIGO Scientific Collaboration and Virgo Collaboration. “Properties of the Binary Neutron Star Merger GW170817”. In: *Phys. Rev. X* 9 (2019), p. 011001.
- [146] LIGO Scientific Collaboration and Virgo Collaboration. “LIGO/Virgo S200213t: Identification of a GW compact binary merger candidate”. In: *GRB Coordinates Network* 27042 (2020).
- [147] LIGO Scientific Collaboration and Virgo Collaboration. “LIGO/Virgo S200213t: Updated Sky Localization”. In: *GRB Coordinates Network* 27096 (2020).
- [148] LIGO Scientific Collaboration, Virgo Collaboration, and Fermi Collaboration. “Gravitational Waves and Gamma-Rays from a Binary Neutron Star Merger: GW170817 and GRB170817A”. In: *The Astrophysical Journal* 848.2 (2017), p. L13.

- [149] LIGO Scientific Collaboration, Virgo Collaboration, and KAGRA Collaboration. *All-sky, all-frequency directional search for persistent gravitational-waves from Advanced LIGO's and Advanced Virgo's first three observing runs*. 2021. eprint: 2110.09834.
- [150] LIGO Scientific Collaboration, Virgo Collaboration, and KAGRA Collaboration. "GW190425: Observation of a Compact Binary Coalescence with Total Mass $\sim 3.4 M_{\odot}$ ". In: *The Astrophysical Journal Letters* 915 (2021), p. L5.
- [151] LIGO Scientific Collaboration, Virgo Collaboration, and KAGRA Collaboration. "GWTC-3: Compact Binary Coalescences Observed by LIGO and Virgo During the Second Part of the Third Observing Run". In: (2021). eprint: 2111.03606.
- [152] LIGO Scientific Collaboration, Virgo Collaboration, and KAGRA Collaboration. *GWTC-3: Compact Binary Coalescences Observed by LIGO and Virgo During the Second Part of the Third Observing Run — Candidate data release*. 2021. DOI: <https://doi.org/10.5281/zenodo.5546665>.
- [153] LIGO Scientific Collaboration, Virgo Collaboration, and KAGRA Collaboration. "Observation of Gravitational Waves from Two Neutron Star-Black Hole Coalescences". In: *The Astrophysical Journal Letters* (2021).
- [154] LIGO Scientific Collaboration, Virgo Collaboration, and KAGRA Collaboration. "Search for Gravitational Waves Associated with Gamma-Ray Bursts Detected by Fermi and Swift during the LIGO-Virgo Run O3a". In: *The Astrophysical Journal* 915.2 (2021), p. 86.
- [155] LIGO Scientific Collaboration, Virgo Collaboration, and KAGRA Collaboration. *Searches for Gravitational Waves from Known Pulsars at Two Harmonics in the Second and Third LIGO-Virgo Observing Runs*. 2021. eprint: 2111.13106.
- [156] LIGO Scientific Collaboration, Virgo Collaboration, and KAGRA Collaboration. *LVK observation plan*. <https://observing.docs.ligo.org/plan/>. [Online; accessed 09-July-2022]. 2022.
- [157] LIGO Scientific Collaboration, Virgo Collaboration, and KAGRA Collaboration. "Search for Gravitational Waves Associated with Gamma-Ray Bursts Detected by Fermi and Swift during the LIGO-Virgo Run O3b". In: *The Astrophysical Journal* 928.2 (2022), p. 186.
- [158] LIGO Scientific Collaboration, Virgo Collaboration, and Kagra Collaboration. "Prospects for observing and localizing gravitational-wave transients with Advanced LIGO, Advanced Virgo and KAGRA". In: *Living Reviews in Relativity* 21.1 (2020), p. 3.
- [159] LIGO Scientific Collaboration et al. "Multi-messenger observations of a binary neutron star merger". In: 848.2 (2017), p. L12.
- [160] LIGO Scientific Collaboration et al. "Search for Gravitational Waves Associated with Fast Radio Bursts Detected by CHIME/FRB During the LIGO-Virgo Observing Run O3a". In: (2022). eprint: 2203.12038.

- [161] V. Lipunov et al. “MASTER global robotic net”. In: *Astronomical Society of India Conference Series*. Vol. 7. Astronomical Society of India Conference Series. 2012.
- [162] D. R. Lorimer. “Binary and Millisecond Pulsars”. In: *Living Reviews in Relativity* 11.1 (2008), p. 8.
- [163] D. R. Lorimer et al. “A Bright Millisecond Radio Burst of Extragalactic Origin”. In: *Science* 318.5851 (2007), pp. 777–780.
- [164] J. D. Lyman et al. *The optical afterglow of the short gamma-ray burst associated with GW170817*. 2018.
- [165] B. Margalit and B. D. Metzger. “The Multi-messenger Matrix: The Future of Neutron Star Merger Constraints on the Nuclear Equation of State”. In: *The Astrophysical Journal* 880.1 (2019), p. L15.
- [166] R. Margutti et al. “An Embedded X-Ray Source Shines through the Aspherical AT 2018cow: Revealing the Inner Workings of the Most Luminous Fast-evolving Optical Transients”. In: *The Astrophysical Journal* 872.1 (2019), p. 18.
- [167] F. J. Masci et al. “The Zwicky Transient Facility: Data Processing, Products, and Archive”. In: *Publications of the Astronomical Society of the Pacific* 131.995 (2018), p. 018003.
- [168] O. McBrien et al. “LIGO/Virgo S191213g: Pan-STARRS1 discovery of a potential optical counterpart”. In: *GRB Coordinates Network* 26485 (2019).
- [169] J. E. McClintock, R. Narayan, and J. F. Steiner. “Black Hole Spin via Continuum Fitting and the Role of Spin in Powering Transient Jets”. In: *Space Science Reviews* 183.1 (2014), pp. 295–322.
- [170] C. McCully and M. Tewes. *Astro-SCRAPPY: Speedy Cosmic Ray Annihilation Package in Python*. 2019. eprint: 1907.032.
- [171] C. Meegan et al. “The FERMI Gamma-Ray Burst Monitor”. In: *The Astrophysical Journal* 702.1 (2009), pp. 791–804.
- [172] J. d. J. Mendoza-Temis et al. “Nuclear robustness of the r process in neutron-star mergers”. In: *Physical Review C* 92 (2015), p. 055805.
- [173] W. Meng-Ru et al. “Fingerprints of Heavy-Element Nucleosynthesis in the Late-Time Lightcurves of Kilonovae”. In: *Phys. Rev. Lett.* 122 (6 2019), p. 062701.
- [174] F. Messina et al. “Quasi-5.5PN TaylorF2 approximant for compact binaries: Point-mass phasing and impact on the tidal polarizability inference”. In: *Phys. Rev. D* 99 (12 2019), p. 124051.
- [175] B. D. Metzger. “Kilonovae”. In: *Living Reviews in Relativity* 23.1 (2019), p. 1.
- [176] B. D. Metzger. “Luminous Fast Blue Optical Transients and Type Ibn/Icn SNe from Wolf-Rayet/Black Hole Mergers”. In: *The Astrophysical Journal* 932.2 (2022), p. 84.

- [177] B. D. Metzger and R. Fernández. “Red or blue? A potential kilonova imprint of the delay until black hole formation following a neutron star merger”. In: *MNRAS* 441 (2014), pp. 3444–3453.
- [178] B. D. Metzger, A. L. Piro, and E. Quataert. “Time-dependent models of accretion discs formed from compact object mergers”. In: *MNRAS* 390 (2008), pp. 781–797.
- [179] B. D. Metzger, T. A. Thompson, and E. Quataert. “On the Conditions for Neutron-Rich Gamma-Ray Burst Outflows”. In: *Astrophys. J.* 676 (2008), p. 1130.
- [180] B. D. Metzger, T. A. Thompson, and E. Quataert. “A magnetar origin for the kilonova ejecta in GW170817”. In: *Astrophys. J.* 856 (2018), p. 101.
- [181] B. D. Metzger et al. “Electromagnetic counterparts of compact object mergers powered by the radioactive decay of r-process nuclei”. In: *Monthly Notices of the Royal Astronomical Society* 406.4 (2010), pp. 2650–2662.
- [182] B. D. Metzger et al. “Neutron-powered precursors of kilonovae”. In: *MNRAS* 446 (2015), pp. 1115–1120.
- [183] M. J. Michalowski et al. “Nature of the unusual transient AT 2018cow from HI observations of its host galaxy”. In: *A&A* 627 (2019), A106.
- [184] Mochkovitch, R. et al. “Prospects for kilonova signals in the gravitational-wave era”. In: *A&A* 651 (2021), A83.
- [185] A. Möller et al. “fink, a new generation of broker for the LSST community”. In: *Monthly Notices of the Royal Astronomical Society* 501.3 (2020), pp. 3272–3288.
- [186] D. G. Monet et al. “The USNO-B Catalog”. In: *The Astronomical Journal* 125.2 (2003), pp. 984–993.
- [187] K. P. Mooley et al. “Superluminal motion of a relativistic jet in the neutron-star merger GW170817”. In: *Nature* 561.7723 (2018), pp. 355–359.
- [188] C. J. Moore, R. H. Cole, and C. P. L. Berry. “Gravitational-wave sensitivity curves”. In: *Classical and Quantum Gravity* 32.1 (2014), p. 015014.
- [189] B. Mours. *Conseil scientifique de l’IN2P3*. http://old.in2p3.fr/actions/conseils_scientifiques/media/Expose_02_2017_B.Mours.pdf. [Online; accessed 09-July-2022]. 2017.
- [190] M.i Nakahata. “History of Solar Neutrino Observations”. In: *arXiv e-prints* (2022), arXiv:2202.12421.
- [191] A. Nathanail et al. “On the opening angle of magnetized jets from neutron-star mergers: the case of GRB170817A”. In: *Monthly Notices of the Royal Astronomical Society* 495.4 (2020), pp. 3780–3787.
- [192] Antonios Nathanail et al. “3D magnetized jet break-out from neutron-star binary merger ejecta: afterglow emission from the jet and the ejecta”. In: *Monthly Notices of the Royal Astronomical Society* 502.2 (2021), pp. 1843–1855.
- [193] V. Nedora et al. “Spiral-wave Wind for the Blue Kilonova”. In: *The Astrophysical Journal* 886.2 (2019), p. L30.

- [194] A. H. Nitz et al. “Rapid detection of gravitational waves from compact binary mergers with PyCBC Live”. In: *Phys. Rev. D* 98 (2018), p. 024050.
- [195] Alexander H. Nitz et al. “Detecting Binary Compact-object Mergers with Gravitational Waves: Understanding and Improving the Sensitivity of the PyCBC Search”. In: *The Astrophysical Journal* 849.2 (2017), p. 118.
- [196] K. Noysena et al. “Limits on the Electromagnetic Counterpart of Binary Black Hole Coalescence at Visible Wavelengths”. In: *The Astrophysical Journal* 886.1 (2019), p. 73.
- [197] P. Nugent, A. Kim, and S. Perlmutter. “ K -Corrections and Extinction Corrections for Type Ia Supernovae”. In: *Publications of the Astronomical Society of the Pacific* 114.798 (2002), pp. 803–819.
- [198] R. Oechslin and H.-T. Janka. “Torus formation in neutron star mergers and well-localized short gamma-ray bursts”. In: *Monthly Notices of the Royal Astronomical Society* 368 (2006), pp. 1489–1499.
- [199] M. Oguri. “Measuring the distance-redshift relation with the cross-correlation of gravitational wave standard sirens and galaxies”. In: *Phys. Rev. D* 93 (2016), p. 083511.
- [200] C. D. Ott. “The gravitational-wave signature of core-collapse supernovae”. In: *Classical and Quantum Gravity* 26.6 (2009), p. 063001.
- [201] B. J. Owen. “Search templates for gravitational waves from inspiraling binaries: Choice of template spacing”. In: *Phys. Rev. D* 53 (1996), pp. 6749–6761.
- [202] Frédéric P. “Gamma-ray bursts at high and very high energies”. In: *Comptes Rendus Physique* 17.6 (2016), pp. 617–631.
- [203] D. R. Pasham et al. “Evidence for a compact object in the aftermath of the extragalactic transient AT2018cow”. In: *Nature Astronomy* 6.2 (2022), pp. 249–258.
- [204] D. A. Perley et al. “The fast, luminous ultraviolet transient AT2018cow: extreme supernova, or disruption of a star by an intermediate-mass black hole?” In: *Monthly Notices of the Royal Astronomical Society* 484.1 (2018), pp. 1031–1049.
- [205] F. Pirani. *Measurement of Classical Gravitation Fields*. The Role of Gravitation in Physics: Report from the 1957 Chapel Hill Conference. Berlin: Max-Planck-Gesellschaft zur Förderung der Wissenschaften. 2011.
- [206] Planck Collaboration. “Planck 2018 results - VI. Cosmological parameters”. In: *A&A* 641 (2020), A6.
- [207] E. Poisson and C. M. Will. “Gravitational waves from inspiraling compact binaries: Parameter estimation using second-post-Newtonian waveforms”. In: *Phys. Rev. D* 52 (1995), pp. 848–855.

- [208] D. Pooley et al. “GW170817 Most Likely Made a Black Hole”. In: *The Astrophysical Journal* 859.2 (2018), p. L23.
- [209] R. Popham, S. E. Woosley, and C. Fryer. “Hyperaccreting Black Holes and Gamma-Ray Bursts”. In: *The Astrophysical Journal* 518 (1999), pp. 356–374.
- [210] S. J. Prentice et al. “The Cow: Discovery of a Luminous, Hot, and Rapidly Evolving Transient”. In: *The Astrophysical Journal* 865.1 (2018), p. L3.
- [211] M. Prouza et al. “FRAM - The Robotic Telescope for the Monitoring of the Wavelength Dependence of the Extinction: Description of Hardware, Data Analysis, and Results”. In: *Advances in Astronomy* 2010 (), p. 849382.
- [212] M. Rakhmanov, J. D. Romano, and J. T. Whelan. “High-frequency corrections to the detector response and their effect on searches for gravitational waves”. In: *Classical and Quantum Gravity* 25.18 (2008), p. 184017.
- [213] J. C. Rastinejad et al. “A Kilonova Following a Long-Duration Gamma-Ray Burst at 350 Mpc”. In: (2022). eprint: 2204.10864.
- [214] James E. Rhoads. “How to Tell a Jet from a Balloon: A Proposed Test for Beaming in Gamma-Ray Bursts”. In: *The Astrophysical Journal* 487 (1997), p. L1.
- [215] A. G. Riess. “A Comprehensive Measurement of the Local Value of the Hubble Constant with 1 km/s/Mpc Uncertainty from the Hubble Space Telescope and the SH0ES Team”. In: (2021). eprint: 2112.04510.
- [216] S. Rosswog. “Fallback accretion in the aftermath of a compact binary merger”. In: *Monthly Notices of the Royal Astronomical Society: Letters* 376 (2007), pp. L48–L51.
- [217] S. Roy, A. S. Sengupta, and P. Ajith. “Effectual template banks for upcoming compact binary searches in Advanced-LIGO and Virgo data”. In: *Phys. Rev. D* 99 (2019), p. 024048.
- [218] S. Roy, A. S. Sengupta, and N. Thakor. “Hybrid geometric-random template-placement algorithm for gravitational wave searches from compact binary coalescences”. In: *Phys. Rev. D* 95 (2017), p. 104045.
- [219] J. Salgado et al. “The ESA Gaia Archive: Data Release 1”. In: *Astronomy and Computing* 21 (2017), pp. 22–26.
- [220] B. S. Sathyaprakash and S. V. Dhurandhar. “Choice of filters for the detection of gravitational waves from coalescing binaries”. In: *Phys. Rev. D* 44 (1991), pp. 3819–3834.
- [221] SDSS collaboration. *Transformation equations for SDSS*. <http://www.sdss3.org/dr8/algorithms/sdssUBVRITransform.php>. [Online; accessed 05-July-2022]. 2013.
- [222] M. Shibata and K. Taniguchi. “Merger of binary neutron stars to a black hole: Disk mass, short gamma-ray bursts, and quasinormal mode ringing”. In: *Phys. Rev. D* 73 (2006), p. 064027.

- [223] D. M. Siegel et al. “Magnetorotational instability in relativistic hypermassive neutron stars”. In: *Phys. Rev. D* 87 (2013), p. 121302.
- [224] X. Siemens et al. “Gravitational wave bursts from cosmic (super)strings: Quantitative analysis and constraints”. In: *Phys. Rev. D* 73 (2006), p. 105001.
- [225] L. P. Singer and L. R. Price. “Rapid Bayesian position reconstruction for gravitational-wave transients”. In: *Phys. Rev. D* 93 (2016), p. 024013.
- [226] S. J. Smartt et al. “A kilonova as the electromagnetic counterpart to a gravitational-wave source”. In: *Nature* 551.7678 (2017), pp. 75–79.
- [227] S. J. Smartt et al. “ATLAS18qqn (AT2018cow) - a bright transient spatially coincident with CGCG 137-068 (60 Mpc)”. In: *The Astronomer’s Telegram* 11727 (2018), p. 1.
- [228] M. Soares-Santos et al. “The Electromagnetic Counterpart of the Binary Neutron Star Merger LIGO/Virgo GW170817. I. Discovery of the Optical Counterpart Using the Dark Energy Camera”. In: *The Astrophysical Journal* 848 (2017), p. L16.
- [229] C. Stachie et al. “Using machine learning for transient classification in searches for gravitational-wave counterparts”. In: *Monthly Notices of the Royal Astronomical Society* 497.2 (2020), pp. 1320–1331.
- [230] D. Steeghs et al. “The Gravitational-wave Optical Transient Observer (GOTO): prototype performance and prospects for transient science”. In: *Monthly Notices of the Royal Astronomical Society* 511.2 (2022), pp. 2405–2422.
- [231] I. A. Steele et al. “The Liverpool Telescope: performance and first results”. In: *Ground-based Telescopes*. Vol. 5489. International Society for Optics and Photonics. 2004, pp. 679–692.
- [232] P. B. Stetson. “Homogeneous Photometry for Star Clusters and Resolved Galaxies. II. Photometric Standard Stars”. In: *The Publications of the Astronomical Society of the Pacific* 112.773 (2000), pp. 925–931.
- [233] P. Stoica and R. Moses. “Spectral Analysis of Signals”. In: Jan. 2005.
- [234] R. Surman et al. “r-Process Nucleosynthesis in Hot Accretion Disk Flows from Black Hole - Neutron Star Mergers”. In: *Astrophys. J. Lett.* 679 (2008), pp. L117–L120.
- [235] N. R. Tanvir et al. “The Emergence of a Lanthanide-rich Kilonova Following the Merger of Two Neutron Stars”. In: *The Astrophysical Journal* 848.2 (2017), p. L27.
- [236] J. H. Taylor and J. M. Weisberg. “A new test of general relativity - Gravitational radiation and the binary pulsar PSR 1913+16”. In: *apj* 253 (1982), pp. 908–920.
- [237] Fermi-GBM Team. In: 524666471 (2017). URL: <https://gcn.gsfc.nasa.gov/other/524666471.fermi>.
- [238] “The characterization of Virgo data and its impact on gravitational-wave searches”. In: *Classical and Quantum Gravity* 29.15 (2012), p. 155002.

- [239] The CHIME/FRB Collaboration. “A bright millisecond-duration radio burst from a Galactic magnetar”. In: *Nature* 587.7832 (2020), pp. 54–58.
- [240] “The population of merging compact binaries inferred using gravitational waves through GWTC-3”. In: (2021). eprint: 2111.03634.
- [241] J. L. Tonry et al. “ATLAS: A High-cadence All-sky Survey System”. In: *Publications of the Astronomical Society of the Pacific* 130.988 (2018), p. 064505.
- [242] E. Troja et al. “The X-ray counterpart to the gravitational-wave event GW170817”. In: *Nature* 551.7678 (2017), pp. 71–74.
- [243] E. Troja et al. “A luminous blue kilonova and an off-axis jet from a compact binary merger at $z=0.1341$ ”. In: *Nature Communications* 9.1 (2018), p. 4089.
- [244] E. Troja et al. “A year in the life of GW 170817: the rise and fall of a structured jet from a binary neutron star merger”. In: *MNRAS* 489 (Oct. 2019), pp. 1919–1926.
- [245] E. Troja et al. “The afterglow and kilonova of the short GRB 160821B”. In: *Monthly Notices of the Royal Astronomical Society* 489.2 (2019), pp. 2104–2116.
- [246] E. Troja et al. “Accurate flux calibration of GW170817: is the X-ray counterpart on the rise?” In: *MNRAS* 510.2 (2021), pp. 1902–1909.
- [247] E Troja et al. “A year in the life of GW170817: the rise and fall of a structured jet from a binary neutron star merger”. In: *Monthly Notices of the Royal Astronomical Society* 489.2 (2019), pp. 1919–1926.
- [248] S. A. Usman, J. C. Mills, and S. Fairhurst. “Constraining the Inclinations of Binary Mergers from Gravitational-wave Observations”. In: *The Astrophysical Journal* 877.2 (2019), p. 82.
- [249] S. A. Usman et al. “The PyCBC search for gravitational waves from compact binary coalescence”. In: *Classical and Quantum Gravity* 33.21 (2016), p. 215004.
- [250] P. Valley et al. “LIGO/Virgo S191213g: LBT spectrum of AT2019wxt (PS19hgw) reveals a type IIb supernova”. In: *GRB Coordinates Network* 26508 (2019).
- [251] P. G. Van Dokkum. “Cosmic-Ray Rejection by Laplacian Edge Detection”. In: *The Publications of the Astronomical Society of the Pacific* 113.789 (2001), pp. 1420–1427.
- [252] J. Veitch et al. “Parameter estimation for compact binaries with ground-based gravitational-wave observations using the LALInference software library”. In: *Phys. Rev. D* 91 (2015), p. 042003.
- [253] V. A. Villar et al. “The Combined Ultraviolet, Optical, and Near-infrared Light Curves of the Kilonova Associated with the Binary Neutron Star Merger GW170817: Unified Data Set, Analytic Models, and Physical Implications”. In: *The Astrophysical Journal* 851.1 (2017), p. L21.
- [254] C. Vogl et al. “LIGO/Virgo S191213g: VLT spectrum of AT2019wxt (PS19hgw) - a probable Ib supernova”. In: *GRB Coordinates Network* 26504 (2019).

- [255] S. J. van der Walt, A. Crellin-Quick, and J. S. Bloom. “SkyPortal: An Astronomical Data Platform”. In: *Journal of Open Source Software* 4.37 (2019).
- [256] J. Weber. “Detection and Generation of Gravitational Waves”. In: *Phys. Rev.* (1960).
- [257] J. Weber. “Evidence for Discovery of Gravitational Radiation”. In: *Phys. Rev. Lett.* 22 (1969), pp. 1320–1324.
- [258] J. Wei et al. *The Deep and Transient Universe in the SVOM Era: New Challenges and Opportunities - Scientific prospects of the SVOM mission*. Research Report. 2016.
- [259] M. C. Weisskopf et al. “Chandra X-ray Observatory (CXO): overview”. In: *X-Ray Optics, Instruments, and Missions III*. Vol. 4012. 2000, pp. 2–16.
- [260] P. Welch. “The use of fast Fourier transform for the estimation of power spectra: A method based on time averaging over short, modified periodograms”. In: *IEEE Transactions on Audio and Electroacoustics* 15.2 (1967), pp. 70–73.
- [261] N. Wiener. “Generalized harmonic analysis”. In: *Acta Mathematica* 55 (1930), pp. 117–258.
- [262] R. L. Workman et al. “Review of Particle Physics”. In: *PTEP* 2022 (2022), p. 083C01.
- [263] C. Xin, C. M. F. Mingarelli, and J. S. Hazboun. “Multimessenger Pulsar Timing Array Constraints on Supermassive Black Hole Binaries Traced by Periodic Light Curves”. In: *The Astrophysical Journal* 915.2 (2021), p. 97.
- [264] S. Yi and K. S. Cheng. “Where Are the Electromagnetic-wave Counterparts of Stellar-mass Binary Black Hole Mergers?” In: *The Astrophysical Journal* 884.1 (2019), p. L12.
- [265] B. Zhang. *The Physics of Gamma-Ray Bursts*. 2018.
- [266] J. Zhu et al. “Long-duration Gamma-ray Burst and Associated Kilonova Emission from Fast-spinning Black Hole–Neutron Star Mergers”. In: (2022). eprint: 2207.10470.
- [267] Y. Zhu et al. “Californium-254 and Kilonova Light Curves”. In: *The Astrophysical Journal* 863.2 (2018), p. L23.
- [268] M. Zimmermann. “Revised estimate of gravitational radiation from Crab and Vela pulsars”. In: *Nature* 271.5645 (1978), pp. 524–525.

Titre: Astronomie Multi-Messagers: de la localisation des sources transitoires d'ondes gravitationnelles au suivi optique.

Mots clés: ciel transitoire, ondes gravitationnelles, LIGO-Virgo

Résumé: L'astronomie multi-messager combine les informations fournies via différents signaux physiques. Cette dernière a pris son essor le 17 août 2017 lors de la détection conjointe d'une onde gravitationnelle (OG) par les détecteurs LIGO et Virgo et d'émissions couvrant tout le spectre électromagnétique des rayons gamma aux ondes radio. La source identifiée est une coalescence de deux étoiles à neutrons à 40 Mpc. Le sursaut gamma est la première contrepartie observée par l'instrument GBM du satellite Fermi, moins de deux secondes après la détection de l'OG. 11h après la fusion, la contrepartie optique, appelée kilonova, est découverte par le télescope Swope. Et quelques semaines après, les signaux X et radio sont découverts par le satellite Chandra et le radiotélescope VLA respectivement. Cet événement a véritablement lancé l'astronomie multi-messager basée sur les OG. Elle a notamment eu pour conséquence la création du réseau GRANDMA dont les objectifs sont:

- Gestion des alertes OG
- Suivi optique
- Caractérisation des candidats
- Interprétation astrophysique

Le développement de l'infrastructure est notamment passé par la création de Muphoten, un code d'analyse photométrique capable de créer des données homogènes, malgré l'hétérogénéité des instruments de GRANDMA. Cette analyse a été développée grâce au suivi de la supernova SN2018cow par de nombreux instruments, incluant certains de GRANDMA. En parallèle de ce développement, GRANDMA a été particulièrement actif pendant la campagne d'acquisition de données par LIGO et Virgo O3 en suivant 49 des 53 alertes publiées. Aucune contrepartie, optique ou autre, n'a été découverte par GRANDMA ou un autre groupe. Mais la campagne a démontré le potentiel du réseau pour le suivi de transitoires optiques rapides tels que les kilonovae. En vue de poursuivre le développement du réseau, et de préparer O4, deux cam-

pagnes ont été organisées par GRANDMA. Pour la première, GRANDMA et sa branche amateur, Kilonova-Catcher, ont suivi 12 alertes produites par le relevé ZTF. Cela a permis de développer les capacités de GRANDMA à caractériser et classer des transitoires optiques via une analyse purement photométrique, ce qui est une des contraintes imposées par le suivi d'alertes OG. D'autre part, cette campagne a permis d'utiliser Muphoten ainsi qu'une autre analyse photométrique indépendante, STD-pipe permettant d'évaluer la présence de biais systématiques dans l'un ou l'autre des codes et de finalement démontrer que les résultats produits étaient cohérents. Pour la seconde campagne de GRANDMA, les observateurs ont suivi les alertes du satellite Swift, détectant des sursauts gamma, afin de trouver les émissions optiques associées à l'émission gamma, appelées afterglow. L'analyse de ces observations est toujours en cours. Cependant, la découverte de contreparties électromagnétiques aux émissions d'OG nécessite l'envoi d'informations fiables dans les premières minutes suivant la détection du signal. L'une des plus cruciales pour le suivi par GRANDMA est la localisation spatiale de la source, évaluée par l'algorithme Bayestar. Afin d'évaluer la consistance des résultats produits par Bayestar, des simulations de fusion d'objets compacts ont été produites et utilisées pour faire un test pourcentage-pourcentage. Ce dernier permet d'évaluer si la reconstruction des paramètres de la source, ce qui inclut la position, est biaisée. Ceci a permis d'identifier le paramètre ξ , codé en dur dans Bayestar, comme pouvant conduire à une surestimation des incertitudes, et in fine, une plus grande aire à couvrir par les instruments de suivi électromagnétique. Des simulations additionnelles, incluant des injections de signaux analysées en ligne par PyCBC Live, ont été faites pour déterminer pourquoi ce paramètre était nécessaire à Bayestar. Celles-ci conduisent à conclure que ξ permet de compenser les différences entre les paramètres de la source et ceux du modèle de forme d'onde utilisés pour localiser la source.

Title: Multi-Messenger astronomy, localisation of transient sources of gravitational waves and optical follow-up of gravitational wave candidates.

Keywords: transient sky, gravitational waves, LIGO-Virgo

Abstract: Multi-messenger astronomy (MMA) aims at combining the information provided by different physical signals. MMA was launched on August, 17th 2017 via the joint detection of a gravitational wave (GW) by the LIGO and Virgo detectors and in the electromagnetic regime over the whole spectrum. This was emitted by a binary neutron stars merger, located at 40 Mpc. The gamma ray burst (GRB) was the first counterpart detected by the GBM instrument of the Fermi satellite less than two seconds after the GW alert. After 11h, the optical counterpart, the so-called kilonova, was discovered by the Swope telescope. Few weeks later, the X-ray and radio signals were discovered by the Chandra and VLA instruments respectively. This event started the GW-based MMA, and led to the creation of the GRANDMA network of telescopes. The main goals of the network are:

- Dealing with the GW alerts
- Optical follow-up
- Candidate counterpart characterisation
- Astrophysical interpretation.

The GRANDMA infrastructure development involved the creation of a photometry pipeline called Muphoten, able to create homogeneous datasets, despite the instrument's heterogeneity. Muphoten was developed via the use of images produced during the follow-up of the supernova SN2018cow by various telescopes, including some GRANDMA instruments. The network was heavily involved in the optical follow-up of the GW alerts produced during the O3 observing run. GRANDMA followed 49 of the 53 alerts publicly distributed by LIGO and Virgo, however, no counterpart was discovered neither by GRANDMA nor by any other group. Despite the non-detection, the campaign demonstrated the network's ability to follow rapidly evolving optical tran-

sients. In order to prepare for the upcoming O4, two campaigns were set up. The first one consisted in the follow-up of 12 alerts produced by the ZTF survey. It allowed GRANDMA's ability to characterise and classify the observed transients. This was done based only on photometric data, which is one of the major constraints imposed by the GW optical follow-up. Moreover, Muphoten along with another independent photometry pipeline were used to produce the datasets used for the analysis. The use of two independent codes allowed us to evaluate whether one of the analyses was biased. It turned out that the results produced by Muphoten and STDpipe were compatible. The second campaign consisted in the follow-up of Swift satellite GRB alerts to find optical counterpart to the gamma emission, the so-called afterglow. The analysis is still ongoing for these observations. On the other hand, detecting electromagnetic counterpart to GW events requires that reliable information produced by the LIGO Virgo detector are rapidly distributed. In particular, one of the most important for GRANDMA is the source spatial localisation. The latter is given by the Bayestar algorithm whose accuracy has been tested. This was done with a percentile-percentile test that evaluates whether the analysis is biased. A first round of compact binary coalescence simulations allowed to identify a hard-coded parameter ξ as particularly sensitive for sky-localisation. It can lead to an overestimation of the localisation uncertainties, that would result into a oversized area to cover with the electromagnetic follow-up instruments. Additional simulations, including an end-to-end online analysis with PyCBC Live, were performed to find why ξ was necessary to implement. Based on these, it is suspected that ξ compensate or the difference between the source parameters and the simulated waveform parameters used for the localisation.

